TECHNISCHE UNIVERSITÄT DRESDEN

Fakultät Maschinenwesen·Institut für Werkstoffwissenschaft·Professur für Materialwissenschaft und Nanotechnik

Dissertation

Nanostructured biosensors with DNA-based receptors for real-time detection of small analytes

Zur Erlangung des akademischen Grades

Doktoringenieurin

Vorgelegt von

Stephanie Klinghammer

geb. Kelle

Geboren am 5. Dezember 1986 in Meißen

Technische Universität Dresden

Fakultät Maschinenwesen

Institut für Werkstoffwissenschaft

Professur für Materialwissenschaft und Nanotechnik

2023

Eingereicht am:
Verteidigt am:

1. Gutachter: Prof. Dr. Ginaurelio Cuniberti (TU Dresden)
2. Gutachter: Prof. Dr. Duncan Sutherland (Aarhus Universitet)
3. Gutachter: PD Dr. Vera Hintze (TU Dresden)

Kurzfassung

In zahlreichen lebenswichtigen Bereichen haben sich Biosensoren als unverzichtbare Messgeräte erwiesen. Der Nachweis von spezifischen Molekülen im Körper für eine frühzeitige Krankheitserkennung erfordert empfindliche und zuverlässige Messmethoden. Ein rasantes Fortschreiten im Bereich der Nanotechnologie führt dabei zur Entwicklung von Materialien mit neuen Eigenschaften, und damit verbunden, auch zu innovativen Anwendungsmöglichkeiten im Bereich der Biosensorik. Das Zusammenspiel von Nanotechnologie und Sensortechnik ermöglicht die Entwicklung von Sensoren mit empfindlicheren Nachweisgrenzen und kürzeren Reaktionszeiten. Die Möglichkeiten zur Integration und Miniaturisierung stellen einen erfolgreichen Einsatz in direkter Patientennähe in Aussicht, sodass Nanobiosensoren die Brücke zwischen Laborddiagnostik und Standardanwendungen schließen können.

Die folgende Arbeit widmet sich der Anwendung von nanostrukturierten Biosensoren für einen empfindlichen, markierungsfreien Nachweis von Analyten in Echtzeit. Ein Hauptaugenmerk liegt dabei auf der kontinuierlichen Messung von Biomarkern mit kompakten Auslesesystemen, die eine direkte Signalmeldung und somit einen Nachweis der Analyten in Echtzeit ermöglichen. Dies erfordert zunächst die sorgfältige Funktionalisierung von Sensoroberflächen mit geeigneten DNA-basierten Rezeptoren. Infolgedessen werden beispielhaft verschiedene Sensorsysteme, Analyten und Charakterisierungsmethoden vorgestellt und universelle Strategien für die erfolgreiche Konfiguration von Nanobiosensorplattformen präsentiert.

Das erste Anwendungsbeispiel widmet sich einem plasmonischen Biosensor, bei dem vertikal ausgerichtete Gold-Nanoantennen Signale mittels sog. lokalisierter Oberflächenplasmonenresonanz (LSPR) erzeugen. Mit dem Sensor konnte erfolgreich die Immobilisierung, das nachträgliche Blocken sowie die anschließende Hybridisierung von DNA nachgewiesen werden. Mithilfe des LSPR-Sensors wurden gleichzeitig grundlegende Hybridisierungsmechanismen auf nanostrukturierten und planaren Oberflächen verglichen und damit verbunden die einzigartigen optischen Eigenschaften metallischer Nanostrukturen betont.

In einem zweiten Anwendungsbeispiel misst ein elektrischer Biosensor kontinuierlich die Konzentration des Stressmarkers Cortisol im menschlichen Speichel. Der direkte, markierungsfreie Nachweis von Cortisol mit Silizium-Nanodraht basierten

Feldeffekttransistoren (SiNW FET) wurde anhand zugrunde liegender Ladungsverteilungen innerhalb des entstandenen Rezeptor-Analyte-Komplexes bewertet, so dass ein Nachweis des Analyten innerhalb der sog. Debye-Länge ermöglicht wird. Die erfolgreiche Strategie zur Oberflächenfunktionalisierung im Zusammenspiel mit dem Einsatz von SiNW FETs auf einem tragbaren Messgerät wurde anhand eines Cortisolnachweises im Speichel belegt. Ein übereinstimmender Vergleich der gemessenen Corisolkonzentrationen mit Werten, die mit einer kommerziellen Alternative ermittelt wurden, verdeutlichen das Potential der entwickelten Plattform.

Zusammenfassend veranschaulichen beide vorgestellten Nanobiosensor-Plattformen die vielseitige und vorteilhafte Leistungsfähigkeit der Systeme für einen kontinuierlichen Nachweis von Biomarkern in Echtzeit und vorzugsweise in Patientennähe.

Abstract

Biosensors have proven to be indispensable in numerous vital areas. For example, detecting the presence and concentration of specific biomarkers requires sensitive and reliable measurement methods. Rapid developments in the field of nanotechnology lead to nanomaterials with new properties and associated innovative applications. Thus, nanotechnology has a far-reaching impact on biosensors' development, e.g., delivery of biosensing devices with greater sensitivity, shorter response times, and precise but cost-effective sensor platforms. In addition, nanobiosensors hold high potential for integration and miniaturization and can operate directly at the point of care - serving as a bridge between diagnostics and routine tests.

This work focuses on applying nanostructured biosensors for the sensitive and label-free detection of analytes in real-time. A distinct aim is the continuous monitoring of biomarkers with compact read-out systems to provide direct, valuable feedback in real-time. The first step in achieving this goal is the adequate functionalization of nanostructured sensor surfaces with suitable receptors to detect analytes of interest. Due to their thermal and chemical stability with the possibility for customizable functionalization, DNA-based receptors are selected. Thereupon, universal strategies for confining nanobiosensor platforms are presented using different sensor systems, analytes, and characterization methods.

As a first application, a plasmonic biosensor based on vertically aligned gold nanoantennas tracked the immobilization, blocking, and subsequent hybridization of DNA by means of localized surface plasmon resonance (LSPR). At the same time, the LSPR sensor was used to evaluate fundamental hybridization mechanisms on nanostructured and planar surfaces, emphasizing the unique optical properties of metallic nanostructures.

In a second application, an electric sensor based on silicon nanowire field-effect transistors (SiNW FET) monitored the level of the stress marker cortisol in human saliva. Based on evaluating the underlying charge distributions within the resulting receptor-analyte complex of molecules, the detection of cortisol within the Debye length is facilitated. Thus, direct, label-free detection of cortisol in human saliva using SiNW FET was successfully applied to the developed platform and compared to cortisol levels obtained using a commercial alternative.

In summary, both presented platforms indicate a highly versatile and beneficial performance of nanobiosensors for continuous detection of biomarkers in real-time and preferably point-of-care (POC).

Abbreviations and symbols

AAO	Anodized aluminum oxide
APTES	3-aminopropyltriethoxysilane
AuNP	Gold nanoparticle
BSA	Bovine serum albumin
CA	Contact angle
CBB	Cortisol binding buffer
CD	Circular dichroism
CRP	C-Reactive protein
D	Drain
DMSO	Dimethyl sulfoxide
DNA	Deoxyribonucleic acid
EDC	N-(3-dimethylaminopropyl)-N′-ethylcarbodiimide
ELISA	Enzyme-linked immunosorbent assay
EtOH	Ethanol
FAM	6-FAM™ Dye Phosphoramidite
FET	Field effect transistor
FI	Fluorescence intensity
FITC	Fluorescein isothiocyanate
G	Gate
HB	Hybridization buffer
HC	Honeycomb shaped
HCl	Hydrochloric acid
HEPES	hydroxyethyl piperazineethanesulfonic acid
LIA	Luminescence Immunoassay
(L)SPR	(Localized) surface plasmon resonance
MCH	Mercaptohexanol
MCU	Microcontroller unit
MeOH	Methanol
MOSFET	Metal-oxide semiconductor field effect transistor
MUX	Multiplexing
NaOH	Sodium hydroxide
NHS	N-hydroxysuccinimide
NW	Nanowire

PBS	Phosphate buffered saline
PCB	Printed circuit board
PDMS	Polydimethylsiloxane
POC	Point-of-care
RE	Reference electrode
RI	Refractive index
RNA	Ribonucleic acid
RT	Room temperature
S	Source
SAM	Self assembles monolayer
SiNW	Silicon nanowire
Std	Standard
TESPSA	3-(triethoxysilyl)propylsuccinic anhydride
TRIS	Tris(hydroxymethyl)aminomethane

λ_D	Debye length (m)
I_{off}	Off-current (A)
I_{on}	On-current (A)
I_{DS}	Source-drain current (A)
V_G	Gate voltage (V)
V_{SD}	Source-drain voltage (V)
V_T	Threshold voltage (V)

Content

1 Introduction

The Covid-19 pandemic, the outbreak of human monkeypox, and the mass fish die-off in the Oder river have demonstrated once more the evident need for the rapid and reliable monitoring of chemical and biological compounds[1,2]. A wide variety of substances can either directly menace human, animal, and plant populations or lead to detrimental skewness of existing systems. Here, potential anomalies can affect individual molecules, whole organisms, or even the complete environment. Thus, the proper detection and monitoring of specific parameters become a critical task and demand for reliable sensing systems, especially in application areas such as the early and personal analysis of disease markers, securing food and industrial safety, and environmental monitoring. In addition, sensing harmful or toxic compounds in liquids or gases can significantly contribute to societal and environmental safety.

With a growing but at the same time aging population worldwide[3], the healthcare sector takes on a unique role in biosensing. The rapid analysis of parameters with low-cost devices in blood, or other body fluids, such as saliva, tears, or sweat, is particularly interesting. Early detection enables not only the diagnosis and consequently the treatment of illnesses in their early stages but also allows to take proper action to curtail diseases.

Biosensors are analytical devices in which a biological capture probe identifies the target analyte, and a transducer converts the biorecognition event into a measurable signal[4]. Consequently, the suitable choice, connection, and integration of both components are crucial in developing biosensors.

Over the last 60 years, biosensors have been found to be promising instruments that can fulfill the criteria for detecting potentially interesting substances, for instance glucose, pH, and specific protein acting as biomarkers for certain diseases, hormones, and pesticides[5,6]. The development of biosensors dates back to 1956 when Leland C. Clark invented the first working electrode for oxygen detection[7]. Further developments of the electrodes with enzymes expanded their application range until 1962, when the first amperometric detection of glucose laid the foundation for modern biosensor systems[8]. Up to now, the majority of the analyses in clinical diagnostics, environmental monitoring, food analysis, and process control are still performed via pricey, time-consuming, and labor intense methods, e.g., enzyme-linked immunosorbent assays (ELISA), polymerase

chain reaction (PCR), or gas chromatography-mass spectrometry (GC-MS). All the methods must be performed in dedicated, central laboratories by trained personnel[9].

However, the idea to scale down biosensors in a way that they can be used at the point-of-care, and preferably in real-time by untrained people became prominent when Terry et al. introduced a highly miniaturized gas chromatograph in 1979[10], and Manz et al. published a theoretical article about miniaturized total chemical analysis systems (μTAS)[11]. The idea of miniaturized chip devices used as diagnostic tools allows observation of various treatment-related parameters on-site without any temporal or spatial delay, especially for patients under clinical observation. Avoiding routine visits during their treatment via online diagnostics and thus avoiding the intense strain of traveling to medical facilities is one of the intentions of miniaturizing biosensors. Furthermore, portable and inexpensive devices lead to fast but inexpensive detection of diseases, making an adequate diagnose accessible for people with lower income or to medical facilities in areas difficult to access, such as rural and remote regions, especially in developing countries.

Here, glucose sensors for people diagnosed with *diabetes mellitus* represent the most prominent example. From an unfeasible manual needle stinging and external measuring of the glucose level in the past, the current glucose monitoring devices allow for permanent, painless, and user-friendly analysis of the glucose level *in vivo*[12]*.* Moreover, the linkage of continuous glucose monitoring(CGM) sensors with insulin pumps and optional algorithms, which use data from CGM to adjust the amount of insulin delivered, enable the development of automated blood glucose regulation systems[13,14]. However, the idea to simplify and miniaturize biosensors extends toward many other analytes, e.g., C-reactive protein, pregnancy hormone CHG, estrogen, Covid-19 virus, cholesterol, lactate[15–18].

Sensor systems request detection strategies that preclude prior chemical labeling steps and for setups that are easy to integrate and use to fulfill the needs mentioned above for a low-cost, portable, and fast biosensor. Here, the emerging field of nano-bio-technology comes into play. With nanomaterials possessing unique physical properties due to their confinement down to the nanometer range, combining them with biological processes such as self-assembly or recognition opens up a wide field of applications, especially biosensing applications.

Nanomaterials facilitate the miniaturization of devices as they provide them with high sensitivity, thanks to the increased surface-to-volume ratio of the materials. Here, the miniaturization concept grants a down-scaling of sensing structures and consequently increases the number of sensors on one chip. Driven by the semiconductor industry, building blocks for electronics can be manufactured down to nanometer dimensions and integrated on a large scale. They can also be applied as sensor elements, e.g., field-effect transistors (FETs). So the first FET-based sensing with silicon nanowires was described by Lieber et al. in 2001, and since then, nanostructured FETs have gained colossal interest for biosensing applications[19].

Besides semiconducting devices, biosensors with transducers using the localized surface plasmon resonance (LSPR) of metal nanostructures, particularly gold structures, stand out due to their unique optical properties. By manipulating the properties of different gold nanostructures via simple engineering of the shape and size, their features can be dramatically improved and customized. Because of the ease of this concept, gold nanostructures operating by means of LSPR have become one of the most investigated nanotechnological tools[20].

The biological part is equally important in using (nanostructured) devices for biosensing applications. Here, biomolecules for detection, which are highly specific to linking target molecules, define the specificity of the whole biosensor. Thus, the compatible selection of these so-called receptor molecules for sensing has to be matched carefully to the aimed application (e.g., DNA hybridization, detection of protein-based biomarkers) while offering high stability throughout the experimental procedure. In addition, the recognition elements should be placed close to or directly at the sensor surface for optimal signal transduction[21].

The use of antibodies as a capture probe is widely used as they exhibit high binding affinities and specificity towards their target[22,23]. Nonetheless, antibodies still suffer from restrictions with expenses, structure, and their unattainability for several important analytes. To close this gap, the search for alternative capture probes spawned the relatively new receptor class of aptamers in 1990[24,25]. Aptamers are relatively short sequences of single-stranded DNA, or RNA, and are typically identified and synthesized in the lab – leading to their description as synthetic antibodies[26]. Aptamers can be engineered against various targets ranging from individual ions via small organics to large proteins[27]. Once developed, the straightforward synthesis of aptamers with the

possibility for attachment of functional groups significantly lowers the costs compared to antibodies. Furthermore, incorporating functional groups allows for oriented immobilization of the receptors, whereas the robustness of the DNA itself contributes to the stability of the chosen sensor system[28,29].

Regarding biosensors for Point-of-Care (POC) diagnostics, biorecognition occurs in rather harsh surroundings under which the stability and robustness of aptamers, compared to antibodies, assure a high sensitivity.

The motivation of this thesis lies in exploring and optimizing the interplay between transducer and receptor in order to develop biosensors with excellent performances. Examination of suitable candidates for both parts, their linkage, and their integration is not only essential for biosensor development itself but also combines research within the edge of material science, physics, (bio-) chemistry, and biotechnology.

For various applications, engineering interfaces and their subsequent biochemical functionalization are considered key steps in developing affinity biosensors to assure selective and sensitive analyte detection. By fulfilling additional boundary conditions, such as the stable receptor attachment under varying conditions and the maintenance of the receptor's functionality while preserving orientation towards the target in solution, the foundation stone for a low-cost, portable and fast biosensor has been laid.

1.1 Scope of the thesis

This work focuses on the biochemical functionalization of nanostructured surfaces to realize adequate biosensor performance with respect to sensitivity and selectivity. Further, evaluating the proposed receptor-analyte interactions using optical and electrical sensing methods, emphasizing the advances of DNA-based receptors, and finally applying those findings to the goal of a point-of-care biosensor that detects label-free analytes in various media.

One of the main goals of this thesis is to link the biological sensing elements with nanostructured transducers for the purpose of biosensing. Accordingly, this work shows suitable routes to attach DNA-based receptors onto two surfaces. To be precise, DNA-based receptors were immobilized on gold nanostructures, i.e., vertically aligned nanowires, for developing an optical biosensor operating by means of localized surface plasmon resonance (LSPR) and on silicon nanowires to develop a field-effect transistor

(FET) based biosensor. For both interfaces, the individual chemical modification strategies are presented, characterized by additional analytical methods, and their functionality and suitability for the aimed target are discussed. Furthermore, by exploring the physical fundamentals of each sensor setup, the advances of each immobilization strategy highlight the suitability of the chosen receptors.

Finally, the biosensing performance of the two platforms is demonstrated by label-free detection of analytes in real-time. First, a plasmonic biosensor based on vertically aligned nanoantennas reliably detected DNA hybridization, while the SiNW-based FETs recognized the stress marker cortisol in human saliva, respectively.

The following **Chapter 2**, "Fundamentals," introduces the general concept of biosensors, including their terminology and benefits that arise when combined with nanotechnology. Then, a separate overview of individual building blocks is presented by exploring DNA as suitable receptors, including their immobilization, and introducing the basics of the two transducer systems used in this research- optical biosensors operating by means of LSPR and electronic sensors based on FETs, respectively.

A detailed description of materials and methods applied in this research, as presented in **Chapter 3**, forms the base for exploring and discussing biosensing strategies.

Chapter 4 focuses on the setup of an optical biosensor that operates in real-time with vertically aligned gold nanoantennas to validate the hybridization of DNA by using two different target strands. Moreover, this chapter is dedicated to fundamentally exploring DNA's impact on densely packed nanostructured vs. planar substrates. A compact optical setup allowed for the evaluation of biorecognition processes in real-time.

In analogy, **Chapter 5** faces strategies to apply silicon nanowires on a portable platform to detect the small analyte cortisol. After presenting, a suitable method to immobilize DNA-based receptors, a separate section deals with the suitability and mechanism of the chosen biorecognition system. In the last step, the implementation of the aptamers and subsequent detection of cortisol using SiNWs arrays are presented. Key moments are the possibility of detecting cortisol directly in saliva without further need for sample treatment and the suitability of the portable platform to operate multiple FETs simultaneously in real-time.

The last **Chapter 6** summarizes the thesis work, addresses the possibility of detecting multiple targets with the two proposed sensor systems, and analyzes future perspectives.

1.2 References

(1) Leibniz-Institut Für Gewässerökologie Und Binnenfischerei. Die Zukunft der Oder : forschungsbasierte Handlungsempfehlungen nach der menschengemachten Umweltkatastrophe. **2022**. https://doi.org/10.4126/FRL01-006431249.

(2) León-Figueroa, D. A.; Bonilla-Aldana, D. K.; Pachar, M.; Romaní, L.; Saldaña-Cumpa, H. M.; Anchay-Zuloeta, C.; Diaz-Torres, M.; Franco-Paredes, C.; Suárez, J. A.; Ramirez, J. D.; Paniz-Mondolfi, A.; Rodriguez-Morales, A. J. The Never-Ending Global Emergence of Viral Zoonoses after COVID-19? The Rising Concern of Monkeypox in Europe, North America and Beyond. *Travel Med. Infect. Dis.* **2022**, *49*, 102362. https://doi.org/10.1016/j.tmaid.2022.102362.

(3) *World Population Prospects 2022: Summary of Results | Population Division*. https://www.un.org/development/desa/pd/content/World-Population-Prospects-2022 (accessed 2022-08-31).

(4) Bhalla, N.; Jolly, P.; Formisano, N.; Estrela, P. Introduction to Biosensors. *Essays Biochem.* **2016**, *60* (1), 1–8. https://doi.org/10.1042/EBC20150001.

(5) Hall, E. A. H.; Hummel, G.; Hall, E. A. H. *Biosensoren: mit 24 Tabellen*; Biotechnologie; Springer: Berlin Heidelberg, 1995.

(6) Bollella, P.; Katz, E. *Biosensors – Recent Advances and Future Challenges*; MDPI, 2021.

(7) Clark, L. C.; Wolf, R.; Granger, D.; Taylor, Z. *Continuous Recording of Blood Oxygen Tensions by Polarography*. *J. Appl. Physiol.* **1953**, *6* (3), 189–193. https://doi.org/10.1152/jappl.1953.6.3.189.

(8) Clark, L. C.; Lyons, C. Electrode Systems for Continuous Monitoring in Cardiovascular Surgery. *Ann. N. Y. Acad. Sci.* **1962**, *102*, 29–45. https://doi.org/10.1111/j.1749-6632.1962.tb13623.x.

(9) *RKI - Labordiagnostische Analysen*. https://www.rki.de/DE/Content/Infekt/Ausbrueche/Labordiagnostik/Labordiagnostik_node.html (accessed 2022-08-31).

(10) Terry, S. C.; Jerman, J. H.; Angell, J. B. A Gas Chromatographic Air Analyzer Fabricated on a Silicon Wafer. *IEEE Trans. Electron Devices* **1979**, *26* (12), 1880–1886. https://doi.org/10.1109/T-ED.1979.19791.

(11) Manz, A.; Graber, N.; Widmer, H. M. Miniaturized Total Chemical Analysis Systems: A Novel Concept for Chemical Sensing. *Sens. Actuators B Chem.* **1990**, *1* (1), 244–248. https://doi.org/10.1016/0925-4005(90)80209-I.

(12) *FreeStyle Libre Diabetes Shop | Diabetesbedarf online bestellen*. https://www.freestylelibre.de/ (accessed 2022-08-31).

(13) Kariyawasam, D.; Morin, C.; Casteels, K.; Le Tallec, C.; Sfez, A.; Godot, C.; Huneker, E.; Garrec, N.; Benhamou, P.-Y.; Polak, M.; Charpentier, G.; Franc, S.; Beltrand, J. Hybrid Closed-Loop Insulin Delivery versus Sensor-Augmented Pump Therapy in Children Aged 6–12 Years: A Randomised, Controlled, Cross-over, Non-Inferiority Trial. *Lancet Digit. Health* **2022**, *4* (3), e158–e168. https://doi.org/10.1016/S2589-7500(21)00271-5.

(14) Boughton, C. K.; Hartnell, S.; Thabit, H.; Mubita, W. M.; Draxlbauer, K.; Poettler, T.; Wilinska, M. E.; Hood, K. K.; Mader, J. K.; Narendran, P.; Leelarathna, L.; Evans, M. L.; Hovorka, R. Hybrid Closed-Loop Glucose Control Compared with Sensor Augmented Pump Therapy in Older Adults with Type 1 Diabetes: An Open-Label Multicentre, Multinational, Randomised, Crossover Study. *Lancet Healthy Longev.* **2022**, *3* (3), e135–e142. https://doi.org/10.1016/S2666-7568(22)00005-8.

(15) *Pregnancy Tests: Digital Tests, Sticks and Kits - Clearblue*. https://www.clearblue.com/pregnancy-tests (accessed 2022-11-01).

(16) *Advanced Digital Ovulation Test: Typically identifies 4 or more Fertile Days*. https://www.clearblue.com/ovulation-tests/advanced-digital (accessed 2022-11-01).

(17) *Accutrend® Plus system*. https://diagnostics.roche.com/global/en/products/instruments/accutrend-plus-ins-754.html#productInfo (accessed 2022-11-01).

(18) *CRP - möLab - Point of Care*. https://www.moelab.de/crp.html (accessed 2022-11-01).

(19) Cui, Y.; Wei, Q.; Park, H.; Lieber, C. M. Nanowire Nanosensors for Highly Sensitive and Selective Detection of Biological and Chemical Species. *Science* **2001**, *293* (5533), 1289–1292. https://doi.org/10.1126/science.1062711.

(20) Si, P.; Razmi, N.; Nur, O.; Solanki, S.; Mouli Pandey, C.; K. Gupta, R.; D. Malhotra, B.; Willander, M.; Zerda, A. de la. Gold Nanomaterials for Optical Biosensing and Bioimaging. *Nanoscale Adv.* **2021**, *3* (10), 2679–2698. https://doi.org/10.1039/D0NA00961J.

(21) Hering, E.; Schönfelder, G. Biologische und medizinische Sensoren. In *Sensoren in Wissenschaft und Technik: Funktionsweise und Einsatzgebiete*; Hering, E., Schönfelder, G., Eds.; Vieweg+Teubner Verlag: Wiesbaden, 2012; pp 547–582. https://doi.org/10.1007/978-3-8348-8635-4_12.

(22) Byrne, B.; Stack, E.; Gilmartin, N.; O'Kennedy, R. Antibody-Based Sensors: Principles, Problems and Potential for Detection of Pathogens and Associated Toxins. *Sensors* **2009**, *9* (6), 4407–4445. https://doi.org/10.3390/s90604407.

(23) Sharma, S.; Byrne, H.; O'Kennedy, R. J. Antibodies and Antibody-Derived Analytical Biosensors. *Essays Biochem.* **2016**, *60* (1), 9–18. https://doi.org/10.1042/EBC20150002.

(24) Ellington, A. D.; Szostak, J. W. In Vitro Selection of RNA Molecules That Bind Specific Ligands. *Nature* **1990**, *346* (6287), 818–822. https://doi.org/10.1038/346818a0.

(25) Robertson, D. L.; Joyce, G. F. Selection in Vitro of an RNA Enzyme That Specifically Cleaves Single-Stranded DNA. *Nature* **1990**, *344* (6265), 467–468. https://doi.org/10.1038/344467a0.

(26) Thiviyanathan, V.; Gorenstein, D. G. Aptamers and the Next Generation of Diagnostic Reagents. *Proteomics Clin. Appl.* **2012**, *6* (0), 563–573. https://doi.org/10.1002/prca.201200042.

(27) Kanwar, J. R.; Roy, K.; Maremanda, N. G.; Subramanian, K.; Veedu, R. N.; Bawa, R.; Kanwar, R. K. Nucleic Acid-Based Aptamers: Applications, Development and Clinical Trials. *Curr. Med. Chem. 22* (21), 2539–2557.

(28) Baldrich, E.; Restrepo, A.; O'Sullivan, C. K. Aptasensor Development: Elucidation of Critical Parameters for Optimal Aptamer Performance. *Anal. Chem.* **2004**, *76* (23), 7053–7063. https://doi.org/10.1021/ac049258o.

(29) Dong, Y. *Aptamers for Analytical Applications: Affinity Acquisition and Method Design*; John Wiley & Sons, 2019.

2 Fundamentals

2.1 Biosensors

Generally speaking, "*a biosensor is defined as a device that measures biological or chemical reactions by generating signals proportional to the concentration of an analyte in the reaction*."[1]

The aim of any biosensor is to detect analytes that are mainly interesting for applications in health care, safety or environmental monitoring, and the biotechnology industry. Various analytes range from antigens, (complementary or mismatching) DNA strands, proteins, and hormones to whole cells, viruses, and microorganisms. However, detecting ions, organic molecules, toxins, and gases such as ammonia or hydrogen sulfide is possible, too. Thus, the potential applications of biosensors in the mentioned fields are numerous. Each biosensor system has its requirements, such as analyte concentration to be measured, the necessary sample volume and concentration, the allowed time to complete the detection, the possibility for reusing and cleaning the biosensor, and the necessary precision of the sensor output in general[2,3].

Consequently, the development of a biosensor typically involves several interdisciplinary tasks. The following chapter briefly introduces the principles of different methods applied to run a working biosensor. In the first part, a general description of biosensors is presented, emphasizing the properties of nanoscaled sensors compared to conventional ones. Before explaining the bio-interface employing receptor-target interactions, a short presentation of two transducer setups, namely optical sensors operating through LSPR, and electronic sensors working as field-effect transistors, follows. A particular focus lies on applying DNA molecules as a receptor to achieve a sensitive and specific biosensing performance.

A usual biosensor consists of the following components; Figure 2-1. The bio-receptor is responsible for the specificity of the sensor towards the analyte. Common bio-receptors are enzymes, antibodies, DNA strands/aptamers, or cells[4], which are immobilized (covalently or non-covalently) interfacing the second component – the transducer. Here, the transducer is the part of the device that converts the arising chemical or biological event into a readable output that can be in various formats, such as electric, optical, acoustic, thermal, piezoelectric, or mass sensitive. The underlying

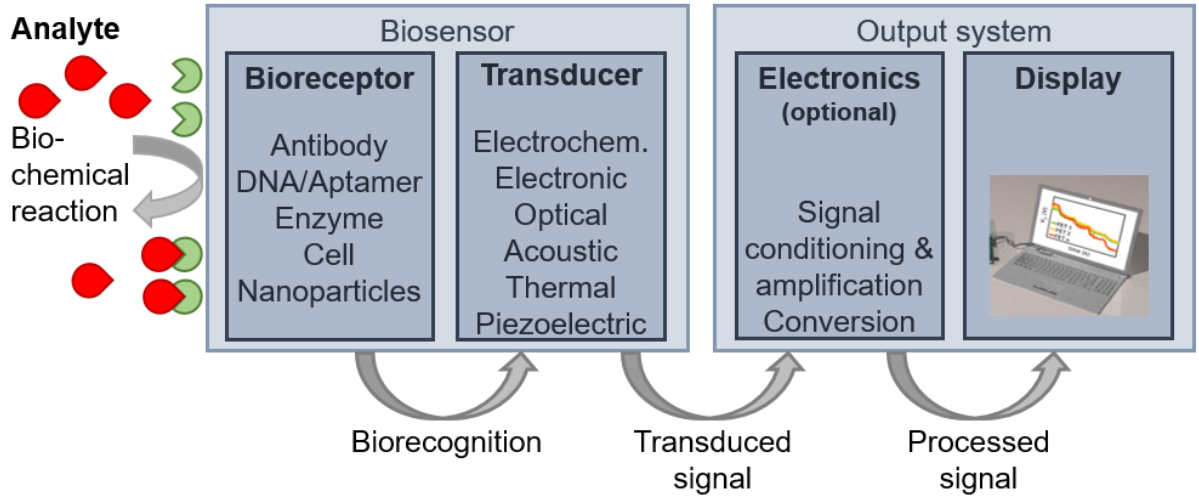

Figure 2-1: Schematic structure of biosensors' elements. The analyte is captured by a bioreceptor and immobilized on the transducer's surface- thereby inducing a change in the transducer's surface ("biorecognition"). The transducer translates the capturing event into a measurable output that can either be directly displayed or further processed for read-out optionally. The sketch is inspired by [1] and modified.

processes are mostly concentration-dependent, so the produced output is proportional to the amount of analyte–bioreceptor interactions[5].

The output system allows for a display and subsequent read-out of the biorecognition event by the user. Depending on the origin of the transducer, a direct (optical) read-out or further signal processing follows. In the latter case, the produced output formats from the transducer are processed by electronic devices, which convert the analog signals to digital ones after optional amplification and conditioning, and thus prepare them for display. The output of the signal is a combination of hard- and software. It displays the sensor's signals in a user friendly-manner by showing either numeric or graphical values.

A biosensor can be grouped either according to the biological specificity conferring mechanism (e.g., aptasensors, enzyme sensors, etc.) or to the mode of signal transduction (e.g., optical, electrochemical sensors, etc.), or a combination of both[6–8]. The possibility of further subdivisions of the classes, such as surface plasmon resonance (SPR) or Raman sensors within the field of optical sensors, or amperometric and potentiometric sensors within the area of electrochemical sensors, underline the broadness of the biosensor field, respectively.

2.2 Influence of nanotechnology on sensor development

Nanotechnology has taken over across various fields of research and development, including classical subjects such as physics, chemistry, electronics, biotechnology, and

medical science, but also in healthcare, civil engineering, food science, industrial safety, and environmental studies. For nanomaterials, defined as materials whose confinement is within the nanometer scale in at least one dimension, the scaling down plays a significant role in determining the material's physical, chemical, and electrical properties[9] as they can differ significantly from those of a bulk material[10].

The ability to manipulate and control materials at a nanometer level has led to new opportunities for biosensor development. Even though the basic scheme of a nanobiosensor is comparable to conventional macro- and micro-counterparts, integrating nanomaterials into transducers attracts great interest as nanoscaled biosensors. They offer enhanced sensitivity and performance compared to conventional biosensors due to the high surface-to-volume ratio and previously mentioned dimensionality with altered physical properties. As a result, do not only the interactions between surfaces and the surrounding environment increase but also the presence of just a few molecules fuels perturbations in the overall material. Furthermore, by using nanomaterials, there is the possibility to detect biochemical reactions directly in cellular organelles or tissues. In addition, in medical diagnosis, detecting events in regions that are difficult to reach and detecting analytes at ultralow concentrations gets feasible[11].

Nanostructured substrates employed by biosensors can be manufactured in various shapes, sizes, materials, etc. Their manufacturing can be divided into top-down or bottom-up fabrication methods. Here, the former methods rely primarily on lithographical pattering techniques; the latter is typically based on chemically synthesized colloidal nanoparticles that are further processed and deposited on substrates[9,12–14]. Herein, only the main basics of both fabrication concepts are introduced; for a detailed overview, the reader is referred to the literature described elsewhere[15–18].

For top-down approaches, nanostructures are created from bulk material by breaking down large pieces of the material to generate nanostructures. Common top-down fabrication approaches include conventional structuring methods such as photolithography, electron beam lithography (EBL), or focused ion beam lithography (FIB), all resulting in arrays of nanostructures with well-defined shapes and sizes. However, despite their high levels of resolution and wide use, especially in the semiconducting industry, the techniques are slow and expensive. In addition, they typically result in a limited patterning area of only a few μm^2.

To fabricate large-scale arrays at a low cost, other methods based on colloidal lithography techniques, such as nanospheres lithography (NSL) or hole-mask colloidal lithography (HCL), have to be mentioned. Both strategies use self-assembled layers of nanoparticles on the substrates as a sacrificial mask for generating nanostructured substrates. Next to these abovementioned approaches, another top-down method includes using porous alumina templates to create vertical nanorods.

In contrast, the bottom-up approach implies the assembly of single atoms and molecules into larger nanostructures. Typically, physical or chemical synthesis routes are the basis for achieving nanostructures. Representative methods are chemical vapor deposition (CVD), physical vapor deposition, plasma or flame spraying synthesis, atomic layer deposition, or atomic or molecular assembly. With the bottom-up method, ultra-fine nanostructures with almost any shape can be generated at a low cost in large quantities. Still, the arrays suffer in terms of keeping control over reaction conditions and thus ache in replicability. In addition, further chemical purification steps of nanoparticles are required to prevent a transfer to large-scale production[13,19].

The small dimension of nanoscaled devices offers excellent potential in terms of integration into read-out systems and for miniaturization of platforms, making nanomaterials particularly interesting for sensing approaches.

2.3 Biorecognition elements

Molecular recognition is one of the main signposts of biosensors. Therefore, an appropriate receptor has to be implemented into the biosensing system to detect the analyte specifically with a biosensor[20,21].

However, the binding of an analyte to its receptor is typically a non-covalent interaction between the two different molecules due to a complex interplay of hydrogen bonds, salt bridges, hydrophobic interactions, van der Waals forces, electrostatic interactions, and structural fitting[22,23]. The recognition develops an equilibrium of the reaction that can be described schematically by

$$\text{analyte} + \text{receptor} \underset{K_D}{\overset{K_A}{\rightleftarrows}} \text{analyte} - \text{receptor complex} \qquad (2.1)$$

and evaluated with the help of the association and dissociation reaction constants K_A and K_D, respectively. The values provide information about the binding stability in which K_A typically scales between 10^7 l/mol and 10^8 l/mol, while K_D levels are between

10^{-5} l/mol (high affinity) and 10^{3} l/mol (low affinity)[24]. A sensor surface functionalization aims to exploit these specific interactions.

Many (bio-) molecules can be applied as receptors for biosensing. Typical representatives to perform the bio-recognition activity are enzymes biosensors, antibodies, aptamers biosensors, nanoparticles, and even whole cells[4]. The need to immobilize the chosen receptor to the transducer's surface unify all sensors but is highly dependent on the substrate and receptor. Numerous strategies for functionalizing different substrates with receptors have been presented and can be read for further studies[13,19,25–27]. This work focuses primarily on single-stranded DNA as receptor molecules with different biosensor systems.

2.3.1 Biorecognition element: DNA

The first DNA biosensor was proposed in 1988[28] and reported DNA detection with a piezoelectric transducer. Since then, DNA biosensors have been broadly studied, and great effort has been devoted to improving the selectivity and sensitivity of DNA biosensors and miniaturization. As a result, DNA detection is of great interest in DNA diagnostics, health care, environmental monitoring, food safety, gene analysis, and forensic applications[29,30].

DNA biosensors have oligonucleotides with a known sequence of bases or a fragment of DNA or RNA with known base sequences as sensing elements. They can operate either based on the highly specific interaction of the complementary DNA strands – hybridization of DNA[31] or as a specific receptor for biochemical/chemical species - as an aptamer[8,32].

DNA is generally well-suited as a biomolecule for model receptor-analyte investigations as it is readily available. In addition, DNA is stable under varying conditions, such as changes in pH, temperature, or in non-physiological conditions. DNA strands can be easily synthesized in vitro at high purification standards without the need for animals and thus show little batch-to-batch variations.

The robustness of DNA allows the regeneration of probe-ligand binding, too. Simply by incubating the surfaces with suitable solvents like NaCl, urea, or guanidine-HCl, as well as by heating until the DNA folding is disturbed and subsequent cooling[33–35].

2.3.2 Aptamers

In 1990, a new class of artificial receptor molecules based on short oligonucleotide sequences was described[36] and called aptamers. Oligonucleotide strands (RNA or DNA) with a length of usually 15 up to 100 bases form characteristic structures, such as quadruplex for guanine-rich aptamers, hairpins, or helical segments, when exposed to ligands [32]. Due to three-dimensional interactions between aptamers and their targets due to complex interactions of hydrogen bonds, electrostatic, and van der Waals interactions, aptamers are highly specific towards their target[37]. In addition, cations such as sodium or magnesium enhance the stability of the aptamer-target complex further[32,38,39]. Aptamers work for various targets such as ions, small chemical molecules, proteins, viruses, and cells[40,41,43–47]. Aptamer development is also possible against toxins that cannot be realized with antibodies as they do not elicit an immune response[48,49].

The Systematic Evolution of Ligands by Exponential enrichment (SELEX) process is used to develop new receptors/aptamers. During several rounds, well-binding sequences are separated from unspecific sequences from a single-stranded DNA(ssDNA) library. In the first step, the selected library is incubated with the immobilized target, and unbound DNA is washed away. Then, by changing the solution, bound molecules are eluted, followed by an enrichment step, and are again incubated with the target until the desired properties of the final detection system, including salt and buffer composition, temperature, and elimination of cross-reactivity by instituting negative controls is selected[50,51].

The capability of modifying DNA strands with functional groups or fluorescent dyes is standard. Typically, without a loss in affinity to its target, using a single functional terminal group allows for a tailorable orientation of probe strands so that active binding sites remain acceptable for the targets.

The short oligonucleotide sequences make aptamers a relatively small receptor molecule[26]. The reduced size is especially beneficial for application in electronic biosensors such as field-effect transistors (FET). Typically, in physiological conditions, FETs are limited in their performance by the presence of an electric double layer, whose thickness can be characterized by the Debye length (λ_D). It is postulated that outside of this layer, no sensing is possible with FETs. However, a detailed discussion of the underlying principles and possible ways to circumvent resulting limitations can be found in 5.2.3.2.

As introduced earlier, aptamers exhibit different structures according to their sequences. As a result, almost any analyte can be chosen for tailoring a suitable aptamer. Aptamers generally are negatively charged on a broader pH range due to their low isoelectric point; however, the whole aptamer- analyte complex is a unique system with individual charge and molecule distributions that can be used for biosensing[52]. A detailed description of underlying processes upon biorecognition and their effects on biosensing is discussed in section 5.3.

As introduced above, the three-dimensional structure formation of DNA, and thus of aptamers, can be disturbed by elevated temperature treatment or regeneration solutions. Therefore, the capability for easy regeneration is a crucial advantage for the application of biosensors and makes DNA-based receptors excellent candidates for biosensing.

2.3.3 Immobilization of receptors

The immobilization of receptors close to a transducer surface while not impeding the specificity is essential for biosensors. In general, the immobilization strategy has to qualify for a stable immobilization of receptors while maintaining not only the native conformation but also preserving biological activity. In addition, an appropriate receptor density and the proper orientation of the molecules on the surface are crucial to prevent steric hindrance of the available bioactive sites. Fulfilling those boundary conditions enable the specific biorecognition between the analyte and surface-tethered ligands[53].

Depending on the receptor, substrate, and later application of the system, many immobilization strategies exist: an attachment of receptors via adsorption/ physisorption, chemisorption, covalent coupling, entrapment/ encapsulation in a matrix, or via specific biological interactions (bioaffinity binding) are standard methods to immobilize receptors on the substrate[54–56]. Several reviews summarize and highlight different strategies concerning their applications to shed light on strategies[57–59].

Within this work, two different biosensing platforms were investigated. Two nanostructured materials, namely gold and silicon, served as a transducer and consequently required tailored immobilization of molecules to achieve sensitive analyte detection. Even though the substrates differ, both platforms unified the need for a stable attachment of DNA-based receptors with an appropriate receptor density and surfaces

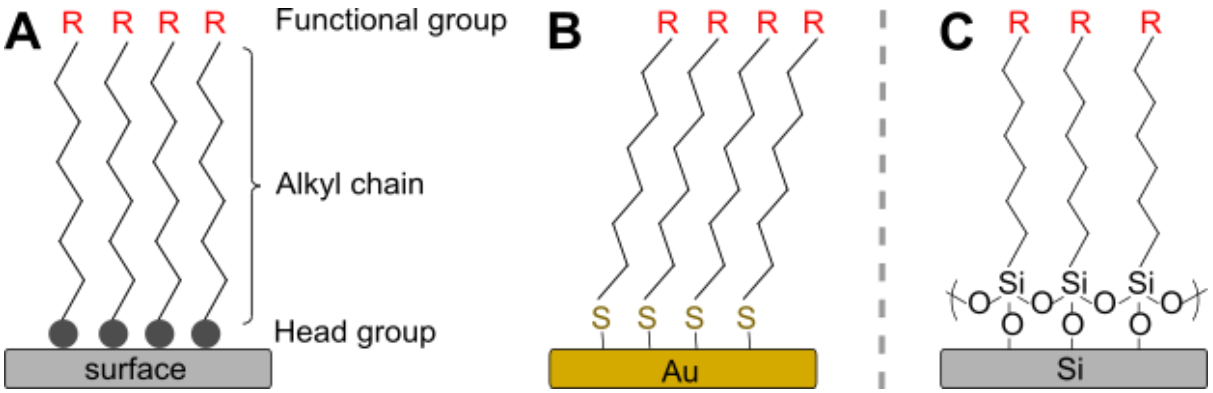

Figure 2-2: Formation of functional SAMs. A) General structure of a SAM formed from organic molecules with an anchoring head group, an alkyl chain $(CH)_n$, and a functional group that can be used to attach further moieties. B) Formation of SAM on gold with thiolated receptors C) Formation of idealized silane monolayer on silicon. In all panels, R refers to functional groups such as amino, carboxyl, hydroxyl, anhydride, etc.

that prevent non-specific adsorption. Furthermore, to maintain the distance between the sensor surface and analyte binding site as minimal as possible and hence to increase the device sensitivity, a covalent binding strategy is favored.

Due to the ease of modification of DNA with various terminal groups, the probe DNA was immobilized on gold via (non-covalent) chemisorption of thiol-chemistry. In contrast, amino-modified DNA was bound covalently to silicon via an anhydride-containing silane linker molecule.

Both systems implement the formation of monolayers on the surfaces. The spontaneous formation of such a monolayer on a surface from organic molecules is referred to as "Self-assembled monolayers (SAMs)"[60]. Here, layers are formed by chemical adsorption /chemisorption from molecules out of a solution or gas phase onto the substrate's surface. The principal structure of these molecules, illustrated in Figure 2-2, comprises the following parts. First, a head group permits the anchoring of the molecules to the surface (e.g., thiols for SAM formation on gold, silanes for SAM formation on metal oxides). Next, a subordinated alkyl chain facilitates the parallel arrangement perpendicular to the surface, and last, a functional/terminal group provides functionality for the attachment of ligands. Mixed SAMs with different molecules can be applied in order to optimize receptor density by varying the ratios but also assure a complete functionalization of the whole surface with molecules and thus prevent unspecific adsorption[61,62].

2.4 Transducer systems

2.4.1 Optical biosensors - surface plasmon resonance

Within the field of optical biosensors, transducers respond to biorecognition by experiencing a change in their optical properties, such as absorption, reflectance, emission (luminescence/ fluorescence), or a change in an interferometric pattern[63,64]. Typically, signal changes are recorded by a photodetector or a spectrometer or even can be seen directly with the naked eye.

Hence, optical biosensors can detect many biological and chemical analytes directly, in real-time, and label-free. Moreover, optical biosensors offer high specificity, sensitivity, small size, and cost-effectiveness and thus make optical biosensors the most common type of biosensor nowadays[2,65].

For optical biosensors, commonly used systems are based on (localized) surface plasmon resonance (SPR), evanescent wave fluorescence, and optical waveguide interferometry. However, detection of labeled analytes with an optical device typically involves a signal generation based on colorimetric, fluorescent, or luminescent methods, a refractive index variation, or light scattering, respectively[2,64,66].

Within this research, an optical biosensor operating through localized surface plasmon resonance (LSPR) allowed the label-free detection of DNA hybridization. Hence, the scope of the following part will be limited to surface plasmon resonance-based biosensors, whose main principle is the detection of refractive index changes close to the surface of metal nanostructures, which are caused by recognition events or chemical reactions.

2.4.1.1 Surface plasmon resonance (SPR)

The SPR is a physical phenomenon observed in the early 20th century by R. W. Wood and Lord Rayleigh[67–69]. The phenomenon occurs at a metal-dielectric interface under the illumination of plane-polarized light at a specific angle. At those conditions, the energy carried by the photons is transferred to collective excitations of free electrons of the metal, called surface plasmons (SPs), at that interface. If the excitation of these oscillations occurs parallel to the metal surface, they are called surface plasmons (evanescent waves), and their generation occurs only at a specific resonance wavelength of light[70].

The generation of surface plasmons depends on the geometry of the plasmonic structure and the environmental parameters, which is the key to using that phenomenon as a biosensor. If the conditions in the metal remain constant, the location of the resonant frequency and the certain angle that triggers SPR is dependent only on the material's refractive index near the metal surface. Therefore, a slight variation in the reflective index of the sensing medium –e.g., by binding a biomolecule to the respective surface- will change the occurrence of SPR and hence makes it possible to detect analytes. By monitoring the reflected light intensity or tracking the resonance angle shifts against time, the amount of bound analyte can be determined in a real-time and label-free matter[2,70–73].

The following Figure 2-3A illustrates schematically the principle of a typical SPR device operating in the Kretschmann configuration. The main component of this arrangement is a highly refractive prism whose base is coated with a metal, usually gold. P-polarized white light is irradiated onto the prism via a side surface at a constant angle of incidence. As mentioned earlier, the excitation of surface plasmons occurs via an evanescent field, which is generated by the reflection of the light at the interface. The field decreases exponentially towards the direction of the metal. As a result, the intensity of refracted light detected with a spectrometer after leaving the prism decreases. The metal coating must be thin to ensure that the momentum transfer from the irradiated light to the surface plasmons can penetrate the entire metal layer. Although the attenuation occurs only at a certain angle of incidence, biorecognition processes at the layer change the refractive index and the angle of incidence. This angular shift characterizes the

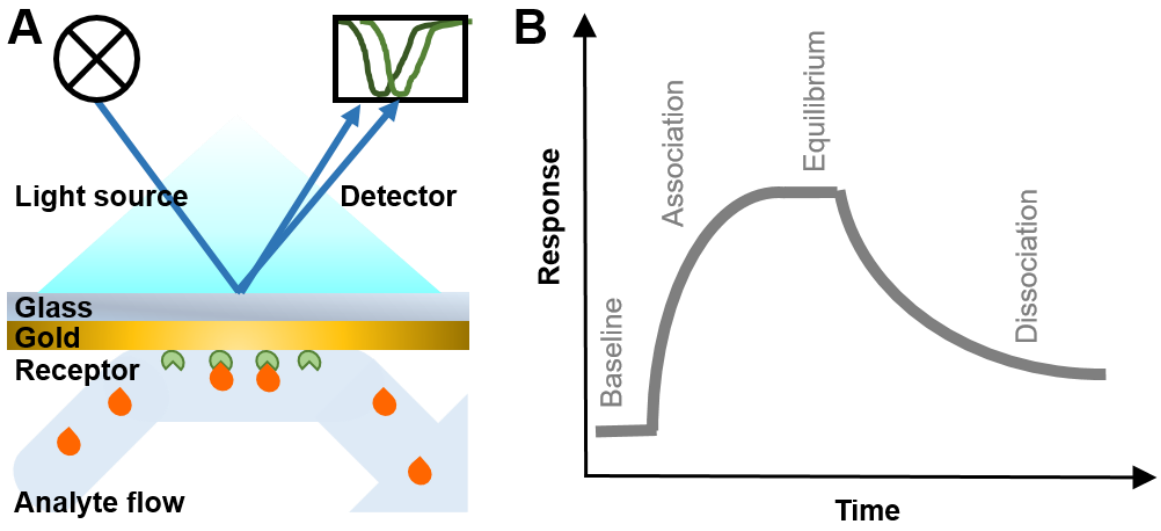

Figure 2-3: A) The principle of SPR instrument operating in Kretschmann configuration and B) typical SPR sensorgram showing the steps of an analytical cycle.

interaction process in a sensorgram, where the angle shift is described as a function of time. Figure 2-3B shows a typical sensorgram: The baseline in the first phase of the sensorgram represents the SPR signal of the receptor-functionalized gold surface. The binding molecules' association with receptors occurs in a second phase, and the SPR signal increases until reaction equilibrium. Subsequent rinsing with buffer introduces the dissociation phase, in which loosely bound analytes are removed, and hence the sensor signal slowly decreases. During this phase, the signal does not return to the baseline level as some analytes stay bound at the surface. A regeneration step can be added to remove bound ligands from receptors without destroying them.

2.4.1.2 Localized surface plasmon resonance

Even though SPR sensing systems dominate the commercial applications of optical biosensors, nanostructures of noble metals exhibit unique optical properties that make them ideal candidates for plasmonic biosensors.

For particles smaller than the incident light wavelength, the illumination with light leads to density oscillations of the conducting electrons within the nanostructures. As the plasmon oscillates "locally" around the nanoparticles with a particular frequency, the optical phenomenon is described by localized surface plasmon resonance [27,70,74–76]. Hence, the presence of LSPR in nanoparticles leads to outstanding absorption- and scattering cross-sections at specific wavelengths and result in bright and intensely colored nanostructures that show distinct peaks in the visible and near-infrared region of the light spectrum[77]. In analogy to the SPR, the electromagnetic field in close vicinity to particle's surfaces is enhanced and declines exponentially[70,78].

The occurring resonance frequency (and thus the position of the peaks in respective extinction spectrum) is dependent on the composition, size, geometry of nanoparticles, their dielectric environment (and refractive index), and particle-particle separation distance[27,79,80].

For example, enhancing the particle size will induce a redshift of the SPR peak as there is a close connection between the plasmon wavelength and particle size due to the spatial distribution of the polarization charges over the surface[81–84]. Compared to the aforementioned sphere-like particles, anisotropic structures cannot only exhibit a shift of the plasmon wavelength but also show multiple LSPR bands. Exemplary samples are nanorods that display two separated plasmon absorption peaks corresponding to the

transverse and the longitudinal modes, respectively. Here, the longitudinal mode is sensitive to the aspect ratio of the rods and can be tuned from visible light to infrared light regions[85,86]. Common materials used for LSPR applications are noble metals, refractory (high temperature stable) metals, transition metal nitrides, conductive oxides, and compositions thereof[87,88]. However, gold is the most widely used material due to its inert (chemical) nature, biocompatibility, and well-established thiol affinity to immobilize receptors.

Apart from the nanostructures' size, material, and shape, the incredibly intense and highly localized electromagnetic (EM) fields induced by LSPR make nanostructures a compassionate transducer system for small changes in the local refractive index[8,70]. In general, if the refractive index of the surrounding medium increases, the extinction spectrum redshifts, and the resonance wavelength rises, respectively. As many organic molecules, such as receptors and ligands, a relatively high refractive index compared to solvent or air results in a redshift and thus serves as the basis for plasmonic biosensing. A graphical overview of possible parameters influencing the LSPR peak position is given in Figure 2-4 below.

Within the evolving field of microfluidics, LSPR-based biosensors became particularly interesting for biosensing applications as the inherent advantages of LSPR in combination with microfluidics are predicted to surmount the shortcomings of SPR sensors. Limitations are sensitivity, throughput capabilities, and potential for miniaturization[77,89]. Furthermore, the possibility to group the advantages of enhanced electromagnetic fields of plasmonics with microfluidic channels allows not only for the manufacturing of

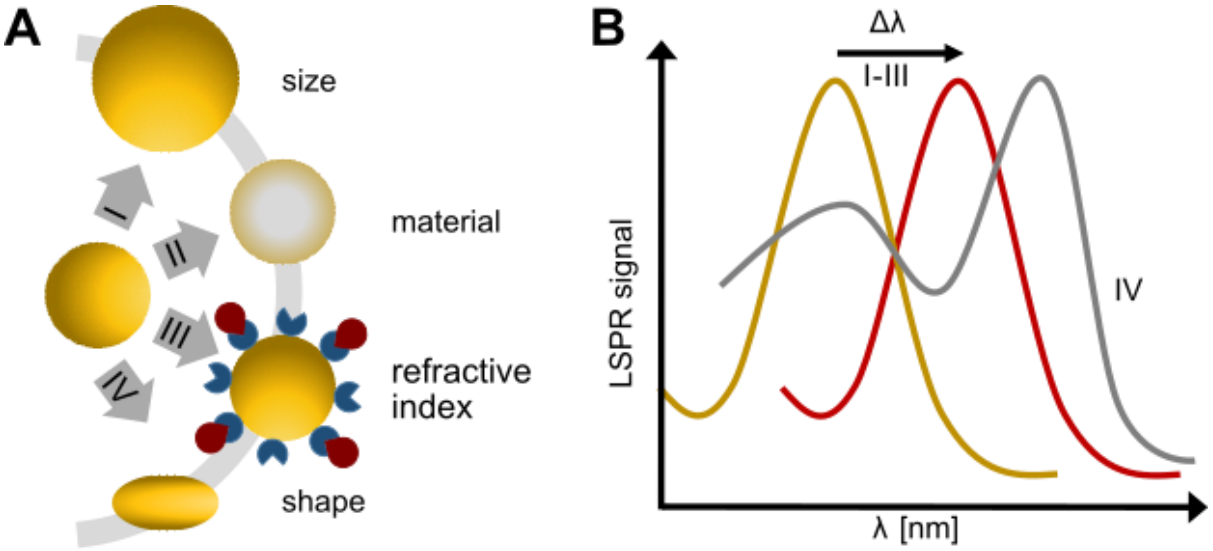

Figure 2-4: A) Change of nanostructure's properties such as size (I), material (II), the refractive index of surrounding medium (III), and shape (IV) cause a shift (I-III) or an appearance of a second (IV) plasmon peak.

compact and portable devices at low cost, but also are capable platforms to detect label-free analytes at low concentrations in real-time.

2.4.2 Electric Biosensors – Field-effect transistors (FETs)

Typically an electrical biosensor detects a biological target on an electrode interface through the generation of a current or a voltage signal (or via a perturbation thereof)[90]. Depending on the signal's cause, electric sensors can be grouped into amperometric/voltammetric, potentiometric, conductometric, impedance biosensors, and field-effect transistors, respectively[91].

This research performed the biodetection of analytes with silicon nanowire field-effect transistors (SiNW FETs). Thus, the scope of the following part will be limited to FETs, which employ transistor technology to measure either the current or the potential of semiconducting channels. They transduce signals of biodetection that either occur directly at the current carrying element or associated gate electrodes[92–94].

2.5 Metal oxide semiconductor field-effect transistor - MOSFET

In a standard approach, FETs are semiconducting devices for amplifying and controlling signals. FETs (i.e., a metal oxide semiconductor field-effect transistor MOSFET) consist of p- or n- doped channels of a semiconducting base material, out of which silicon is by far the most common. The three terminals, source (S), drain (D), and gate (G), which is allocated between the source and the drain and separated by a thin insulating oxide layer, connect the channels, respectively. Panel A in Figure 2-5 illustrates a basic structure of a MOSFET device. A bias between the source and drain of the FET creates a current flow between them, while the gate is used for control of the current through a generated electrical field by the gate. Applying a voltage to the gate develops an electrical field in a vertical direction and hence results in establishing a conductive channel whose size depends on both the external gate field and the selection of the materials. However, a slight change in gate voltage has a relatively significant effect on the current flow between the source and drain. When a gate voltage is applied, the electric field propagates into the channel depending on the polarity and magnitude of the control voltage. Further, each FET can be either a p-channel or n-channel device as they can have their conduction current due to holes or electrons. For further description, the focus is set on the characteristics of a n-channel MOSFET; however, they all work on a shared principle so far.

In the case of n-type semiconductors, a positive gate voltage (V_G) results in the *accumulation* of excess electrons at the surface. Consequently, a higher carrier density appears close to the surface, and the channel becomes more conductive. In contrast, the reduction of the positive gate voltage leads to a *depletion* of the electrons close to the surface, so that carrier density decreases and the channel becomes less conductive. Further, when large negative voltages are applied, excess positive carriers are induced at the surface, and the so-called *inversion* case occurs. For deeper insight into the corresponding theories, the reader is referred to standard literature[95–98].

The associating IV- relations of a MOSFET using transfer characteristics (I_{DS} versus V_{GS}) and output characteristics (I_{DS} versus V_{DS}) emphasize the non-linear correlation between applied voltage and observed current. Figure 2-5B, C below show a typical course of both IV-characteristics for n-channel MOSFET. In brief, the application of different gate voltages V_{GS} allows the MOSFET to work in different operation modes visible in both IV-characteristics. In the cut-off region (red background in Figure 2-5B/C) the MOSFET is off or considered an open-circuit device. Until V_{GS} exceeds the value of the threshold voltage V_T ($V_{GS}<V_T$), there will be no current I_{SD}. However, in the ohmic or linear region (yellow background in Figure 2-5B/C), the MOSFET operates similarly to a resistor: I_{DS} increases proportionally to V_{DS} (with $V_{GS}>V_T$ and $V_{DS}<V_P$). A further rise of V_{SD} above the pinch-off voltage (V_P) results in a plateauing of I_{SD} as the inversion layer

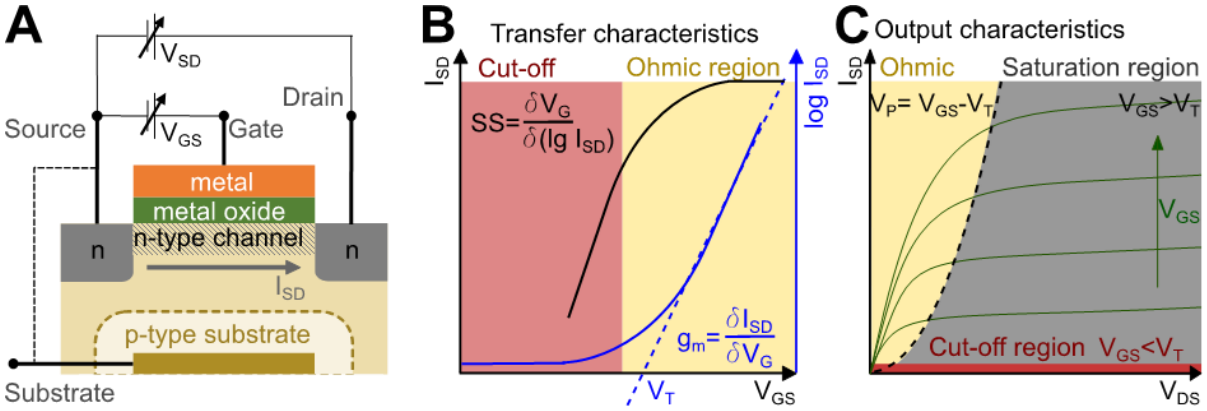

Figure 2-5: Overview of a MOSFET's operation modes and associated IV-characteristics. A) Basic structure of a MOSFET. The n-channel FET consists of a p-type substrate with n-type islands connected to the outside via contacts (source S and drain D). The substrate is covered with an insulating metal oxide layer, and a thin metal layer deposited onto the oxide acts as the gate electrode. Applying a gate voltage V_G between gate and source creates an electric field that attracts electrons from the p-substrate, creating an n-type channel between the s and D terminals. V_G can control the current ISD of this channel. B) Relating transfer characteristics (I_{SD} vs. V_G) of MOSFET plotted in linear (black) and semi-logarithmic (blue) scale. In the ohmic region, I_{SD} depends linearly on $V_{G.,\ and}$ the associating slope represents the transconductance, $g_{m,}$ of the device. The intersect of the linearly fitted transfer curve (blue dotted line) at $I_{SD} = 0$ is frequently defined as V_T. In the cut-off region, I_{SD} correlates exponentially to V_G. The inverse slope of the semi-logarithmic plot is called the subthreshold slope, SS. C) Output characteristics (I_{SD} vs. V_{SD}) of a MOSFET at different V_G values. Different background colors refer to the different operation modes.

builds up. In Figure 2-5C, the dotted line represents the course of the pinch-off voltage, which $V_P = V_{GS}–V_T$ defines. Further, the saturation region (grey background in Figure 2-5C), $V_{GS}>V_T$, and $V_{DS}>V_P$ are hallmarked by constant I_{SD} values.

The threshold voltage V_T is defined as the voltage at which the surface inversion layer just forms. V_T can be extracted graphically from transfer characteristics that can be plotted either in a linear (see blue line in Figure 2-5B) or in a semi-logarithmic (black line) graph. In linear scale, the prolongation of the fitted transfer curve with $I_{SD} = 0$ is commonly defined as V_T [99], whereas the slope of the curve is called transconductance, g_m. Vice versa, the inverse slope of the semi-logarithmic plot is called subthreshold swing S, and V_T is the value at which the transfer curve is steepest. Both values are critical parameters for validating the performance and efficiency of the FET[100,101].

2.5.1.1 Ion-sensitive field-effect transistor - ISFET

Bergveld et al. discovered in 1970 that MOSFETs in direct contact with a liquid solution are sensitive toward ions, i.e., sodium cations, and thus appropriate candidates for pH sensors, too[102]. Although in principle, an ion-sensitive field-effect transistor (ISFET) shares the same basic structure as a MOSFET, as depicted in Figure 2-6 below, an electrolyte solution, which is contacted by a reference electrode (RE), replaces the metal gate – a so-called liquid gate controls current flow[104–106].

Similar to MOSFET, the conductivity depends on the electric field perpendicular to the current's direction and on the potential differences over the gate oxide. As the current is closely connected to interface potential at the oxide/aqueous solution, the conductance

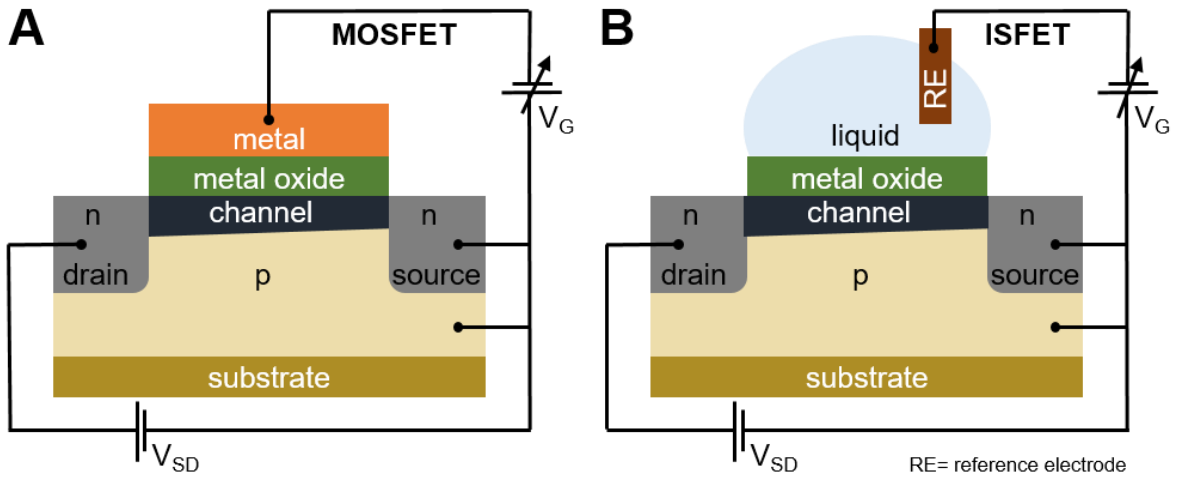

Figure 2-6: Schematic cross-section of A) MOSFET and B) ISFET device. V_G abbreviates gate voltage, whereas V_{SD} refers to source-drain voltage. Despite a similar basic structure, ISFET and MOSFET differ by replacement of the metallic gate of the MOSFET with an electrolyte solution connected to a reference electrode (RE).

in ISFETs depends on the charge situation at the oxide-electrolyte interface. Due to their chemical nature, oxide surfaces carry OH-functionalities, which can be either protonated or deprotonated- depending on the equilibrium conditions with ions of the sample solutions (H^+ and OH^-). Therefore, when the gate oxide of an ISFET meets an aqueous solution, a pH variation will reflect within the SiO_2 surface potential and cause the pH sensitivity of ISFET devices. In general, the performance in terms of selectivity and sensitivity of ISFETs relies on the properties of the electrolyte/insulator interface. Apart from Si/SiO_2 interfaces, other inorganic materials such as Al_2O_3, Si_3N_4, HfO_2, and Ta_2O show enhanced properties concerning pH response, hysteresis, and drift[107–109]. However, well-known surface chemistry routes exist for modifying SiO_2 with covalent attachment of organic (bio) molecules and polymers[105,110].

A more detailed discussion, corroborated by experimental results of the pH response of ISFETs concerning the amphoteric surface SiOH groups, follows in section 5.2.3.3.

In addition to the just mentioned MOSFET-based technologies, there are also organic field-effect transistors (OFET), which are made of polymers, carbon material based (such as graphene and carbon nanotubes (CNTs)) FETs, and ferroelectric FeFET, which are suitable for memory cells, widely used nowadays[111–115].

However, in this work, well-established silicon is still preferred as a material for FETs due to its ease of fabrication and processing. With Si being one of the most abundant elements on earth, it is not only readily available and, therefore, inexpensive to acquire but also offers highly effective semiconducting properties[116]**.** In addition, the naturally growing SiO2 layer, with its insulating properties, further supports the suitability of Si when making electronic chip components. With respect to matured semiconducting industry, SiNW FETs are conceivable with different sizes, shapes, and dopants; that further allows for a highly sensitive dynamic label-free electrical detection of biomolecules[117].

2.5.1.2 NanoFETs

Implementation of nanomaterials to biosensing platforms further boosts their potential for applications as chemical and biological sensing devices[118–120] as contemplated above (see section 2.2.2). Various types of nanomaterials can be applied with FETs, including prominent representatives such as silicon nanowires, zinc oxide

nanowires, CNTs, and graphene. After the discovery of the latter and the emergence of new 2D materials, many of these nanomaterials have been implemented as semiconducting channels in high-performance FETs as they offer unique structural and electronic properties compared to bulk counterparts[13,121,122].

The advantage of using nanoFETs over planar FETs lies, among others, in the utilization of dual- gates (meaning the implementation of an additional gate dielectric), in the high surface-to-volume ratio of the channels, and, as a result thereof, in small cross-sectional conduction pathways that allow for surface potentials that can penetrate the entire material[94,110,123,124]. Furthermore, in contrast to planar FETs, the nanowires act as conduction channels that are fully affected by the surface potentials.

Nanostructures offer size compatibility with biological molecules allowing them to be used as biosensors. Here, charged biomolecules can act locally as an (additional) liquid gate that leads to a subsequent change of surface potentials, forming the basis of target detection with FET[125,126]. A detailed discussion about the effects of surface-tethered biomolecules on FET signals and their surface potential, based on the example of DNA binding to a specific analyte, follows in chapter 5.3.

However, due to the same size in at least one dimension, biological recognition events alter the potential of the nanochannels even at low analyte concentrations. Consequently, the small sizes tremendously enhance the device's sensitivity and biodetection of analytes with wide concentration ranges between micromolar to zeptomolar, and even in some cases, single molecules detection gets possible[127–129].

In summary, the channel's conductivity in FETs strongly depends on the external electric field, as it will control the number of charges in the present channels. These properties help configure FETs as suitable biosensors, as the presence of molecules on a semiconducting surface can also alter the conductance. A modification of the surface with (charged) bioreceptors results in a depletion or accumulation of charge carriers. It influences the FETs by shifting the surface potentials that control charge carriers inside the channels. The associated changes serve as the basis for target detection, respectively. Here, not only the charge at the channel surfaces but also in the nearby surrounding medium is crucial to the function of FETs. The distinct relation of conductance to gate voltage and its generated electrical field makes FETs promising candidates for electrical biosensors in detecting and amplifying signals.

The electronic transducer approach is essential for dense and opaque fluids or tissues, in which optical-based biosensing approaches disqualify[104]. Besides, due to their commercial availability and high-quality (mass) production, FETs are widely used sensing and screening platforms these days[129–131].

2.6 Summary

In this chapter, an introduction to the fundamentals of different components of biosensing was given. Accentuating receptors based on DNA first, a subsequent introduction to two transducer systems, namely optical sensors operating through LSPR and electric sensors based on FETs, followed.

To conclude, the promising properties of DNA-based receptors raised further interest in implementing them into different biosensing platforms. The incorporation of DNA receptors into an optical sensor platform is validated in chapter 4, whereas the integration of aptamers into electrical sensors is presented in chapter 5.

2.7 References

(1) Bhalla, N.; Jolly, P.; Formisano, N.; Estrela, P. Introduction to Biosensors. *Essays Biochem.* **2016**, *60* (1), 1–8. https://doi.org/10.1042/EBC20150001.

(2) Damborský, P.; Švitel, J.; Katrlík, J. Optical Biosensors. *Essays Biochem.* **2016**, *60* (1), 91–100. https://doi.org/10.1042/EBC20150010.

(3) Dey, D.; Goswami, T. Optical Biosensors: A Revolution Towards Quantum Nanoscale Electronics Device Fabrication. *J. Biomed. Biotechnol.* **2011**, *2011*, e348218. https://doi.org/10.1155/2011/348218.

(4) Naresh, V.; Lee, N. A Review on Biosensors and Recent Development of Nanostructured Materials-Enabled Biosensors. *Sensors* **2021**, *21* (4), 1109. https://doi.org/10.3390/s21041109.

(5) Kim, J.; Campbell, A. S.; de Ávila, B. E.-F.; Wang, J. Wearable Biosensors for Healthcare Monitoring. *Nat. Biotechnol.* **2019**, *37* (4), 389–406. https://doi.org/10.1038/s41587-019-0045-y.

(6) Thévenot, D. R.; Toth, K.; Durst, R. A.; Wilson, G. S. Electrochemical Biosensors: Recommended Definitions and Classification1International Union of Pure and Applied Chemistry: Physical Chemistry Division, Commission I.7 (Biophysical Chemistry); Analytical Chemistry Division, Commission V.5 (Electroanalytical Chemistry).1. *Biosens. Bioelectron.* **2001**, *16* (1), 121–131. https://doi.org/10.1016/S0956-5663(01)00115-4.

(7) Hulanicki, A.; Glab, S.; Ingman, F. Chemical Sensors: Definitions and Classification. *Pure Appl. Chem.* **1991**, *63* (9), 1247–1250. https://doi.org/10.1351/pac199163091247.

(8) Hunt, H. K.; Armani, A. M. Label-Free Biological and Chemical Sensors. *Nanoscale* **2010**, *2* (9), 1544–1559. https://doi.org/10.1039/C0NR00201A.

(9) Ramsden, J. *Nanotechnology: An Introduction*; William Andrew, 2011.

(10) Malhotra, B. D.; Ali, M. A. *Nanomaterials for Biosensors: Fundamentals and Applications*; Micro & nano technologies series; Elsevier: Amsterdam, Netherlands, 2018.

(11) Abdel-Karim, R.; Reda, Y.; Abdel-Fattah, A. Review—Nanostructured Materials-Based Nanosensors. *J. Electrochem. Soc.* **2020**, *167* (3), 037554. https://doi.org/10.1149/1945-7111/ab67aa.

(12) Tsakalakos, T.; Ovid'ko, I. A.; Vasudevan, A. K. *Nanostructures: Synthesis, Functional Properties and Application*; Springer Science & Business Media, 2012.

(13) Kumar, C. S. S. R. *Nanomaterials for Biosensors*; John Wiley & Sons, 2007.

(14) Cao, G. *Nanostructures & Nanomaterials: Synthesis, Properties & Applications*; Imperial College Press, 2004.

(15) Biswas, A.; Bayer, I. S.; Biris, A. S.; Wang, T.; Dervishi, E.; Faupel, F. Advances in Top–down and Bottom–up Surface Nanofabrication: Techniques, Applications & Future Prospects. *Adv. Colloid Interface Sci.* **2012**, *170* (1), 2–27. https://doi.org/10.1016/j.cis.2011.11.001.

(16) Abid, N.; Khan, A. M.; Shujait, S.; Chaudhary, K.; Ikram, M.; Imran, M.; Haider, J.; Khan, M.; Khan, Q.; Maqbool, M. Synthesis of Nanomaterials Using Various Top-down and Bottom-up Approaches, Influencing Factors, Advantages, and Disadvantages: A Review. *Adv. Colloid Interface Sci.* **2022**, *300*, 102597. https://doi.org/10.1016/j.cis.2021.102597.

(17) Iqbal, P.; Preece, J. A.; Mendes, P. M. Nanotechnology: The "Top-Down" and "Bottom-Up" Approaches. In *Supramolecular Chemistry*; John Wiley & Sons, Ltd, 2012. https://doi.org/10.1002/9780470661345.smc195.

(18) Jones, M. R.; Osberg, K. D.; Macfarlane, R. J.; Langille, M. R.; Mirkin, C. A. Templated Techniques for the Synthesis and Assembly of Plasmonic Nanostructures. *Chem. Rev.* **2011**, *111* (6), 3736–3827. https://doi.org/10.1021/cr1004452.

(19) Li, S.; Singh, J.; Li, H.; Banerjee, I. A. *Biosensor Nanomaterials*; John Wiley & Sons, 2011.

(20) Chambers, J. P.; Arulanandam, B. P.; Matta, L. L.; Weis, A.; Valdes, J. J. Biosensor Recognition Elements. *Curr. Issues Mol. Biol.* **2008**, *10* (1–2), 1–12.

(21) Morales, M. A.; Halpern, J. M. Guide to Selecting a Biorecognition Element for Biosensors. *Bioconjug. Chem.* **2018**, *29* (10), 3231–3239. https://doi.org/10.1021/acs.bioconjchem.8b00592.

(22) Hering, E.; Schönfelder, G. Biologische und medizinische Sensoren. In *Sensoren in Wissenschaft und Technik*; Hering, E., Schönfelder, G., Eds.; Vieweg+Teubner Verlag: Wiesbaden, 2012; pp 547–582. https://doi.org/10.1007/978-3-8348-8635-4_12.

(23) Christen, P.; Jaussi, R. *Biochemie: eine Einführung mit 40 Lerneinheiten*; Springer-Lehrbuch; Springer: Berlin Heidelberg, 2005.

(24) Winklmair, M.; Weller, M. G.; Mangler, J.; Schlosshauer, B.; Niessner, R. Development of a Highly Sensitive Enzyme-Immunoassay for the Determination of Triazine Herbicides. *Fresenius J. Anal. Chem.* **1997**, *358* (5), 614–622. https://doi.org/10.1007/s002160050479.

(25) Ahoulou, S.; Perret, E.; Nedelec, J.-M. Functionalization and Characterization of Silicon Nanowires for Sensing Applications: A Review. *Nanomaterials* **2021**, *11* (4), 999. https://doi.org/10.3390/nano11040999.

(26) Gu, M. B.; Kim, H.-S. *Biosensors Based on Aptamers and Enzymes*; Springer, 2014.

(27) Anker, J. N.; Hall, W. P.; Lyandres, O.; Shah, N. C.; Zhao, J.; Van Duyne, R. P. Biosensing with Plasmonic Nanosensors. *Nat. Mater.* **2008**, *7* (6), 442–453. https://doi.org/10.1038/nmat2162.

(28) Fawcett, N. C.; Evans, J. A.; Chien, L.-C.; Flowers, N. Nucleic Acid Hybridization Detected by Piezoelectric Resonance. *Anal. Lett.* **1988**, *21* (7), 1099–1114. https://doi.org/10.1080/00032718808055499.

(29) Rafique, B.; Iqbal, M.; Mehmood, T.; Shaheen, M. A. Electrochemical DNA Biosensors: A Review. *Sens. Rev.* **2018**, *39* (1), 34–50. https://doi.org/10.1108/SR-08-2017-0156.

(30) V, K. DNA Biosensors-A Review. *J. Bioeng. Biomed. Sci.* **2017**, *07* (02). https://doi.org/10.4172/2155-9538.1000222.

(31) Sinden, R. R. Introduction to the Structure, Properties, and Reactions of DNA. In *DNA Structure and Function*; Elsevier, 1994; pp 1–57. https://doi.org/10.1016/B978-0-08-057173-7.50006-7.

(32) Lakhin, A. V.; Tarantul, V. Z.; Gening, L. V. Aptamers: Problems, Solutions and Prospects. *Acta Naturae* **2013**, *5* (4), 34–43.

(33) Peterlinz, K. A.; Georgiadis, R. M.; Herne, T. M.; Tarlov, M. J. Observation of Hybridization and Dehybridization of Thiol-Tethered DNA Using Two-Color Surface Plasmon Resonance Spectroscopy. *J. Am. Chem. Soc.* **1997**, *119* (14), 3401–3402. https://doi.org/10.1021/ja964326c.

(34) Andersson, K.; Areskoug, D.; Hardenborg, E. Exploring Buffer Space for Molecular Interactions. *J. Mol. Recognit. JMR* **1999**, *12* (5), 310–315. https://doi.org/10.1002/(SICI)1099-1352(199909/10)12:5<310::AID-JMR470>3.0.CO;2-5.

(35) Schmitt, T. J.; Rogers, J. B.; Knotts, T. A. Exploring the Mechanisms of DNA Hybridization on a Surface. *J. Chem. Phys.* **2013**, *138* (3), 035102. https://doi.org/10.1063/1.4775480.

(36) Ellington, A. D.; Szostak, J. W. In Vitro Selection of RNA Molecules That Bind Specific Ligands. *Nature* **1990**, *346* (6287), 818–822. https://doi.org/10.1038/346818a0.

(37) Luzi, E.; Minunni, M.; Tombelli, S.; Mascini, M. New Trends in Affinity Sensing: Aptamers for Ligand Binding. *TrAC Trends Anal. Chem.* **2003**, *22* (11), 810–818. https://doi.org/10.1016/S0165-9936(03)01208-1.

(38) Hetzke, T.; Vogel, M.; Gophane, D. B.; Weigand, J. E.; Suess, B.; Sigurdsson, S. T.; Prisner, T. F. Influence of Mg2+ on the Conformational Flexibility of a Tetracycline Aptamer. *RNA* **2019**, *25* (1), 158–167. https://doi.org/10.1261/rna.068684.118.

(39) Baldrich, E.; Restrepo, A.; O'Sullivan, C. K. Aptasensor Development: Elucidation of Critical Parameters for Optimal Aptamer Performance. *Anal. Chem.* **2004**, *76* (23), 7053–7063. https://doi.org/10.1021/ac049258o.

(40) Martin, J. A.; Chávez, J. L.; Chushak, Y.; Chapleau, R. R.; Hagen, J.; Kelley-Loughnane, N. Tunable Stringency Aptamer Selection and Gold Nanoparticle Assay for Detection of Cortisol. *Anal. Bioanal. Chem.* **2014**, *406* (19), 4637–4647. https://doi.org/10.1007/s00216-014-7883-8.

(41) Nakatsuka, N.; Cao, H. H.; Deshayes, S.; Melkonian, A. L.; Kasko, A. M.; Weiss, P. S.; Andrews, A. M. Aptamer Recognition of Multiplexed Small-Molecule-Functionalized Substrates. *ACS Appl. Mater. Interfaces* **2018**, *10* (28), 23490–23500. https://doi.org/10.1021/acsami.8b02837.

(42) Zhang, J.; Wang, L.; Pan, D.; Song, S.; Boey, F. Y. C.; Zhang, H.; Fan, C. Visual Cocaine Detection with Gold Nanoparticles and Rationally Engineered Aptamer Structures. *Small* **2008**, *4* (8), 1196–1200. https://doi.org/10.1002/smll.200800057.

(43) Liu, J.; Bai, W.; Niu, S.; Zhu, C.; Yang, S.; Chen, A. Highly Sensitive Colorimetric Detection of 17β-Estradiol Using Split DNA Aptamers Immobilized on Unmodified Gold Nanoparticles. *Sci. Rep.* **2014**, *4*, 7571. https://doi.org/10.1038/srep07571.

(44) Aliakbarinodehi, N.; Jolly, P.; Bhalla, N.; Miodek, A.; De Micheli, G.; Estrela, P.; Carrara, S. Aptamer-Based Field-Effect Biosensor for Tenofovir Detection. *Sci. Rep.* **2017**, *7*, 44409. https://doi.org/10.1038/srep44409.

(45) Raddatz, M.-S. L.; Dolf, A.; Endl, E.; Knolle, P.; Famulok, M.; Mayer, G. Enrichment of Cell-Targeting and Population-Specific Aptamers by Fluorescence-Activated Cell Sorting. *Angew. Chem. Int. Ed Engl.* **2008**, *47* (28), 5190–5193. https://doi.org/10.1002/anie.200800216.

(46) Wang, Y.-X.; Ye, Z.-Z.; Si, C.-Y.; Ying, Y.-B. Application of Aptamer Based Biosensors for Detection of Pathogenic Microorganisms. *Chin. J. Anal. Chem.* **2012**, *40* (4), 634–642. https://doi.org/10.1016/S1872-2040(11)60542-2.

(47) Wandtke, T.; Wędrowska, E.; Szczur, M.; Przybylski, G.; Libura, M.; Kopiński, P. Aptamers—Diagnostic and Therapeutic Solution in SARS-CoV-2. *Int. J. Mol. Sci.* **2022**, *23* (3), 1412. https://doi.org/10.3390/ijms23031412.

(48) Dollins, C. M.; Nair, S.; Sullenger, B. A. Aptamers in Immunotherapy. *Hum. Gene Ther.* **2008**, *19* (5), 443–450. https://doi.org/10.1089/hum.2008.045.

(49) Hong, K. L.; Sooter, L. J. Single-Stranded DNA Aptamers against Pathogens and Toxins: Identification and Biosensing Applications. *BioMed Res. Int.* **2015**, *2015*, 419318. https://doi.org/10.1155/2015/419318.

(50) Kohlberger, M.; Gadermaier, G. SELEX: Critical Factors and Optimization Strategies for Successful Aptamer Selection. *Biotechnol. Appl. Biochem.* **2021**, bab.2244. https://doi.org/10.1002/bab.2244.

(51) Zhuo, Z.; Yu, Y.; Wang, M.; Li, J.; Zhang, Z.; Liu, J.; Wu, X.; Lu, A.; Zhang, G.; Zhang, B. Recent Advances in SELEX Technology and Aptamer Applications in Biomedicine. *Int. J. Mol. Sci.* **2017**, *18* (10), 2142. https://doi.org/10.3390/ijms18102142.

(52) Nakatsuka, N.; Yang, K.-A.; Abendroth, J. M.; Cheung, K.; Xu, X.; Yang, H.; Zhao, C.; Zhu, B.; Rim, Y. S.; Yang, Y.; Weiss, P. S.; Stojanović, M. N.; Andrews, A. M. Aptamer-Field-Effect Transistors Overcome Debye Length Limitations for Small-Molecule Sensing. *Science* **2018**, *362* (6412), 319–324. https://doi.org/10.1126/science.aao6750.

(53) Zourob, M. *Recognition Receptors in Biosensors*; Springer: New York London, 2010.

(54) Nimse, S. B.; Song, K.; Sonawane, M. D.; Sayyed, D. R.; Kim, T. Immobilization Techniques for Microarray: Challenges and Applications. *Sensors* **2014**, *14* (12), 22208–22229. https://doi.org/10.3390/s141222208.

(55) Reis, C.; Sousa, E.; Serpa, J.; Oliveira, R.; Oliveira, R.; Santos, J. DESIGN OF IMMOBILIZED ENZYME BIOCATALYSTS: DRAWBACKS AND OPPORTUNITIES. *Quím. Nova* **2019**. https://doi.org/10.21577/0100-4042.20170381.

(56) Mohamad, N. R.; Marzuki, N. H. C.; Buang, N. A.; Huyop, F.; Wahab, R. A. An Overview of Technologies for Immobilization of Enzymes and Surface Analysis Techniques for Immobilized Enzymes. *Biotechnol. Biotechnol. Equip.* **2015**, *29* (2), 205–220. https://doi.org/10.1080/13102818.2015.1008192.

(57) Sirisha, V.; Jain, A.; Jain, A. Enzyme Immobilization: An Overview on Methods, Support Material, and Applications of Immobilized Enzymes. *Adv. Food Nutr. Res.* **2016**. https://doi.org/10.1016/bs.afnr.2016.07.004.

(58) Kermasha, S.; Gill, J. K. Immobilization of Enzymes and Their Use in Biotechnological Applications. In *Enzymes*; Elsevier, 2021; pp 133–170. https://doi.org/10.1016/B978-0-12-800217-9.00006-X.

(59) Thapa, K.; Liu, W.; Wang, R. Nucleic Acid-Based Electrochemical Biosensor: Recent Advances in Probe Immobilization and Signal Amplification Strategies. *Wiley Interdiscip. Rev. Nanomed. Nanobiotechnol.* **2022**, *14* (1), e1765. https://doi.org/10.1002/wnan.1765.

(60) Bishop, A. R.; Nuzzo, R. G. Self-Assembled Monolayers: Recent Developments and Applications. *Curr. Opin. Colloid Interface Sci.* **1996**, *1* (1), 127–136. https://doi.org/10.1016/S1359-0294(96)80053-7.

(61) Dilimon, V. S.; Rajalingam, S.; Delhalle, J.; Mekhalif, Z. Self-Assembly Mechanism of Thiol, Dithiol, Dithiocarboxylic Acid, Disulfide and Diselenide on Gold: An Electrochemical Impedance Study. *Phys. Chem. Chem. Phys.* **2013**, *15* (39), 16648–16656. https://doi.org/10.1039/C3CP51804C.

(62) Nicosia, C.; Huskens, J. Reactive Self-Assembled Monolayers: From Surface Functionalization to Gradient Formation. *Mater. Horiz.* **2014**, *1* (1), 32–45. https://doi.org/10.1039/C3MH00046J.

(63) Borisov, S. M.; Wolfbeis, O. S. Optical Biosensors. *Chem. Rev.* **2008**, *108* (2), 423–461. https://doi.org/10.1021/cr068105t.

(64) Alarcón-Angeles, G.; Álvarez-Romero, G. A.; Rosati, G.; Parolo, C.; Merkoçi, A. Point-of-Care Sensors in Clinical Environments: Potential and Challenges. In *Reference Module in Biomedical Sciences*; Elsevier, 2022. https://doi.org/10.1016/B978-0-12-822548-6.00106-0.

(65) Ligler, F. S. A Perspective on Optical Biosensors and Integrated Sensor Systems. *Anal. Chem.* **2009**, *81* (2), 519–526. https://doi.org/10.1021/ac8016289.

(66) Singh, P. Surface Plasmon Resonance: A Boon for Viral Diagnostics. In *Reference Module in Life Sciences*; Elsevier, 2017. https://doi.org/10.1016/B978-0-12-809633-8.12245-9.

(67) Wood, R. W. On a Remarkable Case of Uneven Distribution of Light in a Diffraction Grating Spectrum. *Proc. Phys. Soc. Lond.* **1902**, *18* (1), 269–275. https://doi.org/10.1088/1478-7814/18/1/325.

(68) Rayleigh, Lord. On the Dynamical Theory of Gratings. *Proc. R. Soc. Lond. Ser. A* **1907**, *79*, 399–416. https://doi.org/10.1098/rspa.1907.0051.

(69) Wood, R. W. XXVII. Diffraction Gratings with Controlled Groove Form and Abnormal Distribution of Intensity. *Lond. Edinb. Dublin Philos. Mag. J. Sci.* **1912**, *23* (134), 310–317. https://doi.org/10.1080/14786440208637224.

(70) Haes, A. J.; Van Duyne, R. P. A Unified View of Propagating and Localized Surface Plasmon Resonance Biosensors. *Anal. Bioanal. Chem.* **2004**, *379* (7), 920–930. https://doi.org/10.1007/s00216-004-2708-9.

(71) Sonntag, F.; Schilling, N.; Mader, K.; Gruchow, M.; Klotzbach, U.; Lindner, G.; Horland, R.; Wagner, I.; Lauster, R.; Howitz, S.; Hoffmann, S.; Marx, U. Design and Prototyping of a Chip-Based Multi-Micro-Organoid Culture System for Substance Testing, Predictive to Human (Substance) Exposure. *J. Biotechnol.* **2010**, *148* (1), 70–75. https://doi.org/10.1016/j.jbiotec.2010.02.001.

(72) Piliarik, M.; Vaisocherová, H.; Homola, J. Surface Plasmon Resonance Biosensing. *Methods Mol. Biol. Clifton NJ* **2009**, *503*, 65–88. https://doi.org/10.1007/978-1-60327-567-5_5.

(73) *Nano-Inspired Biosensors for Protein Assay with Clinical Applications*; Li, G., Ed.; Elsevier: Amsterdam, Netherlands ; Cambridge, MA, 2019.

(74) Willets, K. A.; Van Duyne, R. P. Localized Surface Plasmon Resonance Spectroscopy and Sensing. *Annu. Rev. Phys. Chem.* **2007**, *58* (1), 267–297. https://doi.org/10.1146/annurev.physchem.58.032806.104607.

(75) Petryayeva, E.; Krull, U. J. Localized Surface Plasmon Resonance: Nanostructures, Bioassays and Biosensing—A Review. *Anal. Chim. Acta* **2011**, *706* (1), 8–24. https://doi.org/10.1016/j.aca.2011.08.020.

(76) *Nanoparticle Technology Handbook*, 1st ed.; Hosokawa, M., Ed.; Elsevier: Amsterdam, Netherlands ; Boston [Mass.], 2007.

(77) Estevez, M.-C.; Otte, M. A.; Sepulveda, B.; Lechuga, L. M. Trends and Challenges of Refractometric Nanoplasmonic Biosensors: A Review. *Anal. Chim. Acta* **2014**, *806*, 55–73. https://doi.org/10.1016/j.aca.2013.10.048.

(78) Mayer, K. M.; Hafner, J. H. Localized Surface Plasmon Resonance Sensors. *Chem. Rev.* **2011**, *111* (6), 3828–3857. https://doi.org/10.1021/cr100313v.

(79) Zhang, J.; Kolhatkar, G.; Ruediger, A. Localized Surface Plasmon Resonance Shift and Its Application in Scanning Near-Field Optical Microscopy. *J. Mater. Chem. C* **2021**, *9* (22), 6960–6969. https://doi.org/10.1039/D1TC00877C.

(80) Xu, T.; Geng, Z. Strategies to Improve Performances of LSPR Biosensing: Structure, Materials, and Interface Modification. *Biosens. Bioelectron.* **2021**, *174*, 112850. https://doi.org/10.1016/j.bios.2020.112850.

(81) Noguez, C. Surface Plasmons on Metal Nanoparticles: The Influence of Shape and Physical Environment. *J. Phys. Chem. C* **2007**, *111* (10), 3806–3819. https://doi.org/10.1021/jp066539m.

(82) Amendola, V.; Meneghetti, M. Size Evaluation of Gold Nanoparticles by UV−vis Spectroscopy. *J. Phys. Chem. C* **2009**, *113* (11), 4277–4285. https://doi.org/10.1021/jp8082425.

(83) He, Y. Q.; Liu, S. P.; Kong, L.; Liu, Z. F. A Study on the Sizes and Concentrations of Gold Nanoparticles by Spectra of Absorption, Resonance Rayleigh Scattering and Resonance Non-Linear Scattering. *Spectrochim. Acta. A. Mol. Biomol. Spectrosc.* **2005**, *61* (13), 2861–2866. https://doi.org/10.1016/j.saa.2004.10.035.

(84) Katyal, J.; Soni, R. K. Size- and Shape-Dependent Plasmonic Properties of Aluminum Nanoparticles for Nanosensing Applications. *J. Mod. Opt.* **2013**, *60* (20), 1717–1728. https://doi.org/10.1080/09500340.2013.856483.

(85) Klinghammer, S.; Uhlig, T.; Patrovsky, F.; Böhm, M.; Schütt, J.; Pütz, N.; Baraban, L.; Eng, L. M.; Cuniberti, G. Plasmonic Biosensor Based on Vertical Arrays of Gold Nanoantennas. *ACS Sens.* **2018**, *3* (7), 1392–1400. https://doi.org/10.1021/acssensors.8b00315.

(86) Huang, X.; El-Sayed, I. H.; Qian, W.; El-Sayed, M. A. Cancer Cell Imaging and Photothermal Therapy in the Near-Infrared Region by Using Gold Nanorods. *J. Am. Chem. Soc.* **2006**, *128* (6), 2115–2120. https://doi.org/10.1021/ja057254a.

(87) Doiron, B.; Mota, M.; Wells, M. P.; Bower, R.; Mihai, A.; Li, Y.; Cohen, L. F.; Alford, N. McN.; Petrov, P. K.; Oulton, R. F.; Maier, S. A. Quantifying Figures of Merit for Localized Surface Plasmon Resonance Applications: A Materials Survey. *ACS Photonics* **2019**, *6* (2), 240–259. https://doi.org/10.1021/acsphotonics.8b01369.

(88) Rehbock, C.; Jakobi, J.; Gamrad, L.; Meer, S. van der; Tiedemann, D.; Taylor, U.; Kues, W.; Rath, D.; Barcikowski, S. Current State of Laser Synthesis of Metal and Alloy Nanoparticles as Ligand-Free Reference Materials for Nano-Toxicological Assays. *Beilstein J. Nanotechnol.* **2014**, *5* (1), 1523–1541. https://doi.org/10.3762/bjnano.5.165.

(89) Lopez, G. A.; Estevez, M.-C.; Soler, M.; Lechuga, L. M. Recent Advances in Nanoplasmonic Biosensors: Applications and Lab-on-a-Chip Integration. *Nanophotonics* **2017**, *6* (1). https://doi.org/10.1515/nanoph-2016-0101.

(90) Grieshaber, D.; MacKenzie, R.; Vörös, J.; Reimhult, E. Electrochemical Biosensors - Sensor Principles and Architectures. *Sensors* **2008**, *8* (3), 1400–1458. https://doi.org/10.3390/s80314000.

(91) Luo, X.; Davis, J. J. Electrical Biosensors and the Label Free Detection of Protein Disease Biomarkers. *Chem. Soc. Rev.* **2013**, *42* (13), 5944–5962. https://doi.org/10.1039/C3CS60077G.

(92) Xu, J.-J. Analytical Aspects of Fet-Based Biosensors. *Front. Biosci.* **2005**, *10* (1–3), 420. https://doi.org/10.2741/1538.

(93) Patolsky, F.; Zheng, G.; Lieber, C. M. Nanowire Sensors for Medicine and the Life Sciences. *Nanomed.* **2006**, *1* (1), 51–65. https://doi.org/10.2217/17435889.1.1.51.

(94) Patolsky, F.; Lieber, C. M. Nanowire Nanosensors. *Mater. Today* **2005**, *8* (4), 20–28. https://doi.org/10.1016/S1369-7021(05)00791-1.

(95) Löcherer, K.-H. *Halbleiterbauelemente*; Springer-Verlag, 2013.

(96) Sze, S. M.; Ng, K. K. *Physics of Semiconductor Devices*, Third edition.; Wiley-Interscience: Hoboken, NJ, 2007.

(97) Oktyabrsky, S.; Ye, P. *Fundamentals of III-V Semiconductor MOSFETs*; Springer Science & Business Media, 2010.

(98) Rashid, M. H. *Power Electronics: Circuits, Devices and Applications*, 3rd edition.; Pearson: Upper Saddle River, N.J, 2003.

(99) Ortiz-Conde, A.; García Sánchez, F. J.; Liou, J. J.; Cerdeira, A.; Estrada, M.; Yue, Y. A Review of Recent MOSFET Threshold Voltage Extraction Methods. *Microelectron. Reliab.* **2002**, *42* (4), 583–596. https://doi.org/10.1016/S0026-2714(02)00027-6.

(100) Brews, J. R. Subthreshold Behavior of Uniformly and Nonuniformly Doped Long-Channel MOSFET. *IEEE Trans. Electron Devices* **1979**, *26* (9), 1282–1291. https://doi.org/10.1109/T-ED.1979.19594.

(101) Sanaullah, M.; Chowdhury, M. H. Subthreshold Swing Characteristics of Multilayer MoS2 Tunnel FET. In *2015 IEEE 58th International Midwest Symposium on Circuits and Systems (MWSCAS)*; IEEE: Fort Collins, CO, USA, 2015; pp 1–4. https://doi.org/10.1109/MWSCAS.2015.7282101.

(102) Bergveld, P. Development of an Ion-Sensitive Solid-State Device for Neurophysiological Measurements. *IEEE Trans. Biomed. Eng.* **1970**, *17* (1), 70–71. https://doi.org/10.1109/tbme.1970.4502688.

(103) Bergveld, P. A Critical Evaluation of Direct Electrical Protein Detection Methods. *Biosens. Bioelectron.* **1991**, *6* (1), 55–72. https://doi.org/10.1016/0956-5663(91)85009-L.

(104) Lee, C.-S.; Kim, S. K.; Kim, M. Ion-Sensitive Field-Effect Transistor for Biological Sensing. *Sensors* **2009**, *9* (9), 7111–7131. https://doi.org/10.3390/s90907111.

(105) Bergveld, P. Thirty Years of ISFETOLOGY: What Happened in the Past 30 Years and What May Happen in the next 30 Years. *Sens. Actuators B Chem.* **2003**, *88* (1), 1–20. https://doi.org/10.1016/S0925-4005(02)00301-5.

(106) Hierlemann, A.; Baltes, H. CMOS-Based Chemical Microsensors. *The Analyst* **2003**, *128* (1), 15–28. https://doi.org/10.1039/b208563c.

(107) Rollo, S.; Rani, D.; Olthuis, W.; Pascual García, C. High Performance Fin-FET Electrochemical Sensor with High-k Dielectric Materials. *Sens. Actuators B Chem.* **2020**, *303*, 127215. https://doi.org/10.1016/j.snb.2019.127215.

(108) Kittl, J. A.; Opsomer, K.; Popovici, M.; Menou, N.; Kaczer, B.; Wang, X. P.; Adelmann, C.; Pawlak, M. A.; Tomida, K.; Rothschild, A.; Govoreanu, B.; Degraeve, R.; Schaekers, M.; Zahid, M.; Delabie, A.; Meersschaut, J.; Polspoel, W.; Clima, S.; Pourtois, G.; Knaepen, W.; Detavernier, C.; Afanas'ev, V. V.; Blomberg, T.; Pierreux, D.; Swerts, J.; Fischer, P.; Maes, J. W.; Manger, D.; Vandervorst, W.; Conard, T.; Franquet, A.; Favia, P.; Bender, H.; Brijs, B.; Van Elshocht, S.; Jurczak, M.; Van Houdt, J.; Wouters, D. J. High-k Dielectrics for Future Generation Memory Devices (Invited Paper). *Microelectron. Eng.* **2009**, *86* (7–9), 1789–1795. https://doi.org/10.1016/j.mee.2009.03.045.

(109) Yota, J.; Shen, H.; Ramanathan, R. Characterization of Atomic Layer Deposition HfO2, Al2O3, and Plasma-Enhanced Chemical Vapor Deposition Si3N4 as Metal–Insulator–Metal Capacitor Dielectric for GaAs HBT Technology. *J. Vac. Sci. Technol. A* **2013**, *31* (1), 01A134. https://doi.org/10.1116/1.4769207.

(110) Sinha, S.; Pal, T. A Comprehensive Review of FET-based PH Sensors: Materials, Fabrication Technologies, and Modeling. *Electrochem. Sci. Adv.* **2021**, 2100147. https://doi.org/10.1002/elsa.202100147.

(111) Surya, S. G.; Raval, H. N.; Ahmad, R.; Sonar, P.; Salama, K. N.; Rao, V. R. Organic Field Effect Transistors (OFETs) in Environmental Sensing and Health Monitoring: A Review. *TrAC Trends Anal. Chem.* **2019**, *111*, 27–36. https://doi.org/10.1016/j.trac.2018.11.027.

(112) Panes-Ruiz, L. A.; Stückemann, T.; Riemenschneider, L.; Löffler, M.; Bezugly, V.; Cuniberti, G. Detection of C-Reactive Protein by Liquid-Gated Carbon Nanotube Field Effect Transistors (LG-CNTFET): A Promising Tool against Antibiotic Resistance. *Eng. Proc.* **2021**, *6* (1), 15. https://doi.org/10.3390/I3S2021Dresden-10114.

(113) Sreejith, S.; Ajayan, J.; Radhika, J. M.; Sivasankari, B.; Tayal, S.; Saravanan, M. A Comprehensive Review on Graphene FET Bio-Sensors and Their Emerging Application in DNA/RNA Sensing & Rapid Covid-19 Detection. *Measurement* **2023**, *206*, 112202. https://doi.org/10.1016/j.measurement.2022.112202.

(114) Zamzami, M. A.; Rabbani, G.; Ahmad, A.; Basalah, A. A.; Al-Sabban, W. H.; Nate Ahn, S.; Choudhry, H. Carbon Nanotube Field-Effect Transistor (CNT-FET)-Based Biosensor for Rapid Detection of SARS-CoV-2 (COVID-19) Surface Spike Protein S1. *Bioelectrochemistry* **2022**, *143*, 107982. https://doi.org/10.1016/j.bioelechem.2021.107982.

(115) Kim, J. Y.; Choi, M.-J.; Jang, H. W. Ferroelectric Field Effect Transistors: Progress and Perspective. *APL Mater.* **2021**, *9* (2), 021102. https://doi.org/10.1063/5.0035515.

(116) *Silicon - Element information, properties and uses | Periodic Table*. https://www.rsc.org/periodic-table/element/14/silicon (accessed 2022-12-06).

(117) Chen, K.-I.; Li, B.-R.; Chen, Y.-T. Silicon Nanowire Field-Effect Transistor-Based Biosensors for Biomedical Diagnosis and Cellular Recording Investigation. *Nano Today* **2011**, *6* (2), 131–154. https://doi.org/10.1016/j.nantod.2011.02.001.

(118) Pachauri, V.; Ingebrandt, S. Biologically Sensitive Field-Effect Transistors: From ISFETs to NanoFETs. *Essays Biochem.* **2016**, *60* (1), 81–90. https://doi.org/10.1042/EBC20150009.

(119) Baraban, L.; Ibarlucea, B.; Baek, E.; Cuniberti, G. Hybrid Silicon Nanowire Devices and Their Functional Diversity. *Adv. Sci.* **2019**, *6* (15), 1900522. https://doi.org/10.1002/advs.201900522.

(120) Kaisti, M. Detection Principles of Biological and Chemical FET Sensors. *Biosens. Bioelectron.* **2017**, *98*, 437–448. https://doi.org/10.1016/j.bios.2017.07.010.

(121) Li, J.; To, S.; You, L.; Sun, Y. Nanostructure Field Effect Transistor Biosensors. In *Encyclopedia of Nanotechnology*; Bhushan, B., Ed.; Springer Netherlands: Dordrecht, 2016; pp 2713–2726. https://doi.org/10.1007/978-94-017-9780-1_338.

(122) Syedmoradi, L.; Ahmadi, A.; Norton, M. L.; Omidfar, K. A Review on Nanomaterial-Based Field Effect Transistor Technology for Biomarker Detection. *Microchim. Acta* **2019**, *186* (11), 739. https://doi.org/10.1007/s00604-019-3850-6.

(123) Elfström, N.; Juhasz, R.; Sychugov, I.; Engfeldt, T.; Karlström, A. E.; Linnros, J. Surface Charge Sensitivity of Silicon Nanowires: Size Dependence. *Nano Lett.* **2007**, *7* (9), 2608–2612. https://doi.org/10.1021/nl0709017.

(124) Bhatt, D.; Panda, S. Dual-Gate Ion-Sensitive Field-Effect Transistors: A Review. *Electrochem. Sci. Adv. n/a* (n/a), e2100195. https://doi.org/10.1002/elsa.202100195.

(125) Sakata, T. Biologically Coupled Gate Field-Effect Transistors Meet in Vitro Diagnostics. *ACS Omega* **2019**, *4* (7), 11852–11862. https://doi.org/10.1021/acsomega.9b01629.

(126) Sung, D.; Koo, J. A Review of BioFET's Basic Principles and Materials for Biomedical Applications. *Biomed. Eng. Lett.* **2021**, *11* (2), 85–96. https://doi.org/10.1007/s13534-021-00187-8.

(127) Macchia, E.; Manoli, K.; Di Franco, C.; Scamarcio, G.; Torsi, L. New Trends in Single-Molecule Bioanalytical Detection. *Anal. Bioanal. Chem.* **2020**, *412* (21), 5005–5014. https://doi.org/10.1007/s00216-020-02540-9.

(128) Macchia, E.; Manoli, K.; Holzer, B.; Di Franco, C.; Ghittorelli, M.; Torricelli, F.; Alberga, D.; Mangiatordi, G. F.; Palazzo, G.; Scamarcio, G.; Torsi, L. Single-Molecule Detection with a Millimetre-Sized Transistor. *Nat. Commun.* **2018**, *9* (1), 3223. https://doi.org/10.1038/s41467-018-05235-z.

(129) Sadighbayan, D.; Hasanzadeh, M.; Ghafar-Zadeh, E. Biosensing Based on Field-Effect Transistors (FET): Recent Progress and Challenges. *TrAC Trends Anal. Chem.* **2020**, *133*, 116067. https://doi.org/10.1016/j.trac.2020.116067.

(130) Wadhera, T.; Kakkar, D.; Wadhwa, G.; Raj, B. Recent Advances and Progress in Development of the Field Effect Transistor Biosensor: A Review. *J. Electron. Mater.* **2019**, *48* (12), 7635–7646. https://doi.org/10.1007/s11664-019-07705-6.

(131) Vu, C.-A.; Chen, W.-Y. Field-Effect Transistor Biosensors for Biomedical Applications: Recent Advances and Future Prospects. *Sensors* **2019**, *19* (19), E4214. https://doi.org/10.3390/s19194214.

3 Materials and methods

3.1 Plasmonic biosensors based on vertically aligned gold nanoantennas

3.1.1 Materials

Multiple DNA sequences with different modifications were used in this study. For all experiments, 25 base-pair-long DNA strands acting as probes were immobilized onto gold surfaces. Hence, probe DNA was modified on its 5' end with a thiol group (HS-) and a C6 linker.

Two complementary DNA strands (cDNA), which differ in length, were studied. Here, a fully complementary DNA strand with the same length as the probe DNA (cDNA 25), and a 100 bp long DNA strand (cDNA 100), where only the first 25 bp is complementary to the probe, were chosen. In addition, a 25 bp long, non-complementary strand (control) was selected for control purposes. The exact sequences of all used DNA strands and their possible modifications are listed in Table 3-1 below; the complementary parts are underlined.

For calculation of the surface coverage of probe DNA on the particular structures, DNA was not only modified with a thiol-group but also with a fluorescent label 6-Carboxyfluorescein (FAM) on the 3'-end.

Table 3-1: In this research used sequences and modifications of DNA strands. The underlined fragments refer to complementary DNA sequences.

Name	Sequence (5 '->3 ')	5 '- modification	3 '- modification
Probe DNA	ATA GGC TCT GCG GAA TAA GGT CTC G	C6- SH	
cDNA 25	CGA GAC CTT ATT CCG CAG AGC CTA T		
cDNA 100	AGG TGG CTC AGG TGC GCC ATA GGT CCC GCA CCT GAG CCA TAT ATG GCT CAG GTG CGC CAT AGG TGG CCA TAG GTT CGA GAC CTT ATT CCG CAG AGC CTA T		
control	ATG CGT ACG TGT TGG AGG ACG TAA C		
DNA_Thio_FAM	CGA GAC CTT ATT CCG CAG AGC CTA T	C6- SH	FAM

All DNA strands were purchased from Biomers.net (Ulm, Germany). Aliquots with a concentration of 100 µM in PBS were prepared and stored at -18°C. Before use, DNA aliquots were heated to 95°C for 5 min and constantly cooled at 2.3°C/min to room temperature, using a MasterCycler (Eppendorf, Hamburg, Germany), and further diluted to desired concentrations, respectively.

Table 3-2 summarizes other chemicals used in this research, their abbreviations, and their suppliers.

Table 3-2: Overview of used chemicals, including their abbreviation and supplier.

Chemical	Abbreviation	Supplier
Magnesium chloride	$MgCl_2$	Fluka analytical
Potassium Phosphate	KH_2PO_4	Roth
Tris(hydroxymethyl)aminomethane	TRIS	Fluka analytical
6- Mercaptohexanol	MCH	Sigma Aldrich
2- Mercaptoethanol		Bio-Rad
Ethylenediaminetetraacetic acid	Na_2EDTA	Sigma Aldrich
Sodium hydroxide	NaOH	Grüssing GmbH
Hydrochloric acid	HCl	Sigma Aldrich
Chloroauric acid	$HAuCl_4$	Chempur
Sodium thiosulfate	$Na_2S_2O_3$	Sigma Aldrich
Sodium sulfite	Na_2SO_3	Sigma Aldrich

3.1.2 Manufacturing of nanoantenna arrays

Collaborators of the Chair of experimental physics/photophysics (IAPP) at TU Dresden manufactured Nanoantenna-based sensors. The exact processes have been published elsewhere[1]. Briefly, nanoantennas were fabricated by depositing gold into nanometer-sized pores of an anodized aluminum oxide (AAO) matrix. Before, different layers of 5 nm titanium, 8 nm gold, and 300 nm of aluminum were sputtered onto glass substrates. Then, the nano-porous aluminum oxide (AAO) layer was created by anodization of the aluminum layer at 26 V in a cooled aqueous solution of 0.3 M sulfuric acid at 0°C. Before filling the AAO matrix with gold, an etching step with 0.03 M NaOH for 25 s was performed to remove residual aluminum and thus open the pores to the bottom gold electrode. Next, the AAO template is filled with gold with the help of an electrochemical reaction of 0.05 M $HAuCl_4$, 0.42 M Na_2SO_3, and 0.42 M $Na_2S_2O_3$. Finally, an etching step with 0.03 M NaOH enables the complete removal of the AAO matrix and

leaves freestanding gold antennas with dimensions of 390 nm in length, 17 nm in diameter, and 63 nm inter-wire spacing.

3.1.3 Surface modification and characterization

3.1.3.1 Immobilization of thiolated receptors to gold surfaces

Effective surface functionalization is a significant process step in developing biosensing techniques. The decent binding of specific receptors to the sensor surface is essential for its performance. On the one hand, they support efficient biomolecular capture; on the other hand, they help amplify the signals the transducer receives.

For the nanoantenna biosensor, which operates by LSPR, the usage of well-established thiol-gold chemistry succeeded in properly binding receptors to sensor surfaces. Prior to treatments, gold nanoantenna arrays and planar gold films were cleaned by diligent immersion in ethanol, acetone, and ddH_20, for 5 min each, followed by an oxygen plasma treatment (SPI SUPPLY PREP2; USA, 100 W, 0.2 mbar) for 2 min. Next, the immobilization of receptors was performed by incubating 5 or 10 µM of probe DNA in immobilization buffer (IB), which is 100 mM potassium phosphate supplemented with 10 mM $MgCl_2$. Samples were left in the dark for designated periods to allow for a severe binding of thiolates probes, as imaged in Figure 3-1A. Following immobilization, an immersion for 30 min in 5 mM 6-Mercapto-1-hexanol (MCH) solution followed. As highlighted in panel B of Figure 3-1, the treatment not only blocked the remaining free surface sites of the gold but also helped to straighten up the DNA probe strands perpendicularly.

Prior to hybridization with two different complementary DNA strands, all substrates were washed with hybridization buffer (HB), which is 10 mM Tris(hydroxymethyl)aminomethane (TRIS) and 20 mM $MgCl_2$ at a pH of 7.4. Hybridization with complementary DNA occurred by exposure of the structures to DNA strands in HB for 15 min up to 24 h, respectively. The concentration of complementary DNA strands ranged from 1 nM to 1 µM, and hybridization experiments were all carried out at a constant flow rate of 10 µl/min, adapted with a high accuracy pump (Harvard Apparatus; Mo. Pump 11 Pico Plus Elite, Holliston, USA).

The studied probe-target system consists of a 25 base pair (bp) long 5' thiol-modified probe oligonucleotide (probe DNA, shown as a blue strand in Figure 3-1), a 25 bp entirely complementary strand (cDNA25,) as well as a 100 bp long partially

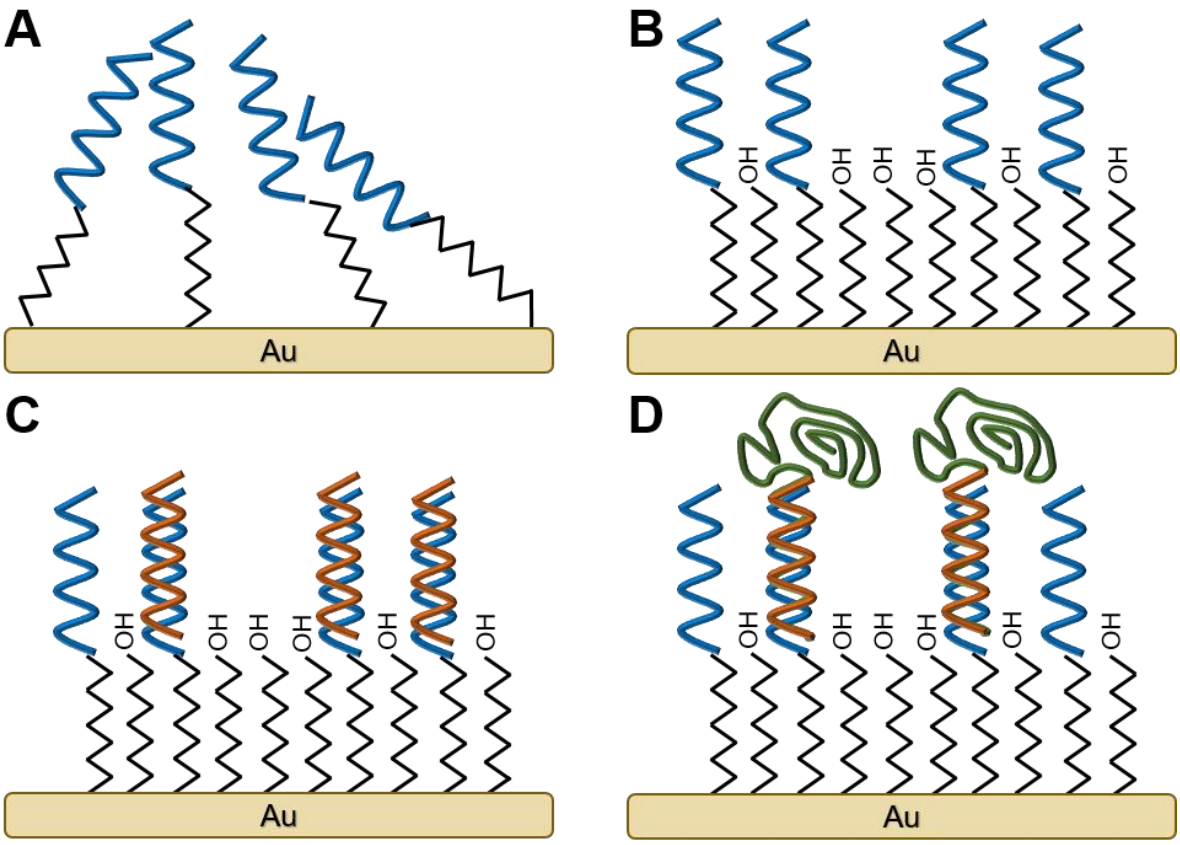

Figure 3-1: Schematic drawing of chemical surface functionalization (Chemical structures are not in their original scale): A) the probe DNA forms a robust layer on gold surfaces due to thiol-gold interactions. B) Backfilling with 6-mercaptohexanol (MCH) leads to a dense self-assembled monolayer with perpendicularly arranged probe DNA. C) Fully complementary DNA strands react with probe DNA, whereas in D) only a fractional overlap of target DNA hybridizes with probe DNA leading to additional DNA on the surface.

complementary strand (cDNA100). In addition, a 25 bp non-complementary DNA strand was used as a control. The different lengths of targets are visualized in panels C and D of Figure 3-1. In panel C, the 25 bp long DNA strand is entirely complementary to the probe, symbolized as an orange strand. However, in panel D, only a fraction of the 100 bp matches: the complementary fraction is represented in orange, whereas the overlapping fraction is pictured in green. All oligonucleotides were purchased from Biomers.net (Ulm, Germany). The exact sequences are given in Table 3-1; the underlined sections represent complementary parts. To prevent interferences such as hairpin structures and to maintain the guanine-cytosine (GC) content at ~50%, the design of the sequences was computed with the help of the algorithm EGNAS[2].

Between hybridization with different targets, the surface was regenerated by rinsing the substrates thoroughly with 500 µl of the following solutions: H_20, 0.1 M Na_2EDTA, H_2O, 0.1 M NaOH, H_2O, and hybridization buffer.

3.1.3.2 Calculation of immobilized receptors and targets via fluorescence intensity

The surface coverage of DNA molecules during each reaction step onto nanostructured and planar substrates was evaluated with the help of fluorescence intensities, as described elsewhere[3]. In addition, the method was chosen to survey the quality of the reaction steps of the applied surface modification protocols.

Planar substrates were fabricated by evaporating 3 nm chromium and 20 nm gold onto freshly cleaned coverslips (Menzel, Ø=13mm, #1.5) in a dual source thermal evaporation unit (Leybold UNIVEX 300, Germany). To calculate the amount of bound DNA, carboxyfluorescein (FAM) -labeled probe DNA was immobilized on relevant substrates as described in section 3.1.3.1, followed by immersion of substrates in freshly prepared 12 mM 2-Mercaptoethanol solution in 0.3x PBS for 16 h. In contrast, the hybridization yield was quantified via the reaction of probe DNA with rhodamine green-labeled complementary DNA. At preassigned time steps, immersion of the substrates in 15 mM NaOH for at least 12 h stopped the chemical reaction. A non-complementary cyanine 3 (CY3)- labeled DNA served for control measurements.

Next, a plate reader (Tecan Infinite® 200 PRO, Switzerland) was used to measure the fluorescence intensity (FI) of all samples; Table 3-3 contains the exact wavelength settings for each labeled DNA strand. Finally, signals were converted into surface coverage based on a previously taken calibration curve.

Table 3-3: Overview of extinction and emission wavelengths (in nm) used in this study to measure fluorescence intensity.

Dye	ABS	EM
FAM/FITC	494	520
Rhodamin Green-X	504	532
CY3	550	570

3.1.3.3 Refractive Index

Biosensors operating through (localized) surface plasmon resonance are highly sensitive to the surrounding entities' refractive indices (RI). Therefore, comparably small changes in the RI create a significant sensor response. Here, (L)SPR sensors do not probe only the RI of (bio-) molecules that are in very close vicinity to the surface but also the RI of the bulk solutions in the background[4]. Consequently, to prevent misinterpretation of signals caused by the bulk solutions, the RI of each buffer has been measured with an

ABBE refractometer. At a wavelength of λ=589 nm, three independent measurements of each buffer were performed, and results were averaged.

3.1.3.4 Reduction of non-specific adsorption

There is a high demand for preventing unspecific adsorption of molecules onto the surfaces as this will limit the performance[5]. In this study, the surfaces were blocked chemically via functionalized self-assembled monolayers (SAMs) of alkane thiols, which build up dense layers that allow only little unspecific adsorption[6]. In this study, the non-specific adsorption of DNA towards differently terminated alkanethiols was evaluated by SPR. Here, SAMs of alkanethiols with similar alkane chain lengths but different terminal functional groups (carboxylic, hydroxylic, and amino groups) were formed via immersion of gold surfaces into 5 mM ethanolic alkanethiol in solutions for 30 min. A surface, which was incubated in ethanol only, served as a control. Next, all prepared substrates were exposed to a solution of 1 µM DNA for 10 min, and the amount of adsorbed DNA on each surface was calculated respectively. The modification, where less DNA adsorbs, reduces non-specific adsorption most.

3.1.4 Measurement setup for detection of analytes

3.1.4.1 Microfluidic integration

Both sensing platforms unify the idea of detecting analytes in fluids in real-time. For the performance of the sensors under aqueous conditions, sensors were implemented into a microfluidic setup, in which tailored holding devices were equipped with Polydimethylsiloxane (PDMS) microfluidic channels to allow for defined analyte flow regimes. Microfluidic channel systems were fabricated with PDMS elastomer (SYLGARD™ 184), bought from Dow Corning (Midland, MI, USA), and further processed as suggested by the manufacturer. Briefly, the silicone elastomer and its curing agent were mixed well in a ratio of 1:10 and degassed for 15 min. Next, the polymer mixture was poured onto a master substrate and cured at 80°C.

3.1.4.2 Continuous biodetection with nanoantenna arrays

Nanoantenna substrates and thin glass slides (VWR, 23mm, #1.5) were connected to working sensors with microfluidic chambers in a layer-wise approach as described previously[7]. For a secure assembly, sensors and substrates were treated with O_2 plasma (SPI SUPPLY PREP2; USA) for 10 s each and linked under moderate pressure to enable

the covalent bonding between the sensor and microfluidic devices. Merged substrates could rest at 65°C for at least 3 h until further usage.

For biosensing, the excitation and the course of the LSPR signals were monitored by measuring the optical absorbance of the nanoantenna assembly. Spectral measurements were performed using a rotatable sample holder and a spectrometer (OceanOptics Maya2000 Pro), while illumination of the sensor assembly was achieved by a halogen lamp (LOT-QuantumDesign). Via incorporation of a Glan-Thompson prism, the p-polarization of light was selected to exclude background signals from s-polarized light, which only excites the short axis resonance. Finally, a fiber connected to the spectrometer collected the transmitted light. For maximal signal acquisition, an angle of incidence Θ of 40° was chosen. The whole setup is illustrated schematically in Figure 3-2 below.

The optical spectra were recorded periodically, and extracted positions of the LSPR were set in relation to time. Here, the spectral positions of the long-axis LSPR were enumerated by fitting the acquired spectral data with two Lorentzian functions.

For a precise and enduring analyte delivery to the nanoantenna array, a flow rate of 10 µl/min inside the microfluidics was kept constant by using a high-accuracy syringe pump (Harvard Apparatus; Mo. Pump 11 Pico Plus Elite, Holliston, USA).

Reference experiments on planar gold surfaces were executed using a surface plasmon resonance spectrometer (Fraunhofer IOF, Jena, Germany), with suiting optically transparent TOPAS® chips (Capitalis, Berlin, Germany), which embrace integrated microlenses and a 50 nm thick gold layer. The SPR device is adopted with a microfluidic system, where analyte delivery was maintained at a flow rate of 10 µl/min and 25°C. Planar gold areas were treated in analogy to the protocols of the section.

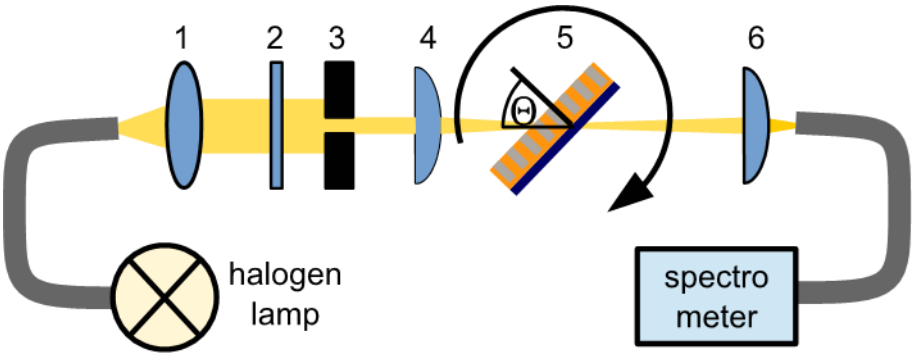

Figure 3-2: Schematic drawing of the optical setup for measuring transmission spectra of nanorod samples: The beam of a halogen lamp is collimated by a lens (1), guided through a Glan-Thompson prism (2) for selection of the p-polarized state, and passes a slit aperture (3). The sample is placed centrally between two cylindrical lenses (4, 6), where the beam is narrowest, on a rotatable sample holder (5). The light is transmitted into a fiber-coupled spectrometer. [Image adapted by courtesy of Dr. Tino Uhlig, IAPP]

3.2 SiNW FET-based real-time monitoring of cortisol

3.2.1 Materials

For detection of the stress marker cortisol with an electronic biosensor based on SINW FETs, specific DNA receptors (aptamers) were used. The DNA sequences of the aptamers, including their modifications, are listed in Table 3-4 below. An 85 bp long aptamer sequence, specific against cortisol, was adopted from Martin et al.[8]. A 76 bp long aptamer, specific against estradiol and published by Liu et al.[9], served as a control.

For biosensing experiments, all aptamers were modified on its 5'-end with a C6 linker and an amino group (-NH_2) for covalent attachment to carboxylic (COOH-) terminated surfaces.

For fluorescence imaging, cortisol aptamers were labeled with the fluorescent dye CY3, whereas the control aptamers were labeled with rhodamine-green. For each aptamer, the 3'- end remained unmodified.

Table 3-4: Sequences and modifications of aptamers used for detection of cortisol.

Name	Sequence (5 '->3 ')	5 '- modific.	3 '- modific.
Cortisol_ amino	GGAATGGATCCACATCCATGGATGGGCAATGCGG GGTGGAGAATGGTTGCCGCACTTCGGCTTCACTG CAGACTTGACGAAGCTT	C6 –NH_2	
Cortisol_ CY3	GGAATGGATCCACATCCATGGATGGGCAATGCGG GGTGGAGAATGGTTGCCGCACTTCGGCTTCACTG CAGACTTGACGAAGCTT	CY3	
Estradiol _amino	GCTTCCAGCTTATTGAATTACACGCAGAGGGTAG CGGCTCTGCGCATTCAATTGCTGCGCGCTGAAGCG C GGAAGC	C6- NH_2	
Estradiol _green	GCTTCCAGCTTATTGAATTACACGCAGAGGGTAG CGGCTCTGCGCATTCAATTGCTGCGCGCTGAAGCG C GGAAGC	Rhodamin Green- X	

All DNA strands were purchased from Biomers.net (Ulm, Germany). Aliquots with a concentration of 100 µM in PBS were stored at -18°C. Prior to use, DNA was heated to 95°C for 5 min and constantly cooled at 2.3°C/min to room temperature using a MasterCycler (Eppendorf, Hamburg, Germany) respectively.

Table 3-5 below presents supplementary chemicals, which were used for the development of a biosensing assay based on FETs.

Table 3-5: List of chemicals, including abbreviations and suppliers, used for the development of a biosensing assay with SiNW FETs

Chemical	Short name	Supplier
3-(triethoxysilyl)propylsuccinic anhydride	TESPSA	ABCR GmbH
3-aminopropyltriethoxysilane	APTES	Sigma Aldrich
N-(3-Dimethylaminopropyl)-N'- ethyl carbodiimide hydrochloride	EDC	Sigma Aldrich
N-hydroxysuccinimide	NHS	Sigma Aldrich
Phosphate buffered saline	PBS	VWR
Sodium chloride	NaCl	Chemical department TU Dresden
Hydrocortisone 3-(O-carboxymethyl)oxime	3 - CMO	Sigma Aldrich
Dimethyl sulfoxide	DMSO	VWR
Tris(hydroxymethyl)aminomethane	TRIS	Fluka analytical
Magnesium chloride	$MgCl_2$	Fluka analytical
Dipotassium hydrogen phosphate	K_2HPO4	Carl Roth
Potassium dihydrogen phosphate	$KHPO4_2$	Carl Roth
Sodium hydroxide	NaOH	
Hydrochloric acid	HCl	Sigma Aldrich
Polydimethylsiloxane (Sylgard 184)	PDMS	Dow Corning
Steroids: β-Estradiol Progesterone Testosterone Cortisone Dehydroepiandrosterone Melatonin Cortisol	DHEA	All Sigma Aldrich, Donated by Prof. Kirschbaum, Biopyschology, TU Dresden
Methanol	MeOH	VWR
Ethanol, absolute ≥ 99.8%	EtOH	VWR
Cortisol Saliva Luminescence Immunoassay	LIA	IBL International
Cortisol Standards (all in µg/dl): 0; 0.015; 0.03; 0.10; 0.40; 1.00; 3.20 in PB incl. 0.1%BSA and 0.1%ProClin	 Std A B C D E F G	IBL International
Gold nanoparticles, 10nm	AuNPs	BBI solutions
hydroxyethyl piperazineethanesulfonic acid	HEPES	Sigma Aldrich

3.2.2 Manufacturing of silicon nanowire field effect transistors (SiNW FETs)

SiNW FETs have been fabricated by collaborators of the Department of Creative IT Engineering at Pohang University of Science and Technology (Postech) and the Division of Electronic Engineering, Jeonbuk National University, South Korea. A detailed description of the fabrication procedure has been published in the past[10].

Briefly, honeycomb nanowires (HC) shaped FETs were fabricated using a top-down approach on an 8-inch silicon-on-insulator wafer with 200 nm oxide and 50 nm top *p*-silicon layers. Active regions, including source/drain and nanowires, were specified with the help of etching the top silicon layer using conventional optical lithography and inductively-coupled plasma reactive-ion etching (ICP-RIE). Nanowires, structured in a honeycomb shape with 50 nm width, were patterned using electron-beam lithography and etched using the ICP-RIE. To avoid a direct connection of source and drain regions to sample solutions, a 2 µm thick SU-8 photoresist as a passivation layer was established.

3.2.3 Integration of SiNW FETs into a portable platform

The provided FETs were integrated into a portable measurement platform, which has been manufactured and described in-depth by collaborators[11–13]. Briefly, the mobile measurement platform consists of three modules: a *measuring unit, a replaceable MUX adapter,* and a *customizable biochip adapter,* allowing continuous and simultaneous measurements of multiple FETs. The measuring unit, including the attached MUX adapter, has been used as provided by collaborators. In this research, the SiNW FETs were integrated into the biochip unit of the system by connecting the terminals of the individual FETs to a tailored printed circuit board (PCB). Chips were fixed on the PCB with conductive epoxy glue, and terminals were linked to PCB with a wire bonder (TPT Wire Bonder GmbH & Co KG, Model HB05, Karlsfeld, Germany). Bonds between substrates and gold wires (25 µm diameter) were created at 60°C with 0.2 s bond time and 30 cN bond force.

3.2.4 Biomodification and characterization of electronic biosensors SiNW FETs

The specific interaction of a sensor with its environment is crucial for its application. The appropriate interface between sensor and receptor is as essential as the successful interplay between receptor and target molecules.

This work presents the immobilization of receptor molecules to oxide surfaces based on the silane 3-(triethoxysilyl) propylsuccinic anhydride (TESPSA). Fluorescence microscopy and contact angle measurements validated the successful functionalization with TESPSA, the subsequent immobilization of receptors, and the biorecognition of the analyte.

The origin of the (electrostatic) interactions, which lead to a successful binding between a receptor and its analyte cortisol, is of particular interest in this study. Three independent methods, namely a colorimetric assay based on gold nanoparticles, circular dichroism, and fluorescence microscopy, have been applied to verify the binding. Furthermore, fluorescence microscopy demonstrates the usability of the system for surface-related assay.

3.2.4.1 Immobilization of aptamers against cortisol to oxide surfaces

The following paragraph describes the experimental procedure for modification of the oxide surface with TESPSA and subsequent immobilization of receptor molecules. The approach is a relatively simple two-step modification process, which has been briefly adopted from Gang et al. [14]. Figure 3-3 shows a sketch of the chemical reactions.

Prior to experiments, FETs and glass slides were cleaned thoroughly by rinsing with DI water, ethanol, acetone, and isopropanol and subsequently dried via an N_2 stream. For hydroxylation of the surfaces, an oxygen plasma treatment for 10 s at 100 W, 0.3 bar (Diener electronic GmbH & CoKG, Ebhausen, Germany) followed. Next, the in this way activated surfaces were exposed to TESPSA for 4 h under vacuum and infrared light. Afterward, samples were transferred to an oven and allowed to rest for at least 30 min at 120°C. The thermal treatment permits stabilization of the silane and avoids the undesired ring opening reaction of the anhydride, resulting in a severe silane layer with anhydride moieties, as shown in Figure 3-3B.

To bind the receptors covalently, 5 µM Amino-modified DNA strands in 1xPBS, supplied with 5 mM $MgCl_2$, were incubated for 1 h on TESPSA modified surface and rinsed with PBS thoroughly. Samples were stored in a humidified chamber to avoid solvent evaporation. Next, samples were immersed for 0.5 h in *standard A,* the cortisol-free standard from the LIA kit that contains 0.1% BSA and 0.1% ProClin, at room temperature to equilibrate surfaces. Figure 3-3C summarizes the reaction of amino-modified receptors

onto anhydride moieties of the silane layer. In a final step, the target is introduced into the system. Figure 3-3D demonstrates the binding of an analyte to its receptor.

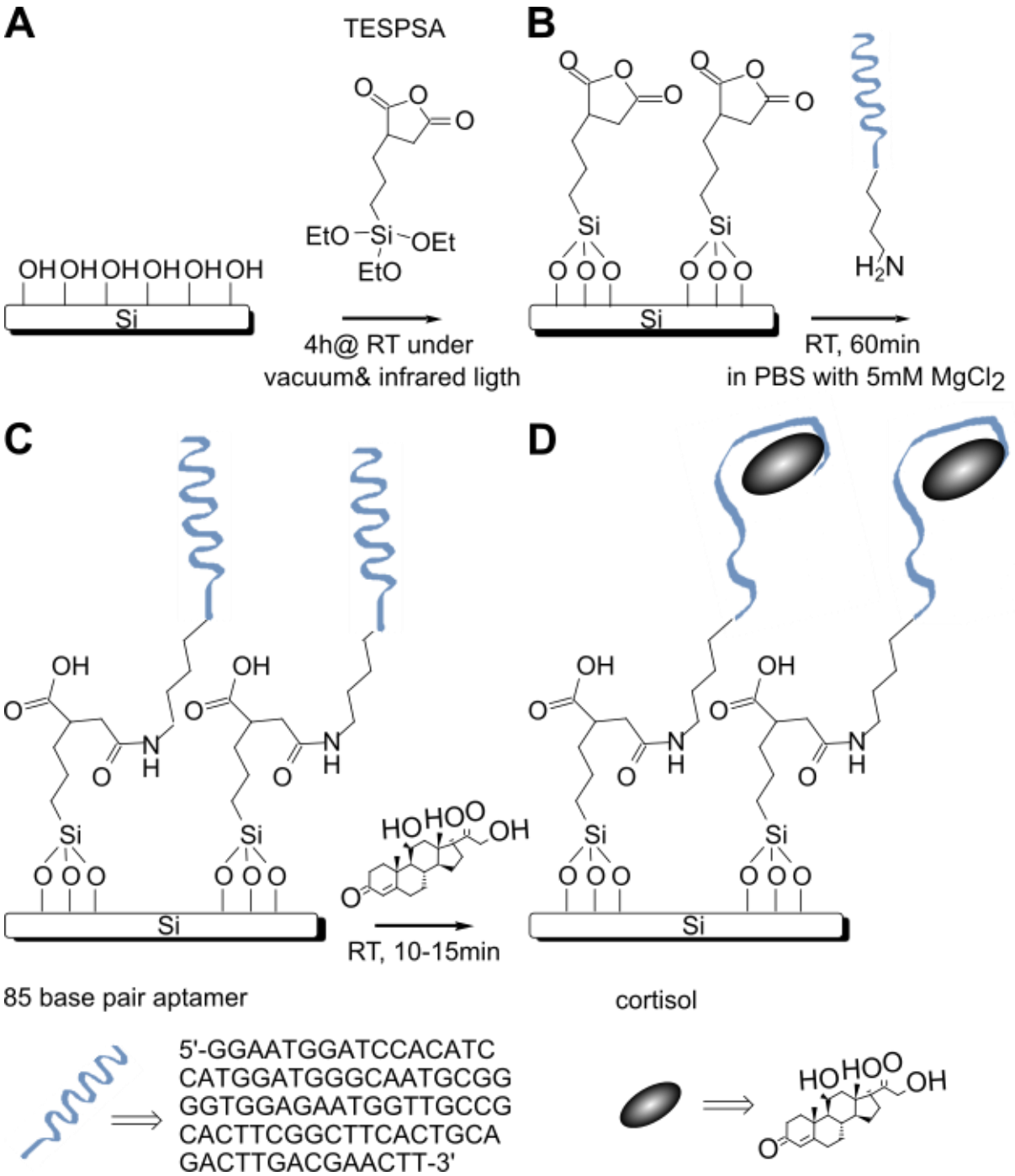

Figure 3-3: Simple two-step biomodification steps of SiNW FETs for biosensing purposes. A) O_2 Plasma treatment creates hydroxylated surfaces of SiNW FETs, which are exposed under vacuum and IR-light to TESPSA for 4 h. B) A homogenous silane layer with anhydride moieties builts up. Further treatment with amino-modified biomolecules, i.e., aptamers against cortisol (blue line), for 1 h at RT leads to (C) covalently linked receptors on SiNW FET. D) Exposure of linked aptamers to analyte cortisol (black ellipse) encourages a binding of the analyte to its receptor by inducing a conformational change.

3.2.4.2 Contact angle

Contact angles (CA) of water drops on each modified surface were determined to assess the quality of the modification steps. All measurements were executed in static sessile drop mode with an OCA20 device (Dataphysics Instruments GmbH, Filderstadt, Germany). Five droplets of deionized water with a volume of 10 µl were dispensed onto substrates with a flow rate of 1 µl/s. The values of each sample are averaged.

3.2.4.3 Colorimetric assay

Commercially available gold nanoparticles (AuNPs) with a diameter of 10 nm and a concentration of ~10 nM were used as given by the manufacturer. The cortisol-targeting aptamer was incubated with AuNPs for 1 h. Next, solutions were diluted 1:1 in 20 mM HEPES buffer, which was supplemented with 2 mM $MgCl_2$ and left overnight on a platform shaker (Heidolph Duomax 1030, Schwabach, Germany) at 5rpm to equilibrate the reaction. Target solutions, namely cortisol, estradiol, testosterone, progesterone, and dopamine, were dissolved to 100 mM in methanol and freshly diluted 1/1000 in 1/3 cortisol binding buffer (CBB). 1x CBB consists of 50 mM Tris, 137 mM NaCl and 5 mM $MgCl_2$ at pH 7.4.

Next, 10 µl of freshly prepared target solutions with analyte concentrations ranging from 0 to 10 µM were incubated with 80 µl of AuNPs solutions for 20 min. After adding 13 µl 1M NaCl to each sample, the absorbances at 650 nm and 520 nm were directly measured with a microplate plate reader (Tecan Infinite 200 PRO, Switzerland). Several control measurements were performed: AuNPs were exposed to 10 µM (in 1/3x CBB) Estradiol, testosterone, progesterone, and dopamine, as well as to a 1/3 x CBB solution that had no target at all. Likewise, AuNPs without linked aptamers were exposed to analyte solutions.

For all samples, the ratio of the two absorbencies (E_{650}/E_{520}) is analyzed and normalized against the spectra of the target-free AuNP solution.

3.2.4.4 Circular dichroism

Circular dichroism spectroscopy (CD) is a method that helps to get insight into the secondary structure of DNA/aptamers and thus allows for tracking of the folding of DNA upon binding. Aptamers were used at a concentration of 5 µM in 1x PBS and incubated for 1h with cortisol ratios ranging from 1:1 to 1:20. Cortisol was diluted from stock in PBS

to desired concentrations, respectively. CD spectra were collected with a Chirascan-Plus spectrophotometer (Applied Photophysics Ltd.). For each sample, three scans from wavelengths of 200 nm to 320 nm with a resolution of 0.5 nm resolution, a bandwidth of 1.0 nm, and a response time of 1 s were acquired. All samples were measured in quartz cuvettes, which were cleaned thoroughly with PBS and N_2 between the individual measurements. Primarily recorded spectra from air and cuvettes were subtracted. The scans shown in the plots average three individual scans.

3.2.4.5 Fluorescence microscopy

A modified functionalization approach has been established to image the aptamer-target interaction by fluorescence microscopy. Terminating the surface with a cortisol-derivate facilitated the subsequent reaction with a fluorescently-labeled aptamer, which could be detected by standard fluorescence microscopy. The cortisol-terminated surface was prepared in analogy to [15]. A supportive sketch of the reaction is shown in Figure 3-4 below.

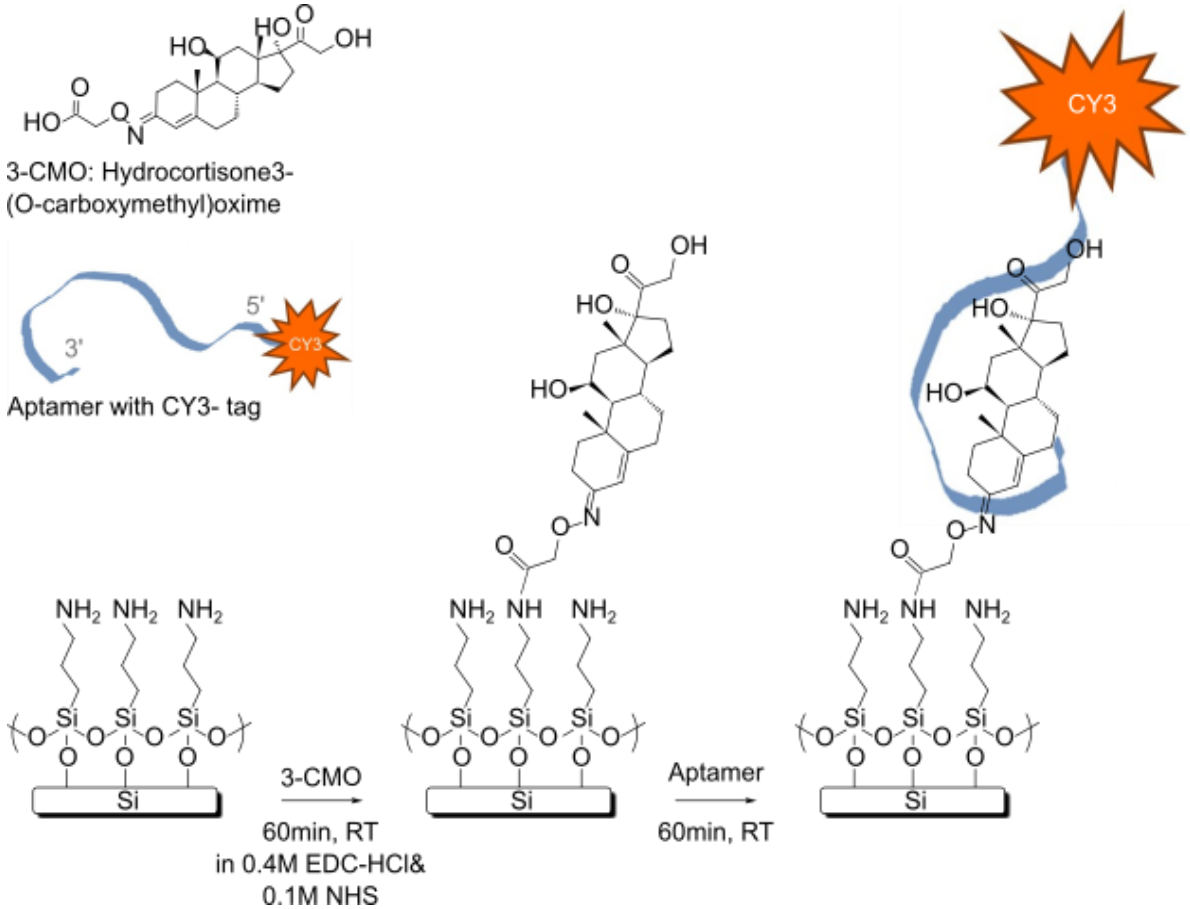

Figure 3-4: Biomodification of SiO_2 surfaces with cortisol-derivate 3-CMO. First, treatment of SiNW FETs with APTES leads to A) Aminoterminated surface. B) Exposure of Cortisol-derivate 3-CMO, supplemented with EDC/NHS, allows for covalent binding of Cortisol-derivate to FETs. C) Fluorescently labeled aptamers bind to modified SiNW FET.

First, oxide surfaces were prepared with amino groups: samples were hydroxylated by oxygen plasma and exposed to a solution of 2.5% APTES in EtOH for 30 min, followed by thermal treatment at 120°C for 30 min to crosslink and stabilize the layer. Meanwhile, a chemical reaction of 10 mM Hydrocortisone 3-(O-carboxymethyl) oxime (3-CMO) in DMSO with 0.1 M NHS in DMSO and aqueous 0.4 M EDC-HCl was performed for 15 min to activate carboxy moieties of the cortisol analog. Each reactant was freshly prepared. Next, the activated cortisol analog solution was incubated with APTES-treated surfaces and left to react for 60 min. Non-bound reactants were removed by washing the surfaces with buffers carefully. Cortisol-targeting aptamers, which have been equipped with a fluorescent CY3 tag at its 5'-end, were diluted in 1x PBS supplemented with 20 mM $MgCl_2$ to designated concentrations. A microarray printer device (NanoPlotter 2.1 with piezoelectric pico-tip, both GeSiM mbH, Radeberg, Germany) was used to spot 50 pl of each aptamer solution onto cortisol-terminated glass slides. During the reaction time of 30 min, the spotting atmosphere was kept at 23°C, 80% r. H. and 1% glycerol were added to the buffer system to prevent the evaporation of the droplets. Prior to imaging with a microscope, all surfaces were washed three times with PBS and dried with an N_2 stream.

Fluorescence microscopy was performed on an Axiovert 200M (Carl Zeiss AG, Oberkochen, Germany) with suiting Zeiss filter No. 15 (ex. 546$\pm$ 12 nm, em. >590 nm). Surfaces were exposed to light for 1 s, and obtained images were analyzed using ImageJ software. For analysis, the fluorescence intensity of the aptamer spots and the background intensities were determined and correlated. The ratio of fluorescence-to-background (FI/B) was calculated for each area individually. Five different spot arrays were analyzed and averaged.

3.2.5 Electric characterization of FETs

An initial electric characterization of the FETs was achieved by recording the output and transfer characteristics before any surface modification. Output characteristics were obtained by sweeping the source-drain-voltage (V_{SD}) from -2 V to +2 V at different gate voltages (V_G) ranging from -2 to +5 V. In contrast, transfer characteristics were collected by sweeping V_G from 0 V to 2 Vat a fixed V_{SD} of 0.1 V.

3.2.5.1 Biodetection with SiNW FETs

Chemically prepared FET chips were mounted into a holder with a microfluidic channel system, as described in section 3.2.3 above and illustrated in chapter 5, figure 3B.

The FETs were operated in a dual-gate mode: gate voltages were applied via the back gate, and the same potentials were employed to solutions via the Ag/AgCl reference electrode, which is incorporated into the tubing system and driven by the measurement unit of the portable platform.

All analyte solutions of interest were guided over the FETs at 21°C with a flow rate of 10 µl/min, adjusted with a syringe pump (PHD 22/2000, Harvard apparatus, Holliston, USA).

For all measurements, a continuous gate sweeping mode[16] to control multiple FETs via a multiplexing process was used. For all time points, gate voltage V_G is continuously swept over the range from 0 V to +2 V with 62.5 mV increments; each V_G value is measured for 45 ms. Meanwhile, source-drain currents I_{SD} are fixed to +0.1 V of each FET. Recording whole FET characteristics throughout all experiments enables a later extraction of threshold voltage V_T at a selected current.

Threshold voltages V_T were extracted from V_G-I_{SD} curves in the steepest region of their transfer characteristics and displayed over time. Unless otherwise stated, threshold voltages were typically derived at I_{SD} values at 10^{-8} A. The emerging shifts ΔV_T of the signal during biosensing were used to gauge the bioprocesses present at the FET interface.

In regards to the detection of the steroid cortisol, a calibration of the system with known cortisol levels was performed first. SiNW FETs have been prepared with receptors as described in section 3.2.4.1They were equilibrated with cortisol-free standards until a stable baseline arose. Subsequently, cortisol standards with concentrations ranging from 0.005 µg/dl up to 3.2 µg/dl were injected for 10 minutes each, followed by a wash with cortisol-free standards to remove unbound molecules. Arising signal shifts were related and served as calibration.

3.2.5.2 Detection of cortisol in human saliva

Four volunteers donated saliva samples on a day at five predefined time points. Salivary samples were collected with a Salivette® tube (Sarstedt, Germany) and stored at -22°C, and thawed to room temperature prior to analysis.

The cortisol concentration with saliva was determined with a commercially available LIA kit, whose test procedure was followed as offered by the company. Briefly, 20 µl of saliva samples, standards for calibration, and controls were incubated for 3 h in the provided wellplate containing immobilized antibodies against cortisol. Next, after a

diligent washing step to remove unbound molecules, a luminescent reactant was introduced for a reaction time of 10 min. A microplate plate reader measured the upcoming luminescence signals (Tecan Infinite 200 PRO, Switzerland). Finally, unknown cortisol concentrations of saliva samples were calculated based on the calibration curve.

Experiments were performed to measure the unknown cortisol levels in saliva samples with FETs in analogy to calibration experiments described in the previous section. First, each saliva sample was diluted at 1:10 in 1xPBS to ensure a stable pH value, and prepared sensors were equilibrated via exposure to the cortisol-free buffer until a stable baseline was achieved. Next, saliva samples were injected for 10 min, followed by washing with cortisol-free buffer. For analysis, the FET signals before the injection of saliva were compared to those obtained after washing. The arising difference ΔV_{TH} was translated to cortisol concentration with the help of previously taken calibration curves. After each saliva detection circle, sensor surfaces were regenerated by introducing 2 M NaCl to the system.

3.3 References

(1) Fiehler, V.; Patrovsky, F.; Ortmann, L.; Derenko, S.; Hille, A.; Eng, L. M. Plasmonic Nanorod Antenna Array: Analysis in Reflection and Transmission. *J. Phys. Chem. C* **2016**, *120* (22), 12178–12186. https://doi.org/10.1021/acs.jpcc.6b02419.

(2) Kick, A.; Bönsch, M.; Mertig, M. EGNAS: An Exhaustive DNA Sequence Design Algorithm. *BMC Bioinformatics* **2012**, *13* (1), 138. https://doi.org/10.1186/1471-2105-13-138.

(3) Demers, L. M.; Mirkin, C. A.; Mucic, R. C.; Reynolds, R. A.; Letsinger, R. L.; Elghanian, R.; Viswanadham, G. A Fluorescence-Based Method for Determining the Surface Coverage and Hybridization Efficiency of Thiol-Capped Oligonucleotides Bound to Gold Thin Films and Nanoparticles. *Anal. Chem.* **2000**, *72* (22), 5535–5541. https://doi.org/10.1021/ac0006627.

(4) Liu, F.; Zhang, X.; Li, K.; Guo, T.; Ianoul, A.; Albert, J. Discrimination of Bulk and Surface Refractive Index Change in Plasmonic Sensors with Narrow Bandwidth Resonance Combs. *ACS Sens.* **2021**, *6* (8), 3013–3023. https://doi.org/10.1021/acssensors.1c00906.

(5) Lichtenberg, J. Y.; Ling, Y.; Kim, S. Non-Specific Adsorption Reduction Methods in Biosensing. *Sensors* **2019**, *19* (11), 2488. https://doi.org/10.3390/s19112488.

(6) Choi, S.; Chae, J. Methods of Reducing Non-Specific Adsorption in Microfluidic Biosensors. *J. Micromechanics Microengineering* **2010**, *20* (7), 075015. https://doi.org/10.1088/0960-1317/20/7/075015.

(7) Gang, A.; Haustein, N.; Baraban, L.; Cuniberti, G. Multifunctional Reversibly Sealable Microfluidic Devices for Patterned Material Deposition Approaches. *RSC Adv* **2015**, *5* (16), 11806–11811. https://doi.org/10.1039/C4RA15785K.

(8) Martin, J. A.; Chávez, J. L.; Chushak, Y.; Chapleau, R. R.; Hagen, J.; Kelley-Loughnane, N. Tunable Stringency Aptamer Selection and Gold Nanoparticle Assay for Detection of Cortisol. *Anal. Bioanal. Chem.* **2014**, *406* (19), 4637–4647. https://doi.org/10.1007/s00216-014-7883-8.

(9) Liu, J.; Bai, W.; Niu, S.; Zhu, C.; Yang, S.; Chen, A. Highly Sensitive Colorimetric Detection of 17β-Estradiol Using Split DNA Aptamers Immobilized on Unmodified Gold Nanoparticles. *Sci. Rep.* **2014**, *4*, 7571. https://doi.org/10.1038/srep07571.

(10) Rim, T.; Kim, K.; Cho, H.; Jeong, W.; Yoon, J.; Kim, Y.; Meyyappan, M.; Baek, C. Electrical Characteristics of Doped Silicon Nanowire Channel Field-Effect Transistor Biosensors. *IEEE Sens. J.* **2017**, *17* (3), 667–673. https://doi.org/10.1109/JSEN.2016.2625420.

(11) Voitsekhivska, T.; Suthau, E.; Wolter, K.-; Baraban, L.; Zörgiebel, F.; Cuniberti, G. Portable Measurement System for Silicon Nanowire Field-Effect Transistor-Based Biosensors. In *Proceedings of the 36th International Spring Seminar on Electronics Technology*; 2013; pp 349–354. https://doi.org/10.1109/ISSE.2013.6648271.

(12) Voitsekhivska, T.; Zörgiebel, F.; Suthau, E.; Wolter, K.-; Bock, K.; Cuniberti, G. PH Measurements of FET-Based (Bio)Chemical Sensors Using Portable Measurement System. In *2015 37th Annual International Conference of the IEEE Engineering in Medicine and Biology Society (EMBC)*; 2015; pp 6445–6448. https://doi.org/10.1109/EMBC.2015.7319868.

(13) Klinghammer, S.; Voitsekhivska, T.; Licciardello, N.; Kim, K.; Baek, C.-K.; Cho, H.; Wolter, K.-J.; Kirschbaum, C.; Baraban, L.; Cuniberti, G. Nanosensor-Based Real-Time Monitoring of Stress Biomarkers in Human Saliva Using a Portable Measurement System. *ACS Sens.* **2020**, *5* (12), 4081–4091. https://doi.org/10.1021/acssensors.0c02267.

(14) Gang, A.; Gabernet, G.; Renner, L. D.; Baraban, L.; Cuniberti, G. A Simple Two-Step Silane-Based (Bio-) Receptor Molecule Immobilization without Additional Binding Site Passivation. *RSC Adv* **2015**, *5* (45), 35631–35634. https://doi.org/10.1039/C5RA04469C.

(15) Tahara, Y.; Huang, Z.; Kiritoshi, T.; Onodera, T.; Toko, K. Development of Indirect Competitive Immuno-Assay Method Using SPR Detection for Rapid and Highly Sensitive Measurement of Salivary Cortisol Levels. *Front. Bioeng. Biotechnol.* **2014**, *2*. https://doi.org/10.3389/fbioe.2014.00015.

(16) Zörgiebel, F. M.; Pregl, S.; Römhildt, L.; Opitz, J.; Weber, W.; Mikolajick, T.; Baraban, L.; Cuniberti, G. Schottky Barrier-Based Silicon Nanowire PH Sensor with Live Sensitivity Control. *Nano Res.* **2014**, *7* (2), 263–271. https://doi.org/10.1007/s12274-013-0393-8.

4 Plasmonic DNA biosensor based on vertical arrays of gold nanoantennas

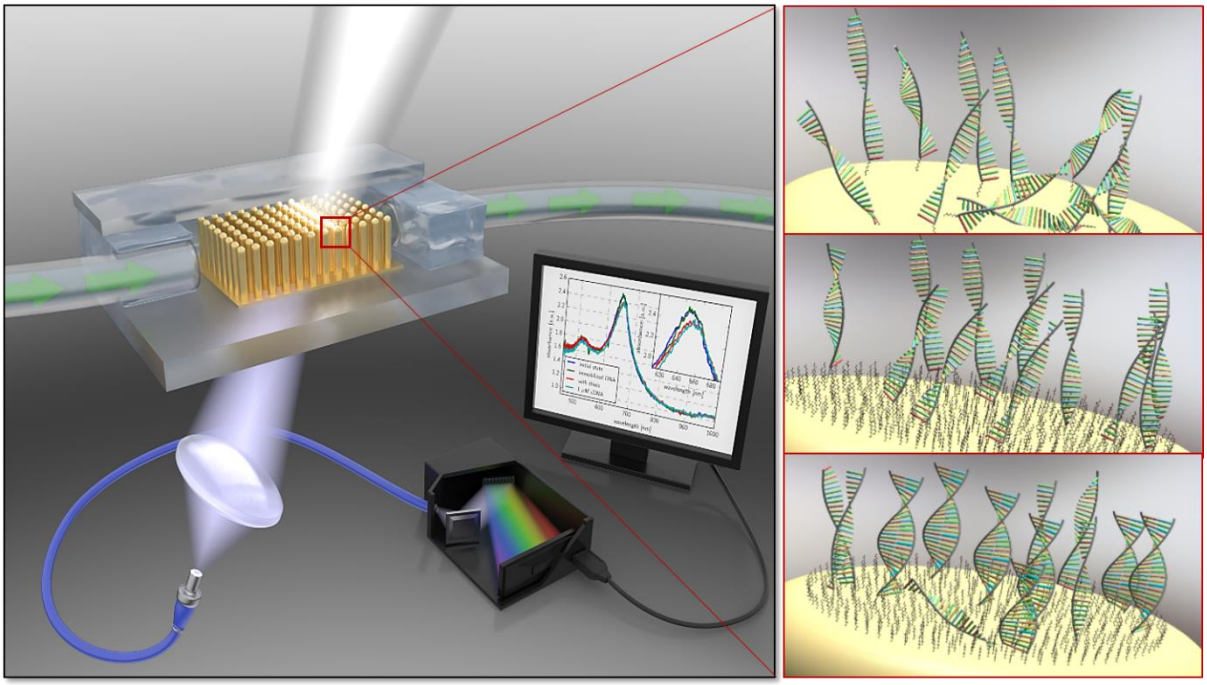

The following chapter announces the development of a refractometric biosensor for detecting label-free biomolecules, i.e., DNA, in real-time. The biosensor consists of vertically aligned gold-nanoantennas manufactured in cooperation with IAPP at TU Dresden and operates by means of localized surface plasmon resonance (LSPR). The position of the LSPR peak depends on the geometry of the rods, to be precise, on the aspect ratio between length and diameter. In addition, surrounding conditions, such as the presence of biomolecules on the surface and their reactions, will also reflect a shift of wavelength. Controlled reaction conditions, including defined flow regimes, have been established by integrating microfluidics into the sensor system. The complete working sensor platform is demonstrated by the label-free and real-time detection of the immobilization and subsequent hybridization of a 25 bp oligonucleotide with two counterparts.

The presented research focuses first on the development, characterization, and appropriate application of surface modifications to guarantee a label-free detection of chosen biomolecules. This implies not only the surface functionalization with receptor molecules but also a suitable backfilling strategy to prevent undesired adsorption of molecules and the strict implementation of the biodetection itself (i.e., efficient

hybridization of oligonucleotides with two lengths). The functionalization and later biosensing success has been confirmed with fluorescence scanning, surface plasmon resonance (SPR), and the developed biosensor.

As a second step, the suitability of the presented nanoantenna biosensor to detect the selected bioreactions was evaluated, and emerging advantages were emphasized. Considering that, a microfluidic setup for controlled conditions and analyte delivery was integrated into the platform, and all bio reactions were monitored in real-time.

The complete study is summarized and published in [1] with S. Klinghammer as the first author.

4.1 Introduction - Optical biosensors operating by means of LSPR

Amongst others, optical sensors using plasmonic (nano)materials have gained great focus as they offer several advantages. Benefits arise not only in regard to analytical approaches but also in terms of multiplexing, photostability, and the facileness for miniaturization without advanced sensor-chip fabrication and instrumentation[2]. From the analytical perspective, fast read-outs of colorimetric assays and the aptitude to detect analytes in ultralow sample volumes at a single-molecule level make nanoplasmonic sensor platforms promising candidates in bioanalysis point-of-care applications, early diagnosis of diseases, and healthcare applications[3–6]. Furthermore, the characteristic sensitivity of plasmonic sensors towards the refractive index (RI) of the local dielectric surrounding – either detectable by a shift of the resonant wavelength or the detection angle - further empowers the potential application fields[7]. Concerning the practical utilization in the field, sensing technologies based on LSPR often offer various advantages over SPR sensors as LSPR sensors typically require simpler instruments and can go beyond the sensitivity of SPR, which is limited by the spectral width. Here, the ease of read-out possibilities advances the application of LSPR-based sensors as data can be obtained using a benchtop UV-visible spectrophotometer[1,8], an equipped smartphone[9,10], or even simply by naked-eye readout[11,12]. Furthermore, LSPR sensors –compared to SPR sensors- show a higher surface sensitivity, whereas the sensitivity to bulk refractive index is lower[13]. Thus, measurements are expected to be more stable and less susceptible to environmental fluctuations[14].

A small reproducibility and uniformity in synthesizing nanostructured particles and arrays on surfaces remain challenging- but not insurmountable. So the efficiency and commercialization of plasmonic sensors start to evolve[3]. Albeit, problems concerning spatial distribution, particle sizes, and shapes result in lower sensitivities than those of SPR sensors and limit the practical application of LSPR sensors[15]. Nevertheless, properties such as portability, cost-effectiveness, and high uniformity remain desired, while the sensors shall be ultrasensitive and selective.

Nanostructures must be manufactured in huge quantities and at a high resolution while being low cost in production to meet those criteria. In this regard, the application of 2D or 3D nano-arrays for plasmonic sensors is favored[16]. Unlike colloidal nanoparticles, nanostructured patterns and nano-arrays are typically arranged in

ordered, periodic geometries on solid substrates[17]. Coherent optical responses of those 2D arrays are hallmarked by strong and narrow spectral features, which in turn originate from the collective behavior of plasmons in nano-arrays[18]. The optical spectra of nanostructures depend on the structure's size, shape, and periodicity. By altering those characteristics, optical properties can be tuned quickly, providing great flexibility. However, 2D nano-arrays for plasmonic sensing have to be manufactured reliably and not only at a low budget with high throughput but also with high resolutions, good uniformity, and offering flexibility for the production of different sizes and shapes[16]. Production strategies based on chemical synthesizes of individual nanoparticles usually lack uniformity and consistency[19,20]. In contrast, low-cost fabrication methods based on nano-sphere lithography suffer from unavoidable defects over a large scope, which will limit their practical use[21]. In contrast, high-quality arrays produced by lithographic approaches such as electron beam, focused-ion, or dip-pen lithography suffer in regard to prices or low throughput, respectively[16,22,23].

Among the fabrication methods for creating 2D nanostructures, using anodic aluminum oxide (AAO) templates seems to overcome mentioned obstacles, as it provides a technique for nano-patterning at low cost and high resolution over large areas[24,25]. Nanostructures are created by the deposition of materials into periodic nanopores of an AAO template, which has been prepared by metal anodization in an acidic solution[26,27]. The process of anodic oxidation of aluminum films has been known and used industrially since the beginning of the previous century[28]. However, the full potential of this method, and associated applications, is mainly featured by the self-ordering properties of nanopores[28–31]. With this technique, large arrays of mainly rod-shaped nanostructures with variations in length, diameter, and distance can be produced[32].

Likewise, templates with available pore sizes between 7 nm and more than 300 nm allow for a broad variety of optical resonance properties[33], which are, amongst material, spatial distribution, and size of nanostructures, dependent on their shape. Furthermore, gold nanorods (AuNR) are anisotropic in their geometry, which causes the superb feature of an extra longitudinal LSPR band on top of the LSPR band in the blue range, which is typical for spherical nanoparticles. This longitudinal LSPR band can be placed at wavelengths up to 1350 nm in the near-infrared region[34] and thus boosts their application for biosensing[34–36], primarily as the position of the longitudinal band can be modulated easily by changing the aspect ratio (AR) of the AuNRs[37,38].

For biosensing purposes, using 2D arrays, where nanostructures are fixed on substrates instead of colloidal nanoparticles in solution, is beneficial for sensing, as higher RI sensitivities and the capability for real-time monitoring and thus for determination of reaction kinetics are supported[39–42]. In addition, the formation of receptor-analyte complexes on the surfaces of the nanostructures causes a concentration-depended red shift of the LSPR bands. Here, analytes can reach from small molecules[43,44] over proteins and enzymes[45–47] to whole bacteria[8], viruses[48], and cells[49,50].

Among the different analytes, sensing nucleic acids plays a key role. Typically, DNA analysis focuses on the hybridization of complementary DNA strands, including response time, sensitivity, and the potential to detect mismatches[51]. Up to now, LSPR sensors, including nanostructured arrays, are capable of fulfilling these demands and can screen the adsorption kinetics of nucleic acid strands quantitatively[52–54].

Likewise, the detection of the folding procedure of DNA strands with LSPR sensors is reported. A measurable red shift of the LSPR bands results from the fact that upon folding, the electromagnetic fields on the surfaces are altered as the molecular density of DNA strands becomes closer to the sensor surface[55,56]. Therefore, LSPR sensors exhibit the tremendous potential to study nucleic acids in terms of their conformation and hybridization properties, examine nucleic acid–drug interactions, and explore the underlying reacting kinetics.

One of the unprecedented challenges in developing biosensors is transferring the systems to point-of-care devices. For plasmonic biosensors, the sensitivity and selectivity trust on the optical resonance that necessitates a lot of effort towards design, fabrication, and miniaturization. Apart from the nanoplasmonic feature itself, two significant parts of the biosensing platforms help to boost the application of plasmonic biosensors in real-life situations: the establishment of microfluidic and optical components. Here, microfluidic systems have to allow for low-loss light transmission (i.e., optically transparent) while being low-cost and scalable in fabrication[57]. Furthermore, microfluidics help to improve biodetection performance by guaranteeing efficient sample delivery, reducing the analyte consumption, and permitting high-throughput and multiplexed analyses[58]. On the other hand, the use of LEDs for illumination and

recognition with CMOS detectors simplifies the miniaturization and integration of optics into sensing platforms and fuels the engineering of handheld devices[48,59,60].

This research aims to develop a user-friendly, compact point-of-care device suitable for detecting label-free analytes in real-time with an appropriate detection limit. The proposed sensor operates by means of LSPR, whose plasmonic features arise from vertically aligned gold nanoantenna arrays – a large-scale, uniform, defect-poor, and densely packed 2D array. Variations of the geometry of the arrays result in a broad tuning of the optical resonance properties. Furthermore, combining the nanoplasmonic sensor with microfluidics facilitates efficient analyte transport in real-time. We demonstrated the working platform by exploring the real-time and label-free biodetection of short oligonucleotides, including underlying reacting kinetics, down to the low ng/µl range.

4.2 Biosensing with vertically aligned gold nanoantennas

4.2.1 Sensor fabrication, characterization, and integration

Highly responsive 2D arrays of vertically aligned nanoantennas were fabricated in close collaboration with the group of Prof. Eng from the Institute of Applied Physics, TU Dresden. Optical characteristics of the nanoantenna arrays are summarized in this thesis, as this is the basis for sensing by means of LSPR.

Figure 4-1A presents the structure of the array, underlining the strived fixation of antennas on substrates. As a result, the plasmonic biosensors exhibit a layer-wise composition with glass substrate (f), acting as supporting material for the whole array, a 7nm thick titanium layer (e), which is essential to promote sufficient adhesion for the subsequent gold underlayer (d). An AAO template (c) with nanopores allows for the synthesis of gold antennas (b) via electrochemical deposition (compare to section 3). After removal of the AAO template, nanoantennas are partly freestanding and can be modified with selected receptors (a). A photograph of the manufactured plasmonic sensor is presented in Figure 4-1 B, accentuating the size of the array. A densely packed array of nanoantennas with a diameter of 17 nm and a length of approx. 400 nm and a center-to-center distance of 63 nm were manufactured so that the gap between the nanorods measures 46 nm at the narrowest part. SEM images in Figure 4-1D show the nanoscopic point of view, underlining the antennas' uniform and defect-poor distribution within the array.

The optical resonance of rod-shaped nanofeatures depends on their aspect ratio (AR) of diameter to length[37]. Figure 1B shows different regions with varying aspect ratios were fabricated, and corresponding extinction spectra were plotted in Figure 1C. All

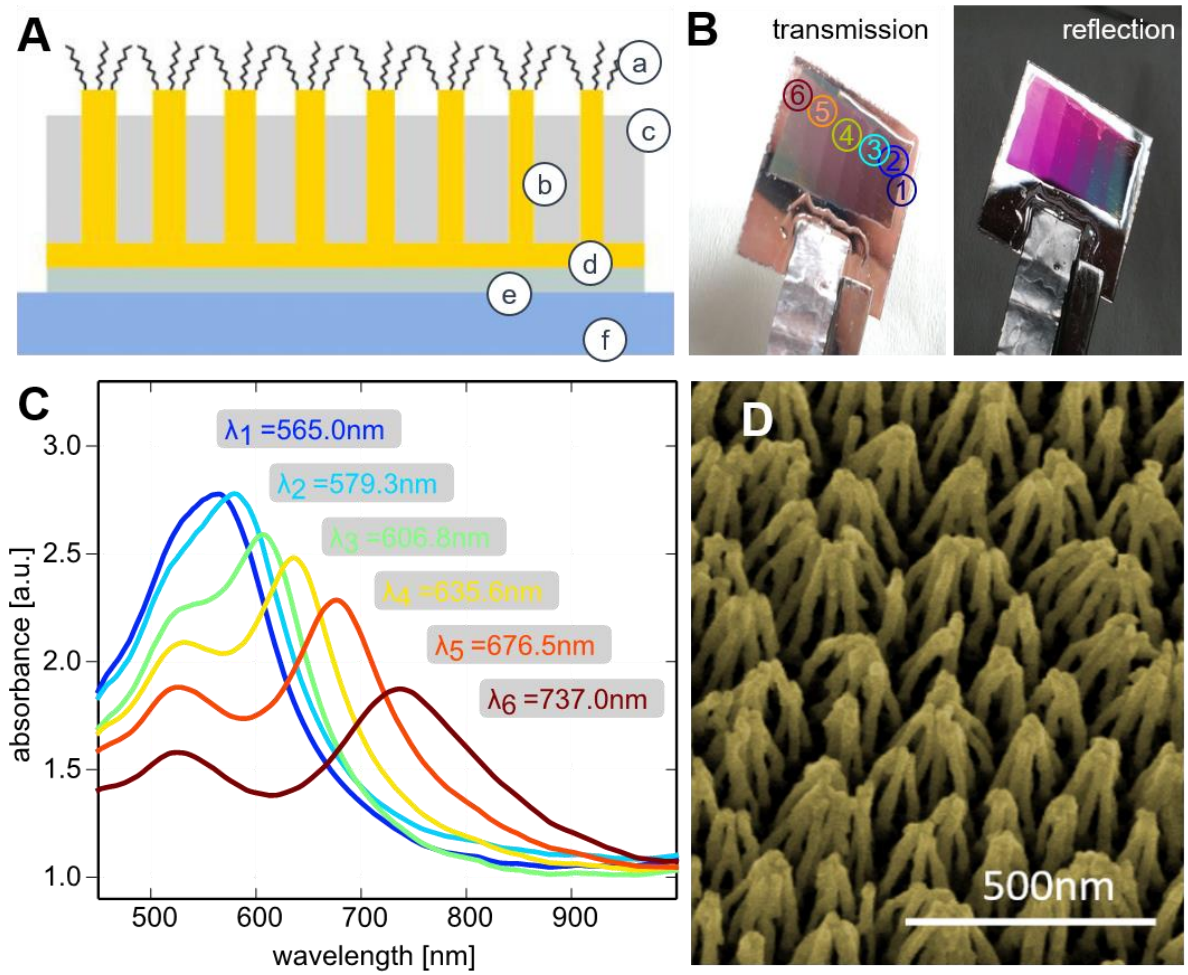

Figure 4-1: Characterization of 2D nanoantenna array used for plasmonic biosensor. A) Schematic cross-section of the nanoantenna array with (a) receptor molecules that have been immobilized on (b) nanoantenna structures, which are embedded partly in (c) AAO matrix. Antennas are linked to gold under layer (d) that in turn is adhered to a linker layer of titanium (e), all fixated on a glass substrate(f). B) Photograph of 2D nanoantenna array. Regions with varying aspect ratios (1-6) were fabricated. C) Extinction spectra of the nanoantenna array's designated regions (1-6). D) SEM image of freestanding rods. [Images provided by courtesy of Dr. T. Uhlig and Dr.-Ing. J. Schütt]

spectra showed two distinct peaks, which refer to the excitation of a plasmon resonance along the rods' short and long axis of the rods. Here, evident peaks at wavelengths of ≈520 nm correspond to the short-axis resonance. In contrast, long-axis resonances range from ≈680 nm to ≈850 nm, depending on the actual AR and the surrounding media. Following the spectra in Figure 4-1C, a tuning of the plasmon wavelengths is possible, as well as refractometric sensing through monitoring the peak position (compared to Figure 4-1B). The intensity of extinction of the spectra depends on the angle of the incident light. For the proposed array, the maximal intensity was found at an angle of 40°, which thus has been set and maintained during further research.

4.2.2 Integration of microfluidics

For biosensing, it is beneficial to enable a system that allows detection in aqueous environments, as bioreactions typically happen under those. At the same time, implementing a microfluidic system features a rapid, locally well-defined, and concise sample delivery and facilitates a synchronized optical read-out. Microfluidic channel systems were realized using PDMS in a layer-wise approach. Here, two glass slides with defined thicknesses were used as top and bottom barriers and manufactured in a multistep procedure described by Gang et al.[61]. Here, traditionally fabricated PDMS chamber systems, in which substrates act as a bottom barrier and PDMS as a top barrier, exhibited weak and less sharp spectra under illumination. In contrast, the modified approach resulted in a tightly sealed channel system with defined geometries and minimal optical signal loss upon biosensing. All fluids are regulated by a syringe pump, which allows for continuous and defined fluidic regimes inside the system, as this is the basis for reliable biosensing[62].

4.2.3 Immobilization of probe DNA and backfilling

The suitability of the proposed nanoantenna array for biosensing was stated at assessed example reactions. The immobilization of short oligonucleotide sequences, subsequent backfilling with alkanethiols, and final hybridization with two targets were explored in real-time and compared to traditional SPR sensors.

The presented assay followed a straightforward and well-known strategy to adhere thiol-terminated biomolecules to the gold surface of the antennas, elicited by the strong affinity between sulfur and gold[44,49,63–65]. A continuous recording of complete absorption spectra upon reactions enables real-time measurements. However, long-axis peak positions were extracted and plotted over time to emphasize emerging signal shifts during reaction time. Figure 4-2A presents the actual absorbance spectra after each reaction step, including a magnification of the peak region. Clearly, with each step, a red shift of the spectra is visible, caused by the accumulation of biomolecules close to the surface of antennas. Figure 4-2B images the nanoantenna array's arising wavelength shift upon the biomolecules' adhesion progress in a time-based resolution.

First, the immobilization process of the 25 bp long receptor (probe – DNA), whose 5’-end termination with thiol-linker promotes reaction with the gold surface, was evaluated. A homogenous layer of probe- DNA built up on nanostructured surfaces during

the diffusion-driven reaction. The idea is to ensure that all possible binding sites of the rods- also those in the gaps between the rods- can be addressed by the receptors. However, for successful sensing, a sufficiently low enough density of receptors is essential to prevent limitations caused by mass transfer effects[66]. Notwithstanding, laminar-driven incubation would be faster than diffusion, but most likely, only the upper parts of the rods would be accessed by receptors due to steric issues. The formation of the homogenous layer of the probe- DNA is reflected in a constant red shift of the LSPR peak (see Figure 4-2B). Here, the signal shift of about ≈1 nm arose during the first 5 h of incubation, leveling off afterward. Several adsorption isotherm models can describe the underlying chemical reaction, which is a chemisorption. Assuming a monolayer of

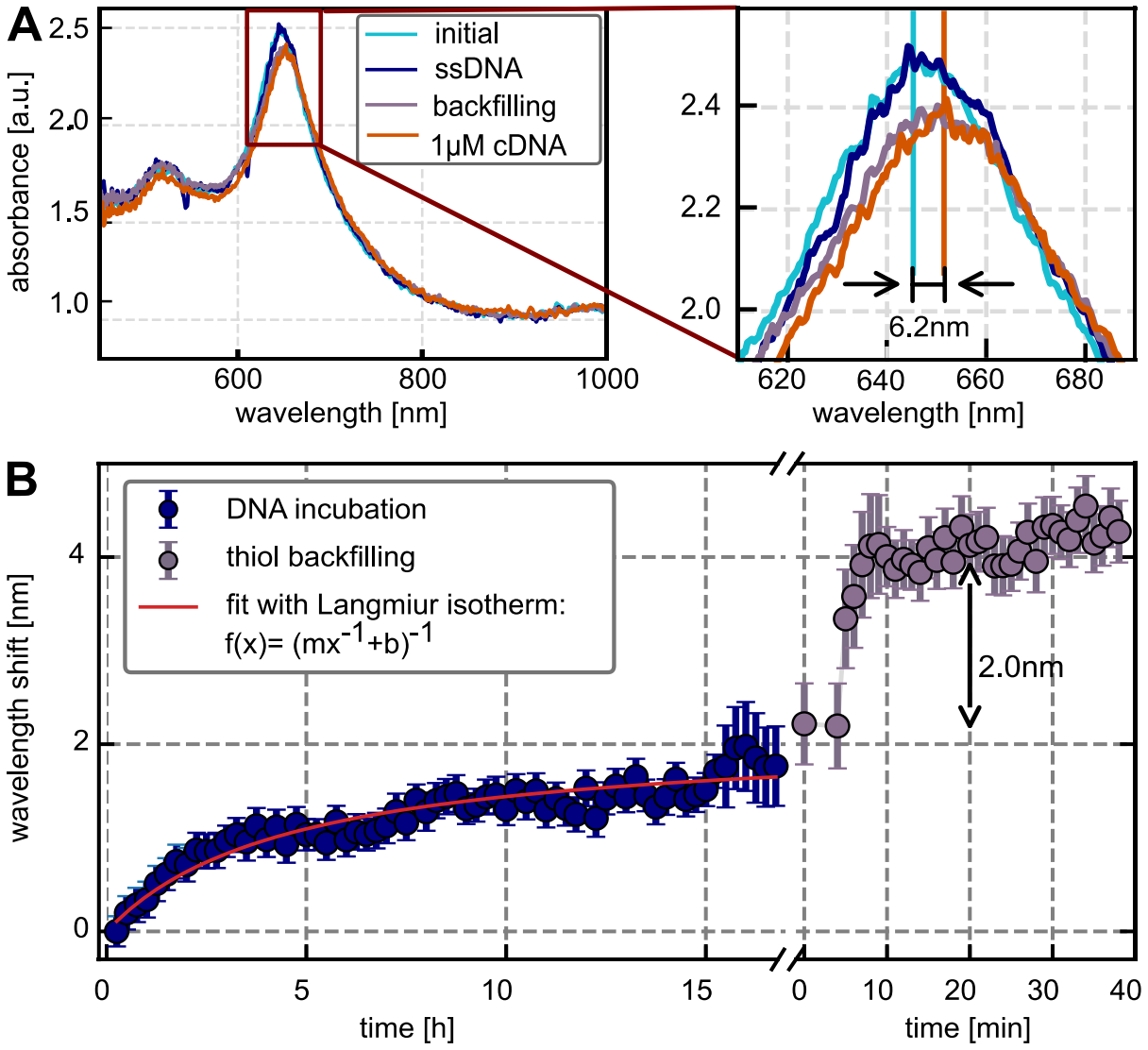

Figure 4-2: A) Optical absorbance spectra of nanoantenna biosensor after modification with several biomolecules. Each modification step led to a redshift of the spectra. The inset shows the magnification of the long axis resonance peak, highlighting the change upon reaction. B) Time-dependent position of the long axis resonance peak during immobilization of probe DNA (blue) and subsequent backfilling with MCH (purple). Kinetics for the formation of probe DNA layer was fitted with a Langmuir isotherm.

receptors, equally accessible binding sites, and no interactions between the binding sites and the receptors, the *Langmuir isotherm* is a reasonable model for describing the reaction. A fitting of the data with a Langmuir-Isotherm suggests a reaction equilibrium at $\Delta\lambda$=2.1 nm; compare the inset in Figure 4-2B for exact parameters. Discrepancies between observed and theoretical data rely on the time, which in theory is required to occupy all surface sites at the nanoantenna sample by a single molecule. Calculations within *Einstein*'s equation of diffusion, assigned with

$$< r^2 >= 6D * \tau \qquad (4.1)$$

have to be made. In equation 4.1, the diffusion coefficient D is defined with $120x10^{-8}cm^2/s$ for a 25 bp ssDNA[67], and the maximum pathway equals r=2 mm in the given channel geometry. As a result, the diffusion time τ is calculated to be around τ=1.53 h and thus falls behind the required incubation time until the signal saturation. Possibly pure geometrical effects dominate the adsorption, and corresponding time scales behave unexpectedly for nanoantenna arrays, as surface structures are known to influence the adhesion of biomolecules[68]. Nevertheless, the observed kinetics agree within the same magnitudes as previously published experimental results[69,70]. For example, Rapisarda et al.[52] conducted comparable LSPR measurements. In their study, the immobilization of 35mer DNA strands to gold nanodisks caused LSPR shifts around 1 nm for DNA immobilization. In contrast to this study, faster association rates are determined due to the different geometric layouts of the sensor.

Subsequent backfilling with mercaptohexanol (MCH) was executed to occupy vacant binding sites, reduce non-specific adsorption, and minimize detrimental interactions between the bound receptors and the gold surface.

Backfilling or blocking is an essential step in enhancing the performance of biosensors. When analytes link non-specifically with the surface due to electrostatic interactions, a lowering of specificity, sensitivity, and reproducibility follows. Therefore, the establishment of an "inactive" background is advantageous[71]. Several approaches for the diminishment of non-specific adsorption, including advantages and drawbacks, have been reviewed recently[72], distinguished into active or passive methods and chemical or physical mechanisms. The assessment of MCH as a suitable backfilling agent in this study is described in section 4.2.7Backfilling suppresses not only the unspecific binding but also sets up receptors upright on the surface (see figure 1B in the previous chapter) so that the analyte can easily reach them. Especially for DNA, this step is crucial, as DNA strands

are known to not only bind perpendicular but also parallel to surface[69], which in turn would inhibit the hybridization with complementary DNA sterically.

The reaction with MCH led to a reorganization within the structure of the organic layer on the surface. In particular, loosely bound probe DNA will be replaced by the much shorter MCH, and a dense self-assembled monolayer builds up[22,73,74] (also compared to Figure 1B in section 3). The process of chemisorption results in an enhancement of molecules on the surface, and thus, a further redshift of the signal of the plasmonic sensor of ~2 nm could be observed. Figure 4-2B displays the emerging signal shift during the blocking step, which reached its final value within only a few minutes- speaking for faster reaction kinetics of the backfilling than for the immobilization itself. These findings agree with the literature claiming that the concentration of molecules and the actual chain length of thiols determine adsorption kinetics, where smaller molecules show faster association rates[75,76]. Both reaction steps unify the same typical trend in adsorption kinetics of thiols to surfaces, where a first rapid step is followed by a second slow step which can be described mathematically with Langmuir isotherms[77,78].

Gold nanoantenna arrays exhibit two distinct peaks within their spectra. Here, the position of the long-axis resonance serves as a measure for biosensing, but it depends on the aspect ratio and the surrounding conditions. Consequently, nanoantenna arrays with sections of varying AR were exposed to the exact solutions of probe DNA and MCH, and the emerging LSPR for each AR was evaluated, respectively. Figure 4-3A illustrates the exemplary absorbance spectra of each section before and after the incubation of probe

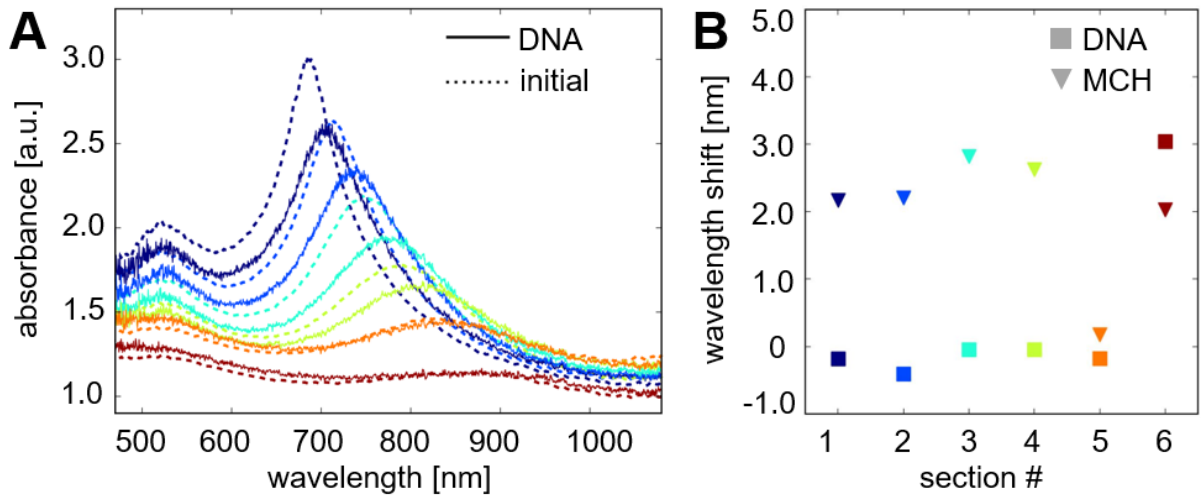

Figure 4-3: Optical response of nanoantennas with varying aspect ratios towards incubation of probe DNA and further backfilling with MCH. A) Absorbance spectra of nanoantennas with varying aspect ratios before (dotted lines) and after (solid lines) incubation with probe DNA. The color scheme refers to different sections (in analogy to Figure 4-1B). B) Shift of extracted LSPR peak position of each section after incubation of DNA (squares) and MCH (triangles).

DNA. In contrast, Figure B summarizes the measured values for each section after modification with DNA and MCH. Only slight differences within less than 0.5 nm were observed after the incubation of probe DNA onto individual sections. With a slightly more considerable variation of 1nm, the incubation of MCH could be detected in each section. Noteworthy, for both modifications, the LSPR shift of section No.6 was an outlier resulting from a less defined long axis peak and thus an artifact of analysis. The equal accounts partly for section No.5, concluding that only arrays with pronounced long-axis resonance peaks are suitable candidates for bio sensing.

4.2.4 Hybridization of complementary DNA strands

The evaluation of hybridization of the selected probe DNA with two different targets, which diverge within their length, is of interest. Hybridization reactions were examined with a nanoantenna array and a conventional SPR device. This study aims to appraise the sensors' capability to detect differently sized molecules. In particular, the unique geometry of the sensor is considered. Here, the densely packed array of vertical nanorods with gaps in between might cause potential difficulties for the longer molecular chains to penetrate these interspaces, leading to reduced binding kinetics and thus lower detection rates.

At first, a 25 bp-long, entirely complementary DNA strand (cDNA) was allowed to bind to the probe DNA. Prior to hybridization with a second set of 100 bp long DNA, where only the first 25 bp match the probe, a dehybridization step removed previously bound cDNA molecules. Solutions with a stepwise increasing target concentration, ranging from 1 nM to 1000 nM, were injected into the fluidic chamber at approximately. 15 min while recording absorbance spectra at intervals of 1 minute. Panel A in Figure 4-4 represents the course of the experiment; orange data points depict the reaction of 25 bp long cDNA, whereas green data points refer to the reaction of 100 bp long cDNA. The short concurrent signal spikes in Figure 4-4A originate from trivial air inclusions inside the channel, which interfere with the optical signal while passing the illuminated area on the sample. To determine the dynamic range of the sensor response, Panel B of Figure 4-4 consolidates the measurements by plotting the long-axis resonance shift in dependence on reaction time.

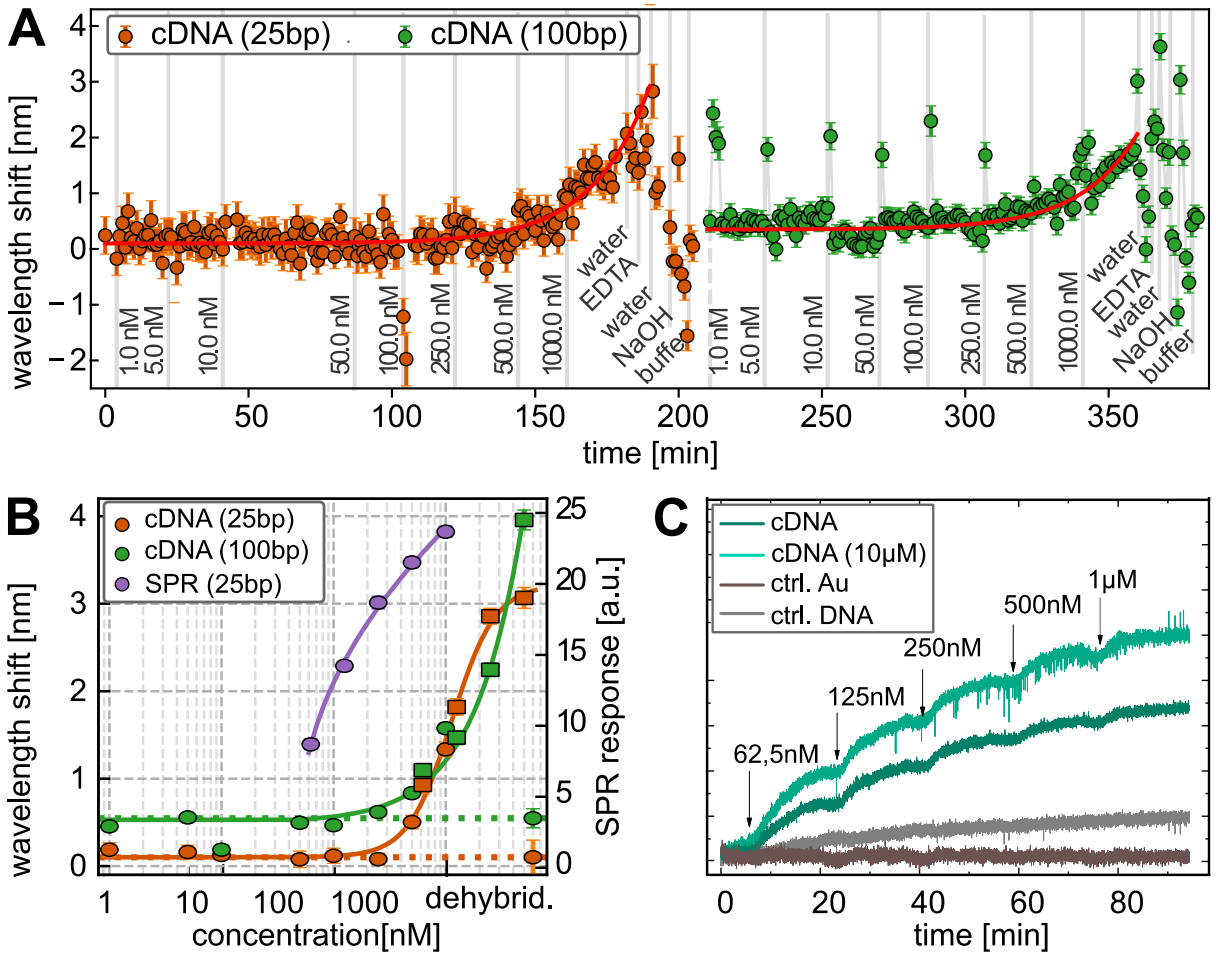

Figure 4-4: Biodetection of hybridization of two complementary DNA strands using nanoantenna array. A) Real-time measurement of hybridization with fully 25bp long complementary DNA (orange data) of different concentrations ranging from 1.0nM up to 1µM, and likewise concentrated 100bp long partial complementary DNA (green data). The shift of the long axis resonance peak is plotted over reaction time. A red shift of the LSPR peak occurred during recognition for both strands. B) Evolving wavelength shifts in dependence on the concentration of both DNA strands show the LSPR sensor's dynamic range. Purple circles show the reference sensor response of 25bp DNA on planar gold surfaces using a commercial SPR device. C) Real-time measurement of the hybridization with fully 25bp long complementary DNA on planar surfaces using a commercial SPR device. [Panel A and B were provided courtesy of Dr. Uhlig]

The LSPR sensor responded significantly at concentrations above 250 nM within a short reaction time for the shorter target DNA. Occurring wavelength shifts leveled off at $\Delta\lambda = (1.33 \pm 0.08)$ nm at $c(cDNA_{25}) = 1$ µM (see the signal in Figure 4-4A at ~165 min). However, signal saturation and consequently a reaction equilibrium could only be observed for cDNA with concentrations higher than 250 nM, as visualized in Figure 4-4A at ~140 min.

In Figure 4-4A, at reaction times between 180 and 200 min, a dehybridization step was performed by rinsing the sensor with EDTA and NaOH. The process induced the removal of all previously hybridized cDNA strands and thus the sensor regeneration. EDTA chelates the present cation $MgCl^{2+}$ while NaOH induces a denaturing of the DNA

strands that in turn causes the breaking of the hydrogen bonds between the two strands[79]. As the sensor signal reaches its initial base level after the denaturing procedure, a successful dehybridization can be assumed (see Figure 4-4A at ~ 210 min and B last data point).

One of the aims of this study is to evaluate the target length's influence on the nanoantenna array's performance. A similar experimental design was repeated with 100bp long DNA strands, where only the first 25 bps complement the probe strand. In analogy to previous results, a resonance shift occurred above a concentration threshold of $c(cDNA_{100})=250$ nM (compared to Figure 4-4A at 310 min). Again, an increasing concentration of the molecules in the solution caused a redshift of the LSPR signal, leading to a final wavelength shift of $\Delta\lambda = (1.58 \pm 0.06)$ nm at 1 µM. Likewise before, sensor signals decreased to initial levels after the dehybridization procedure (compare to Figure 4-4A for time ranges from 360 min to 400 min and Figure 4-4B last green datapoint).

Contrary to expectations, for the 100 bp cDNA, there was barely any saturation of the signal observed (see also Figure 4-4B), indicating that not all possible receptors have bound, and so equilibrium has not been reached yet. Nevertheless, the absolute signal levels during hybridization with more extended targets reach higher values than in hybridization with shorter targets after the same hybridization time. Here, the higher molar mass of longer targets leads to greater overall net changes in the local surrounding of the surface, including the refractive index, and thus causes higher absolute signal values.

Analogous experiments on planar gold surfaces have been performed using a standard SPR device to endorse the seen tendencies on nanoantenna arrays. In Figure 4-4B, purple circles show the occurring signal shifts in dependence on time and concentration, whereas Figure 4-4C portrays the progression of the experiment. Similar to the data observed on the LSPR sensor, the propagating SPR signals increase with increasing target concentrations. Regarding the influence of the target length, there is a comparable hybridization performance on nanostructured and planar surfaces, respectively. After normalizing the signals to their maximum values, both types of surfaces exhibit faster reaction kinetics for shorter DNA fragments than for longer ones. The number of bases is known to be related to hybridization kinetics[80,81]; as the complementary parts involved in this study are the same, the uneven length of the dangling ends determines the kinetics[82]. The overall (L)SPR sensor responses of longer

targets are higher than the signal shift for shorter targets. Since the (L)SPR signal responds to the refractive index or mass changes at the biospecific sensor surface, this observation is simply reasoned by a higher molecular weight for equally concentrated ligands[83,84].

In general, the hybridization of two DNA strands proceeds in two steps. In the first phase, the separated DNA strands coalesce due to attractive forces in the presence of colloidal interactions. Consequently, there is a 50% chance for proper positioning of the strands, which is the 5′-end of one strand goes together with the 3'-end of the other. During the second step, the converged strands move along, ferreting for a proper alignment position[85,86]. DNA strands must "flip" to achieve the correct position depending on the target's orientation towards the probe. After initial contacts of a few base pairs occur, a winding of the two strands around each for proper alignment follows. Finally, the remaining pairs form a duplex structure by zippering [87]. When a probe strand is tethered to the surface, only the target strand can move or reorient in the system[85].

In particular, the hybridization of strands with uneven lengths entails the presence of extra bases, which will not be part of the duplex (dangling ends). Those dangling ends will interact with the surface and stabilize the arising duplexes[88,89]. In addition, the pathway of the target strand towards the probe – either from bulk or from the surface-matters, too. The latter case requires the bending of both strands to achieve the desired position. Schmitt et al.[90] showed that DNA hybridization of strands with unequal length is less favored than the hybridization of equally long strands. The location of the complementary sequence on the target plays subordinated role.

Furthermore, the hybridization of target DNA to surface-tethered probes is influenced by steric issues, the targets' secondary structure, and the probe's binding capacity[91].

The secondary structures of targets and duplexes were predicted with web-based algorithms "AllSub" (targets) and "bifold" (duplex structures)[92]. The algorithms were also performed for probes and shorter targets for completeness. The structure predictions showed no possible intramolecular base pairs within the 25 bp probe nor within the 25 bp target and an entirely complementary duplex when the probe and target react. Figure 4-5A and B below illustrate the most probable structures containing the 100bp target strand. All possible structures, including their free energies, are attached in the appendix, section A.2.

Figure 4-5A shows the most probable secondary structure, including the possibility of forming hairpin structures caused by the intramolecular base pairs. In contrast, the presence of a probe strand alters the secondary structure in a way where a duplex region, visualized in Figure 4 5B by red and blue coloring, and an overlap region, colored in green, are formed. The secondary structures suggest the presence of two competitive reactions in the system, which will determine the overall equilibrium conditions: (1) the hybridization of target and probe competes with (2) the formation of hairpin structures within the cDNA itself. The latter leads to a reduced concentration of "available" target molecules in the solution, suppressing the hybridization. Consequently, a higher (initial) concentration of target molecules would be required to achieve an equilibrium. In this study, the sensor signal during hybridization with longer targets does not level off, most likely due to the abovementioned restrictions.

Bioassays and hence DNA hybridization, too, often exhibit better sensitivities on nanostructures than flat substrates. The increased surface areas with pronounced curvatures induce an enhanced number of capture sites and improve the accessibility of captured probes to targets during hybridization. Both facts contribute to a faster and more efficient binding, thus to a higher sensitivity in the end[93].

Among nanostructured surfaces, arrays of nanoantenna take on a unique role as the densely packed structures can limit the accessibility of biomolecules due to their narrow geometry, hallmarked by reduced interspaces between the rods. Correlating the size of biomolecules to the interspaces' size spells out the challenging situation: with a length of 0.34 nm per base pair[94], the 25 bp long probe DNA is theoretically about 9.5 nm long,

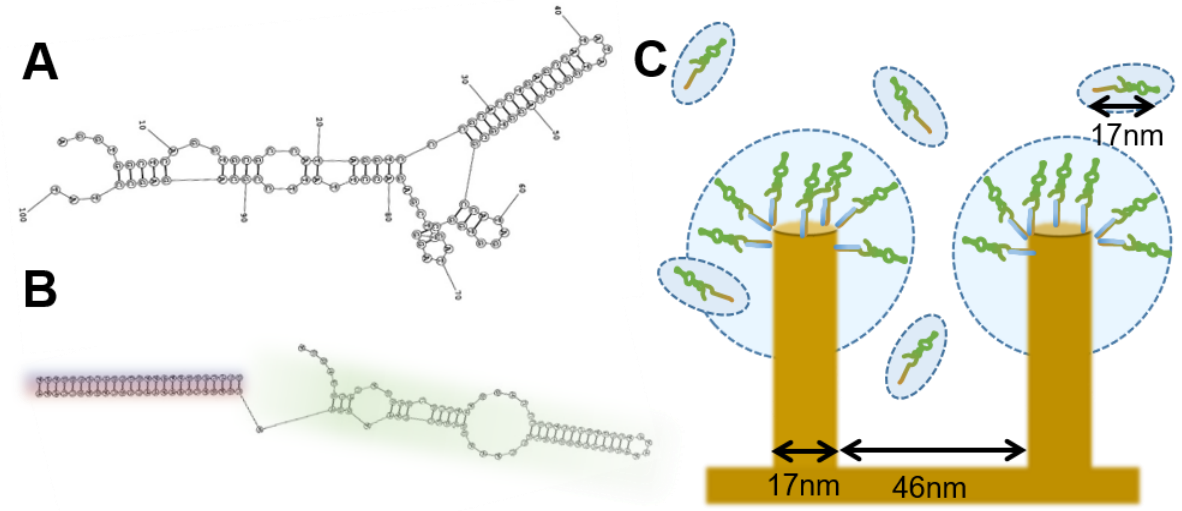

Figure 4-5: A) possible secondary structure of 100bp long target DNA. B) Possible secondary structure of probe-target complex with 100bp long, partially complementary DNA. Both structures were predicted by algorithms provided by [92].

including the ~1 nm C_6-thiol linker. Thus, if the probe DNA adsorbs to complete rods, the initial interrod-distance of 46 nm is reduced by 19 nm, leaving 27 nm "free" space for the targets to penetrate through. In turn, based on the secondary structure of the 100bp cDNA, the size is estimated to range from 13.6 nm (for hairpin structure) to 20.4 nm (for formed duplex), compared to Figure 4-5. Therefore, the actual spaces between the rods, correlated to the size of the DNA, are considered too small for full access. However, as DNA strands are flexible molecules due to their backbone structure, they can bend on the surface up to a certain point so that other target molecules can still penetrate the interspaces. Still, most of the binding reactions are expected to happen on the caps of the rods. Figure 4-5C depicts the present situation. Nevertheless, [85,90] showed that surfaces stabilize DNA hybridization of tethered probe/target complexes compared to their bulk counterparts.

The evaluation of the biorecognition experiments and their kinetic is based on the law of mass action, a rather simple model in which ligand (probe DNA) and analyte (cDNA) collide due to diffusion and form a duplex on the surface (association) if orientation and energy of the molecules fit. The binding response increases during the formation of the complex. As a continuous flow is applied, persistent delivery and removal of the analytes lead to a steady state of the system, expressed by stable sensor signals. Typically, a subsequent signal decline arises from the duplex's dissociation. Figure 4-6A represents a schematical plot of the binding response (RU) versus time that expresses the different stages of a binding event. The biorecognition depends on the analyte concentration, association rate, and dissociation rate constants. In contrast, the number of binding sites and size relations between target and receptor reflect within the overall level of response[95].

As exemplified in Figure 4-5B, only comparatively high detection limits appear after short exposure times. Therefore, the binding of 10 nM of the shorter target was recorded for extended exposure times of up to 24 h to evaluate the interaction kinetics in-depth. Depicted in Figure 4-6C below, the LSPR signal during incubation with 25 bp cDNA showed a red shift of the LSPR wavelength, with saturation at around 2.5 h at $\Delta\lambda \sim 6$ nm before leveling off. However, a moderate signal decline followed, which can be attributed to the dissociation of the analyte. The approximation with a Langmuir isotherm model, marked as a red line in Figure 4-6, suggests a signal plateau at $\Delta\lambda = 5.6$ nm. Still, the fitted data of the Langmuir isotherm deviates slightly from the measured data. The simple and

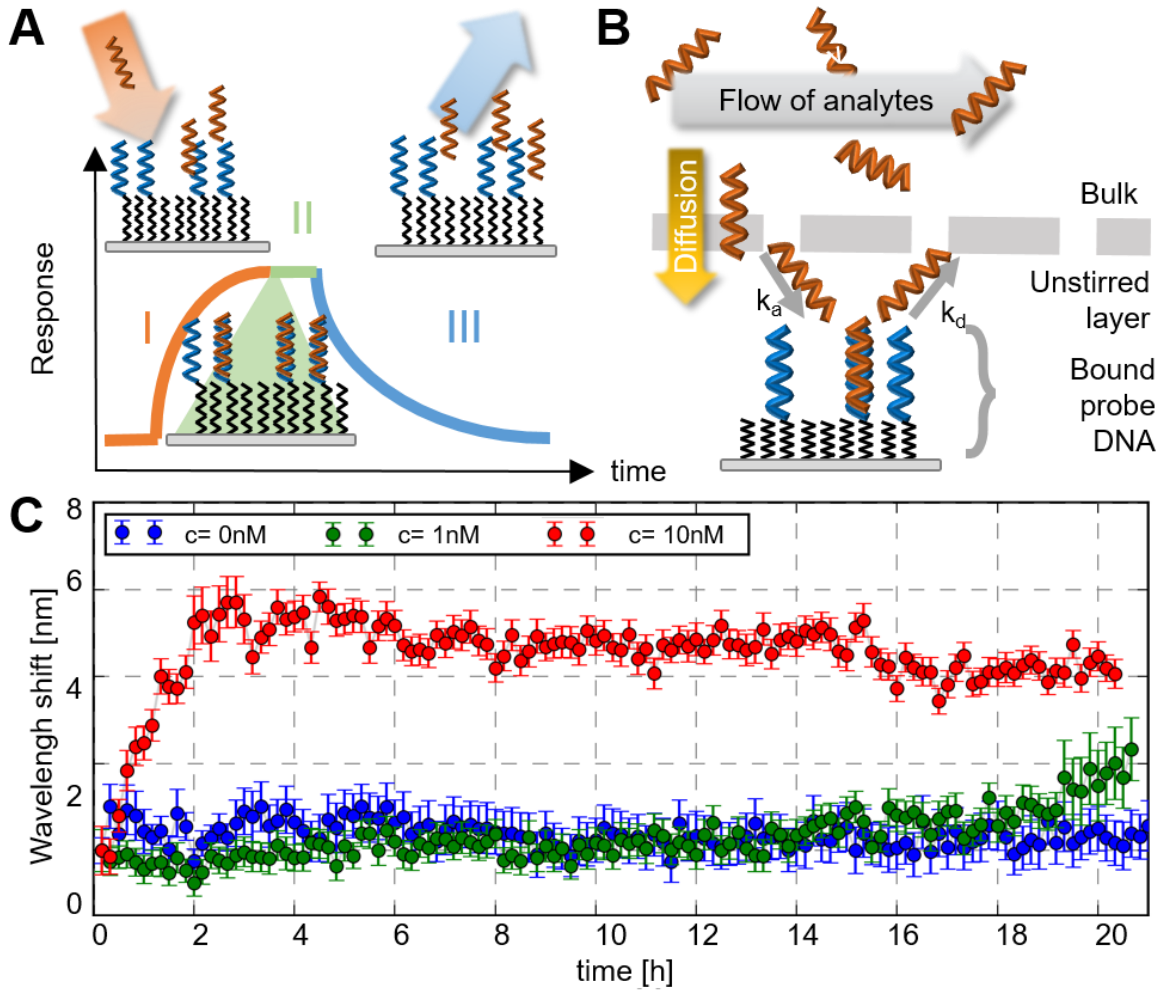

Figure 4-6: A) Schematic drawing of interaction kinetics during biorecognition experiment, consisting of an associating phase (orange part), a steady state (green), and a dissociation phase (blue). B) Sketch of interactions on the surface: Delivery of analytes in bulk via the flow of the buffer solution. Transfer of the analyte to the actual surface with immobilized receptors occurs via diffusion. On the surface, the binding reaction is characterized by its rate constants. C) Long time measurement for hybridization of 10nM entirely complementary cDNA on nanoantenna array. Due to the high affinity of the system, characterized by a slow dissociation rate, the time to steady state is elongated. Therefore, analytes at a relatively low concentration cannot be detected reliably after short exposure.

widely used Langmuir isotherm is a model system whose assumptions exist barely in real systems[96], as surface effects like heterogeneous immobilization or cross-linking of the ligands, mass transfer, and re-association of the analytes affect the interaction kinetics[97,98].

In contrast, the target concentrations of 500 nM or higher could be detected within the first 15 minutes of the reaction, as presented in Figure 4-4A. The additional reduction of concentration to 1 nM target reached saturation after ~24 h, and vice versa, higher target levels of 1 µM accelerated the reaction time to less than 3 min. The observations agree with the literature, where typically, low concentrations of analyte will take longer to reach equilibrium, especially for high-affinity interactions[99,100]. In general, high-affinity

reactions are regulated by their low dissociation rates k_D and low equilibrium constant rates[101]. Equation (1) below describes not only the mathematical background for time t_Θ to reach equilibrium but also emphasizes the dependence on association rate k_a and concentration of analyte c:

$$t_\Theta = \frac{-\ln(1-\Theta)}{k_a C + k_d} \tag{4.2}$$

The more enduring the receptor-target complex, characterized by low k_D values, the longer the incubation time will be incubation time t_Θ to achieve the desired percentage Θ of reaction. Furthermore, equation (4.2) demonstrates that an increase in analyte concentration will lower the required time to achieve equilibrium, similar to this study's findings.

In close relation to the previous paragraph, the importance of setting up suitable fluidic conditions so that the actual bio recognition is not restrained is discussed. The binding event involves two parts: first, analytes are transferred from the bulk solution to the sensor surface through convection or diffusion, commonly known as mass transfer[97,102]. The second step involves the actual binding reaction between receptor and target and can be described with the help of association and dissociation rates. Suppose the diffusion rate is now slower than the actual association rate of the ligand-target complex. In that case, a lack of target molecules at the sensor surface occurs, and reaction kinetics are compromised –the fact is described as mass transfer limitation[103] and schematized in Figure 4-6B. The mass transfer depends on the geometry of the flow cell, the diffusion rate of the analyte molecules, and the flow rate of the fluidics[104]. Consequently, a way to overcome mass transfer limitations is to enhance the diffusion/ convection rate by simply increasing the flow rate[66,102] or reducing possible binding sites by lowering the concentration of immobilized receptors[105].

4.2.5 Surface coverage and hybridization efficiency of DNA

The progress of surface coverage of probe and target DNA on nanostructured and planar gold surfaces has provided insight into the previous conclusions. The quantification of immobilized and hybridized DNA strands allows evaluation of how and to which content the DNA molecules can penetrate the nanoantenna array compared to planar surfaces. For this purpose, fluorescently labeled DNA was incubated at defined concentrations for designated periods, subsequently detached, and fluorescent intensities (FI) were measured. First, the amount of immobilized probe DNA on planar

and nanostructured surfaces is determined. As mentioned in section 4.2.4, apart from the (nano) structure of the surface itself, the number of immobilized receptors will also affect the binding reaction.

Consequently, Table 4-1 summarizes the FI of two differently concentrated probe DNA on planar and structured samples. Here, for probe DNA with concentrations of 5 µM and 2.5 µM surface coverages close to 2.29×10^{13} and 3.09×10^{13} molecules/cm^2 at the planar gold surface are measured. On the other hand, equally concentrated receptors on nanoantenna substrates reduced surface coverages of 1.09×10^{13}/cm^2 and 0.39×10^{13}/cm^2, respectively. For comparison, experimentally determined surface coverages of 2.0×10^{13} up to 6.9×10^{13} molecules/cm^2 are achieved on planar surfaces[65,70,106].

Table 4-1: Overview of surface coverages of immobilized DNA on planar and nanostructured gold surfaces with different concentrations.

Sample	Surface density (x10^{13} molecules/cm^2)
Planar 5.0 µM	2.29
2.5 µM	3.09
Rods 5.0 µM	1.09
2.5µM	0.39

The reduced surface coverage for nanoantennas is contrary to the expectations as reports in the literature typically suggest higher immobilization efficiencies on nanostructures. In contrast to planar substrates, nanostructures possess a higher ratio of surface to volume and enhanced curvatures, which boost the accessibility for DNA molecules and diminish steric hindrances[107,108].

However, in the proposed nanoantenna geometry, specific boundaries occur. The densely packed arrays of nanoantennas are homogenously distributed in size and layout, resulting in comparably small interrod distances, depending on the AR ratio. Consequently, the penetration of DNA molecules into those spaces is restrained, and only the upper parts of the rods are expected to be accessible within reasonable reaction times. A 1 mm^2 large sensor equals an accessible surface area of 0.36×10^{12} nm^2, which is only a third of what is available on the same surface of a planar substrate. Hence, the suppressed number of binding surface sites will lead to a reduced amount of bound receptors, which is coherent with the observed surface coverage on nanoantenna substrates. However, the curvature of antennas still allows for high coverages on the surface, which were additionally guaranteed by adding $MgCl_2$ to probe strands as the salt

minimizes electrostatic repulsion within the phosphate backbone of probe DNA[109]. Anyhow, the subsequent backfilling will reduce the coverage on both substrates because of the desorption of loosely bound DNA[69].

In contrast, Table 4-2 summarizes the hybridization efficiencies at different parameters, which involved altering the surface type, reaction time, and concentration of target molecules. On planar surfaces, the hybridization density of 1 µM cDNA is about $5.66*10^{12}$ molecules/cm^2, which equals a yield of 24.7%. In contrast, the yield of hybridized DNA increased on nanostructured surfaces to 39.1%. In synergy with the immobilization of probe DNA, the curved nature allows for better accessibility of targets – noticeable in terms of higher hybridization efficiency. Contradictory, longer chains will limit the accessibility of the densely packed nanoantenna arrays due to enhanced electrostatic repulsion and steric interferences between the chains and antennas.

Extending the hybridization time from 1 h to 4 h improved the hybridization yield of a 1 µM target from 12.8% to 24.7%. Strikingly, on the nanoantenna substrates, the yield increased up to 39.1%. Analyte solutions with concentrations ranging from 10 nM to 1 µM were allowed to hybridize for 4 h. At low concentrations of 10 nM, only 11.3% of the targets hybridized, whereas, at 100 nM, the yield leveled at 18.9% and even up to 31.1% at 500nm. As remarked above, 1µM resulted in a yield of 24.7%.

Table 4-2: Time and concentration-dependent hybridization efficiency of target DNA. Prior to hybridization, a 5 µM receptor was immobilized on each sample.

Investigated parameter	Sample	Hybridization density (x10^{12} molecules/cm^2)	Yield (%)
Structure	planar nanoantenna	5.66 4.26	24.7 39.1
Time	30 min 1 h 4 h	2.92 2.93 5.66	12.8 12.8 24.7
Concentration of cDNA	500 nM 100 nM 10 nM	7.12 4.34 2.58	31.1 18.9 11.3

All determined hybridization efficiencies are in agreement with values reported in literature[106,110]. The reason behind comparably low yields of ~25% or less relies on the high density of probe DNA, which causes steric and electrostatic hindrances[70,107,111].

Above all, during application as a biosensor by means of LSPR, the nanoantenna array will exhibit more minor wavelength shifts for hybridization than for immobilization since fewer targets than probes bind to the surface.

4.2.6 Refractive index sensing

Biosensing with the nanoantenna array by means of LSPR highly depends on the refractive index (RI) of surrounding media[4,112]. Accordingly, all observed signal shifts of ~1nm to (1.58±0.06) nm are discussed in more detail to actual RI. The RI of any bulk solution, i.e., any buffer with and without DNA, was determined with an ABBE refractometer and related to spectral shifts with the help of a calibration curve. Here, the RI sensitivity was calibrated by measuring the transmission spectra of nanoantennas while adjusting the RI of an ethylene-glycol (EG)/water mixture. Figure 4-7A and C summarize the measured position of the long-axis resonance peak at adjusted RI of EG/water by enhancing the EG volume fraction.

A linear fit of the data showed an RI sensitivity of (102.5 ± 6.6) nm/RIU. The change in the LSPR-peak dependence on RI change is a good measure of the nanostructure

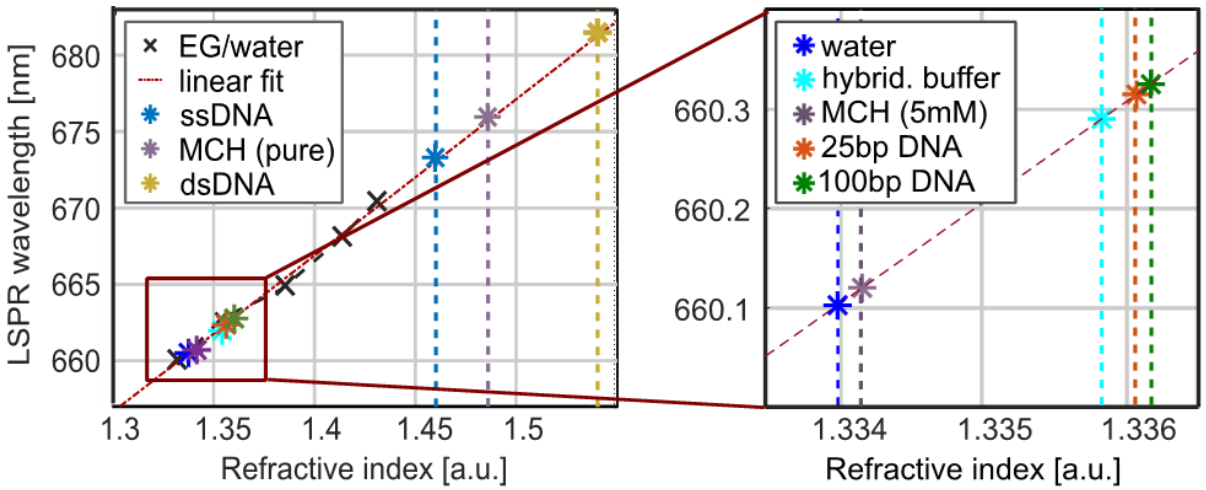

sample	RI (adjusted)	LSPR peak (nm)	Calc. shift (nm)
EG/ water	1.3322 1.354 1.3837 1.412 1.4292	659.74 662.75 664.66 667.87 670.18	
ssDNA*	1.486	675.68	15.57
MCH*	1.46	672.60	12.49
dsDNA*	1.54	681.21	21.10

sample	RI (measured)	Pred. LSPR peak(nm)	Calcul. shift (nm)
Water	1.334	660.11	0.00
Imm. buffer	1.337	660.42	0.31
5mM MCH	1.3342	660.13	0.02
HB	1.3358	660.30	0.19
25bp cDNA	1.3360	660.32	0.21
100bp cDNA	1.3362	660.33	0.22

Figure 4-7: LSPR signal in dependence on the refractive index of the surrounding moieties. The refractive index (RI) of different solutions was correlated to LSPR positions with the help of an ethylene glycol(EG)/water mixture with different ratios (black crosses). A linear fit (red dotted line) of measured RI of EG/water served as calibration for the correlation. Next, the RI of all buffers and biomolecules was measured, and the calibration curve predicted the LSPR shift. The right panel magnifies the region between RI= 1.334 and 1.336 to visualize the used buffer solutions' different RI/LSPR signals. All exact values can be found in the lower table; *data from the literature

sensitivity. Depending on the shape[113,114] and aspect ratio[115–117], the sensitivity differs, with nonspheroidal particles being more sensitive. However, nanostructures attached to substrates exhibit lower sensitivity than their dispersed counterparts[118]. Nevertheless, LSPR sensors in a measurement configuration with a relatively low measurement sensitivity are capable of detecting bio reactions quantitatively[52,119].

Next, the LSPR shifts for all bulk solutions are predicted for the given RI values, visualized in Figure 4-7B. Finally, the measured and projected RI values and the correlated LSPR shifts are summarized in Figure 4-7D.

The differences between the RI of the bulk solutions with and without DNA (see Figure 4-7D) are comparably small, so wavelength shifts caused by the bulk solutions are presumably small, too. With predicted LSPR- shifts ranging from 0.19 nm to 0.22 nm, these changes are significantly lower than the recorded shifts of (1.58±0.06) nm during the hybridization experiment. A comparable situation occurs during immobilization and backfilling. Likewise, pure organic layers of singe- or double-stranded DNA cause continuous red shifts of the signal due to a local increase of RI. Here, the given RI of single-stranded DNA with 1.46, backfilling agent MCH with 1.86, and double-stranded target-probe DNA complex with 1.54[120] would result, as illustrated in Figure 4-7C, in a wavelength shift of about 12.49 nm, 15.57 nm, and even 21.10 nm, respectively. These findings confirm that the measured LSPR shifts are caused by the binding of molecules and not merely by a change in the surrounding medium's RI.

4.2.7 Backfilling and blocking

Preventing non-specific adsorption of excess DNA molecules to the surface requires minimizing free binding sites as otherwise non-specifically bound oligonucleotides would interfere during measurements[121–123] or even cause desorption of thiolated probes[124]. Therefore, to gauge the most suitable agent for blocking, non-specific adsorption of DNA towards differently terminated surfaces, namely carboxyl-, amino-, and hydroxyl- termination, was investigated. Figure 4-8 illustrates the non-specific adsorption towards the mentioned surfaces.

The highest non-specific adsorption occurred on non-backfilled blank gold areas. In contrast, the introduction of charged groups such as amino- and carboxyl- groups decreased unspecific adsorption. The lowest signal change could be detected when

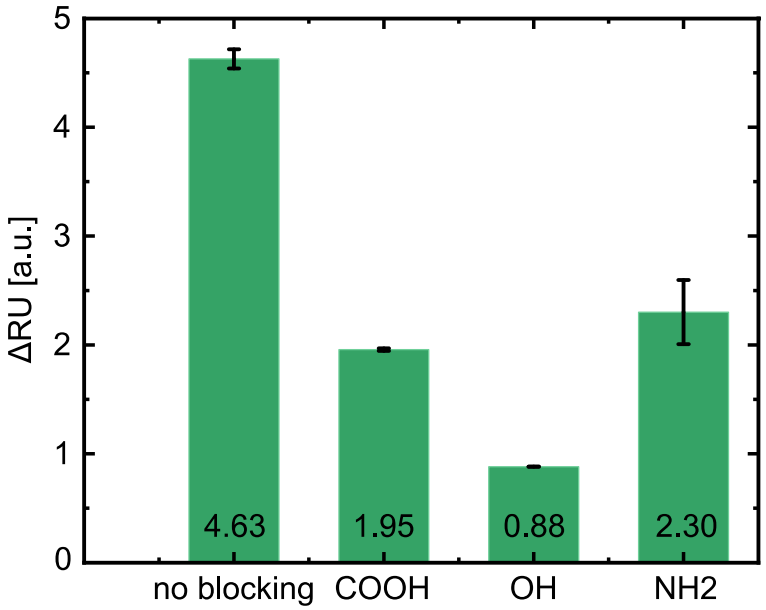

Figure 4-8: Evaluation of non-specific adsorption of target DNA on differently terminated surfaces using SPR. The signal was measured before and after incubation with 1 µM DNA for 1 h.

hydroxyl-terminated surfaces were present. Consequently, mercaptohexanol was chosen as a backfilling agent.

By leaving the gold untreated, the target DNA would stick to blank gold due to electrostatic attraction[125]. However, with the introduction of charges and potentials, the efficiency of binding and hybridizations is known to be affected 80. In other cases, the introduction of negative charges will hinder the binding of DNA, as seen by the injection of carboxylic groups[111]. Nevertheless, the introduction of positive charges will cause enhanced attraction toward negatively charged DNA strands ending up in high non-specific adsorption. However, the introduction of alcohols offers the least desirable environment for binding and facilitating well-formed SAMs on the surface.

4.3 Summary

Nanoplasmonic biosensors demonstrate their applicability as a biosensor, especially for diagnostic uses. However, challenges and limitations remain mainly founded on the need for automation of the complete testing procedure – including sample preparation and analysis, as well as quality assurance. From a physical and chemical perspective, various nanostructures and composites with outstanding optical properties and thus the highest sensitivities can be synthesized. In turn, the development of advanced and automated microfluidic systems, which include separation membranes, pre-concentration chambers, or micro-reactors, emerges concerning automation strategies. Here, the fabrication of microfluidics with multiple channels, which are controlled individually by the help of valves, enables the possibility for multiplexed analysis[127–129]. Furthermore, the automation of fluidics in synergy with plasmonics improves the POC diagnostics of optical sensors[130–132]. Moreover, optimizing biochemical strategies, i.e., the design of new receptors and surface functionalization strategies, further increases the plasmonics application field of plasmonics[57,123,133].

In addition, optical biosensors benefit from intrinsic, light-based technologies: ultimate speed, robustness, tuneability, and integration in miniaturized devices allow for the accomplishment of the strict demands for clinical diagnostics. So, the construction of small and simple devices which can detect analytes in a few minutes while providing accurate prognosis (all of it at the point of care) is emerging.

To reach those ambitious aims, LSPR measurements with a plasmonic sensor were conducted to study the label-free binding of two complementary DNA strands to immobilized DNA probes on gold nanoantennas. Large arrays (~1 cm^2) of vertically aligned, densely packed gold nanorods with confined optical spectra, e.g., pronounced long axis resonance peak at ~650 nm, are the basis of the biosensor. Shifts of the resonance peak during binding were monitored continuously with the help of the integration of a microfluidic channel system. LSPR shifts corresponded to around ~1 nm for DNA immobilization and 1.59 nm for fully complementary DNA strands binding.

Significantly, the adsorption kinetics of immobilization and hybridization of the two complementary DNA strands were analyzed and discussed, too. Determining the surface coverage of DNA on nanostructured and planar samples, as well as involving the refractive indices of surrounding media, corroborates the findings in this research.

All results demonstrate that LSPR measurements performed with nanoantenna arrays can not only monitor the binding of biomolecules quantitatively but also allow for label-free, real-time detection of analytes inside a flow channel with high throughput and a capability for multiplexed measurements. The proposed system is not offering a ready-to-use POC solution yet but embraces the functional understanding and technical implementation of nanoantennas for biosensing applications.

4.4 References

(1) Klinghammer, S.; Uhlig, T.; Patrovsky, F.; Böhm, M.; Schütt, J.; Pütz, N.; Baraban, L.; Eng, L. M.; Cuniberti, G. Plasmonic Biosensor Based on Vertical Arrays of Gold Nanoantennas. *ACS Sens.* **2018**, *3* (7), 1392–1400. https://doi.org/10.1021/acssensors.8b00315.

(2) Brolo, A. G. Plasmonics for Future Biosensors. *Nat. Photonics* **2012**, *6* (11), 709–713. https://doi.org/10.1038/nphoton.2012.266.

(3) Cathcart, N.; Chen, J. I. L. Sensing Biomarkers with Plasmonics. *Anal. Chem.* **2020**, *92* (11), 7373–7381. https://doi.org/10.1021/acs.analchem.0c00711.

(4) Willets, K. A.; Van Duyne, R. P. Localized Surface Plasmon Resonance Spectroscopy and Sensing. *Annu. Rev. Phys. Chem.* **2007**, *58* (1), 267–297. https://doi.org/10.1146/annurev.physchem.58.032806.104607.

(5) Saha, K.; Agasti, S. S.; Kim, C.; Li, X.; Rotello, V. M. Gold Nanoparticles in Chemical and Biological Sensing. *Chem. Rev.* **2012**, *112* (5), 2739–2779. https://doi.org/10.1021/cr2001178.

(6) Huang, X.; El-Sayed, I. H.; Qian, W.; El-Sayed, M. A. Cancer Cell Imaging and Photothermal Therapy in the Near-Infrared Region by Using Gold Nanorods. *J. Am. Chem. Soc.* **2006**, *128* (6), 2115–2120. https://doi.org/10.1021/ja057254a.

(7) Haes, A. J.; Van Duyne, R. P. A Unified View of Propagating and Localized Surface Plasmon Resonance Biosensors. *Anal. Bioanal. Chem.* **2004**, *379* (7), 920–930. https://doi.org/10.1007/s00216-004-2708-9.

(8) Khateb, H.; Klös, G.; Meyer, R. L.; Sutherland, D. S. Development of a Label-Free LSPR-Apta Sensor for Staphylococcus Aureus Detection. *ACS Appl. Bio Mater.* **2020**, *3* (5), 3066–3077. https://doi.org/10.1021/acsabm.0c00110.

(9) Dutta, S.; Saikia, K.; Nath, P. Smartphone Based LSPR Sensing Platform for Bio-Conjugation Detection and Quantification. *RSC Adv.* **2016**, *6* (26), 21871–21880. https://doi.org/10.1039/C6RA01113F.

(10) Fan, Z.; Geng, Z.; Fang, W.; Lv, X.; Su, Y.; Wang, S.; Chen, H. Smartphone Biosensor System with Multi-Testing Unit Based on Localized Surface Plasmon Resonance Integrated with Microfluidics Chip. *Sensors* **2020**, *20* (2), 446. https://doi.org/10.3390/s20020446.

(11) Wang, Y.; Zhou, X.; Xu, C.; Jin, Y.; Li, B. Gold Nanorods as Visual Sensing Platform for Chiral Recognition with Naked Eyes. *Sci. Rep.* **2018**, *8* (1), 5296. https://doi.org/10.1038/s41598-018-23674-y.

(12) Zhang, L.; Salmain, M.; Liedberg, B.; Boujday, S. Naked Eye Immunosensing of Food Biotoxins Using Gold Nanoparticle-Antibody Bioconjugates. *ACS Appl. Nano Mater.* **2019**, *2* (7), 4150–4158. https://doi.org/10.1021/acsanm.9b00598.

(13) Mazzotta, F.; Johnson, T. W.; Dahlin, A. B.; Shaver, J.; Oh, S.-H.; Höök, F. Influence of the Evanescent Field Decay Length on the Sensitivity of Plasmonic Nanodisks and Nanoholes. *ACS Photonics* **2015**, *2* (2), 256–262. https://doi.org/10.1021/ph500360d.

(14) Guo, L.; Jackman, J. A.; Yang, H.-H.; Chen, P.; Cho, N.-J.; Kim, D.-H. Strategies for Enhancing the Sensitivity of Plasmonic Nanosensors. *Nano Today* **2015**, *10* (2), 213–239. https://doi.org/10.1016/j.nantod.2015.02.007.

(15) Zalyubovskiy, S. J.; Bogdanova, M.; Deinega, A.; Lozovik, Y.; Pris, A. D.; An, K. H.; Hall, W. P.; Potyrailo, R. A. Theoretical Limit of Localized Surface Plasmon Resonance Sensitivity to Local Refractive Index Change and Its Comparison to Conventional Surface Plasmon Resonance Sensor. *J. Opt. Soc. Am. A* **2012**, *29* (6), 994. https://doi.org/10.1364/JOSAA.29.000994.

(16) Kasani, S.; Curtin, K.; Wu, N. A Review of 2D and 3D Plasmonic Nanostructure Array Patterns: Fabrication, Light Management and Sensing Applications. *Nanophotonics* **2019**, *8* (12), 2065–2089. https://doi.org/10.1515/nanoph-2019-0158.

(17) Wang, W.; Ramezani, M.; Väkeväinen, A. I.; Törmä, P.; Rivas, J. G.; Odom, T. W. The Rich Photonic World of Plasmonic Nanoparticle Arrays. *Mater. Today* **2018**, *21* (3), 303–314. https://doi.org/10.1016/j.mattod.2017.09.002.

(18) García de Abajo, F. J. Colloquium: Light Scattering by Particle and Hole Arrays. *Rev. Mod. Phys.* **2007**, *79* (4), 1267–1290. https://doi.org/10.1103/RevModPhys.79.1267.

(19) Liu, Z.; Yang, Z.; Peng, B.; Cao, C.; Zhang, C.; You, H.; Xiong, Q.; Li, Z.; Fang, J. Highly Sensitive, Uniform, and Reproducible Surface-Enhanced Raman Spectroscopy from Hollow Au-Ag Alloy Nanourchins. *Adv. Mater.* **2014**, *26* (15), 2431–2439. https://doi.org/10.1002/adma.201305106.

(20) Sepúlveda, B.; Angelomé, P. C.; Lechuga, L. M.; Liz-Marzán, L. M. LSPR-Based Nanobiosensors. *Nano Today* **2009**, *4* (3), 244–251. https://doi.org/10.1016/j.nantod.2009.04.001.

(21) Zhang, X.; Yonzon, C. R.; Van Duyne, R. P. Nanosphere Lithography Fabricated Plasmonic Materials and Their Applications. *J. Mater. Res.* **2006**, *21* (5), 1083–1092. https://doi.org/10.1557/jmr.2006.0136.

(22) Kummer, K.; Vyalikh, D. V.; Gavrila, G.; Kade, A.; Weigel-Jech, M.; Mertig, M.; Molodtsov, S. L. High-Resolution Photoelectron Spectroscopy of Self-Assembled Mercaptohexanol Monolayers on Gold Surfaces. *J. Electron Spectrosc. Relat. Phenom.* **2008**, *163* (1–3), 59–64. https://doi.org/10.1016/j.elspec.2008.02.005.

(23) Pimpin, A.; Srituravanich, W. Review on Micro- and Nanolithography Techniques and Their Applications. *Eng. J.* **2012**, *16* (1), 37–56. https://doi.org/10.4186/ej.2012.16.1.37.

(24) Malinovskis, U.; Poplausks, R.; Apsite, I.; Meija, R.; Prikulis, J.; Lombardi, F.; Erts, D. Ultrathin Anodic Aluminum Oxide Membranes for Production of Dense Sub-20 Nm Nanoparticle Arrays. *J. Phys. Chem. C* **2014**, *118* (16), 8685–8690. https://doi.org/10.1021/jp412689y.

(25) Liu, S.; Tian, J.; Zhang, W. Fabrication and Application of Nanoporous Anodic Aluminum Oxide: A Review. *Nanotechnology* **2021**, *32* (22), 222001. https://doi.org/10.1088/1361-6528/abe25f.

(26) Su, Z.; Zhou, W. Formation Mechanism of Porous Anodic Aluminium and Titanium Oxides. *Adv. Mater.* **2008**, *20* (19), 3663–3667. https://doi.org/10.1002/adma.200800845.

(27) Fiehler, V.; Patrovsky, F.; Ortmann, L.; Derenko, S.; Hille, A.; Eng, L. M. Plasmonic Nanorod Antenna Array: Analysis in Reflection and Transmission. *J. Phys. Chem. C* **2016**, *120* (22), 12178–12186. https://doi.org/10.1021/acs.jpcc.6b02419.

(28) Edwards, J. D.; Keller, F. Formation of Anodic Coatings on Aluminum. *Trans. Electrochem. Soc.* **1941**, *79* (1), 135. https://doi.org/10.1149/1.3071266.

(29) Diggle, J. W.; Downie, T. C.; Goulding, C. W. Anodic Oxide Films on Aluminum. *Chem. Rev.* **1969**, *69* (3), 365–405. https://doi.org/10.1021/cr60259a005.

(30) Masuda, H. Self-Ordering of Cell Arrangement of Anodic Porous Alumina Formed in Sulfuric Acid Solution. *J. Electrochem. Soc.* **1997**, *144* (5), L127. https://doi.org/10.1149/1.1837634.

(31) Masuda, H.; Fukuda, K. Ordered Metal Nanohole Arrays Made by a Two-Step Replication of Honeycomb Structures of Anodic Alumina. *Science* **1995**, *268* (5216), 1466–1468. https://doi.org/10.1126/science.268.5216.1466.

(32) Patrovsky, F.; Fiehler, V.; Derenko, S.; Barth, S.; Bartzsch, H.; Ortstein, K.; Frach, P.; Eng, L. M. Anodization of Sputtered Substoichiometric Aluminum Oxide Thin-Films for Improved Nanorod Array Fabrication. *Mater. Res. Express* **2017**, *4* (5), 055010. https://doi.org/10.1088/2053-1591/aa6e62.

(33) Al-Kaysi, R. O.; Ghaddar, T. H.; Guirado, G. Fabrication of One-Dimensional Organic Nanostructures Using Anodic Aluminum Oxide Templates. *J. Nanomater.* **2009**, *2009*, e436375. https://doi.org/10.1155/2009/436375.

(34) Chen, H.; Shao, L.; Li, Q.; Wang, J. Gold Nanorods and Their Plasmonic Properties. *Chem. Soc. Rev.* **2013**, *42* (7), 2679–2724. https://doi.org/10.1039/c2cs35367a.

(35) Liu, J.; Jalali, M.; Mahshid, S.; Wachsmann-Hogiu, S. Are Plasmonic Optical Biosensors Ready for Use in Point-of-Need Applications? *The Analyst* **2020**, *145* (2), 364–384. https://doi.org/10.1039/C9AN02149C.

(36) Huang, X.; Neretina, S.; El-Sayed, M. A. Gold Nanorods: From Synthesis and Properties to Biological and Biomedical Applications. *Adv. Mater. Deerfield Beach Fla* **2009**, *21* (48), 4880–4910. https://doi.org/10.1002/adma.200802789.

(37) Brioude, A.; Jiang, X. C.; Pileni, M. P. Optical Properties of Gold Nanorods: DDA Simulations Supported by Experiments. *J. Phys. Chem. B* **2005**, *109* (27), 13138–13142. https://doi.org/10.1021/jp0507288.

(38) Kumar, R.; Binetti, L.; Nguyen, T. H.; Alwis, L. S. M.; Agrawal, A.; Sun, T.; Grattan, K. T. V. Determination of the Aspect-Ratio Distribution of Gold Nanorods in a Colloidal Solution Using UV-Visible Absorption Spectroscopy. *Sci. Rep.* **2019**, *9* (1), 17469. https://doi.org/10.1038/s41598-019-53621-4.

(39) Pellas, V.; Hu, D.; Mazouzi, Y.; Mimoun, Y.; Blanchard, J.; Guibert, C.; Salmain, M.; Boujday, S. Gold Nanorods for LSPR Biosensing: Synthesis, Coating by Silica, and Bioanalytical Applications. *Biosensors* **2020**, *10* (10), 146. https://doi.org/10.3390/bios10100146.

(40) Peixoto, L. P. F.; Santos, J. F. L.; Andrade, G. F. S. Plasmonic Nanobiosensor Based on Au Nanorods with Improved Sensitivity: A Comparative Study for Two Different Configurations. *Anal. Chim. Acta* **2019**, *1084*, 71–77. https://doi.org/10.1016/j.aca.2019.07.032.

(41) Mayer, K. M.; Lee, S.; Liao, H.; Rostro, B. C.; Fuentes, A.; Scully, P. T.; Nehl, C. L.; Hafner, J. H. A Label-Free Immunoassay Based Upon Localized Surface Plasmon Resonance of Gold Nanorods. *ACS Nano* **2008**, *2* (4), 687–692. https://doi.org/10.1021/nn7003734.

(42) Huang, C.; Bonroy, K.; Reekmans, G.; Laureyn, W.; Verhaegen, K.; De Vlaminck, I.; Lagae, L.; Borghs, G. Localized Surface Plasmon Resonance Biosensor Integrated with Microfluidic Chip. *Biomed. Microdevices* **2009**, *11* (4), 893–901. https://doi.org/10.1007/s10544-009-9306-8.

(43) Park, J.-H.; Byun, J.-Y.; Mun, H.; Shim, W.-B.; Shin, Y.-B.; Li, T.; Kim, M.-G. A Regeneratable, Label-Free, Localized Surface Plasmon Resonance (LSPR) Aptasensor for the Detection of Ochratoxin A. *Biosens. Bioelectron.* **2014**, *59*, 321–327. https://doi.org/10.1016/j.bios.2014.03.059.

(44) Park, J.-H.; Byun, J.-Y.; Jang, H.; Hong, D.; Kim, M.-G. A Highly Sensitive and Widely Adaptable Plasmonic Aptasensor Using Berberine for Small-Molecule Detection. *Biosens. Bioelectron.* **2017**, *97*, 292–298. https://doi.org/10.1016/j.bios.2017.06.019.

(45) Byun, J.-Y.; Shin, Y.-B.; Li, T.; Park, J.-H.; Kim, D.-M.; Choi, D.-H.; Kim, M.-G. The Use of an Engineered Single Chain Variable Fragment in a Localized Surface Plasmon Resonance Method for Analysis of the C-Reactive Protein. *Chem. Commun.* **2013**, *49* (82), 9497–9499. https://doi.org/10.1039/C3CC45046E.

(46) Wang, Y.; Tang, L. Chemisorption Assembly of Au Nanorods on Mercaptosilanized Glass Substrate for Label-Free Nanoplasmon Biochip. *Anal. Chim. Acta* **2013**, *796*, 122–129. https://doi.org/10.1016/j.aca.2013.08.024.

(47) Cai, J.; Zhang, C.; Liang, C.; Min, S.; Cheng, X.; Li, W. Solution-Processed Large-Area Gold Nanocheckerboard Metasurfaces on Flexible Plastics for Plasmonic Biomolecular Sensing. *Adv. Opt. Mater.* **2019**, *7* (19), 1900516. https://doi.org/10.1002/adom.201900516.

(48) Cetin, A. E.; Kocer, Z. A.; Topkaya, S. N.; Yazici, Z. A. Handheld Plasmonic Biosensor for Virus Detection in Field-Settings. *Sens. Actuators B Chem.* **2021**, *344*, 130301. https://doi.org/10.1016/j.snb.2021.130301.

(49) Li, Y.; Zhang, Y.; Zhao, M.; Zhou, Q.; Wang, L.; Wang, H.; Wang, X.; Zhan, L. A Simple Aptamer-Functionalized Gold Nanorods Based Biosensor for the Sensitive Detection of MCF-7 Breast Cancer Cells. *Chem. Commun. Camb. Engl.* **2016**, *52* (20), 3959–3961. https://doi.org/10.1039/c6cc01014h.

(50) Loyez, M.; Hassan, E. M.; Lobry, M.; Liu, F.; Caucheteur, C.; Wattiez, R.; DeRosa, M. C.; Willmore, W. G.; Albert, J. Rapid Detection of Circulating Breast Cancer Cells Using a Multiresonant Optical Fiber Aptasensor with Plasmonic Amplification. *ACS Sens.* **2020**, *5* (2), 454–463. https://doi.org/10.1021/acssensors.9b02155.

(51) Fong, K. E.; Yung, L.-Y. L. Localized Surface Plasmon Resonance: A Unique Property of Plasmonic Nanoparticles for Nucleic Acid Detection. *Nanoscale* **2013**, *5* (24), 12043–12071. https://doi.org/10.1039/C3NR02257A.

(52) Rapisarda, A.; Giamblanco, N.; Marletta, G. Kinetic Discrimination of DNA Single-Base Mutations by Localized Surface Plasmon Resonance. *J. Colloid Interface Sci.* **2017**, *487*, 141–148. https://doi.org/10.1016/j.jcis.2016.10.026.

(53) Frolov, L.; Dix, A.; Tor, Y.; Tesler, A. B.; Chaikin, Y.; Vaskevich, A.; Rubinstein, I. Direct Observation of Aminoglycoside–RNA Binding by Localized Surface Plasmon Resonance Spectroscopy. *Anal. Chem.* **2013**, *85* (4), 2200–2207. https://doi.org/10.1021/ac3029079.

(54) Joshi, G. K.; Deitz-McElyea, S.; Liyanage, T.; Lawrence, K.; Mali, S.; Sardar, R.; Korc, M. Label-Free Nanoplasmonic-Based Short Noncoding RNA Sensing at Attomolar Concentrations Allows for Quantitative and Highly Specific Assay of MicroRNA-10b in Biological Fluids and Circulating Exosomes. *ACS Nano* **2015**, *9* (11), 11075–11089. https://doi.org/10.1021/acsnano.5b04527.

(55) Qiu, S.; Zhao, F.; Santos, G. M.; Shih, W.-C. Plasmonic Biosensor for Label-Free G-Quadruplexes Detection; Miller, B. L., Cunningham, B. T., Eds.; San Francisco, California, United States, 2016; p 97250F. https://doi.org/10.1117/12.2212318.

(56) Cao, C.; Zhang, J.; Wen, X.; Dodson, S. L.; Dao, N. T.; Wong, L. M.; Wang, S.; Li, S.; Phan, A. T.; Xiong, Q. Metamaterials-Based Label-Free Nanosensor for Conformation and Affinity Biosensing. *ACS Nano* **2013**, *7* (9), 7583–7591. https://doi.org/10.1021/nn401645t.

(57) Soler, M.; Huertas, C. S.; Lechuga, L. M. Label-Free Plasmonic Biosensors for Point-of-Care Diagnostics: A Review. *Expert Rev. Mol. Diagn.* **2019**, *19* (1), 71–81. https://doi.org/10.1080/14737159.2019.1554435.

(58) Choi, S.; Goryll, M.; Sin, L. Y. M.; Wong, P. K.; Chae, J. Microfluidic-Based Biosensors toward Point-of-Care Detection of Nucleic Acids and Proteins. *Microfluid. Nanofluidics* **2011**, *10* (2), 231–247. https://doi.org/10.1007/s10404-010-0638-8.

(59) Tokel, O.; Yildiz, U. H.; Inci, F.; Durmus, N. G.; Ekiz, O. O.; Turker, B.; Cetin, C.; Rao, S.; Sridhar, K.; Natarajan, N.; Shafiee, H.; Dana, A.; Demirci, U. Portable Microfluidic Integrated Plasmonic Platform for Pathogen Detection. *Sci. Rep.* **2015**, *5* (1), 9152. https://doi.org/10.1038/srep09152.

(60) Coskun, A. F.; Cetin, A. E.; Galarreta, B. C.; Alvarez, D. A.; Altug, H.; Ozcan, A. Lensfree Optofluidic Plasmonic Sensor for Real-Time and Label-Free Monitoring of Molecular Binding Events over a Wide Field-of-View. *Sci. Rep.* **2014**, *4* (1), 6789. https://doi.org/10.1038/srep06789.

(61) Gang, A.; Haustein, N.; Baraban, L.; Cuniberti, G. Multifunctional Reversibly Sealable Microfluidic Devices for Patterned Material Deposition Approaches. *RSC Adv* **2015**, *5* (16), 11806–11811. https://doi.org/10.1039/C4RA15785K.

(62) Wang, D.-S.; Fan, S.-K. Microfluidic Surface Plasmon Resonance Sensors: From Principles to Point-of-Care Applications. *Sensors* **2016**, *16* (8), 1175. https://doi.org/10.3390/s16081175.

(63) Kick, A.; Bönsch, M.; Katzschner, B.; Voigt, J.; Herr, A.; Brabetz, W.; Jung, M.; Sonntag, F.; Klotzbach, U.; Danz, N.; Howitz, S.; Mertig, M. DNA Microarrays for Hybridization Detection by Surface Plasmon Resonance Spectroscopy. *Biosens. Bioelectron.* **2010**, *26* (4), 1543–1547. https://doi.org/10.1016/j.bios.2010.07.108.

(64) Parab, H. J.; Jung, C.; Lee, J.-H.; Park, H. G. A Gold Nanorod-Based Optical DNA Biosensor for the Diagnosis of Pathogens. *Biosens. Bioelectron.* **2010**, *26* (2), 667–673. https://doi.org/10.1016/j.bios.2010.06.067.

(65) Peeters, S.; Stakenborg, T.; Reekmans, G.; Laureyn, W.; Lagae, L.; Van Aerschot, A.; Van Ranst, M. Impact of Spacers on the Hybridization Efficiency of Mixed Self-Assembled DNA/Alkanethiol Films. *Biosens. Bioelectron.* **2008**, *24* (1), 72–77. https://doi.org/10.1016/j.bios.2008.03.012.

(66) Myszka, D. G.; He, X.; Dembo, M.; Morton, T. A.; Goldstein, B. Extending the Range of Rate Constants Available from BIACORE: Interpreting Mass Transport-Influenced Binding Data. *Biophys. J.* **1998**, *75* (2), 583–594. https://doi.org/10.1016/S0006-3495(98)77549-6.

(67) Stellwagen, N. C.; Magnusdottir, S.; Gelfi, C.; Righetti, P. G. Measuring the Translational Diffusion Coefficients of Small DNA Molecules by Capillary Electrophoresis. *Biopolymers* **2001**, *58* (4), 390–397. https://doi.org/10.1002/1097-0282(20010405)58:4<390::AID-BIP1015>3.0.CO;2-K.

(68) Prinz, C. N. Interactions between Semiconductor Nanowires and Living Cells. *J. Phys. Condens. Matter* **2015**, *27* (23), 233103. https://doi.org/10.1088/0953-8984/27/23/233103.

(69) Herne, T. M.; Tarlov, M. J. Characterization of DNA Probes Immobilized on Gold Surfaces. *J. Am. Chem. Soc.* **1997**, *119* (38), 8916–8920. https://doi.org/10.1021/ja9719586.

(70) Peterson, A. W.; Heaton, R. J.; Georgiadis, R. M. The Effect of Surface Probe Density on DNA Hybridization. *Nucleic Acids Res.* **2001**, *29* (24), 5163–5168.

(71) Fraioli, R.; Manero Planella, J. M.; Gil Mur, F. J.; Mas-Moruno, C. Blocking Methods to Prevent Non-Specific Adhesion of Mesenchymal Stem Cells to Titanium and Evaluate the Efficiency of Surface Functionalization: Albumin vs Poly(Ethylene Glycol) Coating. *Biomecánica* **2014**, *22* (1). https://doi.org/10.5821/sibb.22.1.4802.

(72) Lichtenberg, J. Y.; Ling, Y.; Kim, S. Non-Specific Adsorption Reduction Methods in Biosensing. *Sensors* **2019**, *19* (11), 2488. https://doi.org/10.3390/s19112488.

(73) Arinaga, K.; Rant, U.; Tornow, M.; Fujita, S.; Abstreiter, G.; Yokoyama, N. The Role of Surface Charging during the Coadsorption of Mercaptohexanol to DNA Layers on Gold: Direct Observation of Desorption and Layer Reorientation. *Langmuir* **2006**, *22* (13), 5560–5562. https://doi.org/10.1021/la060324m.

(74) Levicky, R.; Herne, T. M.; Tarlov, M. J.; Satija, S. K. Using Self-Assembly To Control the Structure of DNA Monolayers on Gold: A Neutron Reflectivity Study. *J. Am. Chem. Soc.* **1998**, *120* (38), 9787–9792. https://doi.org/10.1021/ja981897r.

(75) Peterlinz, K. A.; Georgiadis, R. In Situ Kinetics of Self-Assembly by Surface Plasmon Resonance Spectroscopy. *Langmuir* **1996**, *12* (20), 4731–4740. https://doi.org/10.1021/la9508452.

(76) Karpovich, D. S.; Blanchard, G. J. Direct Measurement of the Adsorption Kinetics of Alkanethiolate Self-Assembled Monolayers on a Microcrystalline Gold Surface. *Langmuir* **1994**, *10* (9), 3315–3322. https://doi.org/10.1021/la00021a066.

(77) Dilimon, V. S.; Rajalingam, S.; Delhalle, J.; Mekhalif, Z. Self-Assembly Mechanism of Thiol, Dithiol, Dithiocarboxylic Acid, Disulfide and Diselenide on Gold: An Electrochemical Impedance Study. *Phys. Chem. Chem. Phys.* **2013**, *15* (39), 16648–16656. https://doi.org/10.1039/C3CP51804C.

(78) Asiaei, S.; Nieva, P.; Vijayan, M. M. Fast Kinetics of Thiolic Self-Assembled Monolayer Adsorption on Gold: Modeling and Confirmation by Protein Binding. *J. Phys. Chem. B* **2014**, *118* (47), 13697–13703. https://doi.org/10.1021/jp509986s.

(79) Ageno, M.; Dore, E.; Frontali, C. The Alkaline Denaturation of DNA. *Biophys. J.* **1969**, *9* (11), 1281–1311. https://doi.org/10.1016/S0006-3495(69)86452-0.

(80) Tang, J.; Sun, Y.; Pang, S.; Han, K. Y. Spatially Encoded Fast Single-Molecule Fluorescence Spectroscopy with Full Field-of-View. *Sci. Rep.* **2017**, *7* (1), 10945. https://doi.org/10.1038/s41598-017-10837-6.

(81) Andrews, R. DNA Hybridisation Kinetics Using Single-Molecule Fluorescence Imaging. *Essays Biochem.* **2021**, *65* (1), 27–36. https://doi.org/10.1042/EBC20200040.

(82) Dickman, R.; Manyanga, F.; Brewood, G. P.; Fish, D. J.; Fish, C. A.; Summers, C.; Horne, M. T.; Benight, A. S. Thermodynamic Contributions of 5'- and 3'-Single Strand Dangling-Ends to the Stability of Short Duplex DNAs. *J. Biophys. Chem.* **2012**, *3* (1), 1–15. https://doi.org/10.4236/jbpc.2012.31001.

(83) Retra, K.; Irth, H.; van Muijlwijk-Koezen, J. E. Surface Plasmon Resonance Biosensor Analysis as a Useful Tool in FBDD. *Drug Discov. Today Technol.* **2010**, *7* (3), e181–e187. https://doi.org/10.1016/j.ddtec.2010.11.012.

(84) Liu, Y.; Wilson, W. D. Quantitative Analysis of Small Molecule–Nucleic Acid Interactions With a Biosensor Surface and Surface Plasmon Resonance Detection. *Methods Mol. Biol. Clifton NJ* **2010**, *613*, 1–23. https://doi.org/10.1007/978-1-60327-418-0_1.

(85) Schmitt, T. J.; Knotts, T. A. Thermodynamics of DNA Hybridization on Surfaces. *J. Chem. Phys.* **2011**, *134* (20), 205105. https://doi.org/10.1063/1.3592557.

(86) Hoefert, M. J.; Sambriski, E. J.; Pablo, J. J. de. Molecular Pathways in DNA-DNA Hybridization of Surface-Bound Oligonucleotides. *Soft Matter* **2011**, *7* (2), 560–566. https://doi.org/10.1039/C0SM00729C.

(87) Ouldridge, T. E.; Šulc, P.; Romano, F.; Doye, J. P. K.; Louis, A. A. DNA Hybridization Kinetics: Zippering, Internal Displacement and Sequence Dependence. *Nucleic Acids Res.* **2013**, *41* (19), 8886–8895. https://doi.org/10.1093/nar/gkt687.

(88) Ambia-Garrido, J.; Vainrub, A.; Pettitt, B. M. Free Energy Considerations for Nucleic Acids with Dangling Ends near a Surface: A Coarse Grained Approach. *J. Phys. Condens. Matter Inst. Phys. J.* **2011**, *23* (32), 325101. https://doi.org/10.1088/0953-8984/23/32/325101.

(89) Kara, M.; Zacharias, M. Stabilization of Duplex DNA and RNA by Dangling Ends Studied by Free Energy Simulations. *Biopolymers* **2014**, *101* (4), 418–427. https://doi.org/10.1002/bip.22398.

(90) Schmitt, T. J.; Rogers, J. B.; Knotts, T. A. Exploring the Mechanisms of DNA Hybridization on a Surface. *J. Chem. Phys.* **2013**, *138* (3), 035102. https://doi.org/10.1063/1.4775480.

(91) Chizhikov, V.; Rasooly, A.; Chumakov, K.; Levy, D. D. Microarray Analysis of Microbial Virulence Factors. *Appl. Environ. Microbiol.* **2001**, *67* (7), 3258–3263. https://doi.org/10.1128/AEM.67.7.3258-3263.2001.

(92) Reuter, J. S.; Mathews, D. H. RNAstructure: Software for RNA Secondary Structure Prediction and Analysis. *BMC Bioinformatics* **2010**, *11* (1), 129. https://doi.org/10.1186/1471-2105-11-129.

(93) Bin, X.; Sargent, E. H.; Kelley, S. O. Nanostructuring of Sensors Determines the Efficiency of Biomolecular Capture. *Anal. Chem.* **2010**, *82* (14), 5928–5931. https://doi.org/10.1021/ac101164n.

(94) *Discovery of DNA Double Helix: Watson and Crick | Learn Science at Scitable*. http://www.nature.com/scitable/topicpage/discovery-of-dna-structure-and-function-watson-397 (accessed 2021-12-09).

(95) Rich, R. L.; Myszka, D. G. Survey of the Year 2007 Commercial Optical Biosensor Literature. *J. Mol. Recognit. JMR* **2008**, *21* (6), 355–400. https://doi.org/10.1002/jmr.928.

(96) Azizian, S.; Eris, S. Chapter 6 - Adsorption Isotherms and Kinetics. In *Interface Science and Technology*; Ghaedi, M., Ed.; Adsorption: Fundamental Processes and Applications; Elsevier, 2021; Vol. 33, pp 445–509. https://doi.org/10.1016/B978-0-12-818805-7.00011-4.

(97) Glaser, R. W. Antigen-Antibody Binding and Mass Transport by Convection and Diffusion to a Surface: A Two-Dimensional Computer Model of Binding and Dissociation Kinetics. *Anal. Biochem.* **1993**, *213* (1), 152–161. https://doi.org/10.1006/abio.1993.1399.

(98) Edwards, P. R.; Gill, A.; Pollardknight, D. V.; Hoare, M.; Buckle, P. E.; Lowe, P. A.; Leatherbarrow, R. J. Kinetics of Protein-Protein Interactions at the Surface of an Optical Biosensor. *Anal. Biochem.* **1995**, *231* (1), 210–217. https://doi.org/10.1006/abio.1995.1522.

(99) Myszka, D. G.; Jonsen, M. D.; Graves, B. J. Equilibrium Analysis of High Affinity Interactions Using BIACORE. *Anal. Biochem.* **1998**, *265* (2), 326–330. https://doi.org/10.1006/abio.1998.2937.

(100) Jarmoskaite, I.; AlSadhan, I.; Vaidyanathan, P. P.; Herschlag, D. How to Measure and Evaluate Binding Affinities. *eLife* **2020**, *9*, e57264. https://doi.org/10.7554/eLife.57264.

(101) Pollard, T. D. A Guide to Simple and Informative Binding Assays. *Mol. Biol. Cell* **2010**, *21* (23), 4061–4067. https://doi.org/10.1091/mbc.e10-08-0683.

(102) Myszka, D. G.; Morton, T. A.; Doyle, M. L.; Chaiken, I. M. Kinetic Analysis of a Protein Antigen-Antibody Interaction Limited by Mass Transport on an Optical Biosensor. *Biophys. Chem.* **1997**, *64* (1), 127–137. https://doi.org/10.1016/S0301-4622(96)02230-2.

(103) Schuck, P.; Zhao, H. The Role of Mass Transport Limitation and Surface Heterogeneity in the Biophysical Characterization of Macromolecular Binding Processes by SPR Biosensing. *Methods Mol. Biol. Clifton NJ* **2010**, *627*, 15–54. https://doi.org/10.1007/978-1-60761-670-2_2.

(104) Squires, T. M.; Messinger, R. J.; Manalis, S. R. Making It Stick: Convection, Reaction and Diffusion in Surface-Based Biosensors. *Nat. Biotechnol.* **2008**, *26* (4), 417–426. https://doi.org/10.1038/nbt1388.

(105) Schasfoort, R. B. M. Chapter 1 Introduction to Surface Plasmon Resonance. **2017**, 1–26. https://doi.org/10.1039/9781788010283-00001.

(106) Steel, A. B.; Herne, T. M.; Tarlov, M. J. Electrochemical Quantitation of DNA Immobilized on Gold. *Anal. Chem.* **1998**, *70* (22), 4670–4677. https://doi.org/10.1021/ac980037q.

(107) Demers, L. M.; Mirkin, C. A.; Mucic, R. C.; Reynolds, R. A.; Letsinger, R. L.; Elghanian, R.; Viswanadham, G. A Fluorescence-Based Method for Determining the Surface Coverage and Hybridization Efficiency of Thiol-Capped Oligonucleotides Bound to Gold Thin Films and Nanoparticles. *Anal. Chem.* **2000**, *72* (22), 5535–5541. https://doi.org/10.1021/ac0006627.

(108) Hill, H. D.; Millstone, J. E.; Banholzer, M. J.; Mirkin, C. A. The Role Radius of Curvature Plays in Thiolated Oligonucleotide Loading on Gold Nanoparticles. *ACS Nano* **2009**, *3* (2), 418–424. https://doi.org/10.1021/nn800726e.

(109) Kick, A.; Bönsch, M.; Kummer, K.; Vyalikh, D. V.; Molodtsov, S. L.; Mertig, M. Controlling Structural Properties of Self-Assembled Oligonucleotide–Mercaptohexanol Monolayers. *J. Electron Spectrosc. Relat. Phenom.* **2009**, *172* (1–3), 36–41. https://doi.org/10.1016/j.elspec.2009.04.002.

(110) Gong, P.; Lee, C.-Y.; Gamble, L. J.; Castner, D. G.; Grainger, D. W. Hybridization Behavior of Mixed DNA/Alkylthiol Monolayers on Gold: Characterization by Surface Plasmon Resonance and 32P Radiometric Assay. *Anal. Chem.* **2006**, *78* (10), 3326–3334. https://doi.org/10.1021/ac052138b.

(111) Wong, I. Y.; Melosh, N. A. An Electrostatic Model for DNA Surface Hybridization. *Biophys. J.* **2010**, *98* (12), 2954–2963. https://doi.org/10.1016/j.bpj.2010.03.017.

(112) Yonzon, C.; Stuart, D.; Zhang, X.; Mcfarland, A.; Haynes, C.; Vanduyne, R. Towards Advanced Chemical and Biological Nanosensors—An Overview. *Talanta* **2005**, *67* (3), 438–448. https://doi.org/10.1016/j.talanta.2005.06.039.

(113) Mayer, K. M.; Hafner, J. H. Localized Surface Plasmon Resonance Sensors. *Chem. Rev.* **2011**, *111* (6), 3828–3857. https://doi.org/10.1021/cr100313v.

(114) Mock, J. J.; Barbic, M.; Smith, D. R.; Schultz, D. A.; Schultz, S. Shape Effects in Plasmon Resonance of Individual Colloidal Silver Nanoparticles. *J. Chem. Phys.* **2002**, *116* (15), 6755–6759. https://doi.org/10.1063/1.1462610.

(115) Anker, J. N.; Hall, W. P.; Lyandres, O.; Shah, N. C.; Zhao, J.; Van Duyne, R. P. Biosensing with Plasmonic Nanosensors. *Nat. Mater.* **2008**, *7* (6), 442–453. https://doi.org/10.1038/nmat2162.

(116) Becker, J.; Trügler, A.; Jakab, A.; Hohenester, U.; Sönnichsen, C. The Optimal Aspect Ratio of Gold Nanorods for Plasmonic Bio-Sensing. *Plasmonics* **2010**, *5* (2), 161–167. https://doi.org/10.1007/s11468-010-9130-2.

(117) Jain, P. K.; El-Sayed, M. A. Surface Plasmon Resonance Sensitivity of Metal Nanostructures: Physical Basis and Universal Scaling in Metal Nanoshells. *J. Phys. Chem. C* **2007**, *111* (47), 17451–17454. https://doi.org/10.1021/jp0773177.

(118) Hegde, H. R.; Chidangil, S.; Sinha, R. K. Refractive Index Sensitivity of Au Nanostructures in Solution and on the Substrate. *J. Mater. Sci. Mater. Electron.* **2021**. https://doi.org/10.1007/s10854-021-07593-9.

(119) Cao, J.; Sun, T.; Grattan, K. T. V. Gold Nanorod-Based Localized Surface Plasmon Resonance Biosensors: A Review. *Sens. Actuators B Chem.* **2014**, *195*, 332–351. https://doi.org/10.1016/j.snb.2014.01.056.

(120) Elhadj, S.; Singh, G.; Saraf, R. F. Optical Properties of an Immobilized DNA Monolayer from 255 to 700 Nm. *Langmuir ACS J. Surf. Colloids* **2004**, *20* (13), 5539–5543.

(121) Ostblom, M.; Liedberg, B.; Demers, L. M.; Mirkin, C. A. On the Structure and Desorption Dynamics of DNA Bases Adsorbed on Gold: A Temperature-Programmed Study. *J. Phys. Chem. B* **2005**, *109* (31), 15150–15160. https://doi.org/10.1021/jp051617b.

(122) Wolf, L. K.; Gao, Y.; Georgiadis, R. M. Sequence-Dependent DNA Immobilization: Specific versus Nonspecific Contributions. *Langmuir ACS J. Surf. Colloids* **2004**, *20* (8), 3357–3361.

(123) Jackman, J. A.; Rahim Ferhan, A.; Cho, N.-J. Nanoplasmonic Sensors for Biointerfacial Science. *Chem. Soc. Rev.* **2017**, *46* (12), 3615–3660. https://doi.org/10.1039/C6CS00494F.

(124) Kimura-Suda, H.; Petrovykh, D. Y.; Tarlov, M. J.; Whitman, L. J. Base-Dependent Competitive Adsorption of Single-Stranded DNA on Gold. *J. Am. Chem. Soc.* **2003**, *125* (30), 9014–9015. https://doi.org/10.1021/ja035756n.

(125) Chen, C.; Wang, W.; Ge, J.; Zhao, X. S. Kinetics and Thermodynamics of DNA Hybridization on Gold Nanoparticles. *Nucleic Acids Res.* **2009**, *37* (11), 3756–3765. https://doi.org/10.1093/nar/gkp230.

(126) Ge, C.; Liao, J.; Yu, W.; Gu, N. Electric Potential Control of DNA Immobilization on Gold Electrode. *Biosens. Bioelectron.* **2003**, *18* (1), 53–58. https://doi.org/10.1016/S0956-5663(02)00115-X.

(127) Aćimović, S. S.; Ortega, M. A.; Sanz, V.; Berthelot, J.; Garcia-Cordero, J. L.; Renger, J.; Maerkl, S. J.; Kreuzer, M. P.; Quidant, R. LSPR Chip for Parallel, Rapid, and Sensitive Detection of Cancer Markers in Serum. *Nano Lett.* **2014**, *14* (5), 2636–2641. https://doi.org/10.1021/nl500574n.

(128) Chen, P.; Chung, M. T.; McHugh, W.; Nidetz, R.; Li, Y.; Fu, J.; Cornell, T. T.; Shanley, T. P.; Kurabayashi, K. Multiplex Serum Cytokine Immunoassay Using Nanoplasmonic Biosensor Microarrays. *ACS Nano* **2015**, *9* (4), 4173–4181. https://doi.org/10.1021/acsnano.5b00396.

(129) Gomez-Cruz, J.; Nair, S.; Manjarrez-Hernandez, A.; Gavilanes-Parra, S.; Ascanio, G.; Escobedo, C. Cost-Effective Flow-through Nanohole Array-Based Biosensing Platform for the Label-Free Detection of Uropathogenic E. Coli in Real Time. *Biosens. Bioelectron.* **2018**, *106*, 105–110. https://doi.org/10.1016/j.bios.2018.01.055.

(130) Casquillas, G. V.; Houssin, T. Microfluidics and Microfluidic Devices : A Review. *Elveflow* **2019**.

(131) Samiei, E.; Tabrizian, M.; Hoorfar, M. A Review of Digital Microfluidics as Portable Platforms for Lab-on a-Chip Applications. *Lab. Chip* **2016**, *16* (13), 2376–2396. https://doi.org/10.1039/C6LC00387G.

(132) Yew, M.; Ren, Y.; Koh, K. S.; Sun, C.; Snape, C. A Review of State-of-the-Art Microfluidic Technologies for Environmental Applications: Detection and Remediation. *Glob. Chall.* **2019**, *3* (1), 1800060. https://doi.org/10.1002/gch2.201800060.

(133) Soler, M.; Lechuga, L. M. Biochemistry Strategies for Label-Free Optical Sensor Biofunctionalization: Advances towards Real Applicability. *Anal. Bioanal. Chem.* **2021**. https://doi.org/10.1007/s00216-021-03751-4.

5 Label-free detection of salivary cortisol with SiNW FET arrays on a portable platform

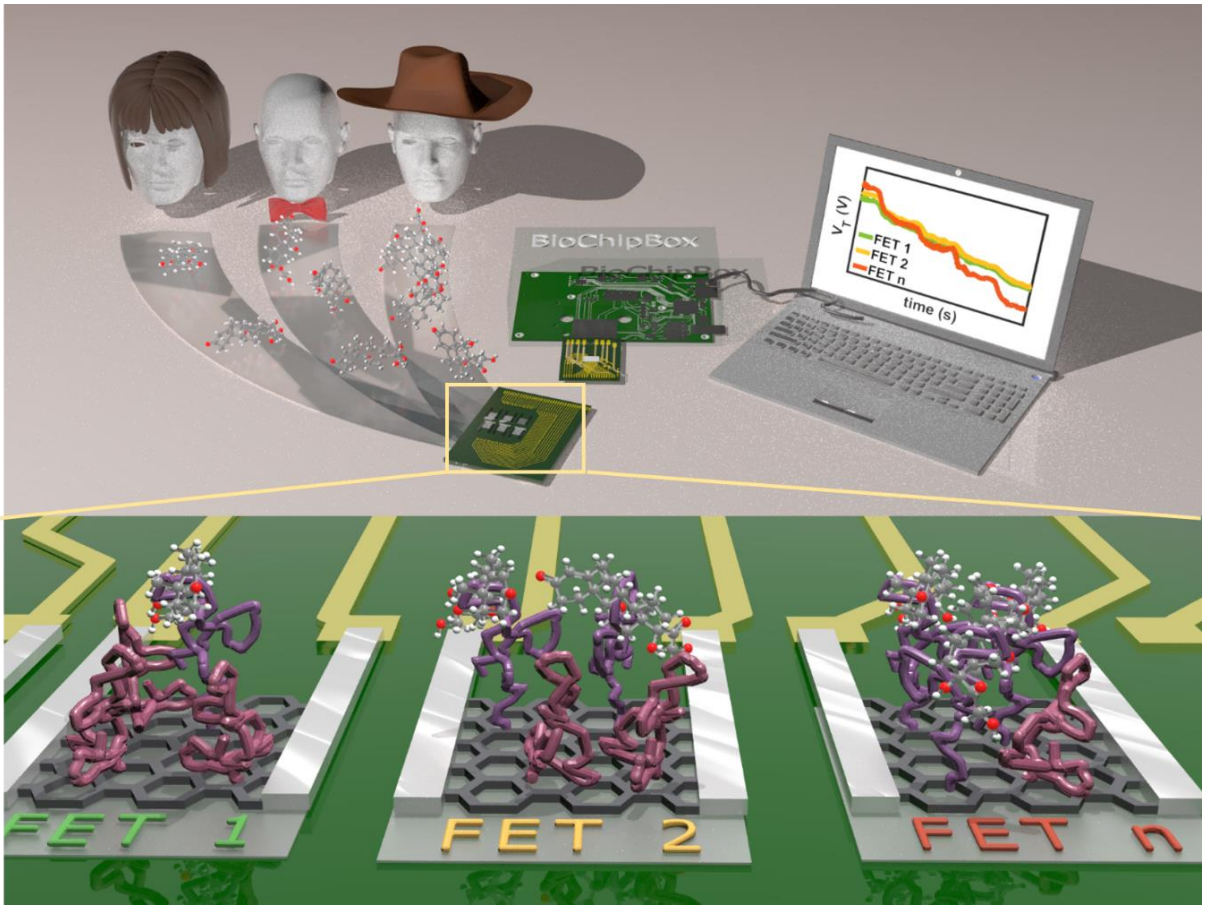

The following chapter presents the route for successful label-free detection of the stress hormone cortisol in human saliva with a portable platform based on an array of silicon nanowire-field effect transistors (SiNW FETs). As proof-of-principle, the cortisol levels from multiple donors were assessed in real-time measurements.

First, the structure and integration of the top-down-manufactured SiNW FETs into a portable system capable of monitoring multiple individual FETs are summarized and followed by a characterization of the electrical properties of the devices with a focus on data acquisition. The working system is validated by simultaneously monitoring the pH of surrounding solutions with multiple FETs.

Next, the focus is on optimizing the bio interface to detect the selected analyte cortisol with silicon nanowires. The array of SiNW FETs was functionalized by a specific DNA aptamer sequence that not only allows for detecting the target-receptor-complex in close vicinity to the sensor surface but also achieves a reliable, sensitive, and selective sensing performance. Upon binding, cortisol induces a conformational change of

negatively charged aptamers, which in turn influence the nanowire's surface potential, allowing for sensitive detection- even under high-ionic strength conditions within the Debye-length of the FETs. The underlying principles of the binding reaction of cortisol to its aptamer were further explored by circular dichroism, colorimetric assay, and fluorescence microscopy.

Ultimately, those findings were related to measured signals of the SiNW FET array and formed the basis for the analysis of (unknown) cortisol levels in the volunteers' saliva. Noteworthy, the cortisol concentrations detected with the SiNW FET platform correlate well with results obtained with commercial immunoassays.

The label-free detection of salivary cortisol levels with SiNW FETs, a portable platform, is summarized in [1] with S. Klinghammer as first author.

5.1 Introduction

Point-of-care sensors are of tremendous interest nowadays as they are utilized for monitoring and supporting diagnostics of various healthcare conditions in a convenient, easy-to-use, and low-cost format. Appreciable POC devices range from well-known pregnancy, CRP, and Covid-19 rapid tests, which "simply" confirm the presence of an analyte, over to glucose and lactate-monitoring devices, which can quantify the analyte of interest. In addition, measuring biomarkers in biofluids can provide information about a person's physical and, depending on the marker, psychological status. Getting insight into this personal information can be used to control medical treatments or implement healthier lifestyle routines.

Stress is one of the most demanding problems facing modern society for keeping a balanced daily lifestyle. From personal circumstances, unemployment, work-related stress, family issues, or disadvantageous work-life balance[2–4] up to more general parameters such as an ongoing global demographic shift with constant competition, fast-moving lifestyles caused a tremendous increase of physiological stress over the last years[4,5]. In addition, current crises such as the COVID-19 pandemic function as an additional stressor, which carries the extra potential for mental health crises of unprecedented dimensions[6–9]. Albeit the Covid-19 pandemic and its consequences affect people worldwide and across all sections of society, the growing stress levels of certain professional groups, e.g., doctors and nursing auxiliary, police officers, and firefighters, can become particularly critical as their performance directly affects the lives of others.

Enhanced stress levels are hallmarked by irritability, constant fatigue, lack of interest, brain pain, and heart attacks[10–13], and misbalanced stress levels, either acute or chronic, can lead to severe diseases such as metabolite disorders /diabetes, obesity, cardiovascular diseases, and psychopathologic disorders (anxiety, depression, Alzheimer, etc.)[10,14–17]. Henceforth, there is a growing demand for methods to monitor and manage stress levels, preferably in real-time and directly at the patient's site. But also, multiple diagnostics protocols have been proposed until now. Usually, stress is diagnosed with psychotherapeutic approaches such as interviewing and counseling, questionnaires, or neurological approaches like electroencephalography (EEGs) and electrocardiogram (ECGs), respectively[18–22]. However, both approaches can bias and are subjective and qualitative in their nature, so a reliable protocol for testing stress response

was provided by establishing the Trier Social Stress Task[23]. As stress correlates with human metabolism, another class of stress measuring devices relies on monitoring unspecific enhanced metabolic parameters such as skin conductance, heart rate, temperature, or breathing rates. The sensors can be incorporated into functional equipment such as wearables, mobile applications, smart watches, or straps/bands[24–26] but are mainly designed for private applications.

A well-founded medical evaluation of stress remains indispensable. A key parameter in medical stress diagnostics describes the steroid hormone cortisol. The biomarker controls metabolic activity such as homeostasis of cardiovascular, immune, renal and endocrine systems as cortisol regulates blood pressure, glucose levels, and carbohydrate cycles[27–29]. The biomarker cortisol can be found in several body fluids such as saliva, urine, sweat, tears, serum, and blood[30,31]. Among those, detecting cortisol in retrievable fluids such as saliva or sweat offers advantages in terms of collection, handling, and potential storage by the patient as their collection methods are non-invasive. Due to its simple *in-situ* availability, saliva is a widely studied fluid for measuring cortisol levels accurately and thus forms the most common source for diagnostics applications[32–36]. The highest salivary cortisol concentrations level is between 0.1 µg/dl and 1 µg/dl during morning hours and reduces gradually during the day until the lowest concentration occurs during night times[37].

Cortisol levels are currently quantified with enzyme-linked immunosorbent assays (ELISA), chromatography, quartz-crystal microbalance (QCM), and surface plasmon resonance (SPR)[38–41]. However, most methods are time-consuming and require complex laboratory equipment and sample delivery to medical facilities, so cortisol levels are temporally delayed and potentially prohibit immediate treatment. Likewise, the abovementioned methods preclude a real-time analysis of the stress marker. Current research confronted this issue aiming to deliver the point-of-care (POC) solution for cortisol and presents suitable platforms based on electrochemical sensors[42–46], electronic sensors [47–50], lateral flow-based immunoassays[51–55], or optical sensors[56,57]. Noteworthy, the platforms mentioned above vary within their substrates from rigid devices over flexible substrates for wearable devices to paper-based substrates. Hogenelst et al.[58] recently reviewed the current promises and challenges in ambulatory cortisol detection. Most studies involve the use of metallic disks and metal or glassy carbon electrodes,

whose self-oxidation and internal resistance can negatively influence the activity of the sensors[58].

Consequently, there is a growing demand for the development of reliable sensor platforms that monitor stress intensities accurately while being integrated into portable, easy-to-use, but cost-effective read-out systems. These marginal conditions claim that proposed sensor systems must be highly versatile as they find application as an analytical instrument that gives a quick response but perceives high sensitivity. In addition, the device should be drafted for using a single operator or a group, either at home, at work, or in a laboratory environment.

Nanoscopic field-effect transistors (FETs) based on silicon nanowires provide significant advantages for biosensing applications as they combine low detection limits, real-time and label-free detection, and simple integration with standard semiconductor-device processing[59]. Target-specific receptors are immobilized at the surfaces of semiconducting nanowires, which act as charge carriers' channels. Interactions with the biomolecules lead to a bio- or chemical gating of those channels. And the associating modulation of device conductance is a direct consequence of the potential surface shift at the nanowire[60]. As the binding effects occur directly at the surface, nanoscaled FETs are particularly promising biosensors due to their enhanced sensitivity to the device[60–62]. Concisely, nanoscaled FETs can reliably detect various biomolecules ranging from small molecules, e.g., dopamine or serotonine[63–65], over proteins[66,67], DNA[68,69], viruses[70,71], up to whole cells[72,73]. Besides biomolecules, their environment matrix and (bio-) chemical reactions can also be monitored in time, too[74–76].

The selection of suitable receptors plays a unique role in biosensing with FETs. Aptamers, DNA strands that bind specifically to an analyte, can detect biomolecules in minimally or even undiluted biofluids[65,77–80]. Aptamers undergo a target–induced rearrangement of their highly negatively charged backbones upon binding - a remarkable feature that produces surface charge perturbations and, consequently, measurable electronic signals. The process relies on specific interactions within the aptamer-target complex. Hence, it is independent of the chemical reactivity or intrinsic charge of the target molecules[65], facilitating the detection of feebly or uncharged molecules in biofluids with electronic biosensors.

Although successful, there are several remaining challenges to applying FETs for detecting analytes in complex media or even in-vivo. For example, nonspecific adsorption

of proteins, lipids, and cells will limit the specific binding of analytes[81]. Therefore, sensors have to operate selectively, sensitively, and in appropriate dynamic ranges in complex environment[82,83], and preparation steps such as washing, separation, and regeneration have to be included, too.

Here we present a portable sensing platform based on the multiplexed array of SiNW FET aptasensors for monitoring the cortisol levels of multiple volunteers. Aptamers are used as short receptors that undergo a conformational change upon binding to cortisol, approximating the biorecognition event to the nanowire surface into the Debye screening length. The compact device enables real-time analyte detection from the sensor array and is applicable as a point-of-care device. We can quantify the concentration of the stress hormone cortisol in human saliva in real-time. Comparing the nanosensor measured cortisol levels and daily trends to those determined with the commercial immunoassays agrees with most of the tested samples. The modular design of the system provides the possibility for tailoring customized applications. In addition, the synchronized readout of multiple sensors grants simultaneous detection of numerous analytes.

5.2 Design, integration, and performance of SiNW FETs into a portable platform

5.2.1 Structure and electrical characteristics of honeycomb SiNW FETs

In this study, sensor chips with arrays of Field effect transistors with silicon nanowires (SiNW FET) in a honeycomb design were fabricated via top-town technology by collaborators from POSTECH, as presented previously[84]. Figure 5-1A displays the schematic design of a sensor chip with 16 individual FETs connected by comparably long electrodes to facilitate the proper implementation of microfluidic channel systems, respectively. Figure 5-1B enlarges the actual sensing area of the FET consisting of honeycomb-structured silicon nanowires (compared to SEM- inset in Figure 5-1B) that are connected by source(S) and drain(D) electrodes and encircled by a reference electrode (RE). A photograph of the complete chip, emphasizing its size with the help of a 5ct coin, is presented in Figure 5-1C.

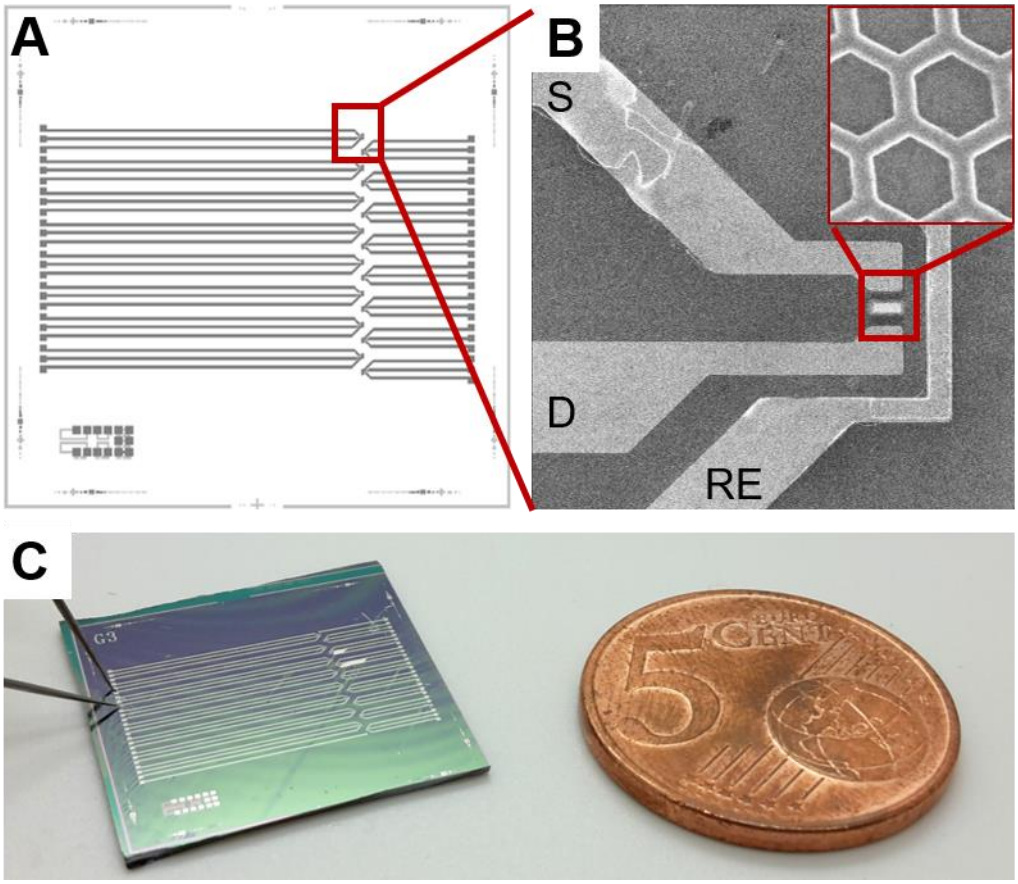

Figure 5-1: Overview screen of SiNW FETs: A) Schematic design of biosensor chips containing 16 individual SiNW FETs, whose long electrodes allow for easy contacting and implementation of microfluidic channels. B) SEM image of one individual SiNW FET. Source(S) and drain (D) electrodes connect FET, and the reference electrode (RE) can be used as an additional gate. The insets emphasize the honeycomb structure of nanowires. C) Real image of manufactured SiNW biosensor chip with 5ct coin for estimation of the size of devices.

The manufactured FETs allow for devices with high reproducibility and low variations between each other. Here, nanostructures of p-doped silicon in a honeycomb structure with 50 nm in diameter and a total sensing area of ~365 µm² were processed (compared to SEM- inset in Figure 5-1B). An additional layer of a photoresist SU8 protects the electrodes during measurements while NW areas remain open.

The honeycomb structure of the nanowire array allows for a remarkable but stable electrical performance, which is hallmarked by little device-to-device variations, a low signal-to-noise ratio, and negligible drain current shifts- while being mechanically robust upon the desired application. The tremendous electrical performance of the devices is summarized in Figure 5-2, employing the transfer and output characteristics of individual FETs. For transfer characteristics (compared to Figure 5-2A), a fixed source-drain voltage (V_{SD}) of 0.1 V was applied while gate voltage V_G was swept. It is noteworthy that transfer characteristics have been recorded under ambient conditions as well as under aqueous conditions. Concomitantly, in Figure 5-2A, the horizontal axis was scaled individually to display each characteristic correctly. Under ambient conditions, presented in Figure 5-2A as a black curve, FETs show less distinct transfer characteristics, so that gate voltage operating between 0 V and 20 V was required to achieve appropriate characteristics, a subthreshold slope of ~4.1 V/dec. In contrast, the red line in Figure 5-2A emphasizes that under aqueous conditions, only V_G values between -2 V to +2 V were required to achieve comparable characteristics with a subthreshold slope of 167 mV/dec. The different behavior is based on a different gate coupling efficiency, which is increased in liquid conditions[85,86].

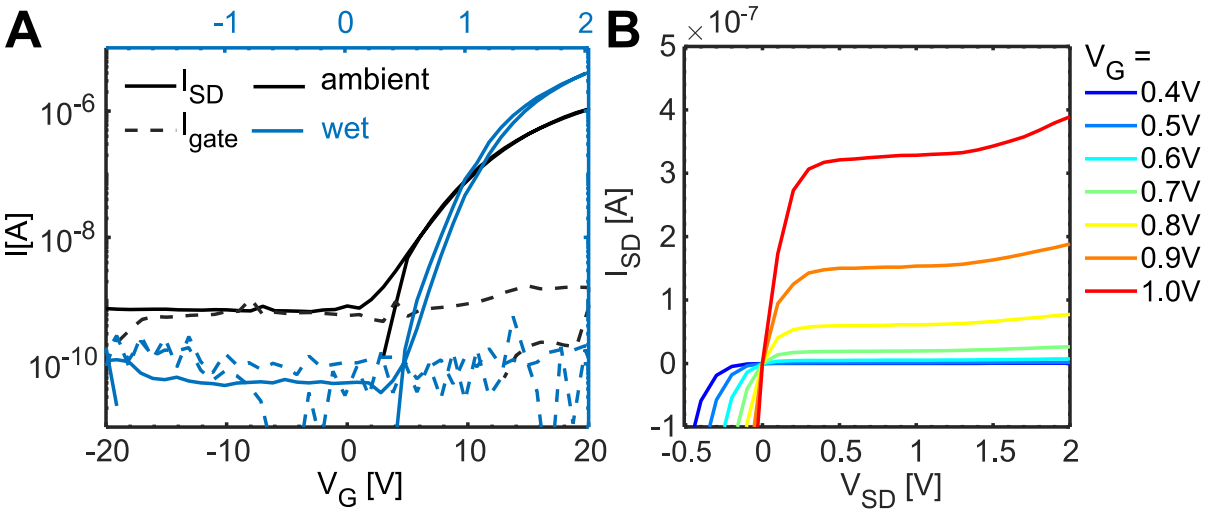

Figure 5-2: Electrical characterization of native SiNW FETs. A) Transfer characteristics of SiNW FETs with V_{SD} 0.1 V under ambient (black line) and liquid (blue line) surroundings. B) Output characteristics of SINW FET.

In contrast, to obtain output characteristics (OC) of the devices, V_{SD} is swept between the adjusted ranges while constant V_G is biased. Summarized in Figure 5-2B, FETs exhibit a typical output characteristic with clear and distinguishable transition, which is beneficial for integrated circuit applications. Equally, Figure 5-2 demonstrates the n-type behavior of FETs with an on/off ratio of $\sim 10^5$ and a fast transition between the two states. In addition, minimal gate leakages corroborate the excellent performance of the device throughout operation (compared to dotted lines in Figure 5-2A).

5.2.2 Integration of SiNW FET into a portable measuring unit

Honeycomb-structured SiNW FETs were integrated into a portable measuring device to allow real-time point-of-care (POC) measurements. The Institute of Electronic Packaging Technology at TU Dresden developed the sensing platform and provided it for use by courtesy. A detailed description of the whole platform is given in [1,87,88].

Three individual units, to be precise, a measuring unit, a multiplexing adapter (MUX- unit), and a biochip adapter, are combined to realize the simultaneous real-time operation of multiple FETs. As delineated in Figure 5 3A below, the measuring unit contains the electrical building parts that are required to power, control, as well as to record all electrical information. Here, suitable software controls the individual FETs within the platform via USB connections. Next, to enable the simultaneous read-out of multiple FETs, the platform incorporates a CMOS-integrated analog multiplexer (MUX) located on an adapter with SD card format contacts. The multiplexing adaptor is further connected to the biochip unit that contains the actual FET chip. As shown in Figure 5-3B, the FET chips are fixated on a PCB, which builds the interface for plug-in connections to the sensing platform. Wire bonds between FETs and the PCB support (compare to Figure 5-3C) permit individual electrical contacts. Finally, a reusable microfluidic channel system, whose fluids are driven by a syringe pump, can be used optionally for sample delivery and completes the platform.

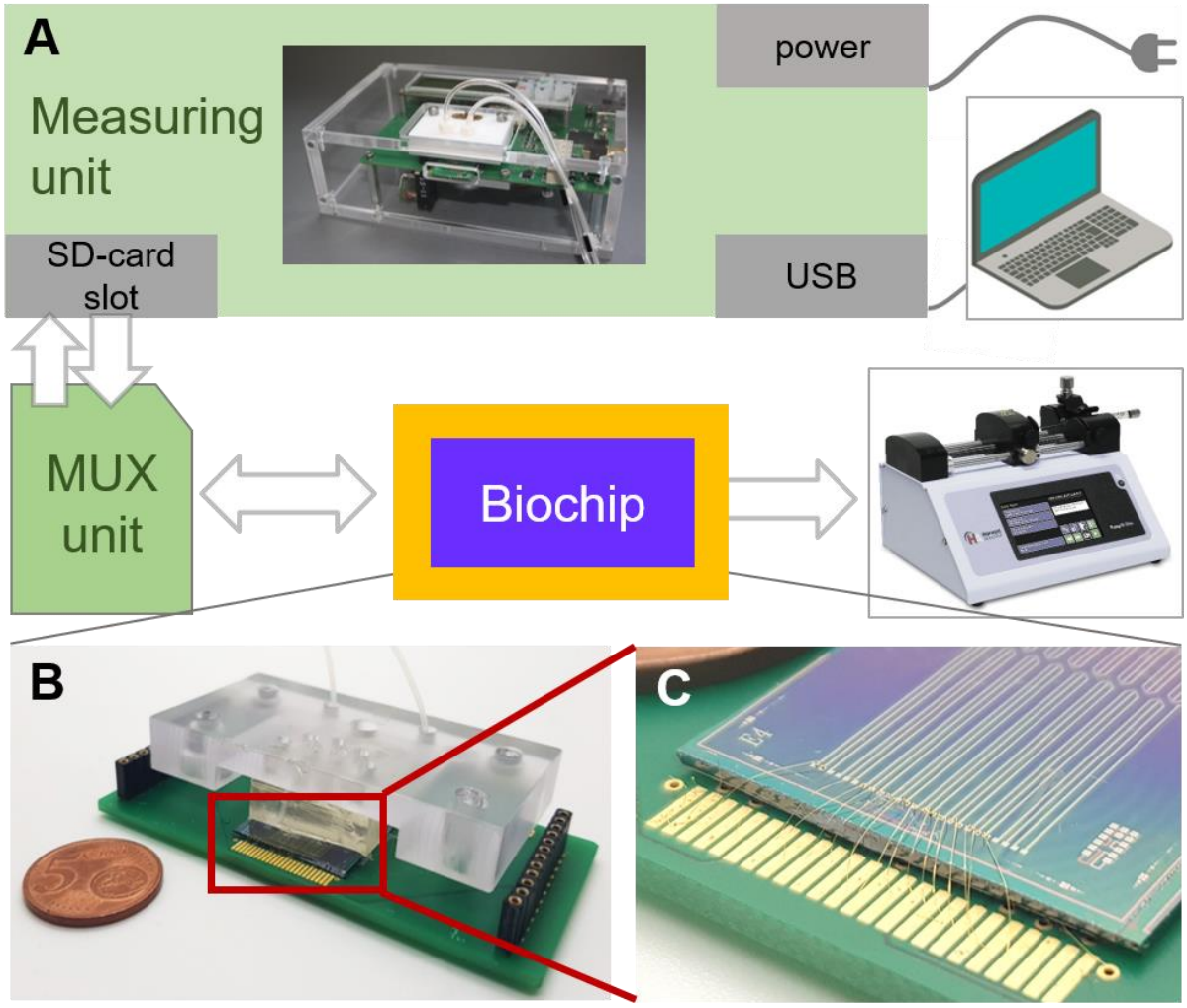

Figure 5-3: Overview of the portable biosensing platform. A) Composition of the structural units. First, the measuring unit comprises electrical hardware, a power supply, and the USB interface for connection to PC. Second, the MUX unit holds a CMOS multiplexer to facilitate simultaneous measurements of multiple FETs. The third is a biochip that consists of actual SiNW FETs. The biochip unit can be optionally combined with microfluidic channels for analyte delivery. B) Image of biochip unit supports SiNW FET sensor chips and holds microfluidic channel blocks. C) Individual electrodes of FETs are connected to its PCB support via microwires.

Figure 5-4 demonstrates the working platform by recording the transfer characteristics of six individual FETs. Further to Figure 5-1A, the layout would allow for the connection of eight FETs, but not all devices work. Please note that the performance of individual FETs differs slightly, such as FET No. 6 (dotted lines in Figure 5-4) exhibits less pronounced transfer characteristics.

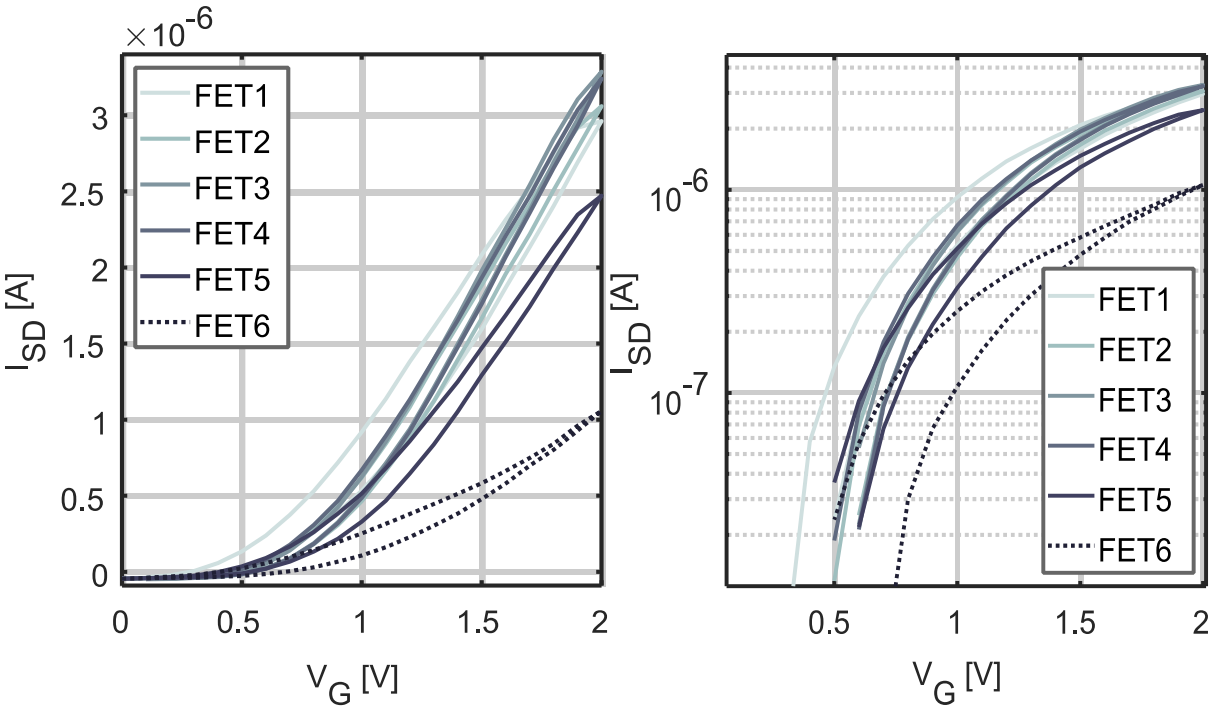

Figure 5-4: Transfer characteristics of six individual SiNW FETs recorded with the portable platform. Acquired transfer characteristics are presented in linear (left) or semi-logarithmic (right) scale to ascertain the subthreshold region of the devices.

In summary, the sensing platform is characterized not only by its portability but also by the possibility of simultaneous sensing of multiple FETs. Furthermore, the construction of the platform employing locally separated building panels allows for highly versatile and adaptable application fields.

5.2.3 Performance of SiNW FET arrays

5.2.3.1 General considerations for sensing with FETs

FETs' transfer- and output characteristics are highly dependent on the environmental conditions (compared to section 2.4.). When a potential is applied, any modification of the surrounding physical conditions will directly impact the surface potential of Si channels as carrier concentration within the channels will change due to accumulation, depletion, or inversion[89]. Here, a modification of the surrounding conditions either originates from the adsorption of ions and biomolecules, from a direct change of the present PH values, or from chemical reactions that undergo a PH change indirectly – all affecting the silicon channel conductivity and hence being a measurable fact that forms the basis for sensing with FETs[59,90,91]. The mechanisms at the SiNW–electrolyte interface come into play when an analyte binds to an immobilized receptor and is enhanced through the resulting charge transfers – causing a concentration-

dependent shift of the current-voltage characteristics. Regardless of the origin of signal changes, FETs are usually suspected of operating most sensitively in the subthreshold (or weak-inversion) regime, which is defined as the region in which gate voltages are below the threshold voltage[92]. Within this regime, surface charges can affect the entire nanowire radius as there is a low carrier concentration, so the screening length is relatively long compared to the radius[93,94]. Consequently, measuring in the subthreshold regime of the FETs is favored for sensing applications.

As an indirect measure for the surface potential (and hence the actual FET signal), the so-called threshold voltage V_T is chosen. Different methods to extract V_T from transfer or IV- characteristics are reported in literature[95,96]. In this study, the intersection of a FET's transfer characteristic at an arbitrarily chosen threshold current, a current chosen within the subthreshold regime, defines threshold voltage V_T. For all FET sensing experiments performed in this research, the threshold voltage is monitored, and signal changes are expressed as changes in V_T.

During all measurements, FET devices operated in a constant sweeping setup, in which V_G strobes continuously between two values. The associating currents I_{SD} were recorded and thus allowed for a complete record of complete IV- characteristics of all FET at any time, facilitating a later extraction of V_T from collected curves. Typically, sensing of FETs is performed by measuring the current at a fixed voltage, as this offers the advantage of receiving resistivity of the device at high measurement rates and thus allows proper resolution at fast signal changes. However, the knowledge of the whole transfer characteristics of each device is beneficial as fluctuations of it serve as the information base for the sensor signal. Consequently, it is crucial to warrant that transfer characteristics of FETs do not change their shape significantly upon detection to prevent a possible misreading of signals[97]. Here, the fast alteration of physical properties, such as phase or ion constitution, can induce significant changes in offset currents[74]. Therefore, measuring as much information as possible on FET characteristics during an experiment is essential[97].

FET devices connected to the portable platform function in a dual-gate mode: the gate voltage V_G is set not only via the back gate but also by an additional liquid gate, whose potential is adjusted with the help of a commercial Ag/AgCl reference electrode. The dual-gate method enhances, on the one hand, the sensitivity of the FETs and offers advantages regarding electromagnetic susceptibility[98–101]. However, please note that gate voltages

ranging from -2 V to 2 V can be applied on the portable platform. As a result, IV-characteristics under ambient conditions typically have been recorded with an external setup described by[97]. However, as foreshadowed in Figure 5-1B, the devices contain a third electrode that can be used as an additional (top) gate to switch the FETs, depending on the desired application.

5.2.3.2 Effects of the electric double layer on the sensing performance of FETs

The basis for sensing with FETs relies on the fact that almost any modification of the surrounding physical conditions will directly impact the surface potential of Si channels. Among those conditions, the composition of the electric double layer (EDL) is one of the key factors that must be considered for biosensing with FETs. The EDL instantly builds up on every surface when exposed to liquids, and its thickness is closely linked to the screening length of the FETs, as ions within the layer shield charge carriers - so that FETs can only detect reliable events happening within the electric double layer. This limitation is widely known and characterized by the so-called "Debye length limitation," where the Debye length is defined as the distance a FET can sense within an electric double layer[102–104]. Based on the Gouy- Chapman-Stern theory, the double-layer width λ_D is given with

$$\lambda_D = \sqrt{\frac{\varepsilon \cdot \varepsilon_0 \cdot k_B \cdot T}{e^2 \cdot c_0}} \qquad (5.1)$$

where ε, ε_0, k_B, and T, refers to relative permittivity in the vacuum, Boltzmann's constant, and temperature, respectively. The elementary charge of the ions is expressed by e, and the concentration of a bulk solution by c_0. Following Eq. 5.1, the Debye-length depends on the media's ionic strength (IS): the lower the IS, the larger the Debye-length. For biodetection, the short Debye-length of physiological media can impair the sensitivity of the FET as the majority of biomolecules (i.e., proteins, antibodies, etc.) are larger in their dimensions than λ_D and a significant (charged) fraction of the molecule is left outside the EDL. In addition, large receptors may have their active binding site outside the EDL, so the FET can't detect the actual binging event. Consequently, for a successful biorecognition, receptor-target- complexes are commonly expected to be placed in close vicinity to the channel surfaces and to have general dimensions that are similar to or smaller than the Debye-length of the surrounding media.

To still detect successful bioreactions with FETs, several attempts have been postulated to overcome the Debye-length-limitation[105–107]. One somewhat simple but common approach is the enhancement of the Debye- length by lowering the ionic strength of the media via dilution[102,108]. Based on equation (5.1), one can calculate that under physiological conditions for 1xPBS λ_D is about 0.7 nm and thus often smaller than the size of possible receptors and receptor-target-complexes. By lowering the electrolyte concentration 10 times fold to 0.1x PBS and further to 0.01x PBS, the Debye lengths add up to 2.4 nm and 7.4 nm, respectively. Depending on the class of receptors and targets, this still cannot be big enough for adequate sensing performance. So usually, proteins (and thus antibodies) range from 3 nm and 15 nm[109], whereas most viruses possess a size between 20 nm and 200 nm, although some viruses can exceed 1000 nm in length[110]. Auxiliary to the consideration of size impairments, the dilution of buffer systems can be challenging for bioreactions. Molecule structures, their activity, and target-receptor affinities may be compromised under low salt conditions, so binding kinetics are unfavorably lowered[111–113]. Accordingly, the buffer and its Debye-length must be carefully matched to the size and binding distance of the target but also to the bioaffinity of the reaction assay[114–116]. Consequently, developing a sensor system is favored, which can detect the analyte of interest under physiological settings rather than encroaching on optimal reaction conditions by diluting the buffer.

Another method to overcome Debye-length-limitation is using alternating currents (AC) instead of direct currents (DC) of drain-source voltage as a collapse of the electric double layer close to the surface leads to better performance. Fast switching of the bias is expected to lead to deeper penetration of the field; target molecules with sizes exceeding the Debye length can be detected[117–120]. Furthermore, engineering the surface is an appropriate approach to enable biodetection in high ionic strength conditions. Further promising attempts rely on surface engineering methods such as providing porous surfaces[121,122] since the value of λ_D increases in concave regions of the channel or attaching additional layers close to the FET surface so that the effective Debye-length is enhanced. Among them, biomolecule permeable polymers such as PEG layers[123–125], polyelectrolyte layers[126–128], or hydrogels[129,130] are promising candidates for achieving the detection of biomolecules in physiological conditions.

Shrinking the size of receptors, i.e., using only fragments of antibodies, nanobodies, or aptamers, will reduce the distance of the bio reaction to the FETs surface so that that reaction might be present within the Debye length[131–133].

As previously described, the SiNW channels are prone to changes in charge carriers close to their surface. Consequently, detection paradigms that rely on rescheduling the detection reaction with another chemical reaction that alters its PH proportionally to the amount of bound target are another promising approach to prevent charge screening limitations as those events happen near the channel surface[65,74,134,135].

For any (bio) sensing experiment, the well-defined delivery of targets to the sensor surface has tremendous importance, as described in more detail in section 4.2.4. Continuous and sufficient delivery of target molecules to receptors via flow will reflect in reliable and fast reaction kinetics[136]. The fluidic regimes are directly linked to the composition and thickness of the EDL and thus - in contrast to optical sensors, indirectly influence the FET's surface potential. Consequently, the FET sensor signal depends on the flow rate at different ionic strengths. Figure 5-5 shows the vulnerability of the FET to flow rates in dependence on the ionic strength of the surrounding media in a relatively simple approach. Buffers with different ionic concentrations of 0 mM, 0.01 mM, and 0.1 mM were guided over FETs, while flow rates were adjusted by simply starting and stopping the connected pump. At minimal ionic strength (compared to the lightest blue part in Figure 5-5), periodic flow rates result in evenly periodically shaped signals of the FET as the arising EDL is relatively unstable. By enhancing the electrolytes ions concentration to

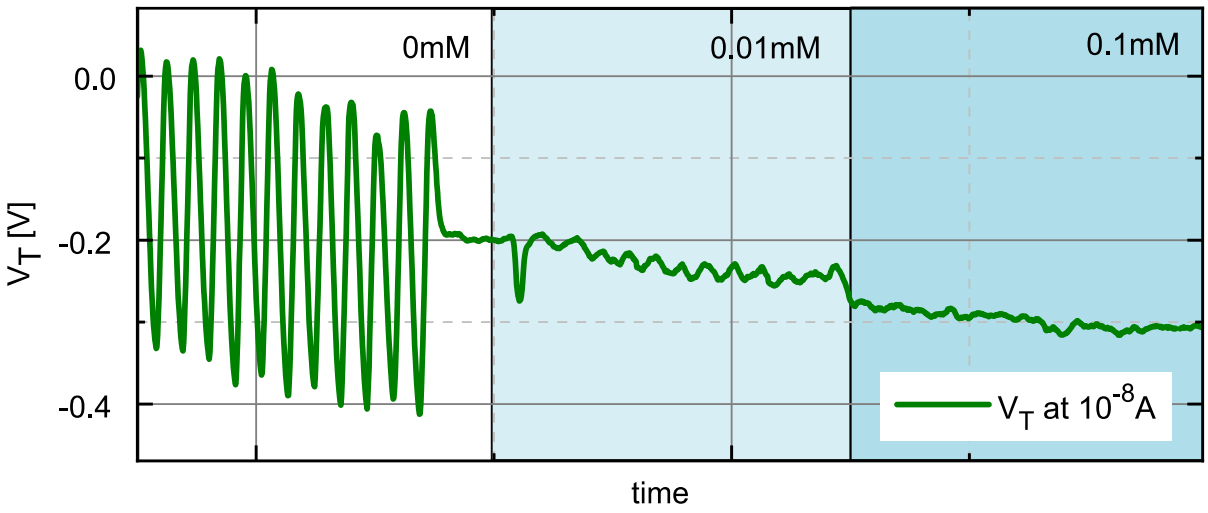

Figure 5-5: Dependence of FET signal upon flow rate at differently concentrated electrolytes. Aqueous solutions with ion concentrations of 0 mM (light blue background), 0.01 mM (intermediate light blue), and 0.1 mM (dark blue region) where guided over FETs with oscillating flow rates. If no ions are present, a rather weak EDL compromise is prone to fluctuations of surrounding fluidic regimes. The effect diminishes until, at 0.1 mM, a stable EDL occurs that is barely influenced by surrounding fluidics.

0.01 mM (compare middle part in Figure 5-5), those effects diminish until, at a physiological level of 0.1 mM (dark blue region in Figure 5-5), the influence of the flow rate becomes negligible. As stated above, a stable EDL arises at the interface of electrolytes and surfaces. Here, the size of EDL depends on the concentration of electrolyte ions and on the present fluidic regime, as faster flow rates will thin the EDL[137]. However, an enhancement of the flow rate will not only cause a movement of the ions inside the EDL but also induces the removal of the diffusive outer layer in the electric double layer. Both terms generate a shift of the surface potential and consequently alter the signal of the FET significantly[138].

The flow rate of the surrounding fluid will affect the electrical properties of FET and the bio-reaction itself. The previous section 4.2.4 has already shed light on underlying dependencies. Briefly, reaction kinetics can be limited by mass transfer, as an analyte in a solution must first diffuse from the bulk to the surface of the FET before it can interact with the immobilized receptor. As the diffusion rate should be faster than the association rate to prevent mass transport limitations, an enhancement of the flow rate is recommended. Unfavorably, increased flow rates go along with the removal of loosely bound target and nonspecifically bound molecules, which in turn will be detected by FET signal changes, too.

In summary, the fragility of SiNW FETs towards the composition of arising EDL through Debye-length applied fluidic regimes and hindered bio-recognition at low IS emphasizes the need for developing biosensing platforms capable of detecting reactions under physiological conditions once more. In addition, it is crucial to find appropriate regimes where the balance between target transport, a stable EDL, and biodetection with FETs is optimized – and to keep this regime as constant as possible.

5.2.3.3 Exemplified PH sensing with SiNW arrays on a portable platform

Measuring the pH of electrolytes with FETs poses a well-defined framework for a FET sensor's physical, chemical, and electrical characterization. Consequently, pH measurements were carried out not only to evaluate individual sensors' qualities but also to underline the suitability of the portable platform for real-time measurements of aqueous solutions simultaneously with multiple sensors. In addition, numerous chemical and biological reactions go along with a variation in pH and thus can form the basis for biodetection.

For evaluating the performance of pH changes, FET sensor chips were mounted into the biochip unit of the system and exposed to buffers with different pH values ranging from 5.8 up to 8.0 while flow rate and ionic strength were kept constant. The signal dependence of five working FETs upon pH change is summarized in Figure 5-6 below. In addition, the temporal course of all FETs upon pH changes is presented to corroborate the capability for real-time measurements.

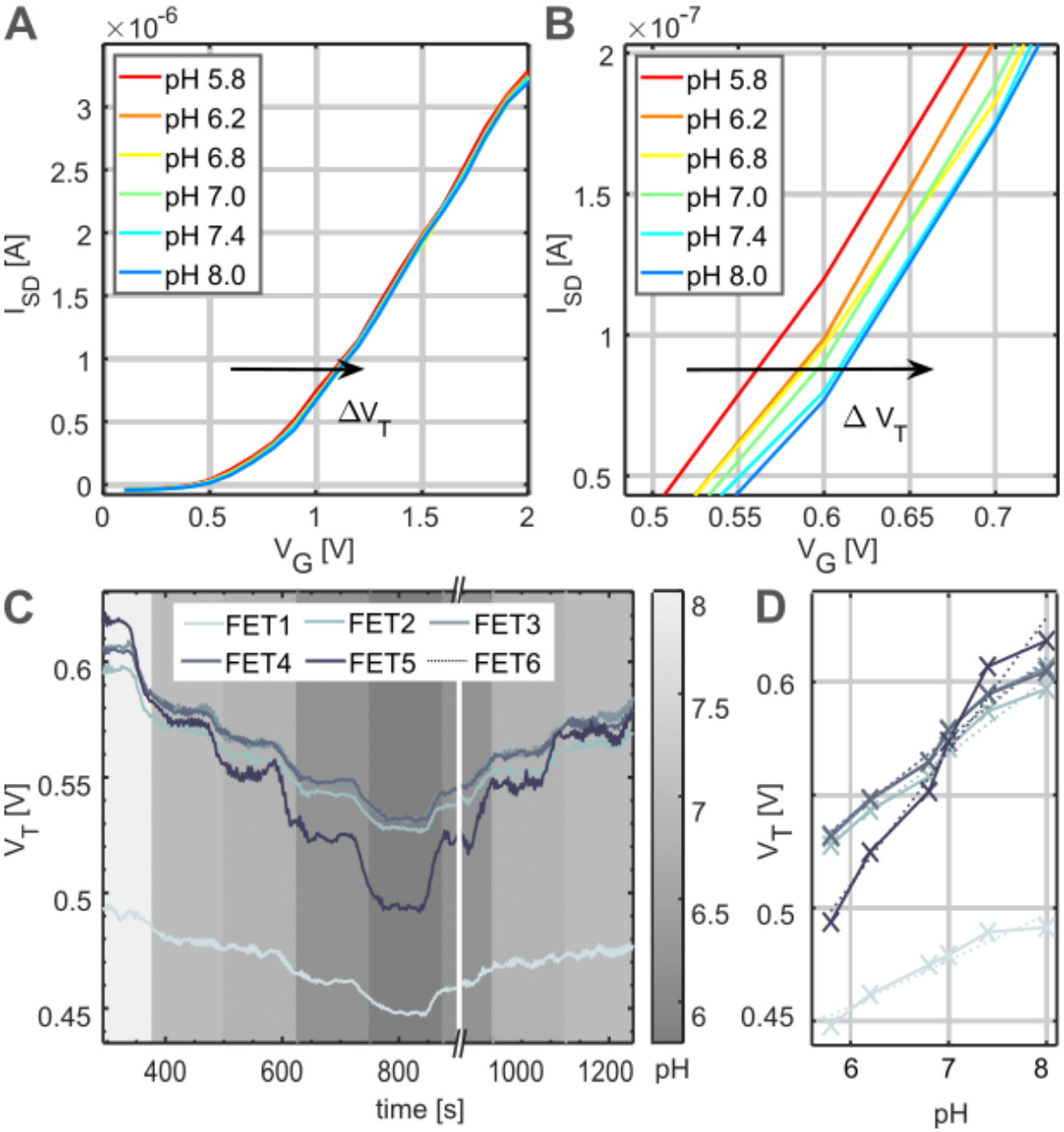

Figure 5-6: Sensing pH with SiNW arrays on a portable platform. A) Transfer characteristics of an individual SiNW FET upon pH change from 5.8 (red) up to 8.0 (blue). B) magnification of the subthreshold region of (A). With increasing pH, an increase of VT goes along. C) Real-time measurement monitoring V_T vs. time of six FETs upon pH change from high (light grey background) to low (dark grey) values and back. D) Extracted VT of each FET (same color scale as in C) based on pH to calculate pH sensitivity as a quality characteristic.

Figure 5-6A and B represent the transfer characteristics of a FET upon increasing pH from 5.8 to 8.0, where panel B is a magnification of the subthreshold region. Increasing pH values correspond to a shift of the IV- curves towards higher V_G values – tantamount to increasing values of the threshold voltage V_T as indicated by the arrow in Figure 5-6A/B. Increasing voltages are caused by the introduction of negative charges to the system, which suppresses electron conduction inside Si channels and thus lowers the source-drain current.

However, Figure 5-6C demonstrates the pH sensitivity of six FETs in real-time, simultaneously recorded with a portable platform. Here, the grey background refers to the different pH values, and the signal V_T for multiple FETs is plotted over time. Most FETs exhibit the same trend: falling pH values result in decreasing V_T values. Referring to Figure 5-4, the performance of individual FETs varies, such as the pH sensitivity of individual FETs differs, too. Figure 5-6D summarizes the pH sensitivity of six individual FETs; data has been extracted from Figure 5-6C and fitted linearly (compare solid line).

On average, pH sensitivities of about 38.0 ± 1.3 mV/pH can be achieved for pH sensing, while the on/off ratios are kept at 10^5. In literature, for SiO_2-covered ISFETs, pH-sensitivities between 35 and 45 mV/pH are reported[139,140], which is comprehensive to values measured with presented FETs (compare Figure 5-6D). Moreover, Figure 5-6C substantiates the real-time sensing performance if the portable platform, such as multiple FETs, reacts simultaneously to external physical properties change, i.e., pH change.

The background of ion/pH sensing with FETs can be explained by the site-binding model developed by Yates et al.[141]. The model can be applied to oxide surfaces, which have a vast number of unfulfilled bonds. When those surfaces are immersed in electrolytic solutions, they acquire a surface charge due to the dissociation of the functional groups on the surface, controlling their interfacial behavior. For example, after the exposition of metal oxide surfaces to water, water molecules will adsorb to the surface, leaving protonated or deprotonated groups at the surface, which in turn leads to a change in the oxide's surface potential. Consequently, the arrangement of ions from the bulk of the electrolyte determines the potential at the surface, which is dependent on electrolyte concentration and surface charge. For instance, SiO_2 exhibits the following electrochemical chemical surface reactions.

$$MH_2^+ \rightleftharpoons \mathrm{M-OH} + H^+ \tag{5.2}$$

$$M-\mathrm{OH} \rightleftharpoons \mathrm{M}-O^- + H^+ \tag{5.3}$$

The first reaction produces positively charged surfaces, whereas the second produces negatively charged ones. The Nernst equation

$$E = E^0 + \frac{RT}{zF} * \ln\left(\frac{c(ox)}{c(red)}\right) \quad (5.4)$$

describes the concentration-dependence of the reduction potential of the symbolic electrochemical reaction

$$red \rightleftharpoons ox + z \cdot e^- \quad (5.5)$$

where E is the actual reduction potential, R is the universal gas constant, F is the Faraday constant, T is the temperature, E^0 is the standard potential, z is the number of electrons, and c is the concentration of chemical species.

A combination of site-binding theory and the Gouy-Chapman-Stern model (compare section 5.2.3.2about EDL and Debye-length) expresses the relationship between the pH of the solution and surface potential (ψ_D) as

$$\Delta\psi = -2.3\alpha\frac{RT}{F}\Delta pH \quad (5.6)$$

where α represents the dimensionless parameter, dependent on the buffer and gate dielectric capacitance, with α ranging from 0 to 1, a maximal sensitivity of 59.5 mV/dec (at 300 K) can be reached - the value is commonly known as the Nernst limit.

The dimensionless parameter α depends on the oxide surface's intrinsic buffer capacity. For SiO_2, these values are relatively low so that typically sensitivities between 35 and 45 mV/pH can be achieved. Altering the materials to high-k oxide layers such as HfO_2 and Al_2O_3[139,142,143], modifying the geometry[144], implementing counter-ions[145], or coating with graphene[146] are some methods to achieve high pH sensitivities. However, applying a dual-gate device creates a capacitive amplification effect, pushing pH sensitivities above the theoretical Nernst limit[99,147].

All FETs operate stably throughout numerous measurements, highlighting their suitability for long time performance. In the presented work, changes of V_G upon experimental progress are presented in terms of subthreshold voltage shifts ΔV_T at selected current I_{SD}, which in turn were within levels in the subthreshold regime as this provides the highest sensitivities[93]. However, for each specific time point, a fingerprint of the complete electrical characteristics of a FET is ensured, and the latter analysis of extracted threshold voltages provides higher sensibilities than measuring at fixed parameters[98,148].

5.3 Detection of biomolecules with SiNW FETs

5.3.1 General considerations for biodetection with FETs

FETs are not only sensitive toward hydrogen ions expressed by pH sensitivity but also to other ions as there is a direct interaction between hydroxyl surface groups and adsorbed anions[145,149,150]. Typically, biomolecules exhibit electrostatic charges under physiological conditions. For example, DNA molecules hold a negatively charged phosphate backbone, while the charge of proteins depends on the isoelectric point (pI) and can be either negative or positive under physiological conditions. The charge significantly affects the sensor devices. Commonly, the more charged the molecule is, the more pronounced the signal change of the FET would appear. However, this only counts if the binding is happening inside EDL and thus within the Debye length.

As mentioned above, sensing with FETs closely connects to changes in the surface potentials, which depend on bound molecules' charges. The occurring electrical signal can be measured either as a result of the movement of charges[65,151], as an impedance-based change due to the appearing biomolecule at the interface[152,153], or as a signal generated by a reporter molecule interrogating with the electric field[154]. All these postulations imply that electronic sensors such as FETs can detect charged molecules easily as their charge interacts with surface potentials directly. However, (Bio-) molecules can interact with FETs by different mechanisms. Here, the charge of the molecules will interact directly with the carriers inside the semiconducting channels. Depending on the biomolecule charge, either by attracting or by repulsion of carriers. In any case, the potential alters so that this mechanism accounts preferably for highly charged molecules and rather large molecules[59,108,155]. A second mechanism relies on the reshuffle of the ionic double layer surrounding the semiconducting channel, which will also reflect changes in the surface potential, too[156,157].

It is assumed that not only will the analyte’s properties reflect FET biosensing, but also the receptor’s conformation and the ligated target-receptor complex will contribute to FET-based detection. In this case, the target molecule's constitution, size, and charge play a subordinated role, such as small and neural (or feebly charged) molecules that can be detected nevertheless. The binding of the target to its receptor will lead to a reshuffle of the ionic composition within the target-receptor complex, which in turn can be detected with FETs. In this regard, some receptors can induce a conformational change

within their structure upon reaction. As a result, ions (and hence charge-) distributions inside receptors will rearrange and cause a modulation of the surface potential, forming the basis for FET signal[65,158].

5.3.2 Sensing aptamers with FETs

Among bioreceptors, aptamers are charged single-stranded DNA or RNA fragments that bind specifically to a target. Being DNA in its nature, aptamers carry a negatively charged but flexible backbone, decorated with alternating sugar (deoxyribose) and phosphate groups, forming a suitable candidate that can be detected with FETs.

Multiple factors contribute to FET sensing using aptamers as receptors. First, their interplay provides a robust system to detect various analytes so that striking aptamer-target affinities allow the detection of analyte concentrations lower than the actual aptamer-target dissociation constant[65]. However, aptamer dissociation constants K_D determined in a solution can differ from those collected when aptamers are immobilized on FET surfaces; even K_D values for the same target varied within the literature—referring to section 5.2.3.3In addition, the size and charge of targets and receptors will reflect within the FET signal directly.

Consequently, negatively charged backbones of the relatively big aptamers will interfere strongly with the conductivity of the FET[159,160]. Additionally, the reduced size of aptamers allows for potential binding sites within the Debye length so that- in contrast to larger antibody-based receptors with comparable K_D values- a partial target capture is detectable, yet[132]. Independent of the size of the analyte, aptamers undergo a conformational change upon binding, which is deeply rooted in the flexibility of the negatively charged backbones. The folding of backbones allows not only for a change in their secondary structure but also causes a reorientation of the structure, which will dominate the FET signal[161–163]. The rearrangement of secondary structures happens, at least partially, in close vicinity to FET surfaces. Counter ions of the electrolyte, which are electrostatically associated with aptamer backbones and FET surfaces, additionally contribute to FET sensing due to their displacement upon folding the aptamer[65,164]. All mentioned signal sources interplay so that any small perturbation of the system will reflect as a charge distribution inside the semiconducting FET channel, hence causing a signal change. Accordingly, aptamer-based FETs are suitable sensor systems for detecting small and uncharged analytes at low concentrations.

To summarize, the surface potential is highly dependent upon any adsorption and a reshuffling of chemical or biological species to the FET surface, making ISFETs ideal signal transducers for detecting all sorts of analytes. To ensure specific systems that only interact with particular analytes, equipment of the surfaces with suitable receptors is essential. The following section describes the chemical modification of oxide surfaces, i.e., silicon dioxide, with aptamers as a specific receptor for detecting cortisol.

5.3.3 Biodetection of the analyte cortisol with SiNW FETs

5.3.3.1 Silane-based surface functionalization

A binding reaction with DNA-aptamer as a receptor was chosen for the sensitive and specific detection of the analyte cortisol. As described in chapter 3, section 2.4, the functionalization of FETs with receptors was realized in an easy two-step process, followed by the bio recognition itself. Briefly, the whole functionalization and bio-recognition process of the analyte cortisol can be divided into three steps:

I. covalent attachment of silane (TSPSA) based linker layer
II. covalent binding of the amino-terminated aptamer to silane
III. biodetection of analyte cortisol via specific but non-covalent, the interaction between cortisol and its aptamer

We chose aptamers over antibodies due to the ease of their use and storage. In addition, aptamers are robust against environmental conditions such as pH and temperature, which makes them suitable candidates for point-of-care biosensors. Furthermore, they can be synthesized chemically with minimal batch-to-batch variations and offer the possibility to modify functional groups to sensor surfaces of choice. Overall, aptamers are known to be specific receptors to their targets while possessing a low immunogenicity[165].

The detection of cortisol with FETs asks for specific aptamers whose sequence was published previously by Martin et al.[166] and has been adopted for this study. Each functionalization step has been verified by static contact angle (CA) measurements, and its impact on FETs has been controlled by recording transfer characteristics. The results and a sketch of the associated chemical reactions are summarized in Figure 5 7 below.

Prior to the deposition of the silane layer, all substrates were treated with plasma to generate a maximum amount of hydroxyl groups at the surface. The presence of hydroxyl groups is mandatory for the covalent binding of the epoxy groups of the silane.

The plasma treatment resulted in very hydrophilic surfaces with a CA of less than 5° (data not shown). Subsequent evaporation of the silane Triethoxysilylpropylsuccinic anhydride (TESPSA) under vacuum followed, and a dense silane layer formed onto silica surfaces. The water contact angle (CA) dropped from 62.4°±3.1° to 46.7° ± 4.1° after deposition (compare Figure 5 7B/C). The measured values are in close agreement with previously reported values for the same surface[167]. Parallel measurements showed that the assembly of TESPSA causes a shift of the transfer characteristics towards higher gate voltages (Figure 5 7G), as expected since TESPSA carries negative charges in its structure. As mentioned before, negative charges of the molecule will reflect in higher threshold voltages (and, in turn, lower source-drain currents) as charges of the bound molecule repel the electrons inside the Si channel. In a second functionalization step, the covalent attachment of amino-modified aptamers to TESPSA prospered. Under a ring opening of the anhydride functionality, the instant binding of amino-terminated receptors succeeds by creating an amide bond, compared to Figure 5 7A. At the same time, water molecules

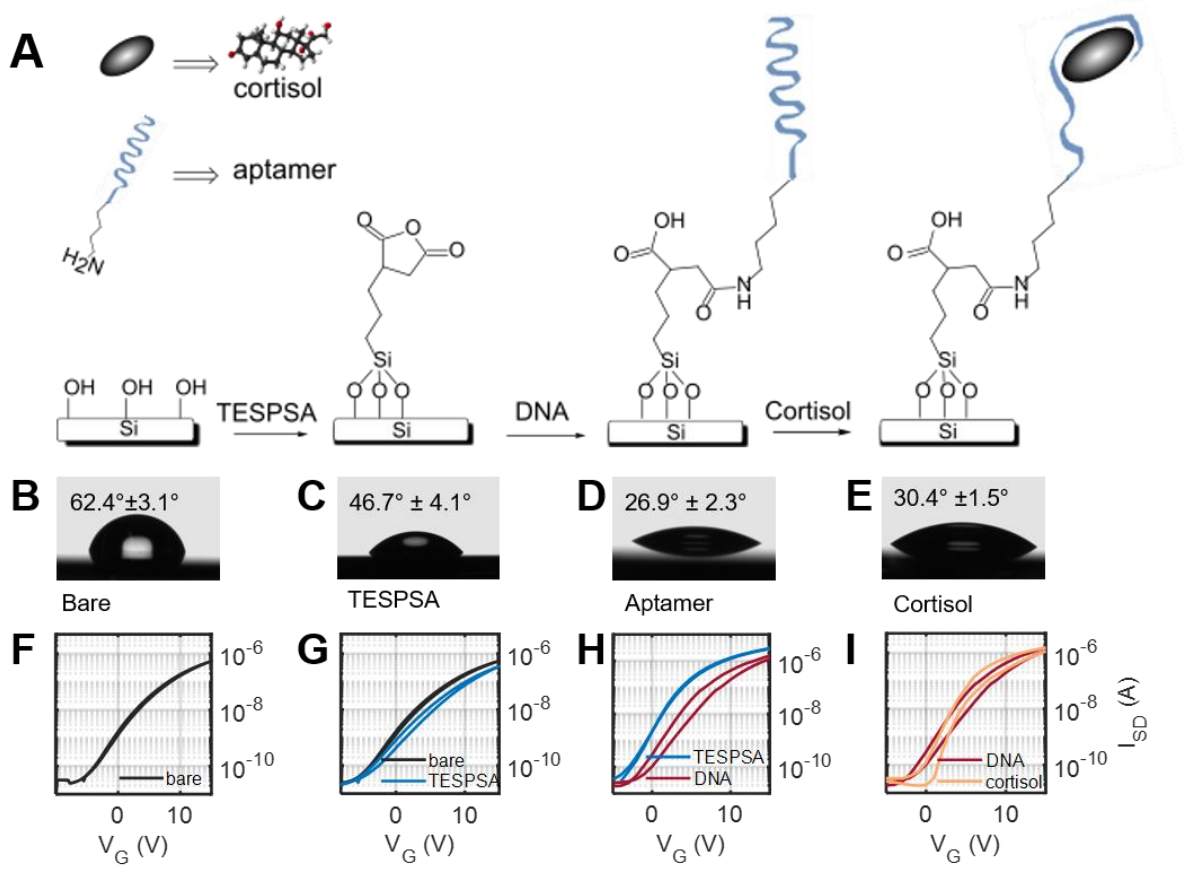

Figure 5-7: A) Chemical reactions to modify SiNW FETs with amino-terminated aptamers further bind the analyte cortisol. First, the silane TESPSA binds covalently to SiO2 via epoxy groups. In a second step, the amino- moiety of the aptamer reacts under a ring opening instantly with the silane and binds the aptamer covalently to the surface. In the last step, the analyte cortisol interacts specifically with its aptamer, accompanied by a conformational change of its structure. B to E show images and numeric values from static water angles on the respective surfaces. F to I represent transfer characteristics of FETs (obtained under ambient conditions) for each functionalization step.

(from the buffer system) also hydrolyze with the anhydride functionalities and create carboxyl groups respectively. To prevent the undesired, premature hydrolyzation of the anhydride moieties with water, thermal treatment of substrates was performed by heating the substrates to 120°C. Successful reaction execution could be monitored by enlarged hydrophilicity of the surfaces with a CA of 26.9°±2.3°, see. At the same time, a further positive voltage shift arose (Figure 5 7D) as negatively charged backbones of the aptamer were introduced to the system.

In a preliminary approach, the biodetection of the analyte cortisol was achieved by subsequent exposure of receptor-treated substrates to cortisol in various concentrations up to 3.2 µg/dl. Figure 5 7E/I show the results for incubation of FETs with the highest concentration of 3.2 µg/dl, whereas Figure 5-8 shows the CA of differently intermediate concentrated cortisol standards, respectively. Here, the hydrophobicity of the surface increases with growing concentrations of cortisol until saturation at ~1 µg/dl, resulting in a lightly enlarged CA of 30.4°±1.5°. The WCA rises from 27° before incubation to 28° after immersion in 0.05 µg/dl and further up to 29.5° when 0.1 µg/dl cortisol is present. The ongoing growth speaks for the constant reaction of aptamers with the target until saturation occurs due to a limited number of binding sites. During binding, the aptamer undergoes a conformational change accompanied by a reorientation of the hydration shells and the hydrophobic fractions of the DNA chains. Those specific and delicate balances between hydrophilic and hydrophobic interactions reflect solid-solution interfacial tensions, which can be measured in terms of contact angles[168–170]. In contrast, the reshuffle of charges inside the DNA strands is expected to give FET signals so that

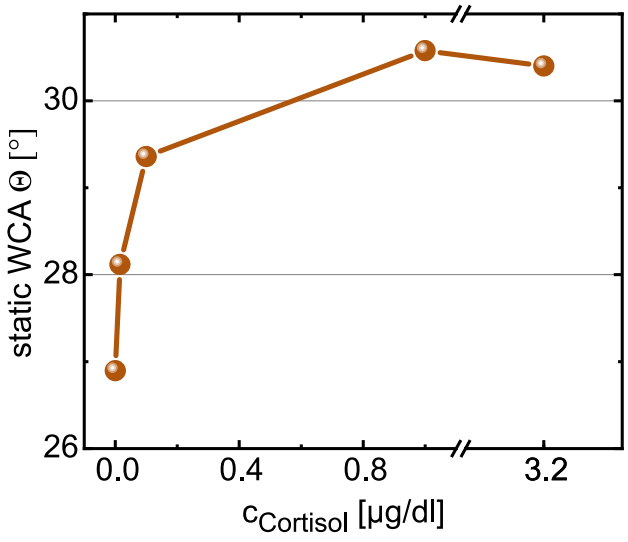

Figure 5-8: Static water contact angle (WCA) of differently concentrated cortisol solutions on aptamer modified substrates.

parallel-obtained IV- characteristics of SiNW FETs responded to the incubation of small molecule cortisol with a negative V_T shift as depicted in Figure 5 7I.

5.3.3.2 Understanding target-receptor interactions

5.3.3.2.1 Colorimetric assay

Colorimetric assays based on the salt-induced aggregation of AuNPs can be used to evaluate the binding of aptamers to their targets[171–174]. A similar colorimetric assay proved the binding of the chosen aptamer to cortisol. The assay is based on the non-covalent, physical adsorption of DNA aptamers onto nanoscaled gold-spheres (AuNPs) so that AuNPs are stabilized in solution and protected against the influence of ions, e.g., by the addition of salt. However, if a specific target is introduced into the system, aptamers will bind and experience a conformational change altering the interaction between DNA and AuNPs. Adding sufficient salt will agglomerate AuNPs because the protective DNA layer has been left. As highlighted in the previous chapter, AuNPs carry size-dependent optical spectra, so the agglomeration of AuNPs is accompanied by a color response from

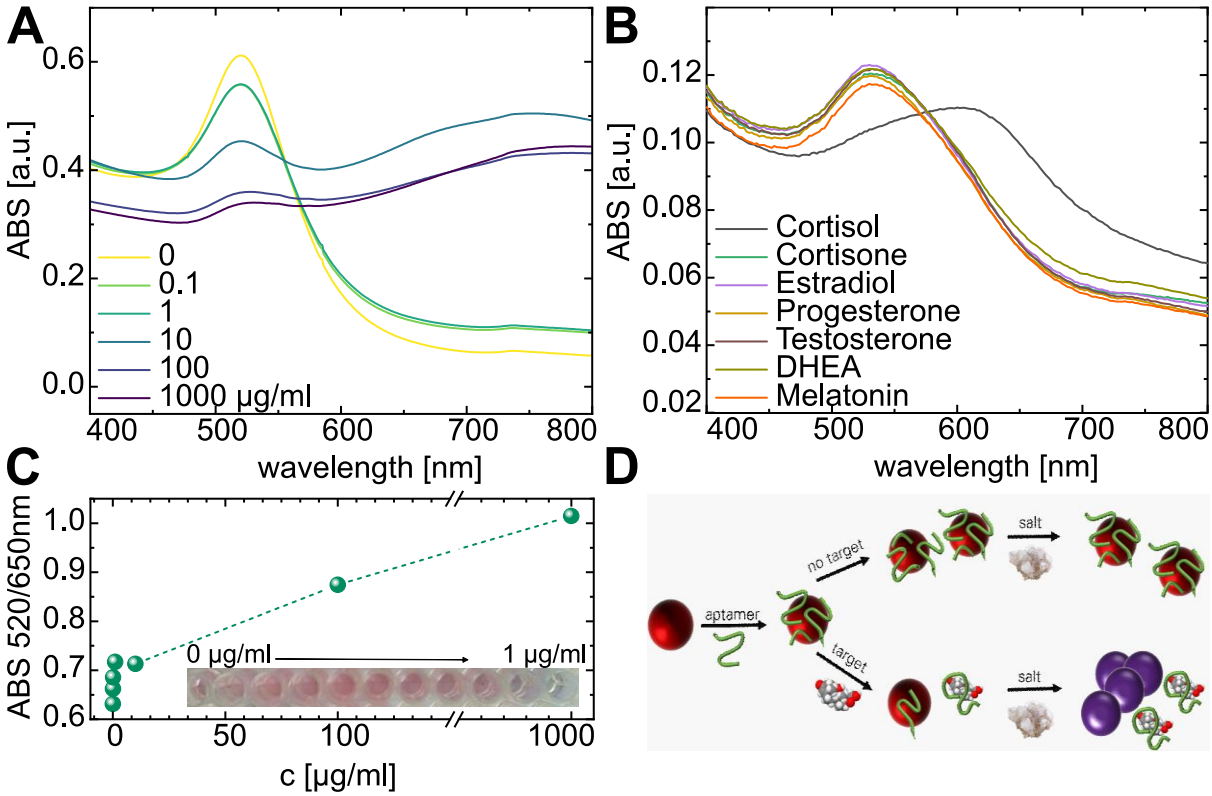

Figure 5-9: Colorimetric determination of cortisol using aptamer-modified gold nanoparticles. A) Absorbance spectra of 10nM AuNPs exposed to cortisol with concentrations between 0 and 1mg/ml after addition of NaCl. B) Absorbance spectra of 10 nM AuNPs exposed to steroids with concentrations of 1mg/ml after addition of NaCl. C) The absorbance ratio at 520 nm to 650 nm quantifies the concentration-dependent agglomeration of AuNPs and can be seen by the naked eye via a color change from red to blue (inset). D) Scheme of the colorimetric assay was well as a photograph highlighting the easily visible color change (lower inset).

red to blue. Figure 5-9A shows absorbance spectra of AuNPs after salt addition upon previous exposure to cortisol, with concentrations ranging from zero to 1mg/ml, respectively. With increasing cortisol concentrations, an enhanced agglomeration of the AuNPs occur visibly by color change (see inset in Figure 5-9D) or by reduced absorbance at 520nm and enhanced absorbance at higher wavelength, respectively. The colorimetric response can be quantified analytically by evaluating absorbance signals at 520nm and 650nm, as illustrated in Figure 5-9C. To ensure the specific reaction of aptamers with the analyte cortisol only, Figure 5-9B shows the absorbance spectra of aptamer-modified AuNPs after incubation with other steroids such as Estradiol, Progesterone, Testosterone, DHEA, Cortisone, and melatonin, respectively. There is no cross-reactivity observed. The mechanism of salt-induced aggregation is depicted schematically in Figure 5-9D.

The performance of the colorimetric assay relies purely on electrostatic interactions between aptamers and AuNPs[171,175,176]. Hence, a rearrangement of charges within the DNA molecules is expected upon folding the secondary structure. This remarkable feature helps detect cortisol with FETs even under physiological conditions, as the relocation of charges due to conformational changes happens in very close proximity to the surface so that events occur within the Debye length.

5.3.3.2.2 Circular dichroism spectroscopy

Circular dichroism spectroscopy (CD) is a method that gives insight into the DNA's secondary structure, which in turn is dependent on the stacking orientation of the base pairs. The DNA backbone consists of sugar moieties that are intrinsically chiral and thus induce a CD signal. At the same time, the base pair are intrinsically non-chiral, so each DNA conformation displays a distinct CD spectrum[177–179]. G-rich sequences of the aptamer can form intra- or intermolecular G-quadruplexes that are readily identified through a positive peak around 295 nm and a negative peak around 270 nm in the CD spectrum[180,181]. Additionally, all G- quadruplexes show a second positive band at ~215nm[182].

The aptamer sequence used in this study was analyzed with a "Quadruplex forming G-Rich Sequences" (QGRS) mapper and scored a G-value of 18, which confirmed the possible formation of G-quadruplex structures[183]. So, peaks at 220 nm, 270 nm, and 295 nm appeared in CD spectra, as shown in Figure 5-10. The direction of the peaks, namely a negative band at 260 nm and a positive peak at 290 nm, indicates that anti-parallel

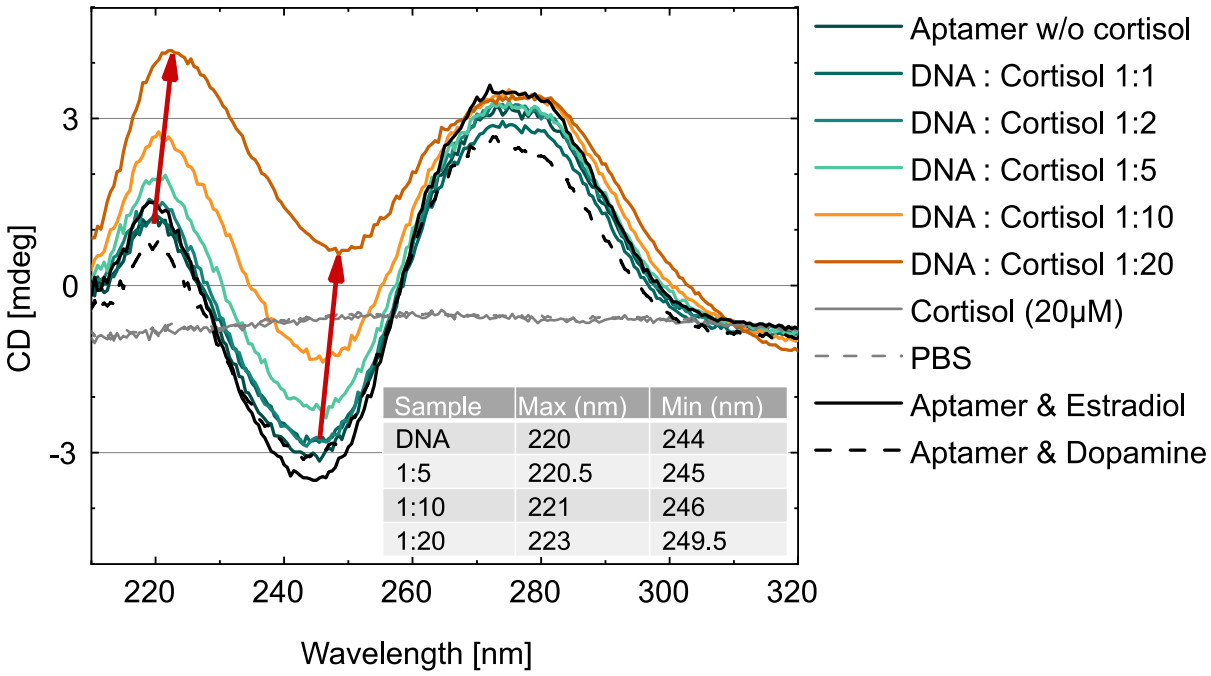

Figure 5-10: CD spectra of DNA solutions between 210 and 320nm with increasing cortisol ratios ranging from cortisol-free (dark green) to 1:20 (orange). DNA-free controls (grey) and DNA exposed to other molecules (black) prove the system's specificity. A shift of the peak position (red arrows) in the CD spectra at ~220 nm and ~245 nm indicate a conformational change of the aptamer. Inset: Values of peaks ~220 nm and ~245 nm, respectively.

structures were formed. The presence of quadruplex structures is significant for improving previously mentioned electrostatic interactions as its structure has twice the negatively charged density per unit length compared to duplex DNA[184].

As the secondary structure of an aptamer is expected to change when interacting with its target, the CD can be used to inform about the nature of this conformational change, too. DNA was incubated with cortisol in growing ratios from 1:1 up to 1:20. As the concentration of cortisol increases, the CD intensities not only increase but also alter their position slightly, consistent with previous reports when aptamers interact with their corresponding targets[65,185–187]. CD spectra of aptamers in PBS, without (dark turquoise line) and with cortisol in different ratios, from 1:1 up to 1:20, are presented in Figure 5-10, respectively. Positive peaks around 220 nm and 280 nm and a negative peak at 245 nm indicate the characteristic pattern of the aptamer (blue arrows). With increasing cortisol concentrations, the position of local peaks and their intensities are shifted towards higher wavelengths testifying to a significant structural transition of DNA structures upon binding. The exact position of peaks for individual cortisol concentrations is denoted in the table in Figure 5-10, respectively.

Incubation with two other small molecules, i.e., dopamine and estradiol, showed no significant change in the CD spectra (black lines). Here, estradiol was chosen as a control

molecule that is very close in its chemical structure to cortisol, and dopamine was chosen as a molecule that directly correlates with cortisol during stress induction[188,189]. Furthermore, the absence of DNA (grey lines) showed no significant peaks in CD spectra.

5.3.3.2.3 Fluorescence microscopy- Surface-capture-assay

For the FET- based detection of cortisol with aptamers as receptors, it is crucial to testify to the capability of the reaction as a surface-capture assay. The receptor is expected to have an active binding site to which the ligand can bind. If receptors are immobilized on a surface, one has to ensure that this active binding site not only shows away from the surface but is also distanced enough to be accessible from the target. In this study, fluorescence microscopy verified the receptor-target complex's suitability. The straight-forwards approach would be to immobilize the receptor as described above and incubate the fluorescently labeled target cortisol. Cortisol is a relatively small molecule with M_W=362.46 g/mol, and common fluorescent dyes with molecules offer sizes in the same order of magnitude, e.g., DAPI has an M_W of 277 g/mol, FITC weights 389 g/mol, and cyanines of ~650 g/mol. So, fluorescently labeled cortisol would presumably double its size, and the affinity to aptamer is downgraded significantly as the fluorophore size might hinder the target sterically. As a result, we modified the functionalization protocol so that immobilization of a carboxyl-terminated cortisol derivate (3-CMO) onto substrates allows for the binding of fluorescently labeled aptamers. Note that Figure 4 in Chapter 3 illustrates the present chemical reaction. The fluorescent label is tagged onto the 5'-end, though, as this is in the standard biodetection assay, the strand binding to the FET's surface. Aptamers with different concentrations, ranging from 0 nM to 500 nM, were spotted on prepared cortisol-modified surfaces with the help of a microarray printer and observed via fluorescence microscopy. Array printing was chosen as it improves sensitivity compared to conventional contact imprint methods[190], and the small size of the arrays enhances analyte affinities in surface-capture assays[191]. Figure 5-11A shows the spot array of CY3-labeled DNA incubated on a 3-CMO surface. Spots with concentrations of 1 nm were detected by fluorescence microscopy. Figure 5-11B emphasizes the selectivity of the assay with the help of a microfluidic channel system, in which four channels provide different surface modifications: Channel 1 was left unmodified, channel 2 had linker APTES without cortisol-derivate, channels 3 and 4 were modified with cortisol-derivate 3-CMO, respectively. After modification,

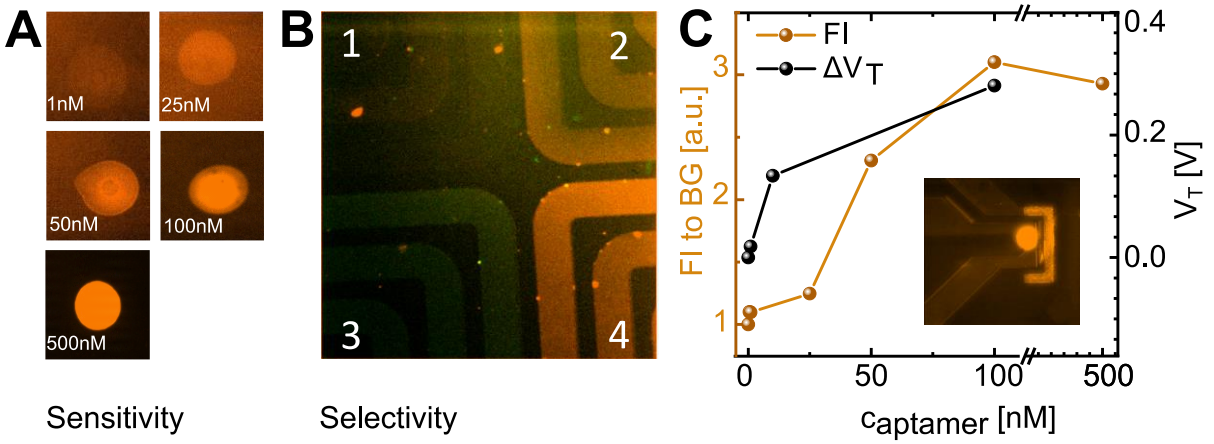

Figure 5-11: Surface capture assay of the aptamer-cortisol complex. A) Spots of CY3-tagged aptamers on a cortisol-modified surface. B) Cortisol-modified surface after incubation of different solutions: 1) 2) 3) 4). C) Fluorescence to background ratio of differently concentrated DNA- spots (orange line) and V_T shift after DNA incubation on cortisol-derivate modified substrates.

channels 1, 2, and 4 were exposed to 500 nM aptamer, whereas channel 3 was exposed to a random DNA sequence labeled with FITC. If there is no modification present, almost no fluorescent signal can be detected (compare channel system 1). The modification with APTES and 3-CMO resulted in detectable signals. Here, the modification with linker-molecule APTES showed fluorescent signals, too, although there is no 3-CMO present. The reason behind this is the positive surface charge of amino groups within the APTES molecule that interact electrostatically with a negative backbone of DNA molecules. The same mechanism applies partly when DNA, which is randomly chosen und thus not specific to aptamers, is exposed to 3-CMO treated surfaces: electrostatically adsorbed DNA creates weak FI signals. However, if a specific aptamer is introduced to 3-CMO-modified surfaces, binding occurs, and strong FI- signals can be observed.

The assay's sensitivity is presented in Figure 5-11C by showing fluorescence signals, expressed as the ratio of background to signal (orange lines). Aptameric concentrations above 1 nM were detected reliably before saturation at 100 nM occurred.

In parallel to fluorescence analysis, target-receptor-binding was monitored using 3-CMO functionalized FETs. In consistency with fluorescence intensity, a growing concentration of aptamers increases relative ΔV_T, which is caused by the accumulation of negatively charged DNA at the sensor surface of FET.

By turning the assay literally upside down, we prove not only the selective and sensitive binding of cortisol to its aptamer but also demonstrate the suitability of the selected aptamer to recognize cortisol in a surface capture assay with FETs.

5.3.4 Detection of cortisol with SiNW FETs

The previous sections 5.2.3 and 5.3.3 revealed the suitability of SiNW FETs for real-time detection of possible analytes with the provided sensing platform and the capability to use aptamers as receptors for sensitive cortisol detection. Consequently, the established protocols are used to evaluate the cortisol concentration with SiNW FETs in real-time. The objective is to determine unknown cortisol levels, preferably under physiological conditions, and thus take a big step forward for point-of-care diagnostics in real-time.

First, FET signals in known concentrations were calibrated upon the introduction of cortisol. Then, after modification with TESPA and aptamer, FETs were exposed to a cortisol-free, physiological buffer system, a 0.1 M phosphate buffer at pH 7.4 with 0.1% BSA and 0.1% ProClin, until a stable baseline level was achieved. Subsequently, the biorecognition of salivary cortisol in physiologically relevant concentrations ranging from 0 µg/dl to 3.2 µg/dl was performed. After a 10 min reaction time, a rinsing step with cortisol-free buffer removed excess cortisol molecules. Consequently, the apparent FET signal shifts were assessed in the following way: V_T values from 100 s before target injection were compared to those V_T values, which were recorded during 100 s after the removal of the excess cortisol, and the obtained difference is expressed as signal change ΔV_T. Figure 5-12A shows the threshold voltage of six FETs upon injection of cortisol in real-time. In contrast, panel B presents the transfer characteristics of one representative FET after cortisol detection with a concentration range between 0µg/dl (light orange line) to 3.2 µg/dl (black); a supportive inset magnifies the most sensitive part of the curves. Cleary, with cumulative cortisol concentrations, the threshold voltage declines so that a left-shift of the transfer characteristics appears. The course of V_T signals in real-time measurements already indicates saturation of the sensors as the signal shifting stagnates after the addition of 0.1 µg/dl (compared to Figure 5-12A and B, respectively). A plot of ΔV_T versus cortisol concentration (see Figure 5-12C) corroborates the previous findings, and a subsequent fitting of the data, indicated by the grey line in Figure 5-12C, enabled the establishment of a calibration curve. Furthermore, the lowest detected concentration was 0.005 µg/dl, and the saturation level occurred at around ~0.2 µg/dl of cortisol and thus forming the dynamic range of the sensor. The sensitivity could be

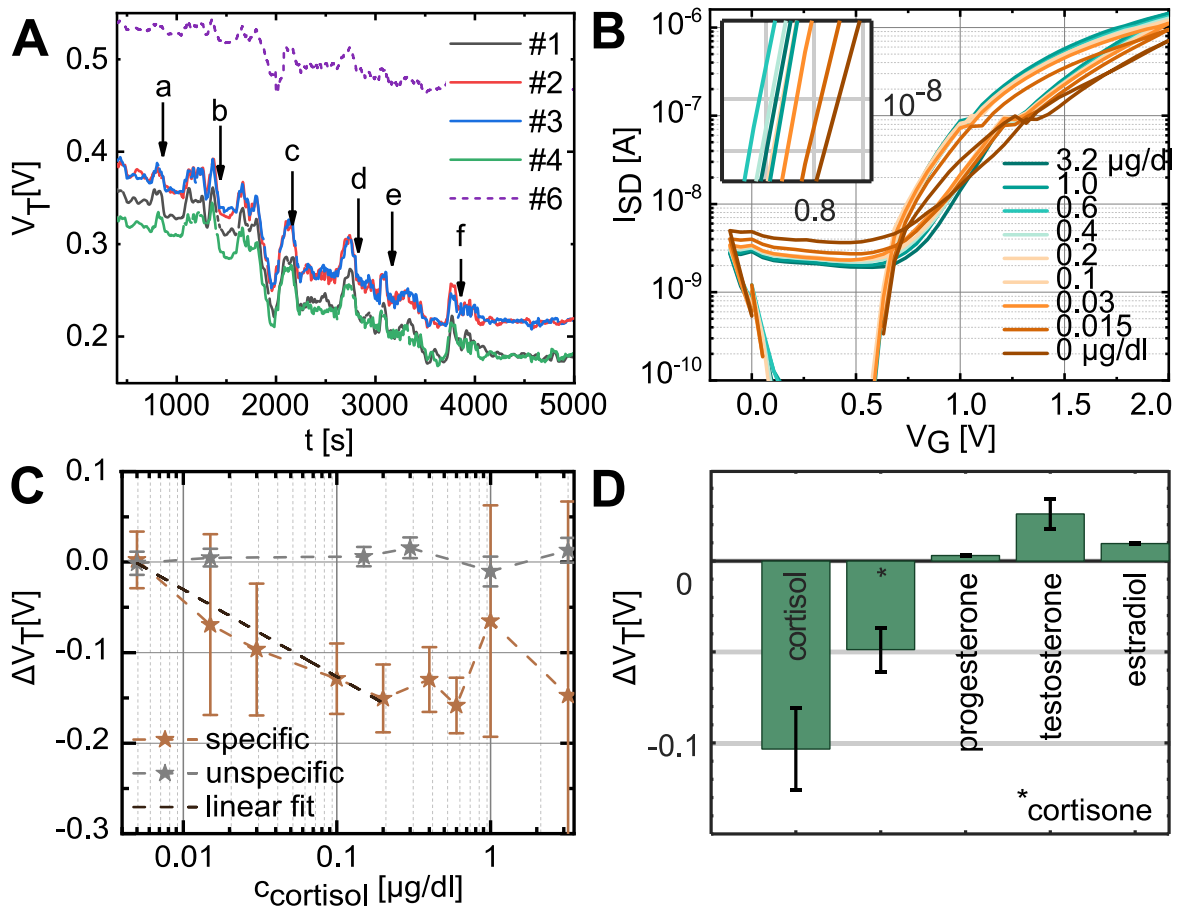

Figure 5-12: Detection of cortisol with SiNW FETs. A) Real-Time Measurement of six individual FETs upon cortisol injection. The arrows mark the point of introduction of cortisol whereas the letters refer to concentration: a) 0.005, b) 0.01, c) 0.015, d) 0.03, e) 0.06, f) 0.1 µg/dl. B) Extracted transfer characteristics of one exemplary FET after reaction with cortisol. The inset magnifies the threshold region at ~10^{-8}A. C) Averaged threshold voltage shift of FETs versus concentration of cortisol for FET modified with aptamers (brown) and unmodified FETS (grey). The dotted line indicates linear fit within the dynamic range of the sensor. D) Threshold voltage shift of aptamer modified FETs upon exposure to other steroids.

associated with the estimated signal decay of around -74.7 mV per decade of cortisol concentration.

A limited number of free binding sites resulting from FETs fabricated in the nanoscale are suspected to be responsible for the sensor's saturation. A short exemplary calculation clarifies the situation: one individual SiNW FET has a surface area of 365 µm^2. With experimentally determined surface coverages of DNA between 2.0x10^{13} and 6.9x10^{13} molecules/cm^2[192,193], an amount of ~7.3x10^7 up to 2.5x10^8 DNA per FET is predicted. Conversely, 0.1 µl of a 0.1 µg/dl cortisol solution already carries 1.66x10^8 molecules and hence levels off in the mentioned orders of magnitude.

Beyond saturation, a further increase in cortisol concentration leads to a reraise and further plateau of ΔV_T. Potentially, this observation can be explained by reorganizing the equilibrium conditions at the FET surface, especially when the le-Châtelier- Braun- the principle is considered. In equilibrium, a system is in a dynamic balance where forward

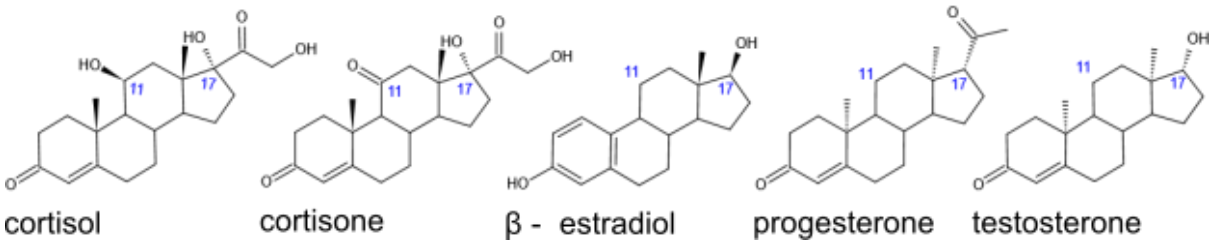

Figure 5-13: Chemical structure of steroids cortisol, cortisone, estradiol, progesterone, and testosterone. Steroids distinguish their structure within functional groups at the C 11 and 17 atom, respectively.

and reserve reactions happen at equal rates. If the chemical equilibrium experiences now an (external) change of reaction parameters such as temperature, pressure, or adding/substracting reactants, the system is out of balance and shifts its reaction rates to reduce the effect of perturbation[194,195]. Considering the change of reactant's concentration in the equilibrium state, which is the case when introducing further cortisol to fully saturated surfaces, the system is expected to be shifted to the side of products. Hence, when all binding sites are occupied and saturation is reached, further introduction of target molecules can result in an exchange of already adsorbed molecules leading to observed signal variations at concentrations of 0.2 µg/dl and higher.

The system's selectivity is presented as a grey line in Figure 5-12C employing the response of unmodified FETs upon cortisol exposure. With increasing cortisol concentrations, only a minimal change of ΔV_T is observed but marginally smaller than detection with specifically functionalized FETs. Equally, Figure 5-12D depicts the sensor response upon reaction with other steroid hormones such as progesterone, estradiol, and testosterone. Again, most signal shifts ΔV_T remain in negligible ranges except cortisone. Here, cortisone and cortisol differ in their chemical structure by only one hydrogen bond at the C-11 atom, so the structural closeness is expected to induce a conformational change of aptamers. In contrast, the other tested steroids differ from cortisol in their functional groups at positions C-17 and C-11 so that aptamers do not fold. An overview of the chemical structures of steroids, including the numbering of interesting carbon atoms C 11 and 17, is presented below in Figure 5-13.

As expounded in section 5.3.3, the detection of molecules in solution with semiconducting FET devices is generally postulated to happen only within the Debye length[102,196,197]. This a fact that accounts particularly when operating in physiological media, where typical Debye lengths are about ~1 nm or less. The size and charge of the target and the receptors will contribute to FET biosensing. Here, small molecules with no or little charges are considered to have less impact on FETs than bigger and charged

molecules[198,199]. Cortisol has a molecular weight of 362 g/mol, which is very little dissociated in the environment, so overall net charge in aqueous solutions can be considered neutral[200]. On the other side, a significant negative charge within the backbones of DNA can affect the FET response throughout, independent of the chemical reactivity or intrinsic charge of the target molecules at all[48,65,201]. So, we postulate that observed signal transduction of FETs upon cortisol detection is presumably not a result of the introduced target charge itself but rather an outcome of conformational change of DNA occurring upon target binding. During the recognition process, aptamers fold into unique structures, including forming stems and loops or transforming double-stranded fragments into single-stranded [202]. All of those changes will result in different secondary structures with different charge distributions than when there is no reaction with the target[203]. Nakatsuka et al.[65] claimed two possible mechanisms: in the first case, the aptamer folds in a way where a considerable portion of the DNA backbone comes closer to the surface of FET. The convergence of negative charges towards the Si surface enhances electrostatic repulsion and increases threshold voltages. Conversely, in the second case, the aptamer backbones withdraw from the surface during reorientation, and fewer negative charges are on the surface. As a result, the threshold voltage declines upon binding- reaction. Both folding mechanisms are expected to happen very close to the surface, to wit within the Debye length of the system. They hence can be detected without further issues in biologically relevant media.

For cortisol recognition, the suitable aptamer is predicted to reorient so that the backbones of DNA move away from the FET channel surface. Indicated by declining threshold voltages upon growing cortisol concentrations, the hypothesis is further supported by the course of CD spectra, where characteristic peaks shift towards higher wavelengths with increasing target concentration.

In the last section, several methods to explore cortisol binding to the chosen aptamer we introduced. All methods showed a sensitive and selective binding reaction between the two molecules.

5.3.4.1 Detection of cortisol in human saliva

Previous findings suggest prosecution of the detection of cortisol with SiNW FETs in saliva without further hindrances.

The developed assay determines salivary cortisol from four volunteers with FETs, and results were compared to those evaluated with a commercially available luminescence immunoassay. Figure 5-14 below presents a typical course of salivary cortisol detection with FETs and subsequent regeneration. All rinsing steps with cortisol-free running buffers are shadowed in gray, whereas the yellow background refers to times under saliva exposure. The introduction of NaCl, visible in the blue background, regenerates the FET surface after detection. The consecutive signal, which is the average V_T of five FETs at 10^{-8} A and shown as a red line in Figure 5-14, illustrates the course of biosensing.

First, a stable baseline achieves by injecting a cortisol-free running buffer. The subsequent addition of saliva resulted in a significant decrease in V_T. With typical pH values between 6.2 and 7.6, where 6.7 is the average pH, saliva has lower pH than the running buffer, and consequently, a decrease in V_T is expected[204]. Additionally, the adsorption of numerous biological entities from salivae, such as proteins, enzymes, and vitamins, onto the FETs' surface contributes to the signal. After a washing step with buffer, a recovery of the FET signal occurs as pH values return to their initial value and biomolecules are removed. The arising difference in the V_T values before saliva

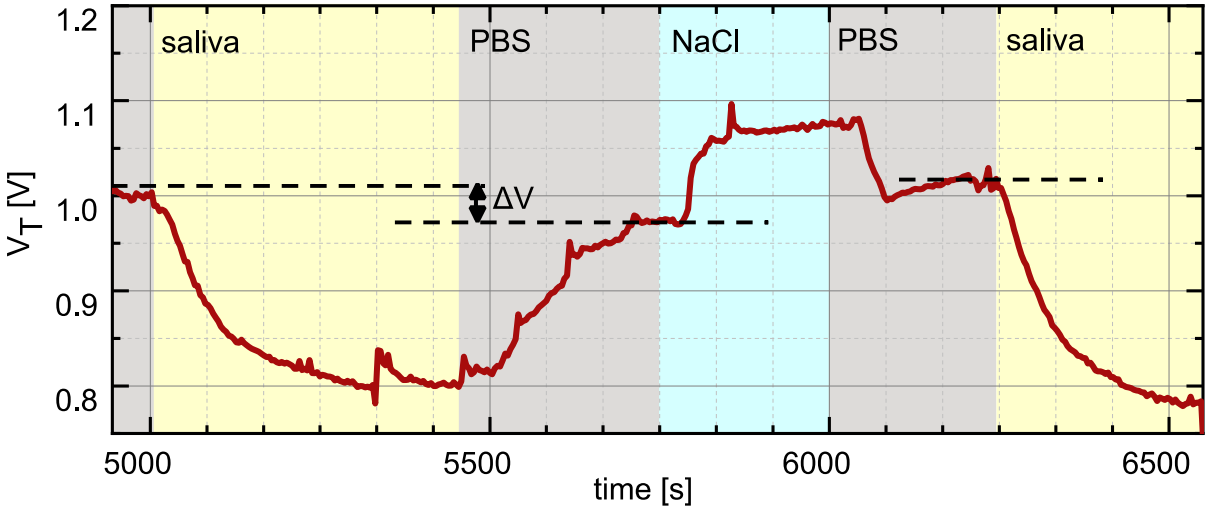

Figure 5-14: Consecutive course of real-time measurement for detection of salivary cortisol. First, the introduction of cortisol-containing saliva (yellow background) lowers FET signals due to different pH than PBS as well as the presence of numerous biological entities. Further injection of PBS (grey) removes the latter and stabilizes pH so that the observed signal difference ΔVT is based on cortisol binding. Then, to regenerate the FET surface, a rinsing step with NaCl (blue background) causes desorption of target molecules. Subsequent rinsing with running buffer PBS (grey) results in starting VT values.

introduction and after rinsing is considered bound to cortisol (compared to V_T signals in Figure 5-14 at t=5000 s and t=5800 s). So, extracted ΔV_T was set in context to cortisol concentration with the help of a previously taken calibration curve (see Figure 5-14).

By doing so, typical cortisol day profiles from four volunteers (A, B, C, and D) were monitored. Typically, the cortisol concentration in a healthy person's saliva is highest directly after waking up and decreases gradually during the day until the lowest levels occur at night. Figure 5-15 below summarizes the obtained data for all volunteers. In Figure 5-15A, measured salivary cortisol levels are plotted against the daytime: cortisol measured with FETs is illustrated in darker colors, whereas data obtained with LIA is presented in brighter colors. Grey background data in Figure 5-15A shows healthy cortisol ranges obtained from reference data of the CIRCORT database study, in which average cortisol levels from >18 000 individuals are collected[205]. The table in Figure 5-15B summarizes all measured values numerally.

Remarkably, all results show typical day profiles with the highest cortisol levels in the morning and declining concentrations throughout the day. There is a clear correspondence between the levels of cortisol measured with FETs and those obtained with LIA. Only at relatively high cortisol levels do the results differ significantly. For example, the morning cortisol levels from volunteers A (orange) and B (blue) were calculated with FETs to be ~0.3 µg/dl and ~0.59 µg/dl. Conversely, LIA confirmed levels of 0.75 µg/dl for volunteer A and 0.46 µg/dl for volunteer B, respectively. Eventual saturation issues of the FET devices root the discrepancy. The earlier taken calibration

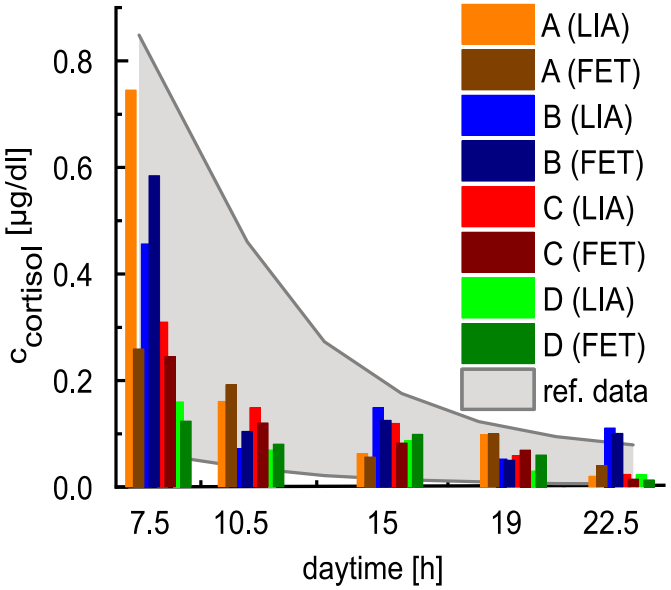

volunteer	Cortisol meas. with LIA (µg/dl)	Cortisol meas. with FET(µg/dl)
A	0.745 0.161 0.063 0.099 0.021	0.259 0.192 0.056 0.100 0.040
B	0.457 0.072 0.149 0.053 0.111	0.585 0.105 0.125 0.050 0.101
C	0.310 0.149 0.120 0.059 0.024	0.245 0.121 0.083 0.070 0.015
D	0.160 0.070 0.088 0.030 0.024	0.124 0.081 0.100 0.060 0.014

Figure 5-15: Overview of salivary cortisol levels. A) Day profile of cortisol from four individuals obtained via FET (dark colors) and LIA (bright colors), including reference data from CIRCORT database (grey background). B) Tabular overview of cortisol levels obtained via LIA and FET.

curve (compare Figure 5-12C) suggests a saturation between 0.2 and 0.4 µg/dl. It thus reveals that the dynamic range of the FET nanosensor cannot cover the whole range of physiological interesting cortisol levels, which can spread up to 1.5 µg/dl[206,207]. However, a controlled serial dilution of the samples, especially for samples taken during morning hours, can remedy this.

After a circle of cortisol detection, regeneration of the FET surface follows. By adding a 2 M NaCl solution, the electrostatic interaction between the target and aptamer is reversed in a way that cortisol releases from the surface without damaging the aptamer, allowing for new usage of the sensor[208,209]. Likewise, after regeneration of the FETs, the V_T levels return to initial values before saliva injection so that complete removal of cortisol is predicted, compared to signals at (t=5000 s and t=6300 s in Figure 5-14).

Concisely, the primary process of detecting salivary cortisol instantaneously (including regeneration of the sensor) takes only a few minutes and can be performed in real-time and in a portable manner - making the introduced sensor system a powerful tool for point-of-care monitoring.

5.4 Summary

The findings in this chapter demonstrate the reliable performance of SiNW-based FET to detect label-free cortisol in high ionic strength media in real-time on a portable sensing platform.

First, (electrical) characteristics and integration of top-down manufactured FETs with nanostructured silicon nanowires in a honeycomb design (SiNW FETs) into a portable platform are evaluated, and the performance of integrated FETs is benchmarked by monitoring pH values of multiple FETs in real-time. FETs showed excellent, sharp, and stable electrical properties with on/off- ratios at 10^5 and steep subthreshold slopes. As a precursor for biosensing, their pH sensitivity of 38.0 ± 1.3 mV/pH has been determined in real-time on a portable device, while on/off ratios are kept at 10^5.

Furthermore, a suitable two-step surface functionalization strategy is presented to bind specific aptamers as receptors for detecting cortisol and verified by contact angle and FET measurements. In addition, the appropriateness of chosen aptamers to fold precisely upon interaction with target cortisol was evaluated with the help of CD, colorimetric assay, and FET biosensing. Finally, the aptitude to process the protocols in terms of a surface-capture assay has been proven by fluorescence microscopy.

The key feature of this research is the label-free detection of the small molecule cortisol in physiological solutions such as saliva with SiNW FETs. Usually, biosensing with FETs is closely connected to shielding issues caused by the electrical double layer, limiting the sensitivity of FETs in high ionic strength media. In this context, FETs are suspected to detect large and charged molecules easily. However, to overcome those limitations, the background of the biorecognition of the target-receptor-complex is studied by colorimetric assay and circular dichroism. After the introduction of cortisol, the unique aptamer complex is found to experience a reorientation of its secondary structure, including a reshuffle of the intramolecular charges that FETs can detect. Here, the reorientation of charges occurs in close vicinity to the sensor surface so that Debye-length limitation can be vanquished and the detection of small, uncharged analyte cortisol in physiological solutions becomes possible.

As proof of concept, cortisol levels ranging from 0.005 µg/dl up to 0.2 µg/dl were detected until saturation of the sensor system occurred. In addition, salivary cortisol

levels from volunteers were determined and were found to closely match those values, which were obtained with a commercial LIA kit.

Apart from the optimization of the biodetection assay itself, the integration of SiNW FETs into a portable platform allows not only for real-time biosensing of cortisol but also for point-of-care detection. Initially applied for stress marker analysis, the presented platform provides a powerful tool for detecting various targets. Furthermore, the possibility for custom-demanded functionalization with antibodies, aptamers, or any receptor of choice, as well as the easy integration of the sensors with plug connections, holds high potential for user-friendly application.

5.5 References

(1) Klinghammer, S.; Voitsekhivska, T.; Licciardello, N.; Kim, K.; Baek, C.-K.; Cho, H.; Wolter, K.-J.; Kirschbaum, C.; Baraban, L.; Cuniberti, G. Nanosensor-Based Real-Time Monitoring of Stress Biomarkers in Human Saliva Using a Portable Measurement System. *ACS Sens.* **2020**, *5* (12), 4081–4091. https://doi.org/10.1021/acssensors.0c02267.

(2) Lohmann-Haislah, A. *Stressreport Deutschland 2012: psychische Anforderungen, Ressourcen und Befinden*; Stressreport Deutschland; Bundesanstalt für Arbeitsschutz und Arbeitsmedizin: Dortmund, 2012.

(3) Delph, A. *Stress: Stressfaktoren erkennen und vorbeugen*; neobooks Self-Publishing, 2014.

(4) Bhargava, D.; Trivedi, H. A Study of Causes of Stress and Stress Management among Youth. *IRA-Int. J. Manag. Soc. Sci. ISSN 2455-2267* **2018**, *11* (3), 108. https://doi.org/10.21013/jmss.v11.n3.p1.

(5) Jackson, M. The Stress of Life: A Modern Complaint? *Lancet* **2014**, *383* (9914), 300–301.

(6) Cerqueira, T. R. do C.; Batista, S. G.; de Mello, E. B.; DosSantos, M. F.; Tuñas, I. T. de C. Impact of the COVID-19 Pandemic on Stress, Sleep, and Oral Health in University Students. *Front. Pain Res.* **2021**, *2*.

(7) Lakhan, R.; Agrawal, A.; Sharma, M. Prevalence of Depression, Anxiety, and Stress during COVID-19 Pandemic. *J. Neurosci. Rural Pract.* **2020**, *11* (4), 519–525. https://doi.org/10.1055/s-0040-1716442.

(8) Pfefferbaum, B.; North, C. S. Mental Health and the Covid-19 Pandemic. *N. Engl. J. Med.* **2020**, *383* (6), 510–512. https://doi.org/10.1056/NEJMp2008017.

(9) Pfeifer, L. S.; Heyers, K.; Ocklenburg, S.; Wolf, O. T. Stress Research during the COVID-19 Pandemic and Beyond. *Neurosci. Biobehav. Rev.* **2021**, *131*, 581–596. https://doi.org/10.1016/j.neubiorev.2021.09.045.

(10) Yaribeygi, H.; Panahi, Y.; Sahraei, H.; Johnston, T. P.; Sahebkar, A. The Impact of Stress on Body Function: A Review. *EXCLI J.* **2017**, *16*, 1057–1072. https://doi.org/10.17179/excli2017-480.

(11) Monroe, S. M.; Harkness, K.; Simons, A. D.; Thase, M. E. Life Stress and the Symptoms of Major Depression. *J. Nerv. Ment. Dis.* **2001**, *189* (3), 168–175. https://doi.org/10.1097/00005053-200103000-00005.

(12) Schneiderman, N.; Ironson, G.; Siegel, S. D. STRESS AND HEALTH: Psychological, Behavioral, and Biological Determinants. *Annu. Rev. Clin. Psychol.* **2005**, *1*, 607–628. https://doi.org/10.1146/annurev.clinpsy.1.102803.144141.

(13) Mariotti, A. The Effects of Chronic Stress on Health: New Insights into the Molecular Mechanisms of Brain–Body Communication. *Future Sci. OA* **2015**, *1* (3). https://doi.org/10.4155/fso.15.21.

(14) Bairey Merz, C. N.; Dwyer, J.; Nordstrom, C. K.; Walton, K. G.; Salerno, J. W.; Schneider, R. H. Psychosocial Stress and Cardiovascular Disease: Pathophysiological Links. *Behav. Med. Wash. DC* **2002**, *27* (4), 141–147. https://doi.org/10.1080/08964280209596039.

(15) Chaby, L. E.; Cavigelli, S. A.; Hirrlinger, A. M.; Caruso, M. J.; Braithwaite, V. A. Chronic Unpredictable Stress during Adolescence Causes Long-Term Anxiety. *Behav. Brain Res.* **2015**, *278*, 492–495. https://doi.org/10.1016/j.bbr.2014.09.003.

(16) Nation, D. A.; Hong, S.; Jak, A. J.; Delano-Wood, L.; Mills, P. J.; Bondi, M. W.; Dimsdale, J. E. Stress, Exercise, and Alzheimer's Disease: A Neurovascular Pathway. *Med. Hypotheses* **2011**, *76* (6), 847–854. https://doi.org/10.1016/j.mehy.2011.02.034.

(17) Cohen, S.; Janicki-Deverts, D.; Miller, G. E. Psychological Stress and Disease. *JAMA* **2007**, *298* (14), 1685–1687. https://doi.org/10.1001/jama.298.14.1685.

(18) Goodie, J. L.; Larkin, K. T.; Schauss, S. Validation of the Polar Heart Rate Monitor for Assessing Heart Rate During Physical and Mental Stress. *J. Psychophysiol.* **2000**, *14* (3), 159–164. https://doi.org/10.1027//0269-8803.14.3.159.

(19) Pelcovitz, D.; van der Kolk, B.; Roth, S.; Mandel, F.; Kaplan, S.; Resick, P. Development of a Criteria Set and a Structured Interview for Disorders of Extreme Stress (SIDES). *J. Trauma. Stress* **1997**, *10* (1), 3–16. https://doi.org/10.1002/jts.2490100103.

(20) Fliege, H.; Rose, M.; Arck, P.; Levenstein, S.; Klapp, B. F. PSQ - Perceived Stress Questionnaire. *Perceived Stress Questionnaire (PSQ; Levenstein, S., Prantera, C., Varvo, V., Scribano, M.L., Berto, E., Luzi, C. & Andreoli, A., 1993) - German modified version* **2009**. http://dx.doi.org/10.23668/psycharchives.351.

(21) Lewis, R. S.; Weekes, N. Y.; Wang, T. H. The Effect of a Naturalistic Stressor on Frontal EEG Asymmetry, Stress, and Health. *Biol. Psychol.* **2007**, *75* (3), 239–247. https://doi.org/10.1016/j.biopsycho.2007.03.004.

(22) Hosseini, S. A.; Khalilzadeh, M. A. Emotional Stress Recognition System Using EEG and Psychophysiological Signals: Using New Labelling Process of EEG Signals in Emotional Stress State. In *2010 International Conference on Biomedical Engineering and Computer Science*; 2010; pp 1–6. https://doi.org/10.1109/ICBECS.2010.5462520.

(23) Kirschbaum, C.; Pirke, K.-M.; Hellhammer, D. H. The 'Trier Social Stress Test' – A Tool for Investigating Psychobiological Stress Responses in a Laboratory Setting. *Neuropsychobiology* **1993**, *28* (1–2), 76–81. https://doi.org/10.1159/000119004.

(24) Peake, J. M.; Kerr, G.; Sullivan, J. P. A Critical Review of Consumer Wearables, Mobile Applications, and Equipment for Providing Biofeedback, Monitoring Stress, and Sleep in Physically Active Populations. *Front. Physiol.* **2018**, *9*. https://doi.org/10.3389/fphys.2018.00743.

(25) Sagl, G.; Resch, B.; Petutschnig, A.; Kyriakou, K.; Liedlgruber, M.; Wilhelm, F. H. Wearables and the Quantified Self: Systematic Benchmarking of Physiological Sensors. *Sensors* **2019**, *19* (20), 4448. https://doi.org/10.3390/s19204448.

(26) Kyriakou, K.; Resch, B.; Sagl, G.; Petutschnig, A.; Werner, C.; Niederseer, D.; Liedlgruber, M.; Wilhelm, F.; Osborne, T.; Pykett, J. Detecting Moments of Stress from Measurements of Wearable Physiological Sensors. *Sensors* **2019**, *19* (17), 3805. https://doi.org/10.3390/s19173805.

(27) Hellhammer, D. H.; Wüst, S.; Kudielka, B. M. Salivary Cortisol as a Biomarker in Stress Research. *Psychoneuroendocrinology* **2009**, *34* (2), 163–171. https://doi.org/10.1016/j.psyneuen.2008.10.026.

(28) Sher, L. Type D Personality: The Heart, Stress, and Cortisol. *QJM Mon. J. Assoc. Physicians* **2005**, *98* (5), 323–329. https://doi.org/10.1093/qjmed/hci064.

(29) Fraser, R.; Ingram, M. C.; Anderson, N. H.; Morrison, C.; Davies, E.; Connell, J. M. Cortisol Effects on Body Mass, Blood Pressure, and Cholesterol in the General Population. *Hypertens. Dallas Tex 1979* **1999**, *33* (6), 1364–1368. https://doi.org/10.1161/01.hyp.33.6.1364.

(30) Levine, A.; Zagoory-Sharon, O.; Feldman, R.; Lewis, J. G.; Weller, A. Measuring Cortisol in Human Psychobiological Studies. *Physiol. Behav.* **2007**, *90* (1), 43–53. https://doi.org/10.1016/j.physbeh.2006.08.025.

(31) Russell, E.; Koren, G.; Rieder, M.; Van Uum, S. H. M. The Detection of Cortisol in Human Sweat: Implications for Measurement of Cortisol in Hair. *Ther. Drug Monit.* **2014**, *36* (1), 30–34. https://doi.org/10.1097/FTD.0b013e31829daa0a.

(32) Zhu, C.; Yuan, C.; Ren, Q.; Wei, F.; Yu, S.; Sun, X.; Zheng, S. Comparative Analysis of the Effects of Collection Methods on Salivary Steroids. *BMC Oral Health* **2021**, *21* (1), 352. https://doi.org/10.1186/s12903-021-01722-w.

(33) Restituto, P.; Galofré, J. C.; Gil, M. J.; Mugueta, C.; Santos, S.; Monreal, J. I.; Varo, N. Advantage of Salivary Cortisol Measurements in the Diagnosis of Glucocorticoid Related Disorders. *Clin. Biochem.* **2008**, *41* (9), 688–692. https://doi.org/10.1016/j.clinbiochem.2008.01.015.

(34) Teruhisa, U.; Ryoji, H.; Taisuke, I.; Tatsuya, S.; Fumihiro, M.; Tatsuo, S. Use of Saliva for Monitoring Unbound Free Cortisol Levels in Serum. *Clin. Chim. Acta* **1981**, *110* (2), 245–253. https://doi.org/10.1016/0009-8981(81)90353-3.

(35) Vining, R. F.; McGinley, R. A.; Maksvytis, J. J.; Ho, K. Y. Salivary Cortisol: A Better Measure of Adrenal Cortical Function than Serum Cortisol. *Ann. Clin. Biochem.* **1983**, *20 (Pt 6)*, 329–335. https://doi.org/10.1177/000456328302000601.

(36) Trilck, M.; Flitsch, J.; Lüdecke, D. K.; Jung, R.; Petersenn, S. Salivary Cortisol Measurement--a Reliable Method for the Diagnosis of Cushing's Syndrome. *Exp. Clin. Endocrinol. Diabetes Off. J. Ger. Soc. Endocrinol. Ger. Diabetes Assoc.* **2005**, *113* (4), 225–230. https://doi.org/10.1055/s-2005-837667.

(37) Aardal, E.; Holm, A.-C. Cortisol in Saliva - Reference Ranges and Relation to Cortisol in Serum. *Clin. Chem. Lab. Med.* **1995**, *33* (12). https://doi.org/10.1515/cclm.1995.33.12.927.

(38) Klopfenstein, B. J.; Purnell, J. Q.; Brandon, D. D.; Isabelle, L. M.; DeBarber, A. E. Determination of Cortisol Production Rates with Contemporary Liquid Chromatography–Mass Spectrometry to Measure Cortisol-D3 Dilution after Infusion of Deuterated Tracer. *Clin. Biochem.* **2011**, *44* (5), 430–434. https://doi.org/10.1016/j.clinbiochem.2010.12.008.

(39) Tahara, Y.; Huang, Z.; Kiritoshi, T.; Onodera, T.; Toko, K. Development of Indirect Competitive Immuno-Assay Method Using SPR Detection for Rapid and Highly Sensitive Measurement of Salivary Cortisol Levels. *Front. Bioeng. Biotechnol.* **2014**, *2*. https://doi.org/10.3389/fbioe.2014.00015.

(40) Mitchell, J. S.; Lowe, T. E.; Ingram, J. R. Rapid Ultrasensitive Measurement of Salivary Cortisol Using Nano-Linker Chemistry Coupled with Surface Plasmon Resonance Detection. *The Analyst* **2009**, *134* (2), 380–386. https://doi.org/10.1039/b817083p.

(41) Ito, T.; Aoki, N.; Kaneko, S.; Suzuki, K. Highly Sensitive and Rapid Sequential Cortisol Detection Using Twin Sensor QCM. *Anal. Methods* **2014**, *6* (18), 7469–7474. https://doi.org/10.1039/C4AY01387E.

(42) Manickam, P.; Pasha, S. K.; Snipes, S. A.; Bhansali, S. A Reusable Electrochemical Biosensor for Monitoring of Small Molecules (Cortisol) Using Molecularly Imprinted Polymers. *J. Electrochem. Soc.* **2017**, *164* (2), B54–B59. https://doi.org/10.1149/2.0781702jes.

(43) Sekar, M.; Pandiaraj, M.; Bhansali, S.; Ponpandian, N.; Viswanathan, C. Carbon Fiber Based Electrochemical Sensor for Sweat Cortisol Measurement. *Sci. Rep.* **2019**, *9* (1), 1–14. https://doi.org/10.1038/s41598-018-37243-w.

(44) Sanghavi, B. J.; Moore, J. A.; Chávez, J. L.; Hagen, J. A.; Kelley-Loughnane, N.; Chou, C.-F.; Swami, N. S. Aptamer-Functionalized Nanoparticles for Surface Immobilization-Free Electrochemical Detection of Cortisol in a Microfluidic Device. *Biosens. Bioelectron.* **2016**, *78*, 244–252. https://doi.org/10.1016/j.bios.2015.11.044.

(45) Cheng, C.; Li, X.; Xu, G.; Lu, Y.; Low, S. S.; Liu, G.; Zhu, L.; Li, C.; Liu, Q. Battery-Free, Wireless, and Flexible Electrochemical Patch for in Situ Analysis of Sweat Cortisol via near Field Communication. *Biosens. Bioelectron.* **2021**, *172*, 112782. https://doi.org/10.1016/j.bios.2020.112782.

(46) Parlak, O.; Keene, S. T.; Marais, A.; Curto, V. F.; Salleo, A. Molecularly Selective Nanoporous Membrane-Based Wearable Organic Electrochemical Device for Noninvasive Cortisol Sensing. *Sci. Adv.* **2018**, *4* (7), eaar2904. https://doi.org/10.1126/sciadv.aar2904.

(47) Jang, H.-J.; Lee, T.; Song, J.; Russell, L.; Li, H.; Dailey, J.; Searson, P. C.; Katz, H. E. Electronic Cortisol Detection Using an Antibody-Embedded Polymer Coupled to a Field-Effect Transistor. *ACS Appl. Mater. Interfaces* **2018**, *10* (19), 16233–16237. https://doi.org/10.1021/acsami.7b18855.

(48) Wang, B.; Zhao, C.; Wang, Z.; Yang, K.-A.; Cheng, X.; Liu, W.; Yu, W.; Lin, S.; Zhao, Y.; Cheung, K. M.; Lin, H.; Hojaiji, H.; Weiss, P. S.; Stojanović, M. N.; Tomiyama, A. J.; Andrews, A. M.; Emaminejad, S. Wearable Aptamer-Field-Effect Transistor Sensing System for Noninvasive Cortisol Monitoring. *Sci. Adv.* **2022**, *8* (1), eabk0967. https://doi.org/10.1126/sciadv.abk0967.

(49) Torrente-Rodríguez, R. M.; Tu, J.; Yang, Y.; Min, J.; Wang, M.; Song, Y.; Yu, Y.; Xu, C.; Ye, C.; IsHak, W. W.; Gao, W. Investigation of Cortisol Dynamics in Human Sweat Using a Graphene-Based Wireless MHealth System. *Matter* **2020**, *2* (4), 921–937. https://doi.org/10.1016/j.matt.2020.01.021.

(50) Ku, M.; Kim, J.; Won, J.-E.; Kang, W.; Park, Y.-G.; Park, J.; Lee, J.-H.; Cheon, J.; Lee, H. H.; Park, J.-U. Smart, Soft Contact Lens for Wireless Immunosensing of Cortisol. *Sci. Adv.* **2020**, *6* (28), eabb2891. https://doi.org/10.1126/sciadv.abb2891.

(51) Zangheri, M.; Cevenini, L.; Anfossi, L.; Baggiani, C.; Simoni, P.; Di Nardo, F.; Roda, A. A Simple and Compact Smartphone Accessory for Quantitative Chemiluminescence-Based Lateral Flow Immunoassay for Salivary Cortisol Detection. *Biosens. Bioelectron.* **2015**, *64*, 63–68. https://doi.org/10.1016/j.bios.2014.08.048.

(52) Choi, S.; Kim, S.; Yang, J.-S.; Lee, J.-H.; Joo, C.; Jung, H.-I. Real-Time Measurement of Human Salivary Cortisol for the Assessment of Psychological Stress Using a Smartphone. *Sens. Bio-Sens. Res.* **2014**, *2*, 8–11. https://doi.org/10.1016/j.sbsr.2014.08.001.

(53) Apilux, A.; Rengpipat, S.; Suwanjang, W.; Chailapakul, O. Development of Competitive Lateral Flow Immunoassay Coupled with Silver Enhancement for Simple and Sensitive Salivary Cortisol Detection. *EXCLI J.* **2018**, *17*, 1198–1209. https://doi.org/10.17179/excli2018-1824.

(54) Dalirirad, S.; Steckl, A. J. Aptamer-Based Lateral Flow Assay for Point of Care Cortisol Detection in Sweat. *Sens. Actuators B Chem.* **2019**, *283*, 79–86. https://doi.org/10.1016/j.snb.2018.11.161.

(55) Stevens, R. C.; Soelberg, S. D.; Near, S.; Furlong, C. E. Detection of Cortisol in Saliva with a Flow-Filtered, Portable Surface Plasmon Resonance Biosensor System. *Anal. Chem.* **2008**, *80* (17), 6747–6751. https://doi.org/10.1021/ac800892h.

(56) Yamaguchi, M.; Katagata, H.; Tezuka, Y.; Niwa, D.; Shetty, V. Automated-Immunosensor with Centrifugal Fluid Valves for Salivary Cortisol Measurement. *Sens. Bio-Sens. Res.* **2014**, *1*, 15–20. https://doi.org/10.1016/j.sbsr.2014.07.001.

(57) Kim, S.; Lee, B.; Reeder, J. T.; Seo, S. H.; Lee, S.-U.; Hourlier-Fargette, A.; Shin, J.; Sekine, Y.; Jeong, H.; Oh, Y. S.; Aranyosi, A. J.; Lee, S. P.; Model, J. B.; Lee, G.; Seo, M.-H.; Kwak, S. S.; Jo, S.; Park, G.; Han, S.; Park, I.; Jung, H.-I.; Ghaffari, R.; Koo, J.; Braun, P. V.; Rogers, J. A. Soft, Skin-Interfaced Microfluidic Systems with Integrated Immunoassays, Fluorometric Sensors, and Impedance Measurement Capabilities. *Proc. Natl. Acad. Sci. U. S. A.* **2020**, *117* (45), 27906–27915. https://doi.org/10.1073/pnas.2012700117.

(58) Hogenelst, K.; Soeter, M.; Kallen, V. Ambulatory Measurement of Cortisol: Where Do We Stand, and Which Way to Follow? *Sens. Bio-Sens. Res.* **2019**, *22*, 100249. https://doi.org/10.1016/j.sbsr.2018.100249.

(59) Kaisti, M. Detection Principles of Biological and Chemical FET Sensors. *Biosens. Bioelectron.* **2017**, *98*, 437–448. https://doi.org/10.1016/j.bios.2017.07.010.

(60) Elfström, N.; Juhasz, R.; Sychugov, I.; Engfeldt, T.; Karlström, A. E.; Linnros, J. Surface Charge Sensitivity of Silicon Nanowires: Size Dependence. *Nano Lett.* **2007**, *7* (9), 2608–2612. https://doi.org/10.1021/nl0709017.

(61) Shoorideh, K.; Chui, C. O. On the Origin of Enhanced Sensitivity in Nanoscale FET-Based Biosensors. *Proc. Natl. Acad. Sci. U. S. A.* **2014**, *111* (14), 5111–5116. https://doi.org/10.1073/pnas.1315485111.

(62) Li, J.; Zhang, Y.; To, S.; You, L.; Sun, Y. Effect of Nanowire Number, Diameter, and Doping Density on Nano-FET Biosensor Sensitivity. *ACS Nano* **2011**, *5* (8), 6661–6668. https://doi.org/10.1021/nn202182p.

(63) Sessi, V.; Ibarlucea, B.; Seichepine, F.; Klinghammer, S.; Ibrahim, I.; Heinzig, A.; Szabo, N.; Mikolajick, T.; Hierlemann, A.; Frey, U.; Weber, W. M.; Baraban, L.; Cuniberti, G. Multisite Dopamine Sensing With Femtomolar Resolution Using a CMOS Enabled Aptasensor Chip. *Front. Neurosci.* **2022**, *16*.

(64) Aliakbarinodehi, N.; Jolly, P.; Bhalla, N.; Miodek, A.; De Micheli, G.; Estrela, P.; Carrara, S. Aptamer-Based Field-Effect Biosensor for Tenofovir Detection. *Sci. Rep.* **2017**, *7*, 44409. https://doi.org/10.1038/srep44409.

(65) Nakatsuka, N.; Yang, K.-A.; Abendroth, J. M.; Cheung, K.; Xu, X.; Yang, H.; Zhao, C.; Zhu, B.; Rim, Y. S.; Yang, Y.; Weiss, P. S.; Stojanović, M. N.; Andrews, A. M. Aptamer-Field-Effect Transistors Overcome Debye Length

Limitations for Small-Molecule Sensing. *Science* **2018**, *362* (6412), 319–324. https://doi.org/10.1126/science.aao6750.

(66) Wang, W. U.; Chen, C.; Lin, K.; Fang, Y.; Lieber, C. M. Label-Free Detection of Small-Molecule–Protein Interactions by Using Nanowire Nanosensors. *Proc. Natl. Acad. Sci. U. S. A.* **2005**, *102* (9), 3208–3212. https://doi.org/10.1073/pnas.0406368102.

(67) Ibarlucea, B.; Fawzul Akbar, T.; Kim, K.; Rim, T.; Baek, C.-K.; Ascoli, A.; Tetzlaff, R.; Baraban, L.; Cuniberti, G. Ultrasensitive Detection of Ebola Matrix Protein in a Memristor Mode. *Nano Res.* **2018**, *11* (2), 1057–1068. https://doi.org/10.1007/s12274-017-1720-2.

(68) Hahm, J.; Lieber, C. M. Direct Ultrasensitive Electrical Detection of DNA and DNA Sequence Variations Using Nanowire Nanosensors. *Nano Lett.* **2004**, *4* (1), 51–54. https://doi.org/10.1021/nl034853b.

(69) Gao, Z.; Agarwal, A.; Trigg, A. D.; Singh, N.; Fang, C.; Tung, C.-H.; Fan, Y.; Buddharaju, K. D.; Kong, J. Silicon Nanowire Arrays for Label-Free Detection of DNA. *Anal. Chem.* **2007**, *79* (9), 3291–3297. https://doi.org/10.1021/ac061808q.

(70) Patolsky, F.; Zheng, G.; Hayden, O.; Lakadamyali, M.; Zhuang, X.; Lieber, C. M. Electrical Detection of Single Viruses. *Proc. Natl. Acad. Sci.* **2004**, *101* (39), 14017–14022. https://doi.org/10.1073/pnas.0406159101.

(71) Berto, M.; Vecchi, E.; Baiamonte, L.; Condò, C.; Sensi, M.; Di Lauro, M.; Sola, M.; De Stradis, A.; Biscarini, F.; Minafra, A.; Bortolotti, C. A. Label Free Detection of Plant Viruses with Organic Transistor Biosensors. *Sens. Actuators B Chem.* **2019**, *281*, 150–156. https://doi.org/10.1016/j.snb.2018.10.080.

(72) Tran, D. P.; Winter, M. A.; Wolfrum, B.; Stockmann, R.; Yang, C.-T.; Pourhassan-Moghaddam, M.; Offenhäusser, A.; Thierry, B. Toward Intraoperative Detection of Disseminated Tumor Cells in Lymph Nodes with Silicon Nanowire Field Effect Transistors. *ACS Nano* **2016**, *10* (2), 2357–2364. https://doi.org/10.1021/acsnano.5b07136.

(73) Cohen-Karni, T.; Qing, Q.; Li, Q.; Fang, Y.; Lieber, C. M. Graphene and Nanowire Transistors for Cellular Interfaces and Electrical Recording. *Nano Lett.* **2010**, *10* (3), 1098–1102. https://doi.org/10.1021/nl1002608.

(74) Schütt, J.; Ibarlucea, B.; Illing, R.; Zörgiebel, F. M.; Pregl, S.; Nozaki, D.; Weber, W. M.; Mikolajick, T.; Baraban, L.; Cuniberti, G. Compact Nanowire Sensors Probe Microdroplets. *Nano Lett.* **2016**, *16* (8), 4991–5000. https://doi.org/10.1021/acs.nanolett.6b01707.

(75) Klinghammer, S.; Rauch, S.; Pregl, S.; Uhlmann, P.; Baraban, L.; Cuniberti, G. Surface Modification of Silicon Nanowire Based Field Effect Transistors with Stimuli Responsive Polymer Brushes for Biosensing Applications. *Micromachines* **2020**, *11* (3), 274. https://doi.org/10.3390/mi11030274.

(76) Ibarlucea, B.; Rim, T.; Baek, C. K.; de Visser, J. A. G. M.; Baraban, L.; Cuniberti, G. Nanowire Sensors Monitor Bacterial Growth Kinetics and Response to Antibiotics. *Lab. Chip* **2017**, *17* (24), 4283–4293. https://doi.org/10.1039/C7LC00807D.

(77) Li, H.; Dauphin-Ducharme, P.; Ortega, G.; Plaxco, K. W. Calibration-Free Electrochemical Biosensors Supporting Accurate Molecular Measurements Directly in Undiluted Whole Blood. *J. Am. Chem. Soc.* **2017**, *139* (32), 11207–11213. https://doi.org/10.1021/jacs.7b05412.

(78) Fernandez, R. E.; Umasankar, Y.; Manickam, P.; Nickel, J. C.; Iwasaki, L. R.; Kawamoto, B. K.; Todoki, K. C.; Scott, J. M.; Bhansali, S. Disposable Aptamer-Sensor Aided by Magnetic Nanoparticle Enrichment for Detection of Salivary Cortisol Variations in Obstructive Sleep Apnea Patients. *Sci. Rep.* **2017**, *7* (1), 17992. https://doi.org/10.1038/s41598-017-17835-8.

(79) Cheung, K. M.; Yang, K.-A.; Nakatsuka, N.; Zhao, C.; Ye, M.; Jung, M. E.; Yang, H.; Weiss, P. S.; Stojanović, M. N.; Andrews, A. M. Phenylalanine Monitoring via Aptamer-Field-Effect Transistor Sensors. *ACS Sens.* **2019**, *4* (12), 3308–3317. https://doi.org/10.1021/acssensors.9b01963.

(80) Zhao, C.; Cheung, K. M.; Huang, I.-W.; Yang, H.; Nakatsuka, N.; Liu, W.; Cao, Y.; Man, T.; Weiss, P. S.; Monbouquette, H. G.; Andrews, A. M. Implantable Aptamer–Field-Effect Transistor Neuroprobes for in Vivo Neurotransmitter Monitoring. *Sci. Adv.* **2021**, *7* (48), eabj7422. https://doi.org/10.1126/sciadv.abj7422.

(81) Meyers, S. R.; Grinstaff, M. W. Biocompatible and Bioactive Surface Modifications for Prolonged In Vivo Efficacy. *Chem. Rev.* **2012**, *112* (3), 1615–1632. https://doi.org/10.1021/cr2000916.

(82) Rong, G.; Corrie, S. R.; Clark, H. A. In Vivo Biosensing: Progress and Perspectives. *ACS Sens.* **2017**, *2* (3), 327–338. https://doi.org/10.1021/acssensors.6b00834.

(83) Lafleur, J. P.; Jönsson, A.; Senkbeil, S.; Kutter, J. P. Recent Advances in Lab-on-a-Chip for Biosensing Applications. *Biosens. Bioelectron.* **2015**. https://doi.org/10.1016/j.bios.2015.08.003.

(84) Rim, T.; Kim, K.; Cho, H.; Jeong, W.; Yoon, J.; Kim, Y.; Meyyappan, M.; Baek, C. Electrical Characteristics of Doped Silicon Nanowire Channel Field-Effect Transistor Biosensors. *IEEE Sens. J.* **2017**, *17* (3), 667–673. https://doi.org/10.1109/JSEN.2016.2625420.

(85) Pud, S.; Li, J.; Sibiliev, V.; Petrychuk, M.; Kovalenko, V.; Offenhäusser, A.; Vitusevich, S. Liquid and Back Gate Coupling Effect: Toward Biosensing with Lowest Detection Limit. *Nano Lett.* **2014**, *14* (2), 578–584. https://doi.org/10.1021/nl403748x.

(86) Zadorozhnyi, I.; Pud, S.; Vitusevich, S.; Petrychuk, M. Features of the Gate Coupling Effect in Liquid-Gated Si Nanowire FETs. In *2015 International Conference on Noise and Fluctuations (ICNF)*; 2015; pp 1–4. https://doi.org/10.1109/ICNF.2015.7288625.

(87) Voitsekhivska, T.; Technische Universität Dresden. *Highly Adaptable Multiplexing Platform Technology for Biochemical Sensing Applications*; Dresden, 2020.

(88) Voitsekhivska, T.; Suthau, E.; Wolter, K.-J. CMOS Multiplexer for Portable Biosensing System with Integrated Microfluidic Interface; IEEE, 2014; pp 173–178. https://doi.org/10.1109/ECTC.2014.6897285.

(89) Tixier-Mita, A.; Ihida, S.; Ségard, B.-D.; Cathcart, G. A.; Takahashi, T.; Fujita, H.; Toshiyoshi, H. Review on Thin-Film Transistor Technology, Its Applications, and Possible New Applications to Biological Cells. *Jpn. J. Appl. Phys.* **2016**, *55* (4S), 04EA08. https://doi.org/10.7567/JJAP.55.04EA08.

(90) Manimekala, T.; Sivasubramanian, R.; Dharmalingam, G. Nanomaterial-Based Biosensors Using Field-Effect Transistors: A Review. *J. Electron. Mater.* **2022**, *51* (5), 1950–1973. https://doi.org/10.1007/s11664-022-09492-z.

(91) Xu, J.-J. Analytical Aspects of Fet-Based Biosensors. *Front. Biosci.* **2005**, *10* (1–3), 420. https://doi.org/10.2741/1538.

(92) Segura, J.; Hawkins, C. F. *CMOS Electronics: How It Works, How It Fails*; John Wiley & Sons, 2004.

(93) Gao, X. P. A.; Zheng, G.; Lieber, C. M. Subthreshold Regime Has the Optimal Sensitivity for Nanowire FET Biosensors. *Nano Lett.* **2010**, *10* (2), 547. https://doi.org/10.1021/nl9034219.

(94) Chuang, H.-S.; Ho, Y.-P. *Advances in Biosensing Technology for Medical Diagnosis*; Bentham Science Publishers, 2020.

(95) Ortiz-Conde, A.; García-Sánchez, F. J.; Muci, J.; Terán Barrios, A.; Liou, J. J.; Ho, C.-S. Revisiting MOSFET Threshold Voltage Extraction Methods. *Microelectron. Reliab.* **2013**, *53* (1), 90–104. https://doi.org/10.1016/j.microrel.2012.09.015.

(96) Ortiz-Conde, A.; García Sánchez, F. J.; Liou, J. J.; Cerdeira, A.; Estrada, M.; Yue, Y. A Review of Recent MOSFET Threshold Voltage Extraction Methods. *Microelectron. Reliab.* **2002**, *42* (4), 583–596. https://doi.org/10.1016/S0026-2714(02)00027-6.

(97) Zörgiebel, F. Silicon Nanowires for Biosensor Applications, TU Dresden, Dresden, 2017.

(98) Zörgiebel, F. M.; Pregl, S.; Römhildt, L.; Opitz, J.; Weber, W.; Mikolajick, T.; Baraban, L.; Cuniberti, G. Schottky Barrier-Based Silicon Nanowire PH Sensor with Live Sensitivity Control. *Nano Res.* **2014**, *7* (2), 263–271. https://doi.org/10.1007/s12274-013-0393-8.

(99) Knopfmacher, O.; Tarasov, A.; Fu, W.; Wipf, M.; Niesen, B.; Calame, M.; Schönenberger, C. Nernst Limit in Dual-Gated Si-Nanowire FET Sensors. *Nano Lett.* **2010**, *10* (6), 2268–2274. https://doi.org/10.1021/nl100892y.

(100) Duarte-Guevara, C.; Lai, F.-L.; Cheng, C.-W.; Reddy, B.; Salm, E.; Swaminathan, V.; Tsui, Y.-K.; Tuan, H. C.; Kalnitsky, A.; Liu, Y.-S.; Bashir, R. Enhanced Biosensing Resolution with Foundry Fabricated Individually Addressable Dual-Gated ISFETs. *Anal. Chem.* **2014**, *86* (16), 8359–8367. https://doi.org/10.1021/ac501912x.

(101) Bhatt, D.; Panda, S. Dual-gate Ion-sensitive Field-effect Transistors: A Review. *Electrochem. Sci. Adv.* **2021**. https://doi.org/10.1002/elsa.202100195.

(102) Stern, E.; Wagner, R.; Sigworth, F. J.; Breaker, R.; Fahmy, T. M.; Reed, M. A. Importance of the Debye Screening Length on Nanowire Field Effect Transistor Sensors. *Nano Lett.* **2007**, *7* (11), 3405–3409. https://doi.org/10.1021/nl071792z.

(103) Pachauri, V.; Ingebrandt, S. Biologically Sensitive Field-Effect Transistors: From ISFETs to NanoFETs. *Essays Biochem.* **2016**, *60* (1), 81–90. https://doi.org/10.1042/EBC20150009.

(104) Matsumoto, K.; Ohno, Y.; Maehashi, K. Utilizing Research into Electrical Double Layers as a Basis for the Development of Label-Free Biosensors Based on Nanomaterial Transistors. *Nanobiosensors Dis. Diagn.* **2015**, 1. https://doi.org/10.2147/NDD.S40316.

(105) Kesler, V.; Murmann, B.; Soh, H. T. Going beyond the Debye Length: Overcoming Charge Screening Limitations in Next-Generation Bioelectronic Sensors. *ACS Nano* **2020**, *14* (12), 16194–16201. https://doi.org/10.1021/acsnano.0c08622.

(106) Zheng, Z.; Zhang, H.; Zhai, T.; Xia, F. Overcome Debye Length Limitations for Biomolecule Sensing Based on Field Effective Transistors†. *Chin. J. Chem.* **2021**, *39* (4), 999–1008. https://doi.org/10.1002/cjoc.202000584.

(107) Falina, S.; Syamsul, M.; Rhaffor, N. A.; Sal Hamid, S.; Mohamed Zain, K. A.; Abd Manaf, A.; Kawarada, H. Ten Years Progress of Electrical Detection of Heavy Metal Ions (HMIs) Using Various Field-Effect Transistor (FET) Nanosensors: A Review. *Biosensors* **2021**, *11* (12), 478. https://doi.org/10.3390/bios11120478.

(108) Curreli, M.; Rui Zhang; Ishikawa, F. N.; Hsiao-Kang Chang; Cote, R. J.; Chongwu Zhou; Thompson, M. E. Real-Time, Label-Free Detection of Biological Entities Using Nanowire-Based FETs. *IEEE Trans. Nanotechnol.* **2008**, *7* (6), 651–667. https://doi.org/10.1109/TNANO.2008.2006165.

(109) Erickson, H. P. Size and Shape of Protein Molecules at the Nanometer Level Determined by Sedimentation, Gel Filtration, and Electron Microscopy. *Biol. Proced. Online* **2009**, *11* (1), 32–51. https://doi.org/10.1007/s12575-009-9008-x.

(110) Louten, J. Virus Structure and Classification. In *Essential Human Virology*; Elsevier, 2016; pp 19–29. https://doi.org/10.1016/B978-0-12-800947-5.00002-8.

(111) Bollella, P.; Katz, E. *Biosensors – Recent Advances and Future Challenges*; MDPI, 2021.

(112) Lloret, N.; Frederiksen, R. S.; Møller, T. C.; Rieben, N. I.; Upadhyay, S.; Vico, L. D.; Jensen, J. H.; Nygård, J.; Martinez, K. L. Effects of Buffer Composition and Dilution on Nanowire Field-Effect Biosensors. *Nanotechnology* **2012**, *24* (3), 035501. https://doi.org/10.1088/0957-4484/24/3/035501.

(113) Roberts, D.; Keeling, R.; Tracka, M.; van der Walle, C. F.; Uddin, S.; Warwicker, J.; Curtis, R. Specific Ion and Buffer Effects on Protein-Protein Interactions of a Monoclonal Antibody. *Mol. Pharm.* **2015**, *12* (1), 179–193. https://doi.org/10.1021/mp500533c.

(114) Stern, E.; Vacic, A.; Rajan, N. K.; Criscione, J. M.; Park, J.; Ilic, B. R.; Mooney, D. J.; Reed, M. A.; Fahmy, T. M. Label-Free Biomarker Detection from Whole Blood. *Nat. Nanotechnol.* **2010**, *5* (2), 138–142. https://doi.org/10.1038/nnano.2009.353.

(115) Reddy, B.; Salm, E.; Bashir, R. Electrical Chips for Biological Point-of-Care Detection. *Annu. Rev. Biomed. Eng.* **2016**, *18* (1), 329–355. https://doi.org/10.1146/annurev-bioeng-071813-104643.

(116) M. Lowe, B.; Sun, K.; Zeimpekis, I.; Skylaris, C.-K.; G. Green, N. Field-Effect Sensors – from PH Sensing to Biosensing: Sensitivity Enhancement Using Streptavidin–Biotin as a Model System. *Analyst* **2017**, *142* (22), 4173–4200. https://doi.org/10.1039/C7AN00455A.

(117) Kulkarni, G. S.; Zhong, Z. Detection beyond the Debye Screening Length in a High-Frequency Nanoelectronic Biosensor. *Nano Lett.* **2012**, *12* (2), 719–723. https://doi.org/10.1021/nl203666a.

(118) Tran, D. P.; Winter, M.; Yang, C.-T.; Stockmann, R.; Offenhäusser, A.; Thierry, B. Silicon Nanowires Field Effect Transistors: A Comparative Sensing Performance between Electrical Impedance and Potentiometric Measurement Paradigms. *Anal. Chem.* **2019**, *91* (19), 12568–12573. https://doi.org/10.1021/acs.analchem.9b03559.

(119) Lemay, S. G.; Laborde, C.; Renault, C.; Cossettini, A.; Selmi, L.; Widdershoven, F. P. High-Frequency Nanocapacitor Arrays: Concept, Recent Developments, and Outlook. *Acc. Chem. Res.* **2016**, *49* (10), 2355–2362. https://doi.org/10.1021/acs.accounts.6b00349.

(120) Zong, X.; Zhu, R. ZnO Nanorod-Based FET Biosensor for Continuous Glucose Monitoring. *Sens. Actuators B Chem.* **2018**, *255*, 2448–2453. https://doi.org/10.1016/j.snb.2017.09.037.

(121) Hwang, M. T.; Heiranian, M.; Kim, Y.; You, S.; Leem, J.; Taqieddin, A.; Faramarzi, V.; Jing, Y.; Park, I.; van der Zande, A. M.; Nam, S.; Aluru, N. R.; Bashir, R. Ultrasensitive Detection of Nucleic Acids Using Deformed Graphene Channel Field Effect Biosensors. *Nat. Commun.* **2020**, *11* (1), 1543. https://doi.org/10.1038/s41467-020-15330-9.

(122) Shoorideh, K.; Chui, C. O. On the Origin of Enhanced Sensitivity in Nanoscale FET-Based Biosensors. *Proc. Natl. Acad. Sci. U. S. A.* **2014**, *111* (14), 5111–5116. https://doi.org/10.1073/pnas.1315485111.

(123) Gao, N.; Gao, T.; Yang, X.; Dai, X.; Zhou, W.; Zhang, A.; Lieber, C. M. Specific Detection of Biomolecules in Physiological Solutions Using Graphene Transistor Biosensors. *Proc. Natl. Acad. Sci.* **2016**, *113* (51), 14633–14638. https://doi.org/10.1073/pnas.1625010114.

(124) Gutiérrez-Sanz, Ó.; Andoy, N. M.; Filipiak, M. S.; Haustein, N.; Tarasov, A. Direct, Label-Free, and Rapid Transistor-Based Immunodetection in Whole Serum. *ACS Sens.* **2017**, *2* (9), 1278–1286. https://doi.org/10.1021/acssensors.7b00187.

(125) Gao, N.; Zhou, W.; Jiang, X.; Hong, G.; Fu, T.-M.; Lieber, C. M. General Strategy for Biodetection in High Ionic Strength Solutions Using Transistor-Based Nanoelectronic Sensors. *Nano Lett.* **2015**, *15* (3), 2143–2148. https://doi.org/10.1021/acs.nanolett.5b00133.

(126) Piccinini, E.; Alberti, S.; Longo, G. S.; Berninger, T.; Breu, J.; Dostalek, J.; Azzaroni, O.; Knoll, W. Pushing the Boundaries of Interfacial Sensitivity in Graphene FET Sensors: Polyelectrolyte Multilayers Strongly Increase the Debye Screening Length. *J. Phys. Chem. C* **2018**, *122* (18), 10181–10188. https://doi.org/10.1021/acs.jpcc.7b11128.

(127) Hasler, R.; Reiner-Rozman, C.; Fossati, S.; Aspermair, P.; Dostalek, J.; Lee, S.; Ibáñez, M.; Bintinger, J.; Knoll, W. Field-Effect Transistor with a Plasmonic Fiber Optic Gate Electrode as a Multivariable Biosensor Device. *ACS Sens.* **2022**, *7* (2), 504–512. https://doi.org/10.1021/acssensors.1c02313.

(128) Wang, Y.-Y.; Burke, P. Polyelectrolyte Multilayer Electrostatic Gating of Graphene Field-Effect Transistors. *Nano Res.* **2014**. https://doi.org/10.1007/s12274-014-0525-9.

(129) Bay, H. H.; Vo, R.; Dai, X.; Hsu, H.-H.; Mo, Z.; Cao, S.; Li, W.; Omenetto, F. G.; Jiang, X. Hydrogel Gate Graphene Field-Effect Transistors as Multiplexed Biosensors. *Nano Lett.* **2019**, *19* (4), 2620–2626. https://doi.org/10.1021/acs.nanolett.9b00431.

(130) Dumitru, L. M.; Manoli, K.; Magliulo, M.; Ligonzo, T.; Palazzo, G.; Torsi, L. A Hydrogel Capsule as Gate Dielectric in Flexible Organic Field-Effect Transistors. *APL Mater.* **2015**, *3* (1), 014904. https://doi.org/10.1063/1.4901124.

(131) Elnathan, R.; Kwiat, M.; Pevzner, A.; Engel, Y.; Burstein, L.; Khatchtourints, A.; Lichtenstein, A.; Kantaev, R.; Patolsky, F. Biorecognition Layer Engineering: Overcoming Screening Limitations of Nanowire-Based FET Devices. *Nano Lett.* **2012**, *12* (10), 5245–5254. https://doi.org/10.1021/nl302434w.

(132) Maehashi, K.; Katsura, T.; Kerman, K.; Takamura, Y.; Matsumoto, K.; Tamiya, E. Label-Free Protein Biosensor Based on Aptamer-Modified Carbon Nanotube Field-Effect Transistors. *Anal. Chem.* **2007**, *79* (2), 782–787. https://doi.org/10.1021/ac060830g.

(133) Filipiak, M. S.; Rother, M.; Andoy, N. M.; Knudsen, A. C.; Grimm, S.; Bachran, C.; Swee, L. K.; Zaumseil, J.; Tarasov, A. Highly Sensitive, Selective and Label-Free Protein Detection in Physiological Solutions Using Carbon Nanotube Transistors with Nanobody Receptors. *Sens. Actuators B Chem.* **2018**, *255*, 1507–1516. https://doi.org/10.1016/j.snb.2017.08.164.

(134) Chen, H.; Zhao, X.; Xi, Z.; Zhang, Y.; Li, H.; Li, Z.; Shi, H.; Huang, L.; Shen, R.; Tao, J.; Wang, T. A New Biosensor Detection System to Overcome the Debye Screening Effect: Dialysis-Silicon Nanowire Field Effect Transistor. *Int. J. Nanomedicine* **2019**, *14*, 2985–2993. https://doi.org/10.2147/IJN.S198734.

(135) Ono, T.; Kanai, Y.; Inoue, K.; Watanabe, Y.; Nakakita, S.; Kawahara, T.; Suzuki, Y.; Matsumoto, K. Electrical Biosensing at Physiological Ionic Strength Using Graphene Field-Effect Transistor in Femtoliter Microdroplet. *Nano Lett.* **2019**, *19* (6), 4004–4009. https://doi.org/10.1021/acs.nanolett.9b01335.

(136) Schasfoort, R. B. M. Chapter 2:History and Physics of Surface Plasmon Resonance. In *Handbook of Surface Plasmon Resonance*; 2017; pp 27–59. https://doi.org/10.1039/9781788010283-00027.

(137) Lambourne, R.; Strivens, T. A. *Paint and Surface Coatings: Theory and Practice.*; Woodhead Pub.: Cambridge, 1999.

(138) Kim, D. R.; Lee, C. H.; Zheng, X. Probing Flow Velocity with Silicon Nanowire Sensors. *Nano Lett.* **2009**, *9* (5), 1984–1988. https://doi.org/10.1021/nl900238a.

(139) Chen, S.; Bomer, J. G.; Carlen, E. T.; van den Berg, A. Al2O3/Silicon NanoISFET with Near Ideal Nernstian Response. *Nano Lett.* **2011**, *11* (6), 2334–2341. https://doi.org/10.1021/nl200623n.

(140) Rim, T.; Meyyappan, M.; Baek, C.-K. Optimized Operation of Silicon Nanowire Field Effect Transistor Sensors. *Nanotechnology* **2014**, *25* (50), 505501. https://doi.org/10.1088/0957-4484/25/50/505501.

(141) Yates, D. E.; Levine, S.; Healy, T. W. Site-Binding Model of the Electrical Double Layer at the Oxide/Water Interface. *J. Chem. Soc. Faraday Trans. 1 Phys. Chem. Condens. Phases* **1974**, *70* (0), 1807–1818. https://doi.org/10.1039/F19747001807.

(142) Dorvel, B. R.; Reddy, B.; Go, J.; Duarte Guevara, C.; Salm, E.; Alam, M. A.; Bashir, R. Silicon Nanowires with High-k Hafnium Oxide Dielectrics for Sensitive Detection of Small Nucleic Acid Oligomers. *ACS Nano* **2012**, *6* (7), 6150–6164. https://doi.org/10.1021/nn301495k.

(143) Zafar, S.; D'Emic, C.; Afzali, A.; Fletcher, B.; Zhu, Y.; Ning, T. Optimization of PH Sensing Using Silicon Nanowire Field Effect Transistors with HfO2 as the Sensing Surface. *Nanotechnology* **2011**, *22* (40), 405501. https://doi.org/10.1088/0957-4484/22/40/405501.

(144) Parizi, K. B.; Yeh, A. J.; Poon, A.; Wong, H. Exceeding Nernst Limit (59mV/PH): CMOS-Based PH Sensor for Autonomous Applications. *2012 Int. Electron Devices Meet.* **2012**. https://doi.org/10.1109/IEDM.2012.6479098.

(145) Parizi, K. B.; Xu, X.; Pal, A.; Hu, X.; Wong, H. S. P. ISFET PH Sensitivity: Counter-Ions Play a Key Role. *Sci. Rep.* **2017**, *7* (1), 41305. https://doi.org/10.1038/srep41305.

(146) Jung, S.-H.; Seo, Y.-M.; Gu, T.; Jang, W.; Kang, S.-G.; Hyeon, Y.; Hyun, S.-H.; Lee, J.-H.; Whang, D. Super-Nernstian PH Sensor Based on Anomalous Charge Transfer Doping of Defect-Engineered Graphene. *Nano Lett.* **2021**, *21* (1), 34–42. https://doi.org/10.1021/acs.nanolett.0c02259.

(147) Spijkman, M.; Smits, E. C. P.; Cillessen, J. F. M.; Biscarini, F.; Blom, P. W. M.; de Leeuw, D. M. Beyond the Nernst-Limit with Dual-Gate ZnO Ion-Sensitive Field-Effect Transistors. *Appl. Phys. Lett.* **2011**, *98* (4), 043502. https://doi.org/10.1063/1.3546169.

(148) Ibarlucea, B.; Römhildt, L.; Zörgiebel, F. M.; Pregl, S.; Vahdatzadeh, M.; Weber, W. M.; Mikolajick, T.; Opitz, J.; Baraban, L.; Cuniberti, G. Gating Hysteresis as an Indicator for Silicon Nanowire FET Biosensors; 2018. https://doi.org/10.3390/app8060950.

(149) Tarasov, A.; Wipf, M.; Stoop, R. L.; Bedner, K.; Fu, W.; Guzenko, V. A.; Knopfmacher, O.; Calame, M.; Schönenberger, C. Understanding the Electrolyte Background for Biochemical Sensing with Ion-Sensitive Field-Effect Transistors. *ACS Nano* **2012**, *6* (10), 9291–9298. https://doi.org/10.1021/nn303795r.

(150) Huang, W.; Diallo, A. K.; Dailey, J. L.; Besar, K.; Katz, H. E. Electrochemical Processes and Mechanistic Aspects of Field-Effect Sensors for Biomolecules. *J. Mater. Chem. C* **2015**, *3* (25), 6445–6470. https://doi.org/10.1039/C5TC00755K.

(151) Bergveld, P. Thirty Years of ISFETOLOGY: What Happened in the Past 30 Years and What May Happen in the next 30 Years. *Sens. Actuators B Chem.* **2003**, *88* (1), 1–20. https://doi.org/10.1016/S0925-4005(02)00301-5.

(152) Liu, Y.; Hedström, M.; Chen, D.; Fan, X.; Mattiasson, B. A Capacitive DNA Sensor-Based Test for Simple and Sensitive Analysis of Antibiotic Resistance in Field Setting. *Biosens. Bioelectron.* **2015**, *64*, 255–259. https://doi.org/10.1016/j.bios.2014.08.084.

(153) Schütt, J.; Sandoval Bojorquez, D. I.; Avitabile, E.; Oliveros Mata, E. S.; Milyukov, G.; Colditz, J.; Delogu, L. G.; Rauner, M.; Feldmann, A.; Koristka, S.; Middeke, J. M.; Sockel, K.; Fassbender, J.; Bachmann, M.; Bornhäuser, M.; Cuniberti, G.; Baraban, L. Nanocytometer for Smart Analysis of Peripheral Blood and Acute Myeloid Leukemia: A Pilot Study. *Nano Lett.* **2020**, *20* (9), 6572–6581. https://doi.org/10.1021/acs.nanolett.0c02300.

(154) Lubin, A. A.; Plaxco, K. W. Folding-Based Electrochemical Biosensors: The Case for Responsive Nucleic Acid Architectures. *Acc. Chem. Res.* **2010**, *43* (4), 496–505. https://doi.org/10.1021/ar900165x.

(155) Syu, Y.-C.; Hsu, W.-E.; Lin, C.-T. Review—Field-Effect Transistor Biosensing: Devices and Clinical Applications. *ECS J. Solid State Sci. Technol.* **2018**, *7* (7), Q3196–Q3207. https://doi.org/10.1149/2.0291807jss.

(156) Fujimoto, T.; Awaga, K. Electric-Double-Layer Field-Effect Transistors with Ionic Liquids. *Phys. Chem. Chem. Phys.* **2013**, *15* (23), 8983–9006. https://doi.org/10.1039/C3CP50755F.

(157) Du, H.; Lin, X.; Xu, Z.; Chu, D. Electric Double-Layer Transistors: A Review of Recent Progress. *J. Mater. Sci.* **2015**, *50* (17), 5641–5673. https://doi.org/10.1007/s10853-015-9121-y.

(158) Park, H.-J.; Kim, S. K.; Park, K.; Lyu, H.-K.; Lee, C.-S.; Chung, S. J.; Yun, W. S.; Kim, M.; Chung, B. H. An ISFET Biosensor for the Monitoring of Maltose-Induced Conformational Changes in MBP. *FEBS Lett.* **2009**, *583* (1), 157–162. https://doi.org/10.1016/j.febslet.2008.11.039.

(159) Kim, K. S.; Lee, H.-S.; Yang, J.-A.; Jo, M.-H.; Hahn, S. K. The Fabrication, Characterization and Application of Aptamer-Functionalized Si-Nanowire FET Biosensors. *Nanotechnology* **2009**, *20* (23), 235501. https://doi.org/10.1088/0957-4484/20/23/235501.

(160) Kawarada, H.; Ruslinda, A. R. Diamond Electrolyte Solution Gate FETs for DNA and Protein Sensors Using DNA/RNA Aptamers. *Phys. Status Solidi A* **2011**, *208* (9), 2005–2016. https://doi.org/10.1002/pssa.201100503.

(161) Chang, J.; Zhou, G.; Gao, X.; Mao, S.; Cui, S.; Ocola, L. E.; Yuan, C.; Chen, J. Real-Time Detection of Mercury Ions in Water Using a Reduced Graphene Oxide/DNA Field-Effect Transistor with Assistance of a Passivation Layer. *Sens. Bio-Sens. Res.* **2015**, *5*, 97–104. https://doi.org/10.1016/j.sbsr.2015.07.009.

(162) Jun, J.; Lee, J. S.; Shin, D. H.; Jang, J. Aptamer-Functionalized Hybrid Carbon Nanofiber FET-Type Electrode for a Highly Sensitive and Selective Platelet-Derived Growth Factor Biosensor. *ACS Appl. Mater. Interfaces* **2014**, *6* (16), 13859–13865. https://doi.org/10.1021/am5032693.

(163) Hao, Z.; Zhu, Y.; Wang, X.; Rotti, P. G.; DiMarco, C.; Tyler, S. R.; Zhao, X.; Engelhardt, J. F.; Hone, J.; Lin, Q. Real-Time Monitoring of Insulin Using a Graphene Field-Effect Transistor Aptameric Nanosensor. *ACS Appl. Mater. Interfaces* **2017**, *9* (33), 27504–27511. https://doi.org/10.1021/acsami.7b07684.

(164) Godin, M.; Tabard-Cossa, V.; Miyahara, Y.; Monga, T.; Williams, P. J.; Beaulieu, L. Y.; Bruce Lennox, R.; Grutter, P. Cantilever-Based Sensing: The Origin of Surface Stress and Optimization Strategies. *Nanotechnology* **2010**, *21* (7), 075501. https://doi.org/10.1088/0957-4484/21/7/075501.

(165) Lakhin, A. V.; Tarantul, V. Z.; Gening, L. V. Aptamers: Problems, Solutions and Prospects. *Acta Naturae* **2013**, *5* (4), 34–43.

(166) Martin, J. A.; Chávez, J. L.; Chushak, Y.; Chapleau, R. R.; Hagen, J.; Kelley-Loughnane, N. Tunable Stringency Aptamer Selection and Gold Nanoparticle Assay for Detection of Cortisol. *Anal. Bioanal. Chem.* **2014**, *406* (19), 4637–4647. https://doi.org/10.1007/s00216-014-7883-8.

(167) Lee, M.; Boettiger, D.; Ducheyne, P.; J Composto, R. Self-Assembled Monolayers of Omega-Functional Silanes: A Platform for Understanding Cellular Adhesion at the Molecular Level. In *Departmental Papers (BE)*; 2007; pp 1–16.

(168) Fan, Y.; Xie, Y.; Zhao, Z.; Zhao, Y.; Yu, R.; Liu, X.; Lin, Y.; Lin, C. Wettability Read-out Strategy for Aptamer Target Binding Based on a Recognition/Hydrophobic Bilayer Surface. *Chem. Commun.* **2020**, *56* (46), 6225–6228. https://doi.org/10.1039/D0CC01936D.

(169) Zhan, S.; Pan, Y.; Gao, Z. F.; Lou, X.; Xia, F. Biological and Chemical Sensing Applications Based on Special Wettable Surfaces. *TrAC Trends Anal. Chem.* **2018**, *108*, 183–194. https://doi.org/10.1016/j.trac.2018.09.001.

(170) Maiolo, D.; Federici, S.; Ravelli, L.; Depero, L. E.; Hamad-Schifferli, K.; Bergese, P. Nanomechanics of Surface DNA Switches Probed by Captive Contact Angle. *J. Colloid Interface Sci.* **2013**, *402*, 334–339. https://doi.org/10.1016/j.jcis.2013.03.069.

(171) Peng, Y.; Li, L.; Mu, X.; Guo, L. Aptamer-Gold Nanoparticle-Based Colorimetric Assay for the Sensitive Detection of Thrombin. *Sens. Actuators B Chem.* **2013**, *177*, 818–825. https://doi.org/10.1016/j.snb.2012.12.004.

(172) Liu, J.; Bai, W.; Niu, S.; Zhu, C.; Yang, S.; Chen, A. Highly Sensitive Colorimetric Detection of 17β-Estradiol Using Split DNA Aptamers Immobilized on Unmodified Gold Nanoparticles. *Sci. Rep.* **2014**, *4*, 7571. https://doi.org/10.1038/srep07571.

(173) Chen, S.-J.; Huang, Y.-F.; Huang, C.-C.; Lee, K.-H.; Lin, Z.-H.; Chang, H.-T. Colorimetric Determination of Urinary Adenosine Using Aptamer-Modified Gold Nanoparticles. *Biosens. Bioelectron.* **2008**, *23* (11), 1749–1753. https://doi.org/10.1016/j.bios.2008.02.008.

(174) Elghanian, R.; Storhoff, J. J.; Mucic, R. C.; Letsinger, R. L.; Mirkin, C. A. Selective Colorimetric Detection of Polynucleotides Based on the Distance-Dependent Optical Properties of Gold Nanoparticles. *Science* **1997**, *277* (5329), 1078–1081. https://doi.org/10.1126/science.277.5329.1078.

(175) Zheng, Y.; Wang, Y.; Yang, X. Aptamer-Based Colorimetric Biosensing of Dopamine Using Unmodified Gold Nanoparticles. *Sens. Actuators B Chem.* **2011**, *156* (1), 95–99. https://doi.org/10.1016/j.snb.2011.03.077.

(176) Gaviña, P.; Parra, M.; Gil, S.; M. Costero, A. Red or Blue? Gold Nanoparticles in Colorimetric Sensing. In *Gold Nanoparticles - Reaching New Heights*; Rahman, M., Mohammed Asiri, A., Eds.; IntechOpen, 2019. https://doi.org/10.5772/intechopen.80052.

(177) Kypr, J.; Kejnovská, I.; Renčiuk, D.; Vorlíčková, M. Circular Dichroism and Conformational Polymorphism of DNA. *Nucleic Acids Res.* **2009**, *37* (6), 1713–1725. https://doi.org/10.1093/nar/gkp026.

(178) Rodger, A. Nucleic Acid Circular Dichroism. In *Encyclopedia of Biophysics*; Roberts, G. C. K., Ed.; Springer: Berlin, Heidelberg, 2013; pp 1759–1761. https://doi.org/10.1007/978-3-642-16712-6_632.

(179) Gray, D. M.; Ratliff, R. L.; Vaughan, M. R. [19] Circular Dichroism Spectroscopy of DNA. In *Methods in Enzymology*; DNA Structures Part A: Synthesis and Physical Analysis of DNA; Academic Press, 1992; Vol. 211, pp 389–406. https://doi.org/10.1016/0076-6879(92)11021-A.

(180) Mergny, J.-L.; Phan, A.-T.; Lacroix, L. Following G-Quartet Formation by UV-Spectroscopy. *FEBS Lett.* **1998**, *435* (1), 74–78. https://doi.org/10.1016/S0014-5793(98)01043-6.

(181) Vorlíčková, M.; Kejnovská, I.; Sagi, J.; Renčiuk, D.; Bednářová, K.; Motlová, J.; Kypr, J. Circular Dichroism and Guanine Quadruplexes. *Methods* **2012**, *57* (1), 64–75. https://doi.org/10.1016/j.ymeth.2012.03.011.

(182) Ranjbar, B.; Gill, P. Circular Dichroism Techniques: Biomolecular and Nanostructural Analyses- A Review. *Chem. Biol. Drug Des.* **2009**, *74* (2), 101–120. https://doi.org/10.1111/j.1747-0285.2009.00847.x.

(183) Kikin, O.; D'Antonio, L.; Bagga, P. S. QGRS Mapper: A Web-Based Server for Predicting G-Quadruplexes in Nucleotide Sequences. *Nucleic Acids Res.* **2006**, *34* (suppl_2), W676–W682. https://doi.org/10.1093/nar/gkl253.

(184) Roxo, C.; Kotkowiak, W.; Pasternak, A. G-Quadruplex-Forming Aptamers—Characteristics, Applications, and Perspectives. *Molecules* **2019**, *24* (20), 3781. https://doi.org/10.3390/molecules24203781.

(185) McGinely, N. L.; Plumb, J. A.; Wheate, N. J. DNA-Based Aptamer Fails as a Simultaneous Cancer Targeting Agent and Drug Delivery Vehicle for a Phenanthroline-Based Platinum(II) Complex. *J. Inorg. Biochem.* **2013**, *128*, 124–130. https://doi.org/10.1016/j.jinorgbio.2013.07.021.

(186) Chen, N.; Zhu, Y.; Feng, Z.; Wang, Q.; Qin, S.; Quan, K.; Huang, J.; Liu, J.; Yang, X.; Wang, K. Selection of Aptamers for Hydrophobic Drug Docetaxel To Improve Its Solubility. *ACS Appl. Bio Mater.* **2018**, *1* (1), 168–174. https://doi.org/10.1021/acsabm.8b00073.

(187) Rachwal, P. A.; Findlow, I. S.; Werner, J. M.; Brown, T.; Fox, K. R. Intramolecular DNA Quadruplexes with Different Arrangements of Short and Long Loops. *Nucleic Acids Res.* **2007**, *35* (12), 4214–4222. https://doi.org/10.1093/nar/gkm316.

(188) Pruessner, J. C.; Champagne, F.; Meaney, M. J.; Dagher, A. Dopamine Release in Response to a Psychological Stress in Humans and Its Relationship to Early Life Maternal Care: A Positron Emission Tomography Study Using [11C]Raclopride. *J. Neurosci.* **2004**, *24* (11), 2825–2831. https://doi.org/10.1523/JNEUROSCI.3422-03.2004.

(189) Marinelli, M.; Piazza, P. V. Interaction between Glucocorticoid Hormones, Stress and Psychostimulant Drugs*. *Eur. J. Neurosci.* **2002**, *16* (3), 387–394. https://doi.org/10.1046/j.1460-9568.2002.02089.x.

(190) Römhildt, L.; Pahlke, C.; Zörgiebel, F.; Braun, H.-G.; Opitz, J.; Baraban, L.; Cuniberti, G. Patterned Biochemical Functionalization Improves Aptamer-Based Detection of Unlabeled Thrombin in a Sandwich Assay. *ACS Appl. Mater. Interfaces* **2013**, *5* (22), 12029–12035. https://doi.org/10.1021/am4038245.

(191) Dandy, D. S.; Wu, P.; Grainger, D. W. Array Feature Size Influences Nucleic Acid Surface Capture in DNA Microarrays. *Proc. Natl. Acad. Sci. U. S. A.* **2007**, *104* (20), 8223–8228. https://doi.org/10.1073/pnas.0606054104.

(192) Peterson, A. W.; Heaton, R. J.; Georgiadis, R. M. The Effect of Surface Probe Density on DNA Hybridization. *Nucleic Acids Res.* **2001**, *29* (24), 5163–5168.

(193) Klinghammer, S.; Uhlig, T.; Patrovsky, F.; Böhm, M.; Schütt, J.; Pütz, N.; Baraban, L.; Eng, L. M.; Cuniberti, G. Plasmonic Biosensor Based on Vertical Arrays of Gold Nanoantennas. *ACS Sens.* **2018**, *3* (7), 1392–1400. https://doi.org/10.1021/acssensors.8b00315.

(194) De Heer, J. The Principle of Le Châtelier and Braun. *J. Chem. Educ.* **1957**, *34* (8), 375. https://doi.org/10.1021/ed034p375.

(195) Hołyst, R.; Poniewierski, A. *Thermodynamics for Chemists, Physicists and Engineers*; Springer Science & Business Media, 2012.

(196) Nair, P. R.; Alam, M. A. Screening-Limited Response of NanoBiosensors. *Nano Lett.* **2008**, *8* (5), 1281–1285. https://doi.org/10.1021/nl072593i.

(197) Zhang, G.-J.; Chua, J. H.; Chee, R.-E.; Agarwal, A.; Wong, S. M.; Buddharaju, K. D.; Balasubramanian, N. Highly Sensitive Measurements of PNA-DNA Hybridization Using Oxide-Etched Silicon Nanowire Biosensors. *Biosens. Bioelectron.* **2008**, *23* (11), 1701–1707. https://doi.org/10.1016/j.bios.2008.02.006.

(198) Elfström, N.; Karlström, A. E.; Linnros, J. Silicon Nanoribbons for Electrical Detection of Biomolecules. *Nano Lett.* **2008**, *8* (3), 945–949. https://doi.org/10.1021/nl080094r.

(199) Zheng, G.; Patolsky, F.; Cui, Y.; Wang, W. U.; Lieber, C. M. Multiplexed Electrical Detection of Cancer Markers with Nanowire Sensor Arrays. *Nat. Biotechnol.* **2005**, *23* (10), 1294–1301. https://doi.org/10.1038/nbt1138.

(200) Sheibani, S.; Capua, L.; Kamaei, S.; Akbari, S. S. A.; Zhang, J.; Guerin, H.; Ionescu, A. M. Extended Gate Field-Effect-Transistor for Sensing Cortisol Stress Hormone. *Commun. Mater.* **2021**, *2* (1), 1–10. https://doi.org/10.1038/s43246-020-00114-x.

(201) Arroyo-Currás, N.; Somerson, J.; Vieira, P. A.; Ploense, K. L.; Kippin, T. E.; Plaxco, K. W. Real-Time Measurement of Small Molecules Directly in Awake, Ambulatory Animals. *Proc. Natl. Acad. Sci.* **2017**, *114* (4), 645–650. https://doi.org/10.1073/pnas.1613458114.

(202) Feagin, T. A.; Maganzini, N.; Soh, H. T. Strategies for Creating Structure-Switching Aptamers. *ACS Sens.* **2018**, *3* (9), 1611–1615. https://doi.org/10.1021/acssensors.8b00516.

(203) Ruscito, A.; DeRosa, M. C. Small-Molecule Binding Aptamers: Selection Strategies, Characterization, and Applications. *Front. Chem.* **2016**, *4*. https://doi.org/10.3389/fchem.2016.00014.

(204) Baliga, S.; Muglikar, S.; Kale, R. Salivary PH: A Diagnostic Biomarker. *J. Indian Soc. Periodontol.* **2013**, *17* (4), 461–465. https://doi.org/10.4103/0972-124X.118317.

(205) Miller, R.; Stalder, T.; Jarczok, M.; Almeida, D. M.; Badrick, E.; Bartels, M.; Boomsma, D. I.; Coe, C. L.; Dekker, M. C. J.; Donzella, B.; Fischer, J. E.; Gunnar, M. R.; Kumari, M.; Lederbogen, F.; Oldehinkel, A. J.; Power, C.; Rosmalen, J. G.; Ryff, C. D.; Subramanian, S. V.; Tiemeier, H.; Watamura, S. E.; Kirschbaum, C. The CIRCORT Database: Reference Ranges and Seasonal Changes in Diurnal Salivary Cortisol Derived from a Meta-Dataset Comprised of 15 Field Studies. *Psychoneuroendocrinology* **2016**, *73*, 16–23. https://doi.org/10.1016/j.psyneuen.2016.07.201.

(206) Bani-Issa, W.; Radwan, H.; Marzooq, F. A.; Awar, S. A.; Al-Shujairi, A. M.; Samsudin, A. R.; Khasawneh, W.; Albluwi, N. <p>Salivary Cortisol, Subjective Stress and Quality of Sleep Among Female Healthcare Professionals</P>. *J. Multidiscip. Healthc.* **2020**, *13*, 125–140. https://doi.org/10.2147/JMDH.S229396.

(207) Kobayashi, H.; Miyazaki, Y. Distribution Characteristics of Salivary Cortisol Measurements in a Healthy Young Male Population. *J. Physiol. Anthropol.* **2015**, *34* (1), 30. https://doi.org/10.1186/s40101-015-0068-0.

(208) Andersson, K.; Areskoug, D.; Hardenborg, E. Exploring Buffer Space for Molecular Interactions. *J. Mol. Recognit. JMR* **1999**, *12* (5), 310–315. https://doi.org/10.1002/(SICI)1099-1352(199909/10)12:5<310::AID-JMR470>3.0.CO;2-5.

(209) Goode, J. A.; Rushworth, J. V. H.; Millner, P. A. Biosensor Regeneration: A Review of Common Techniques and Outcomes. *Langmuir* **2015**, *31* (23), 6267–6276. https://doi.org/10.1021/la503533g.

6 Summary and outlook

6.1 Summary

The previous chapters substantiate the importance of an adequate selection, linkage, and integration of the individual components of a biosensor. The matching of receptors to the transducers' surface is crucial for achieving suitable devices. Understanding the underlying biorecognition principles at the interface helps to engineer appropriate sensing systems for the aimed application.

This thesis presents suitable platforms for two applications to fulfill the need for a sensitive and fast biosensor. On the one hand, a plasmonic device based on vertically aligned gold nanoantennas tracked the DNA hybridization by means of LSPR. On the other hand, an electric SiNW-based FET sensor monitored salivary cortisol. Both realize the label-free detections of biomolecules in real-time measurements.

The goal of developing a point-of-care device unifies both platforms and asks for the design of relatively compact read-out devices. Further, both arrangements were combined with microfluidic support that allows continuous reaction monitoring. Finally, the choice of DNA-based receptors for biorecognition further associates both systems.

However, the investigated biosensing platforms differ mainly in the transducers' materials, their operation mode, the chosen target, and thus the latter application purpose. While gold nanoantennas allowed for sensing by means of LSPR to explore fundamental hybridization mechanisms of complementary DNA on nanostructures, silicon nanowires were used to monitor the level of the small molecule cortisol in the saliva of volunteers electrically.

Here, to engineer suitable interfaces for the different applications, the interplay of the two different nanostructures with DNA-based receptors was evaluated for the goal of biosensing. So, two different biochemical functionalization strategies are presented within this thesis to meet each sensor's requirements. Furthermore, the later biorecognition with associating target molecules was explored using optical and electrochemical methods in both approaches.

First, the reliable detection of DNA and its hybridization was demonstrated for gold surfaces. For this purpose, vertically aligned gold antennas could be fabricated in large areas hallmarked by defect-poorness, high density, and distinct geometries. Changing the aspect ratio resulted in varying optical properties; long-axis resonance peaks between

685 and 851nm could be adjusted. The real-time suitability of the biosensor was demonstrated via this setup's continuous recording of the optical spectra with measurements carried out inside a flow channel at high throughput.

A modification step based on thiol chemistry was applied to gold substrates to immobilize the receptor DNA. Further investigations concerning the pre-treatment of the substrates with plasma and backfilling with mercaptohexanol resulted in an enhanced probe DNA with high availability for complementary DNA hybridization. The immobilization, blocking, and subsequent (de)hybridization of the oligonucleotide onto nanoantennas were monitored by means of LSPR in real-time and compared to conventional SPR. In addition, the performance of the nanostructured sensor was assessed by varying the lengths (25bp and 100bp) and concentrations of associating target DNA. Successful surface modification was evidenced by measuring the fluorescence intensities of DNA samples on the respective substrates. The supplemental reaction with non-target DNA verified the specific binding between the probe and target DNA. All binding processes were reversible by the introduction of chemical denaturation agents. The functionalization with organic molecules caused redshifts in LSPR. Upon immobilization, a redshift of 1 nm was detected; further backfilling and hybridization led to a peak shift of 2 and 5 nm for 25 and 100 bp, respectively. The correlation between the refractive index and the sensing signal was demonstrated by adjusting the RI of ethylene glycol/water mixtures and tracking the associating spectral positions of the nanoantennas. Based on these results, it is concluded that the accumulation of probe and target molecules causes the measured redshifts.

With the advances mentioned earlier, the performance of the plasmonic biosensor can be quickly coordinated to various applications and targets by simply tailoring the aspect ratio of diameter to length.

In a second application, the detection of the stress biomarker cortisol in saliva could be demonstrated using SINW-based FET arrays, which are mounted on a portable platform. Further, the modular system of the portable platform with plug connections allows for easy integration of the sensors. The tailored functionalization of the nanoscopic FET sensor with aptamers enabled a label-free, sensitive, and selective detection.

First, device characterizations demonstrated the capability of the portable platform to run multiple FETs simultaneously for sensing purposes. Implemented into microfluidic

channels, numerous FETs demonstrated a high sensitivity towards surface chemistry changes by means of measuring pH values. Assessing the pH in real-time served as a precursor for biosensing.

A covalent attachment strategy of the DNA-based receptors to the nanowires was chosen to exploit their sensitivities for biosensing purposes. Hence, SiNWs were functionalized using a TESPSA-based surface modification approach, allowing for a direct attachment of amino-modified receptor molecules. The successful surface modification steps were tracked using contact angle measurements and fluorescence microscopy.

For the detection of cortisol, a specific aptamer, which experiences a conformational change by altering its secondary structure upon binding to the target, was chosen as the receptor. The interaction of the aptamer with the analyte cortisol was surveyed with a colorimetric assay based on AuNPS, circular dichroism, and fluorescence microscopy to prove the functionality of the aptamer after immobilization. The previous methods indicate that a rearrangement of the intramolecular charges within the DNA backbone accompanies the conformational change. Furthermore, the process happens close to the surface of the NWs and thus overcomes the usual Debye screening length limitations.

The performance of the FET in physiological buffers and saliva is demonstrated by monitoring the salivary cortisol levels in the buffer and saliva. Cortisol levels from four volunteers ranging from around 0.05 µg/dL up to 0.6 µg/dL (while the average calibrated dynamic range of the devices represents 0.005–0.3 µg/dL) were evaluated with FETs and successfully compared to the values obtained with a commercial LIA kit.

The platform provides a potentially powerful tool for detecting various targets, as there is the possibility for custom-demanded functionalization with antibodies, aptamers, or any receptor of choice. Further, the modular system envisions a high potential for the goal of a user-friendly point-of-care device.

6.2 Perspectives – toward multiplexed biosensing applications

Within this thesis, two conceptions of biosensors were established and successfully applied by demonstrating the detection of selected analytes in real-time. Although both sensors showed reliable performances within the detection of their aimed application, further improvement towards the analysis of multiple parameters shall be considered.

In general, biomarkers and their concentrations echo the biological processes of an organism. They thus are a sign of normal or abnormal process, of a condition, or the presence and severity of a disease[1]. However, due to the heterogeneous nature of many diseases, the kind and concentration of biomarkers can vary at different stages of diseases. Among others, exemplary diseases are multiple sclerosis, Alzheimer's, and Parkinson's, as there is no single specific biomarker for direct diagnosis detected yet, but different biomarkers are involved[2–5]. Furthermore, multiplexed biosensors can be applied to defining the proteomic state of cellular organisms, which involves the analysis of thousands of proteins in a single experiment, helping to understand their function, and how their expression changes in health and disease[6–8]. Consequently, the analysis of a single biomarker might be insufficient to provide enough information for diagnostics or to monitor certain diseases' progress. Therefore, multiplexed biosensing strategies have become a focal point for developing next-generation sensors[9–11].

Two promising levers can be used with the biosensing platforms mentioned above to accomplish this goal. On the one hand, integrating microfluidics, which permits parallel delivery and mixing of different solutions, is required[10,12,13]. On the other hand, spatial multiplexing involves the individual modification and read-out of each biosensor[9,10,14,15].

Apart from the multiplexing strategies mentioned above (incl. the creation of barcodes with microfluidic channels), other methods based on temporal division[16–18], frequency division[19], and particle-based multiplexing[20] have been reported. However, those strategies are disregarded in this thesis as they are barely includable with the here presented platforms.

The simple application of PDMS microfluidic channel networks within the two platforms is a promising approach due to its ease of use. Here, simple designs of parallel channel networks and the incorporation of crossed channels empower multiparameter analysis[10,21–24]. Moreover, the use of PDMS is rapid, low-cost, easy, and reduces time in prototyping and optimizing the designed channel systems[25].

Further, the employment of droplet-based microfluidics offers the potential to achieve high throughput while being simple and robust at the same time[26]. In droplet microfluidics, each droplet captures one experimental condition so that different reaction parameters can be adjusted, and multiparameter analysis is inspired[27–29]. The suitability to combine this approach with the rapid detection capability of FETs has been demonstrated by Schütt et al. in-house, who carried out the enzymatic test for glucose detection with SiNW FETs[30].

However, for vertically aligned antennas, the mentioned approaches are rather tricky to realize as antennas might disturb droplets or require further improvement of channel designs to prevent leakage. However, multiplexed detection of analytes with LSPR sensors is documented[31–35].

Multiplexing strategies following a spatial division are widely described as this configuration involves minimal detection interferences and compatibility with most measurement methods. The first approach of multiplexed electrical biosensors dates back to 2005 when Zheng et al. detected multiple cancer biomarkers using silicon nanowires[36]. In addition, electronic biosensors' suitability for multiplexed applications has been demonstrated by detecting multiple biomarkers against Alzheimer's disease, sepsis, and other metabolites[14,37–40].

Even though complete multiparameter analysis with the proposed platforms has not been fully achieved yet, the first steps were performed to reach this goal. Figure 6-1A envisions the concept of achieving a multiplexed sensing application with portable SiNW FETs. First, spot patterns for individual modification of single FETs with nanoplotting devices are created, compared to Figure 6-1B. Then, the beforehand designed spot patterns were successfully transferred to single FETs (compare Figure 6-1C) with the help of automatic image recognition software (compare to Figure 6-1D). As proof of

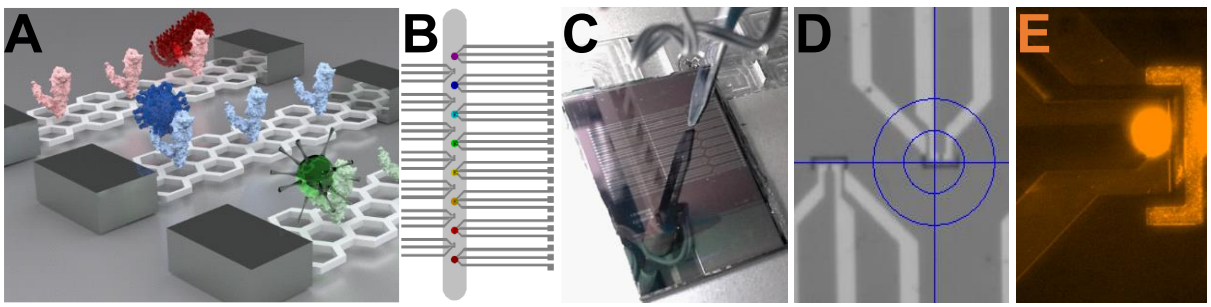

Figure 6-1: Conceptual image of spatially multiplexed SiNW FETs. A) Individually functionalized FETs allow for the detection of different biomarkers. B) Concept for spot plan to individual modification of FETs: the used design and interconnections allow for the detection of eight biomarkers. C) Photography of nanoplotting step whose spot pattern is automatically recognized with D) the help of image recognition software. E) Nanoplotted spot on a single FET device

concept, Figure 6-1E shows the modification of a FET with fluorescently labeled aptamer against cortisol. The operating sensing performance of this FET can be surveyed in Figure 5-11, respectively.

In summary, within the presented methods, FET arrays on a single chip can be functionalized and evaluated independently at the same time. The mentioned advances result in a promising indication to detect multiple analytes from a single sample. Further, harmonizing tailored spotting arrays to existing designs of biosensors provides a very versatile, suitable toolbox for future scientific investigations as well as for further engineering of facile PoC sensing setups. They are finding aimed applications not only in SiNW-based biosensing but also in the greater field of bionanotechnology.

6.3 References

(1) Califf, R. M. Biomarker Definitions and Their Applications. *Exp. Biol. Med.* **2018**, *243* (3), 213–221. https://doi.org/10.1177/1535370217750088.

(2) Barichello, T.; Generoso, J. S.; Singer, M.; Dal-Pizzol, F. Biomarkers for Sepsis: More than Just Fever and Leukocytosis—a Narrative Review. *Crit. Care* **2022**, *26* (1), 14. https://doi.org/10.1186/s13054-021-03862-5.

(3) Ziemssen, T.; Akgün, K.; Brück, W. Molecular Biomarkers in Multiple Sclerosis. *J. Neuroinflammation* **2019**, *16* (1), 272. https://doi.org/10.1186/s12974-019-1674-2.

(4) Parnetti, L.; Gaetani, L.; Eusebi, P.; Paciotti, S.; Hansson, O.; El-Agnaf, O.; Mollenhauer, B.; Blennow, K.; Calabresi, P. CSF and Blood Biomarkers for Parkinson's Disease. *Lancet Neurol.* **2019**, *18* (6), 573–586. https://doi.org/10.1016/S1474-4422(19)30024-9.

(5) Blennow, K.; Zetterberg, H. Biomarkers for Alzheimer's Disease: Current Status and Prospects for the Future. *J. Intern. Med.* **2018**, *284* (6), 643–663. https://doi.org/10.1111/joim.12816.

(6) *HUPO - Home*. https://hupo.org/ (accessed 2022-09-23).

(7) Adhikari, S.; Nice, E. C.; Deutsch, E. W.; Lane, L.; Omenn, G. S.; Pennington, S. R.; Paik, Y.-K.; Overall, C. M.; Corrales, F. J.; Cristea, I. M.; Van Eyk, J. E.; Uhlén, M.; Lindskog, C.; Chan, D. W.; Bairoch, A.; Waddington, J. C.; Justice, J. L.; LaBaer, J.; Rodriguez, H.; He, F.; Kostrzewa, M.; Ping, P.; Gundry, R. L.; Stewart, P.; Srivastava, S.; Srivastava, S.; Nogueira, F. C. S.; Domont, G. B.; Vandenbrouck, Y.; Lam, M. P. Y.; Wennersten, S.; Vizcaino, J. A.; Wilkins, M.; Schwenk, J. M.; Lundberg, E.; Bandeira, N.; Marko-Varga, G.; Weintraub, S. T.; Pineau, C.; Kusebauch, U.; Moritz, R. L.; Ahn, S. B.; Palmblad, M.; Snyder, M. P.; Aebersold, R.; Baker, M. S. A High-Stringency Blueprint of the Human Proteome. *Nat. Commun.* **2020**, *11* (1), 5301. https://doi.org/10.1038/s41467-020-19045-9.

(8) Melton, L. Proteomics in Multiplex. *Nature* **2004**, *429* (6987), 105–107. https://doi.org/10.1038/429101a.

(9) Gil Rosa, B.; Akingbade, O. E.; Guo, X.; Gonzalez-Macia, L.; Crone, M. A.; Cameron, L. P.; Freemont, P.; Choy, K.-L.; Güder, F.; Yeatman, E.; Sharp, D. J.; Li, B. Multiplexed Immunosensors for Point-of-Care Diagnostic Applications. *Biosens. Bioelectron.* **2022**, *203*, 114050. https://doi.org/10.1016/j.bios.2022.114050.

(10) Araz, M. K.; Tentori, A. M.; Herr, A. E. Microfluidic Multiplexing in Bioanalyses. *J. Lab. Autom.* **2013**, *18* (5), 350–366. https://doi.org/10.1177/2211068213491408.

(11) Jarockyte, G.; Karabanovas, V.; Rotomskis, R.; Mobasheri, A. Multiplexed Nanobiosensors: Current Trends in Early Diagnostics. *Sensors* **2020**, *20* (23), 6890. https://doi.org/10.3390/s20236890.

(12) Sohrabi, S.; Kassir, N.; Moraveji, M. K. Droplet Microfluidics: Fundamentals and Its Advanced Applications. *RSC Adv.* **2020**, *10* (46), 27560–27574. https://doi.org/10.1039/D0RA04566G.

(13) Seemann, R.; Brinkmann, M.; Pfohl, T.; Herminghaus, S. Droplet Based Microfluidics. *Rep. Prog. Phys.* **2011**, *75* (1), 016601. https://doi.org/10.1088/0034-4885/75/1/016601.

(14) Kim, K.; Kim, M.-J.; Kim, D. W.; Kim, S. Y.; Park, S.; Park, C. B. Clinically Accurate Diagnosis of Alzheimer's Disease via Multiplexed Sensing of Core Biomarkers in Human Plasma. *Nat. Commun.* **2020**, *11* (1), 119. https://doi.org/10.1038/s41467-019-13901-z.

(15) Gao, W.; Emaminejad, S.; Nyein, H. Y. Y.; Challa, S.; Chen, K.; Peck, A.; Fahad, H. M.; Ota, H.; Shiraki, H.; Kiriya, D.; Lien, D.-H.; Brooks, G. A.; Davis, R. W.; Javey, A. Fully Integrated Wearable Sensor Arrays for Multiplexed in Situ Perspiration Analysis. *Nature* **2016**, *529* (7587), 509–514. https://doi.org/10.1038/nature16521.

(16) Balakrishnan, K. R.; Whang, J. C.; Hwang, R.; Hack, J. H.; Godley, L. A.; Sohn, L. L. Node-Pore Sensing Enables Label-Free Surface-Marker Profiling of Single Cells. *Anal. Chem.* **2015**, *87* (5), 2988–2995. https://doi.org/10.1021/ac504613b.

(17) Zhao, C.; Thuo, M. M.; Liu, X. A Microfluidic Paper-Based Electrochemical Biosensor Array for Multiplexed Detection of Metabolic Biomarkers. *Sci. Technol. Adv. Mater.* **2013**, *14* (5), 054402. https://doi.org/10.1088/1468-6996/14/5/054402.

(18) Liang, T.; Jiang, N.; Zhou, S.; Wang, X.; Xu, Y.; Wu, C.; Kirsanov, D.; Legin, A.; Wan, H.; Wang, P. Multiplexed All-Solid-State Ion-Sensitive Light-Addressable Potentiometric Sensor (ISLAPS) System Based on Silicone-Rubber for Physiological Ions Detection. *Anal. Chim. Acta* **2021**, *1179*, 338603. https://doi.org/10.1016/j.aca.2021.338603.

(19) Vaidyanathan, R.; Van Leeuwen, L. M.; Rauf, S.; Shiddiky, M. J. A.; Trau, M. A Multiplexed Device Based on Tunable Nanoshearing for Specific Detection of Multiple Protein Biomarkers in Serum. *Sci. Rep.* **2015**, *5*. https://doi.org/10.1038/srep09756.

(20) Liu, R.; Wang, N.; Kamili, F.; Sarioglu, A. F. Microfluidic CODES: A Scalable Multiplexed Electronic Sensor for Orthogonal Detection of Particles in Microfluidic Channels. *Lab. Chip* **2016**, *16* (8), 1350–1357. https://doi.org/10.1039/c6lc00209a.

(21) Hong, S.-L.; Tang, M.; Chen, Z.; Ai, Z.; Liu, F.; Wang, S.; Zhang, N.; Liu, K. High-Performance Multiplex Microvalves Fabrication and Using for Tumor Cells Staining on a Microfluidic Chip. *Biomed. Microdevices* **2019**, *21* (4), 87. https://doi.org/10.1007/s10544-019-0434-5.

(22) Zakharova, M.; Carmo, M. A. P. do; Helm, M. W. van der; Le-The, H.; Graaf, M. N. S. de; Orlova, V.; Berg, A. van den; Meer, A. D. van der; Broersen, K.; Segerink, L. I. Multiplexed Blood–Brain Barrier Organ-on-Chip. *Lab. Chip* **2020**, *20* (17), 3132–3143. https://doi.org/10.1039/D0LC00399A.

(23) L. Garcia-Cordero, J.; J. Maerkl, S. Multiplexed Surface Micropatterning of Proteins with a Pressure-Modulated Microfluidic Button-Membrane. *Chem. Commun.* **2013**, *49* (13), 1264–1266. https://doi.org/10.1039/C2CC37740C.

(24) de Hoyos-Vega, J. M.; Gonzalez-Suarez, A. M.; Garcia-Cordero, J. L. A Versatile Microfluidic Device for Multiple Ex Vivo/in Vitro Tissue Assays Unrestrained from Tissue Topography. *Microsyst. Nanoeng.* **2020**, *6* (1), 40. https://doi.org/10.1038/s41378-020-0156-0.

(25) Duffy, D. C.; McDonald, J. C.; Schueller, O. J.; Whitesides, G. M. Rapid Prototyping of Microfluidic Systems in Poly(Dimethylsiloxane). *Anal. Chem.* **1998**, *70* (23), 4974–4984. https://doi.org/10.1021/ac980656z.

(26) Baker, M. Digital PCR Hits Its Stride. *Nat. Methods* **2012**, *9* (6), 541–544. https://doi.org/10.1038/nmeth.2027.

(27) Cedillo-Alcantar, D. F.; Han, Y. D.; Choi, J.; Garcia-Cordero, J. L.; Revzin, A. Automated Droplet-Based Microfluidic Platform for Multiplexed Analysis of Biochemical Markers in Small Volumes. *Anal. Chem.* **2019**, *91* (8), 5133–5141. https://doi.org/10.1021/acs.analchem.8b05689.

(28) Brouzes, E.; Medkova, M.; Savenelli, N.; Marran, D.; Twardowski, M.; Hutchison, J. B.; Rothberg, J. M.; Link, D. R.; Perrimon, N.; Samuels, M. L. Droplet Microfluidic Technology for Single-Cell High-Throughput Screening. *Proc. Natl. Acad. Sci.* **2009**, *106* (34), 14195–14200. https://doi.org/10.1073/pnas.0903542106.

(29) Cui, J. Q.; Cui, B.; Liu, F. X.; Lin, Y.; Yao, S. A Multiplexable Microfluidic Injector for Versatile Encoding of Droplets. *Sens. Actuators B Chem.* **2022**, *371*, 132573. https://doi.org/10.1016/j.snb.2022.132573.

(30) Schütt, J.; Ibarlucea, B.; Illing, R.; Zörgiebel, F. M.; Pregl, S.; Nozaki, D.; Weber, W. M.; Mikolajick, T.; Baraban, L.; Cuniberti, G. Compact Nanowire Sensors Probe Microdroplets. *Nano Lett.* **2016**, *16* (8), 4991–5000. https://doi.org/10.1021/acs.nanolett.6b01707.

(31) Chen, J.-S.; Chen, P.-F.; Lin, H. T.-H.; Huang, N.-T. A Localized Surface Plasmon Resonance (LSPR) Sensor Integrated Automated Microfluidic System for Multiplex Inflammatory Biomarker Detection. *The Analyst* **2020**, *145* (23), 7654–7661. https://doi.org/10.1039/D0AN01201G.

(32) Chen, P.; Chung, M. T.; McHugh, W.; Nidetz, R.; Li, Y.; Fu, J.; Cornell, T. T.; Shanley, T. P.; Kurabayashi, K. Multiplex Serum Cytokine Immunoassay Using Nanoplasmonic Biosensor Microarrays. *ACS Nano* **2015**, *9* (4), 4173–4181. https://doi.org/10.1021/acsnano.5b00396.

(33) Aćimović, S. S.; Ortega, M. A.; Sanz, V.; Berthelot, J.; Garcia-Cordero, J. L.; Renger, J.; Maerkl, S. J.; Kreuzer, M. P.; Quidant, R. LSPR Chip for Parallel, Rapid, and Sensitive Detection of Cancer Markers in Serum. *Nano Lett.* **2014**, *14* (5), 2636–2641. https://doi.org/10.1021/nl500574n.

(34) Chengjun Huang; Putzeys, J.; Jian Ye; Reekmans, G.; Verhaegen, K.; Lagae, L.; Verstreken, K.; Borghs, G. Lable-Free Biosensor Based on Localized Surface Plasmon Resonance in a Multi-Channel Microfluidic Chip. In *2009 IEEE Sensors Applications Symposium*; IEEE: New Orleans, LA, USA, 2009; pp 43–46. https://doi.org/10.1109/SAS.2009.4801774.

(35) Soler, M.; Belushkin, A.; Cavallini, A.; Kebbi-Beghdadi, C.; Greub, G.; Altug, H. Multiplexed Nanoplasmonic Biosensor for One-Step Simultaneous Detection of Chlamydia Trachomatis and Neisseria Gonorrhoeae in Urine. *Biosens. Bioelectron.* **2017**, *94*, 560–567. https://doi.org/10.1016/j.bios.2017.03.047.

(36) Zheng, G.; Patolsky, F.; Cui, Y.; Wang, W. U.; Lieber, C. M. Multiplexed Electrical Detection of Cancer Markers with Nanowire Sensor Arrays. *Nat. Biotechnol.* **2005**, *23* (10), 1294–1301. https://doi.org/10.1038/nbt1138.

(37) Krivitsky, V.; Zverzhinetsky, M.; Patolsky, F. Redox-Reactive Field-Effect Transistor Nanodevices for the Direct Monitoring of Small Metabolites in Biofluids toward Implantable Nanosensors Arrays. *ACS Nano* **2020**, *14* (3), 3587–3594. https://doi.org/10.1021/acsnano.9b10090.

(38) Krivitsky, V.; Zverzhinetsky, M.; Krivitsky, A.; Hsiung, L.-C.; Naddaka, V.; Gabriel, I.; Lefler, S.; Conroy, J.; Burstein, L.; Patolsky, F. Cellular Metabolomics by a Universal Redox-Reactive Nanosensors Array: From the Cell Level to Tumor-on-a-Chip Analysis. *Nano Lett.* **2019**, *19* (4), 2478–2488. https://doi.org/10.1021/acs.nanolett.9b00052.

(39) Zupančič, U.; Jolly, P.; Estrela, P.; Moschou, D.; Ingber, D. E. Graphene Enabled Low-Noise Surface Chemistry for Multiplexed Sepsis Biomarker Detection in Whole Blood. *Adv. Funct. Mater.* **2021**, *31* (16), 2010638. https://doi.org/10.1002/adfm.202010638.

(40) Bay, H. H.; Vo, R.; Dai, X.; Hsu, H.-H.; Mo, Z.; Cao, S.; Li, W.; Omenetto, F. G.; Jiang, X. Hydrogel Gate Graphene Field-Effect Transistors as Multiplexed Biosensors. *Nano Lett.* **2019**, *19* (4), 2620–2626. https://doi.org/10.1021/acs.nanolett.9b00431.

7 List of publications

7.1 Peer-reviewed publications

Bockholt, R.; Paschke, S.; Heubner, La.; Ibarlucea, B.; Laupp, A.; Janićijević, Ž.; **Klinghammer, S.**; Balakin, S.; Maitz, Ma.; Werner, C.; Baraban, L.; Spieth, P. M. Real-Time Monitoring of Blood Parameters in the Intensive Care Unit: State-of-the-Art and Perspectives. *J. Clin. Med.* **2022**.

Sessi, V.; Ibarlucea, B.; Seichepine, F.; **Klinghammer, S.**; Ibrahim, I.; Heinzig, A.; Szabo, N.; Mikolajick, T.; Hierlemann, A.; Frey, U.; Weber, W. M.; Baraban, L.; Cuniberti, G. Multisite Dopamine Sensing With Femtomolar Resolution Using a CMOS Enabled Aptasensor Chip. *Front. Neurosci.* **2022**, *16*.

Klinghammer, S.; Voitsekhivska, T.; Licciardello, N.; Kim, K.; Baek, C.-K.; Cho, H.; Wolter, K.-J.; Kirschbaum, C.; Baraban, L.; Cuniberti, G. Nanosensor-Based Real-Time Monitoring of Stress Biomarkers in Human Saliva Using a Portable Measurement System. *ACS Sens.* **2020**, *5* (12), 4081–4091. https://doi.org/10.1021/acssensors.0c02267.

Klinghammer, S.; Rauch, S.; Pregl, S.; Uhlmann, P.; Baraban, L.; Cuniberti, G. Surface Modification of Silicon Nanowire Based Field Effect Transistors with Stimuli-Responsive Polymer Brushes for Biosensing Applications. *Micromachines* **2020**, *11* (3), 274. https://doi.org/10.3390/mi11030274.

Klinghammer, S.; Uhlig, T.; Patrovsky, F.; Böhm, M.; Schütt, J.; Pütz, N.; Baraban, L.; Eng, L. M.; Cuniberti, G. Plasmonic Biosensor Based on Vertical Arrays of Gold Nanoantennas. *ACS Sens.* **2018**, *3* (7), 1392–1400. https://doi.org/10.1021/acssensors.8b00315.

7.2 Publications in preparation

Klinghammer, S. et al., Hemocompatible Electrochemical Sensors for Continuous Monitoring of Biomarkers in Blood

Co-Author in Timpel, J. et al., Sensors for *in situ* Monitoring of Oral and Dental Health Parameters in Saliva

7.3 Selected international conferences

Klinghammer, S. et al. “Nanosensor- basierter Nachweis von Stressbiomarker Cortisol im menschlichen Speichel in Echtzeit mit einem tragbaren Messsystem”, *talk* at conference “4. DGZ-Gemeinschaftstagung des DGZ-Verbundes” , November 26 - 28, 2020, online

Klinghammer, S. et al. “Multiplexed (bio)-sensing platform for detection of cortisol and further steroids“, *poster* at conference “Nanonet International conference of the International Helmholtz Research School for Nanoelectronic Networks”, October 8 - 11, 2019, Dresden, Germany

Klinghammer et al. “Multiplexed detection of steroids with silicon nanowire field-effect- transistors”, *talk* at “NanoBioSensors conference”, September 4 - 5, 2017, Dresden, Germany

Klinghammer, S. et al. “Multiplexed sensing of steroids with silicon nanowire field-effect- transistors”, *talk* at the conference “Trends in Nanotechnology”, June 5 – 9, 2017, Dresden, Germany

Klinghammer, S. et al., “Multiplexed sensing of small molecules with silicon nanowire field- effect- transistors”, *poster* at the “annual DPG Spring Meeting of condensed matter section”, March 19 – 24, 2017, Dresden, Germany

Uhlig T., Klinghammer S., “Biosensing with plasmonic gold nanorod arrays”, *poster* at the “Annual DPG Spring Meeting of condensed matter section”, March 19 – 24, 2017, Dresden, Germany

Kelle, S. et al. “Plasmonic Nanobiosensors: Development and fabrication of a prototype for innovative diagnostics of diseases, *Poster* at “International Conference on Functional Integrated nano Systems (NanoFIS)”, December 3 – 5, 2014, Graz, Austria

8 Acknowledgments

Tba☺

9 Versicherung

Diese Arbeit wurde am Institut für Werkstoffwissenschaft der Technischen Universität Dresden unter der wissenschaftlichen Betreuung von Prof. Dr. Gianaurelio Cuniberti durchgeführt.

Hiermit versichere ich, dass ich die vorliegende Arbeit ohne unzulässige Hilfe Dritter und ohne Benutzung anderer als der angegebenen Hilfsmittel angefertigt habe; die aus fremden Quellen direkt oder indirekt übernommenen Gedanken sind als solche kenntlich gemacht. Bei der Auswahl und Auswertung des Materials sowie bei der Herstellung des Manuskripts habe ich Unterstützung von folgenden Personen erhalten:

Dr. Bergoi Ibarlucea	(Korrekturlesen der gesamten Arbeit)
Dr. Larysa Baraban	(Korrekturlesen der gesamten Arbeit)
Dr.- Ing. Andreas Pönicke	(Korrekturlesen der gesamten Arbeit)
Anita Jakschik	(Korrekturlesen der Kurzfassung und Thesen)
Dr. Leif Riemenschneider	(Korrekturlesen der Kurzfassung)
Dr.- Ing. Felix Zörgiebel	(Matlab-Programm für SiNW FET Plattform)
Dr.- Ing. Tetiana Voitsekhivska	(Bereitstellung Hardware MUXER Platform)
Dr. Tino Uhlig	(Bereitstellung von Nanoantennen und Messaufbau LSPR Plattform)

Weitere Personen waren an der geistigen Herstellung der vorliegenden Arbeit nicht beteiligt. Insbesondere habe ich nicht die Hilfe eines kommerziellen Promotionsberaters in Anspruch genommen. Dritte haben von mir keine geldwerten Leistungen für Arbeiten erhalten, die in Zusammenhang mit dem Inhalt der vorgelegten Dissertation stehen. Die Arbeit wurde bisher weder im Inland noch im Ausland in gleicher oder ähnlicher Form einer anderen Prüfungsbehörde vorgelegt.

Darüber hinaus erkenne ich die Promotionsordnung der Fakultät Maschinenwesen der Technischen Universität Dresden vom 01.07.2001 an.

Dresden, den
Stephanie Klinghammer

A Appendix

A.1 Protocols

A.1.1 Functionalization of gold antennas with thiolated DNA

Clean substrates	• Immerse substrates in water, acetone, and isopropanol under ultrasound, 5min each • N_2 dry • Oxygen plasma treatment of substrates for 2min
Microfluidic channel	• Attach quickly after plasma treatment PDMS channels (see section A.1.4) • rest under appropriate pressure for 1h
Functionalization with thiolated DNA	• Inject via tubing system 1-10µM thiol-modified DNA, react for at least 16h • Rinse
Backfilling	• Inject 5mM mercaptohexanol solution • React for 30min • Rinse

A.1.2 Functionalization of SiO_2 with TESPSA and amino-modified receptors

Clean substrates	• Immerse substrates in water, acetone, and isopropanol under ultrasound, 5min each • N_2 dry • Activation of substrates with oxygen plasma
TESPSA	• Place TESPSA aliquot in an open container into a Petri dish • Place substrates next to TESPSA, close the Petri dish • Apply vacuum and infrared light for 4h
Curing	• Vent vacuum • Cure substrates at 120°C for at least 2h
Functionalization with NH_2-receptor	• Add 1-10µM amino-modified receptor in amine-free buffer (e.g., 1x PBS) dropwise

	• OR: Place prepared samples in nanoplotter and imprint receptors according to the spot plan • Incubate for 1h • Rinse with PBS

A.1.3 Functionalization with APTES and carboxyl-modified receptors

Clean substrates	• See A.1.2
Preparation APTES	• 2 % silane solution in 95:5 (vol/vol) absolute ethanol/water mixture • hydrolysis for 10 min • sample immersion for 0.5h • rinse in absolute ethanol (3 x) • N2 dry
Curing	• incubation in an oven at 120°C for 20 min
Preparation of COOH-containing receptor	• Prepare 0.1M NHS in DMSO & 0.4M EDC-HCl in dI water • Mix 10 mM receptor with carboxyl group with 0.4 M EDC and 0.1 M NHS in a ratio 1:1:1 • Incubate for 30 min to activate the carboxyl group • add activated solution to APTES- modified surface and incubate for 60 min • rinse with buffer

A.1.4 Preparation of microfluidic channels via soft lithography

Pre-polymer mixing	• Mix PDMS- base and curing agent 10:1 (by weight) • Degas under vacuum until no more air bubbles are visible
Casting	• Pour gas-free mixture onto a master structure • Put a metal frame around the structure to prevent leakage and • *insert tubing into liquid PDMS (for LSPR sensing)
Curing	• At 70°C (for at least 5h)
Mold disassembly	• Peel cured PDMS carefully from a master structure

	• cut into proper geometry using a scalpel • *punch channel in- and outlets using a biopsy needle (for FET sensing)
Attach to LSPR sensors	• Activation of PDMS and substrate in oxygen plasma for 5 seconds • Align channel geometry over the associating sensing structures • Press the two surfaces together (to form covalent Si-O-Si bonds)
Attach to FET sensors	• Align channel geometry over the associating sensing structures

A.2 Predicted secondary structures

The secondary structures of complementary targets and formed duplexes were predicted with web-based algorithms "AllSub" (targets) and "bifold"(duplex)[1]. The algorithms were also executed for probes and shorter targets but showed no possible intramolecular base pairs within the 25bp probe or the 25bp target.

A.2.1 Secondary structures of 100base pair target without probe-strands

Structure 1

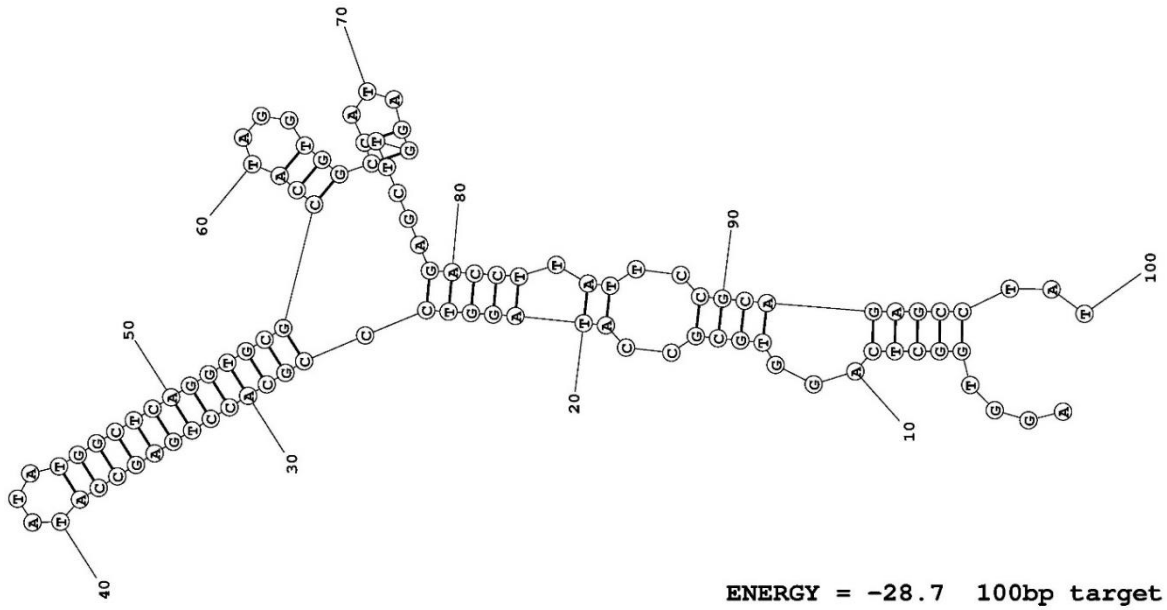

Structure 2

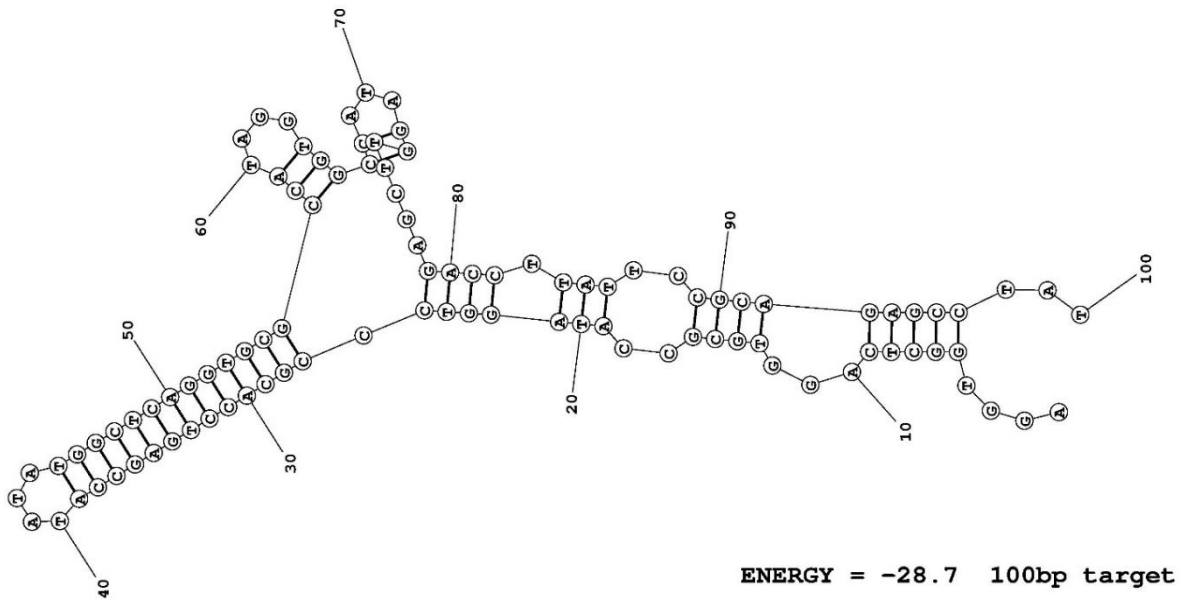

[1] Jessica S. Reuter and David H. Mathews, 'RNAstructure: Software for RNA Secondary Structure Prediction and Analysis', *BMC Bioinformatics*, 11.1 (2010), 129 <https://doi.org/10.1186/1471-2105-11-129>.

Structure 3

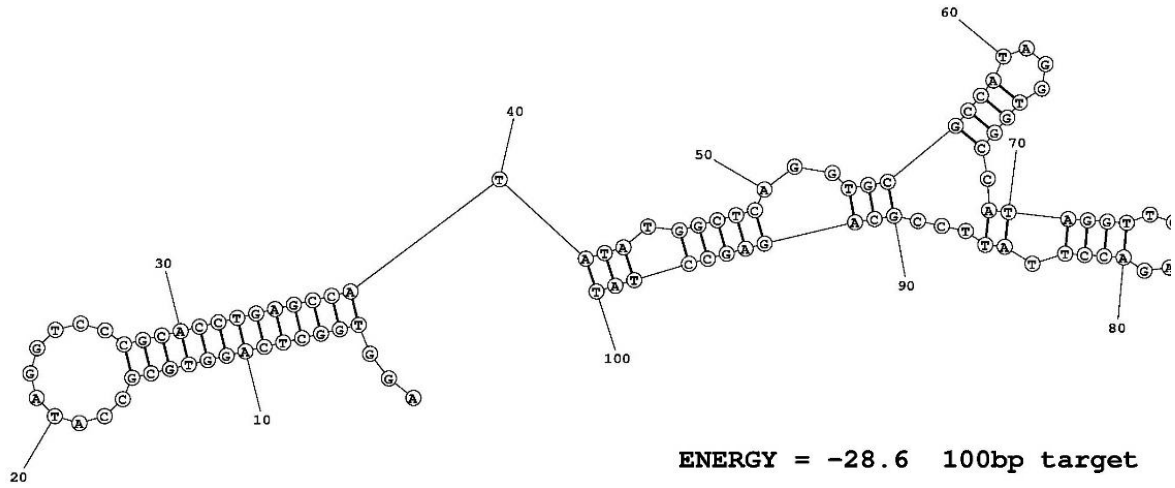

Structure 4

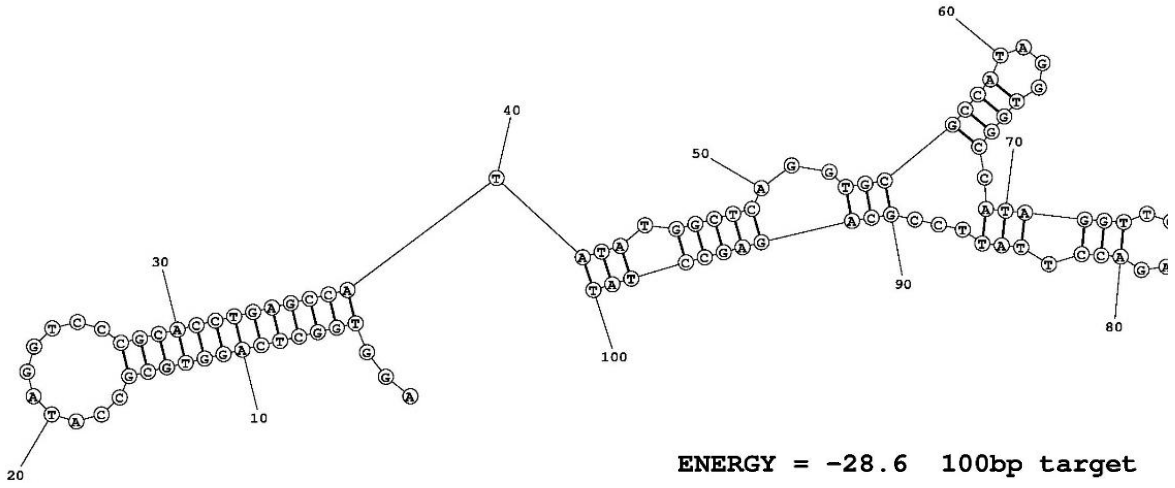

Structure 5

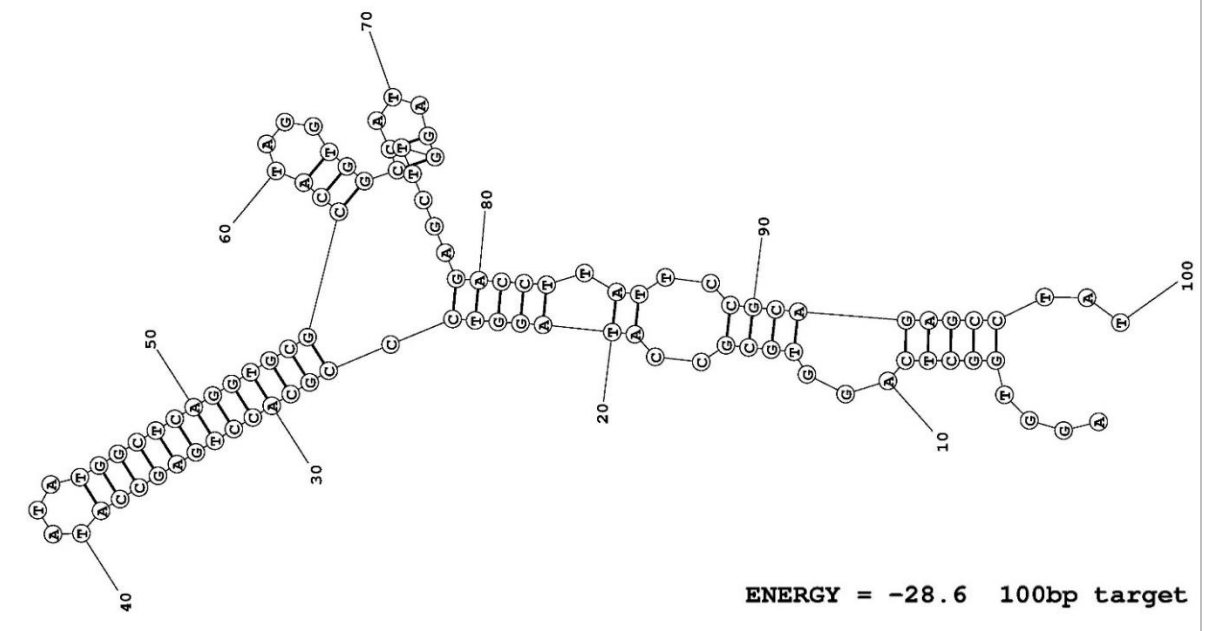

Structure 6

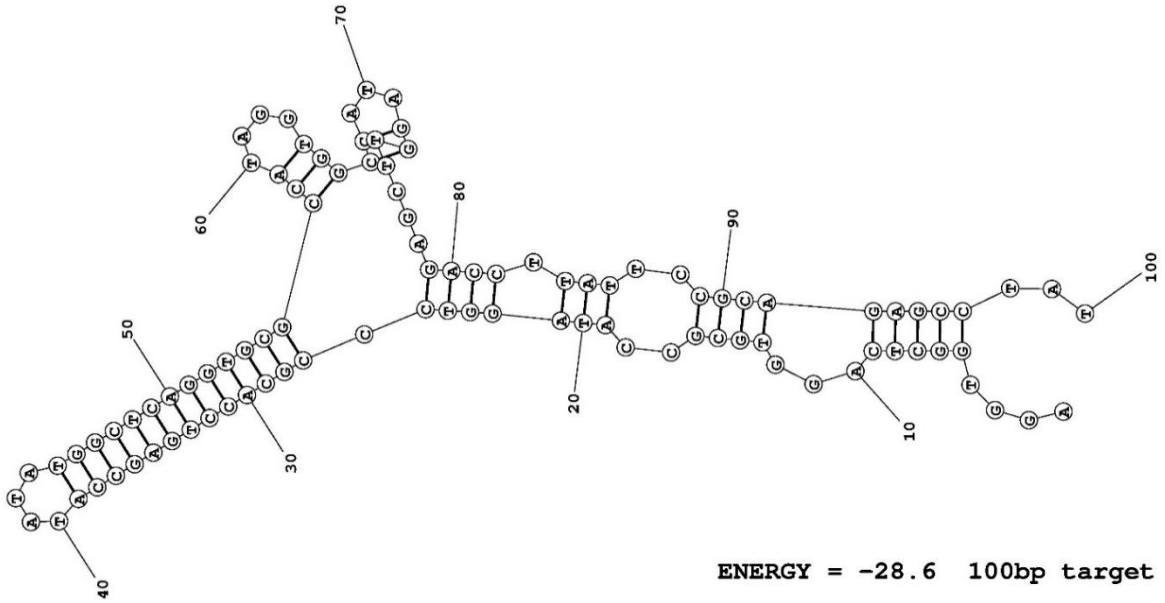

Structure 7

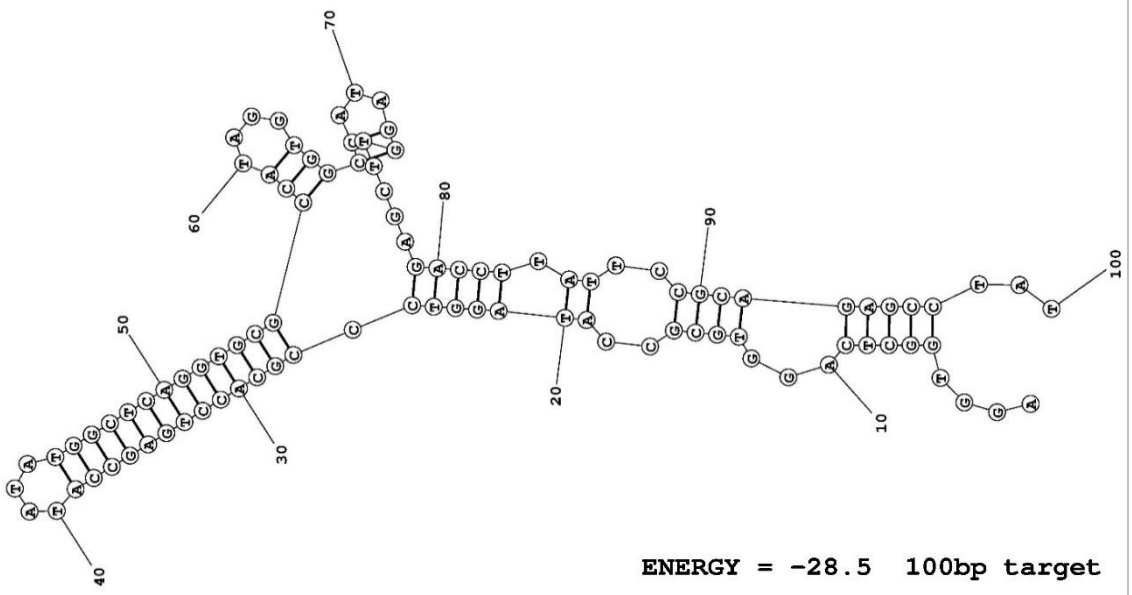

Structure 8

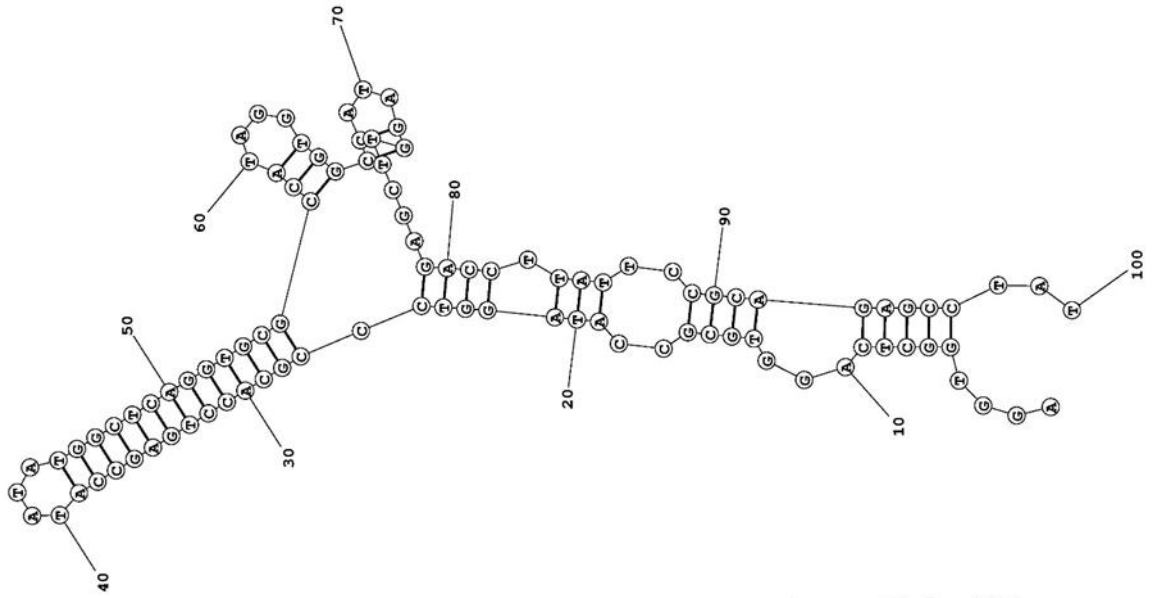

Structure 9

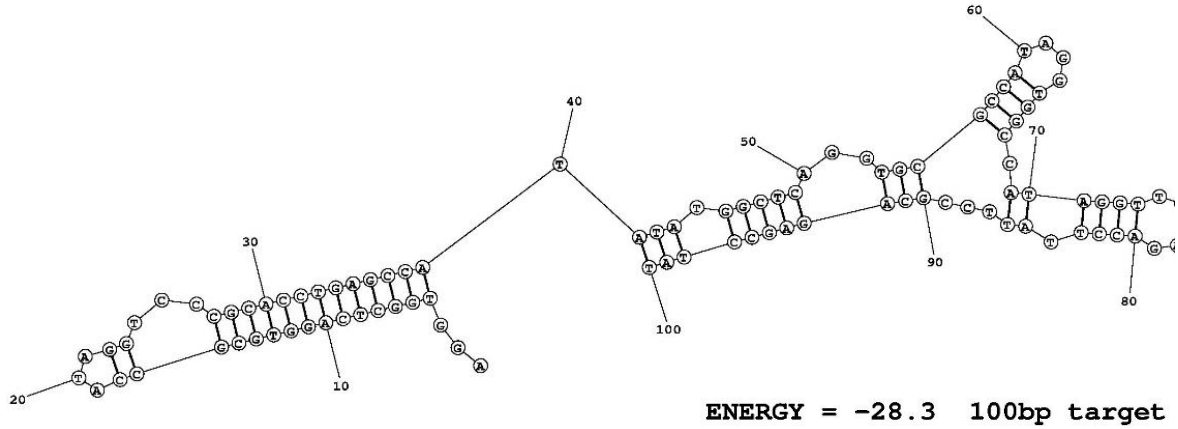

Structure 10

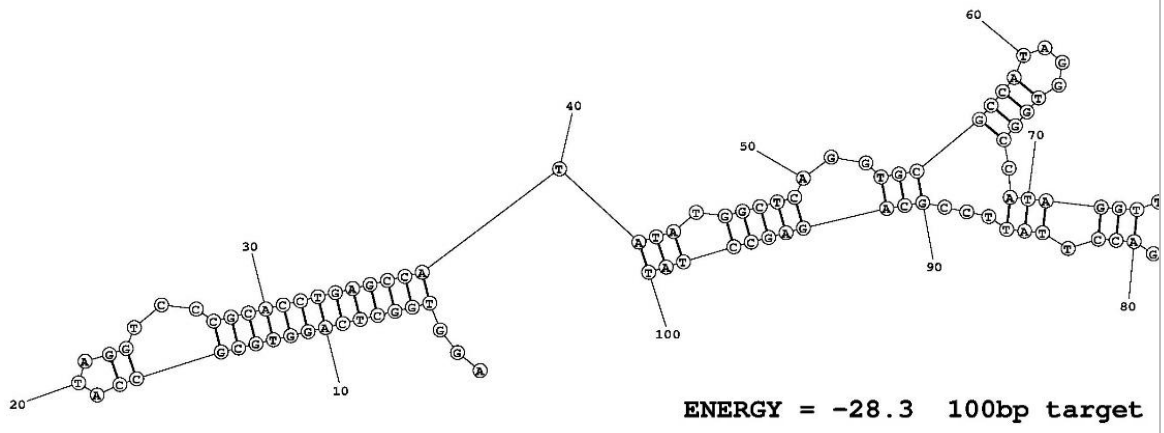

Structure 11

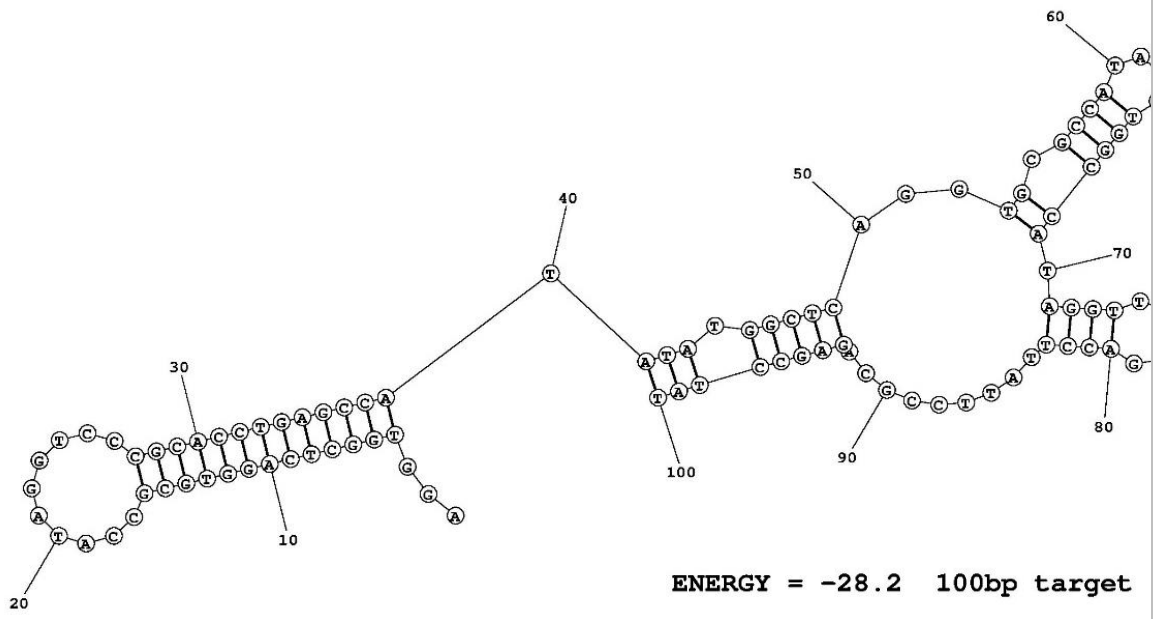

Structure 12

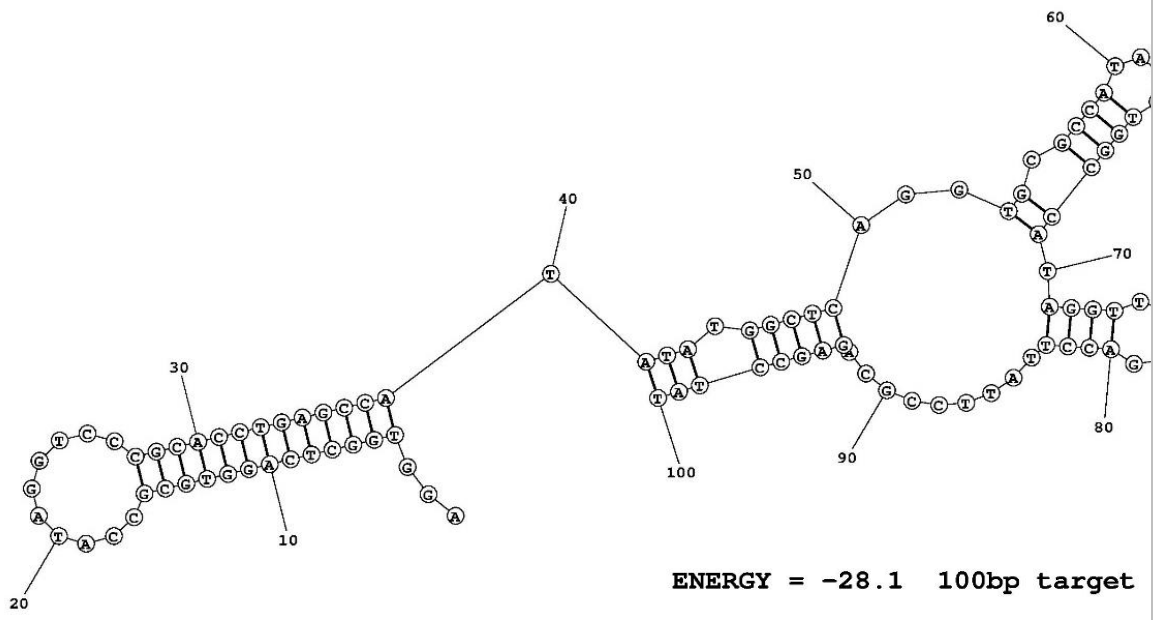

Structure 13

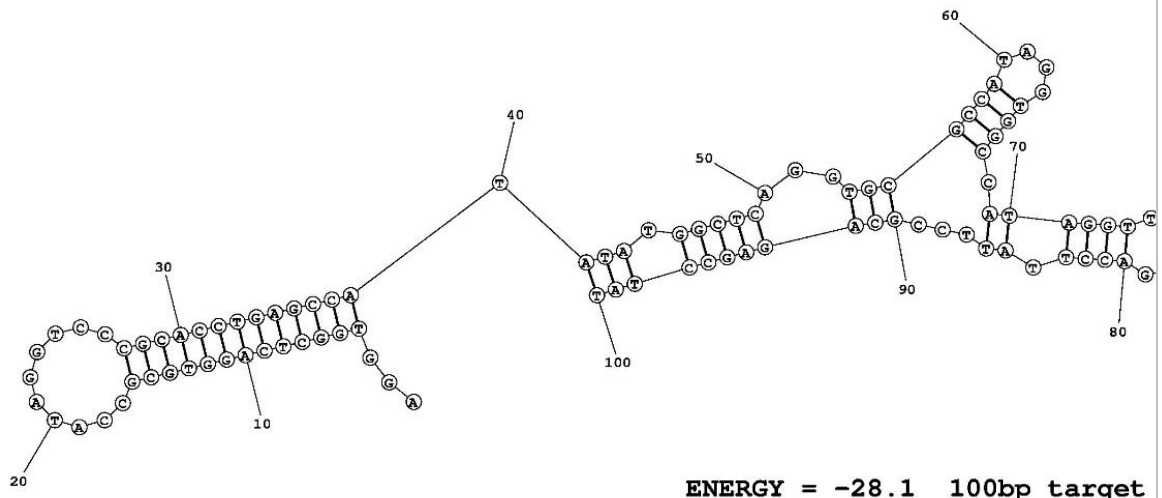

Structure 14

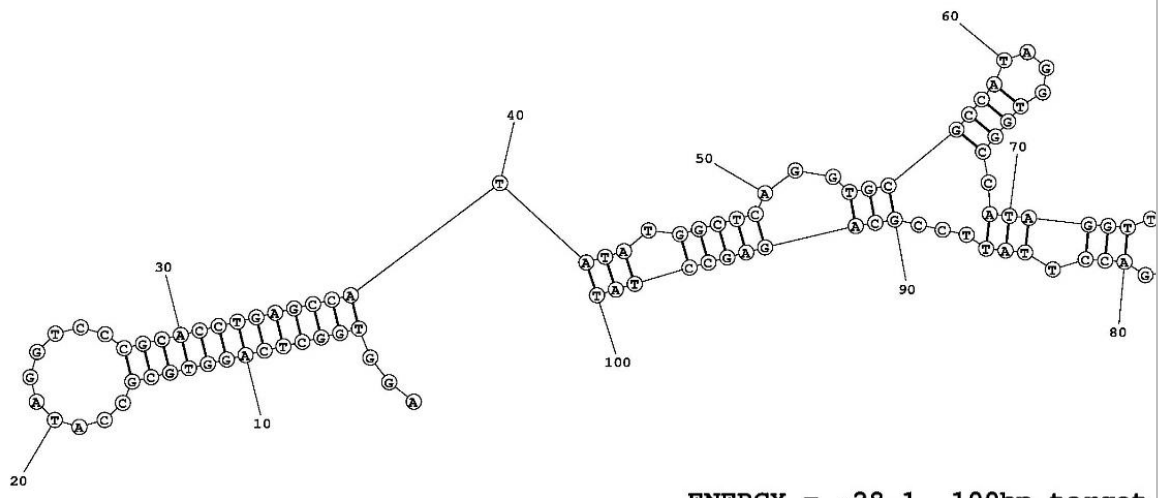

A.2.2 Secondary structures of 100base pair target with 25 base pair probe-strand

Structure 1

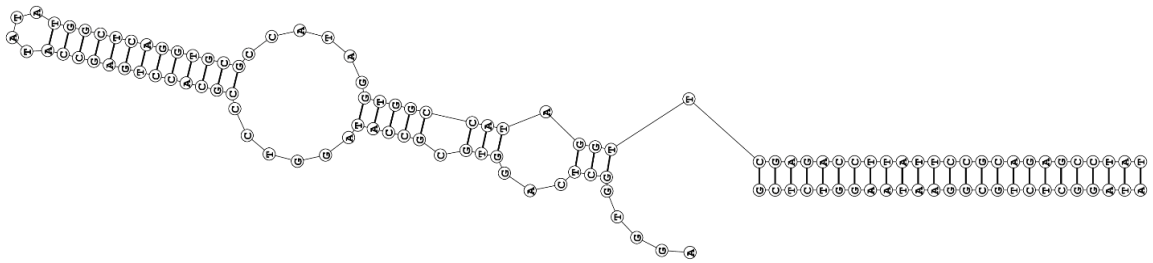

ENERGY = −87.5 probe_ 100bp target

Structure 2

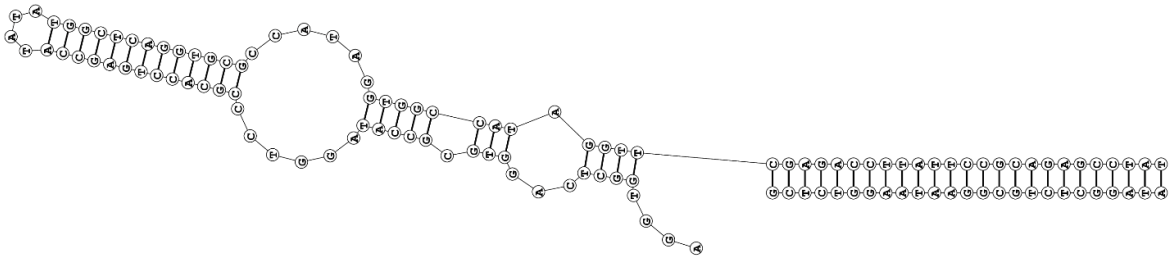

ENERGY = −87.3 probe_ 100bp target

Structure 3

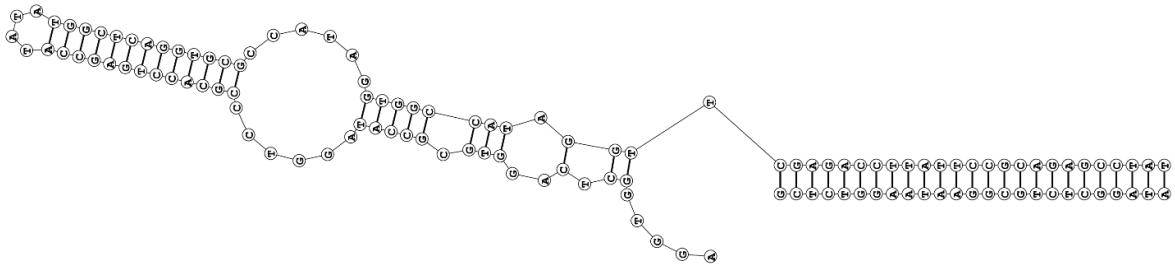

ENERGY = −86.7 probe_ 100bp target

Structure 4

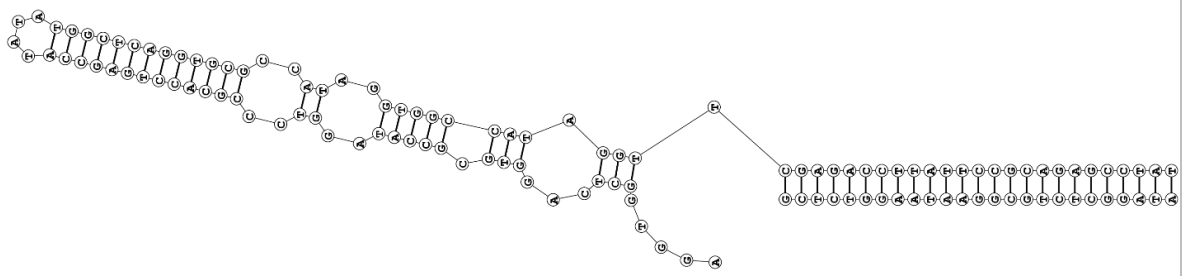

ENERGY = −86.2 probe_ 100bp target

Structure 5

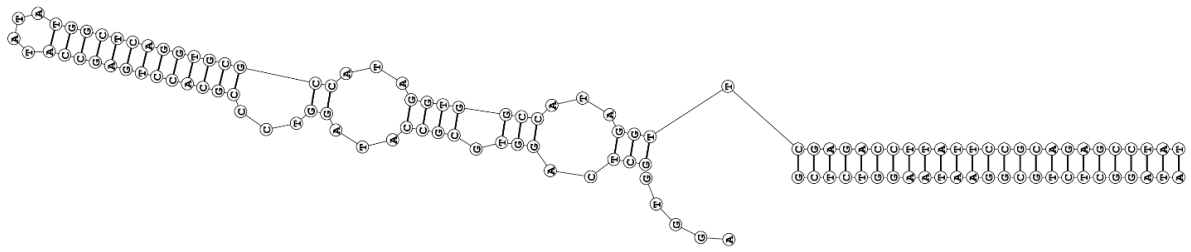

ENERGY = -86.1 probe_ 100bp target

Structure 6

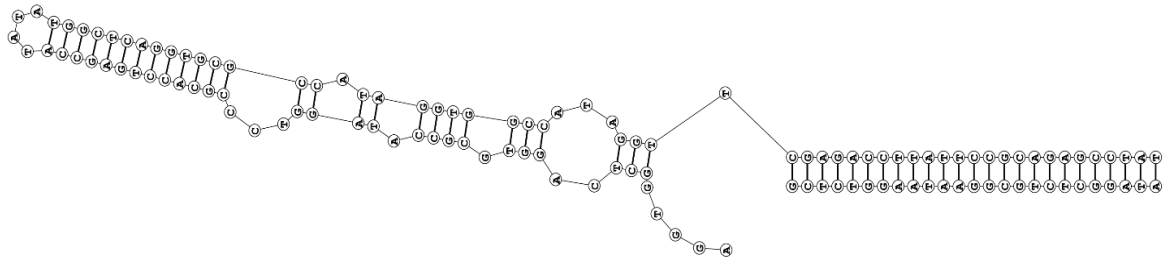

ENERGY = -86.0 probe_ 100bp target

Structure 7

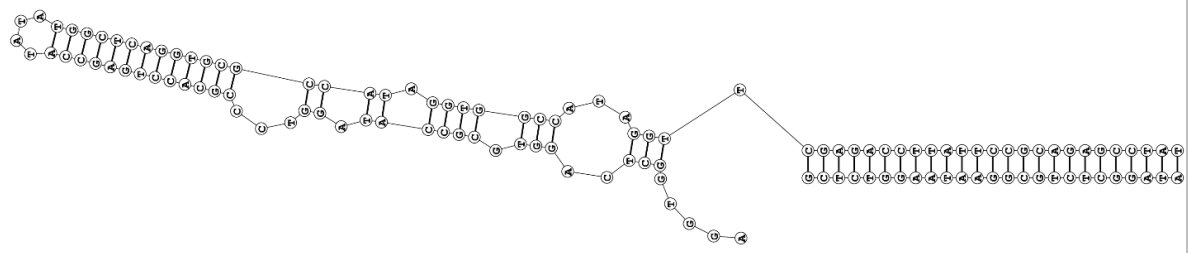

ENERGY = -85.8 probe_ 100bp target

Structure 8

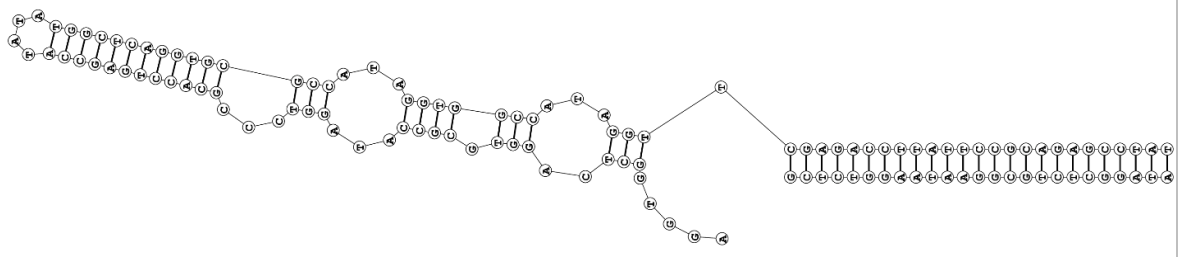

ENERGY = -85.7 probe_ 100bp target

Structure 9

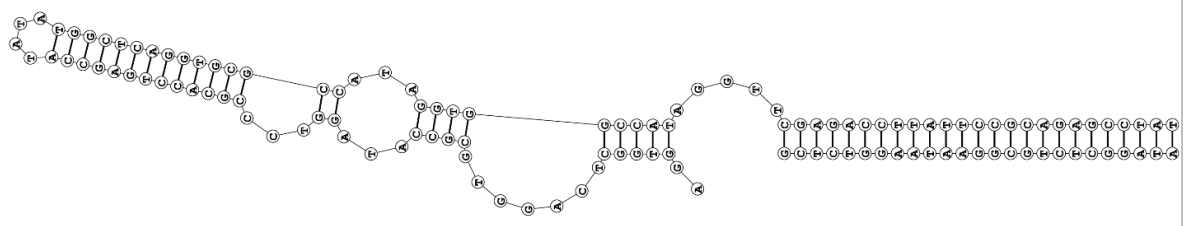

ENERGY = −85.4 probe_ 100bp target

Structure 10

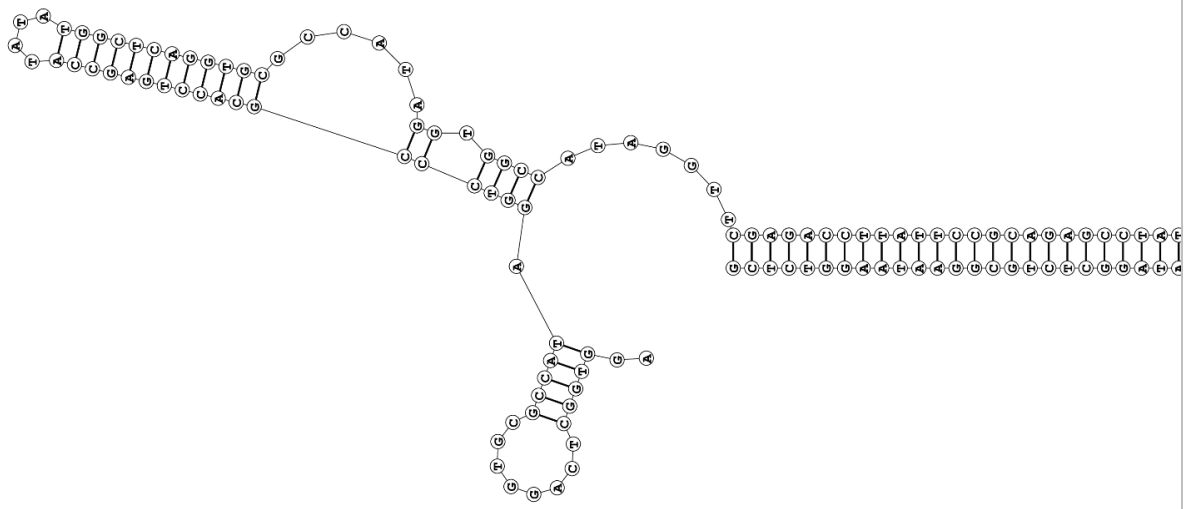

Structure 11

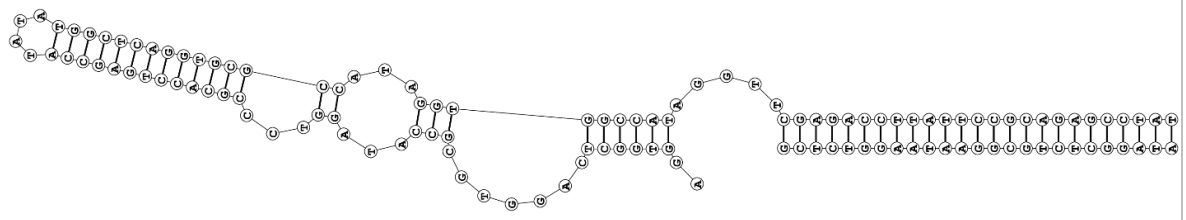

ENERGY = −85.1 probe_ 100bp target

Structure 12

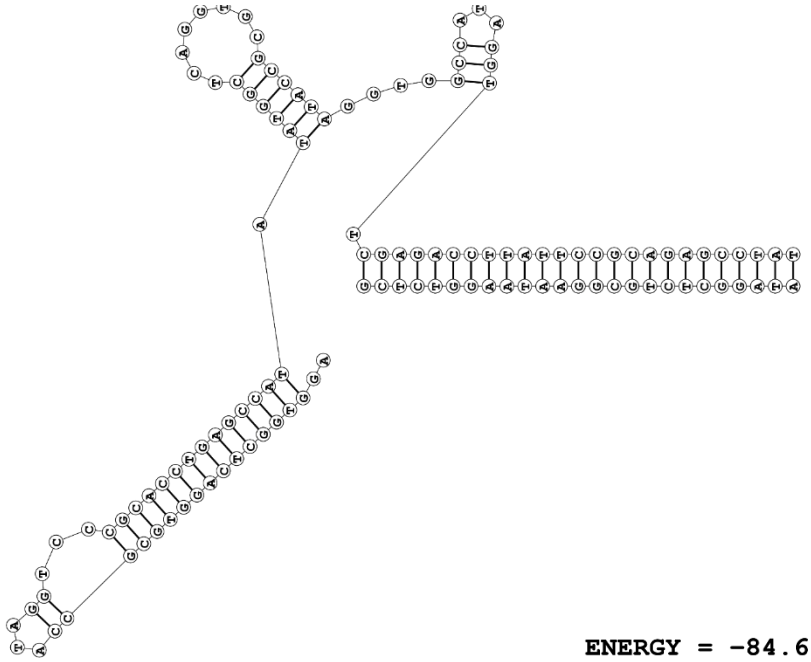

ENERGY = -84.6 probe_ 100bp target

Structure 13

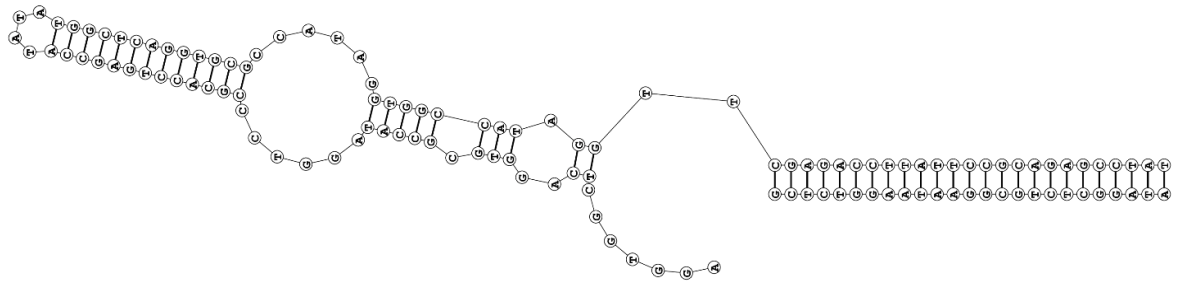

ENERGY = -84.4 probe_ 100bp target

Structure 14

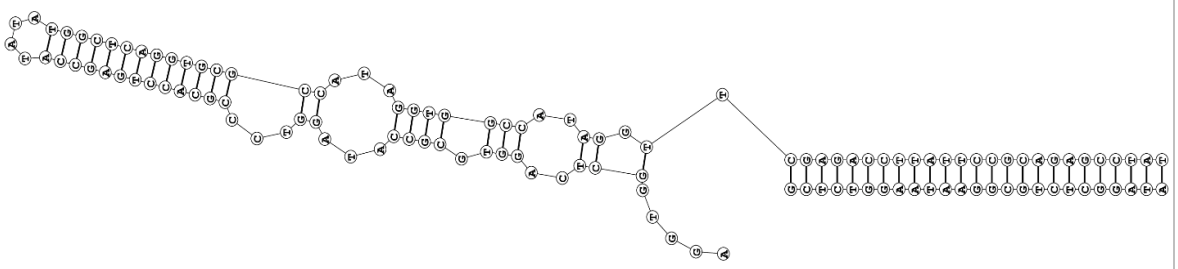

ENERGY = -84.3 probe_ 100bp target

Structure 15

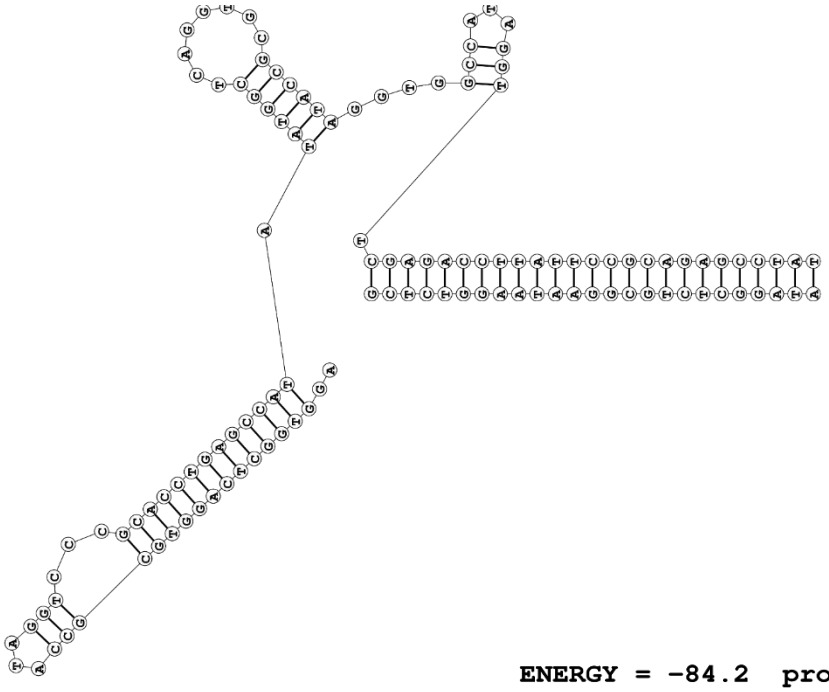

Structure 16

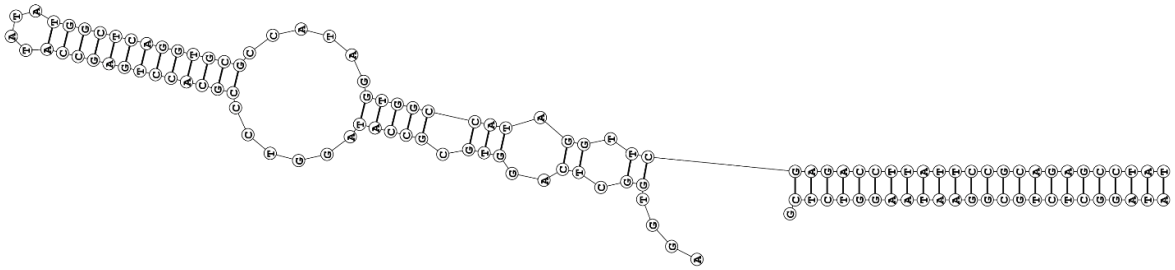

Structure 17

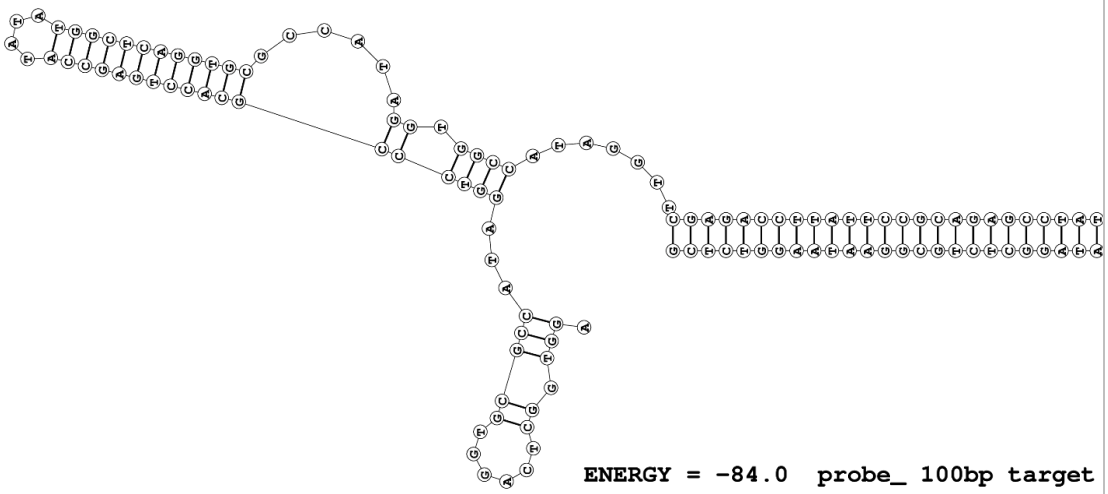

Structure 18

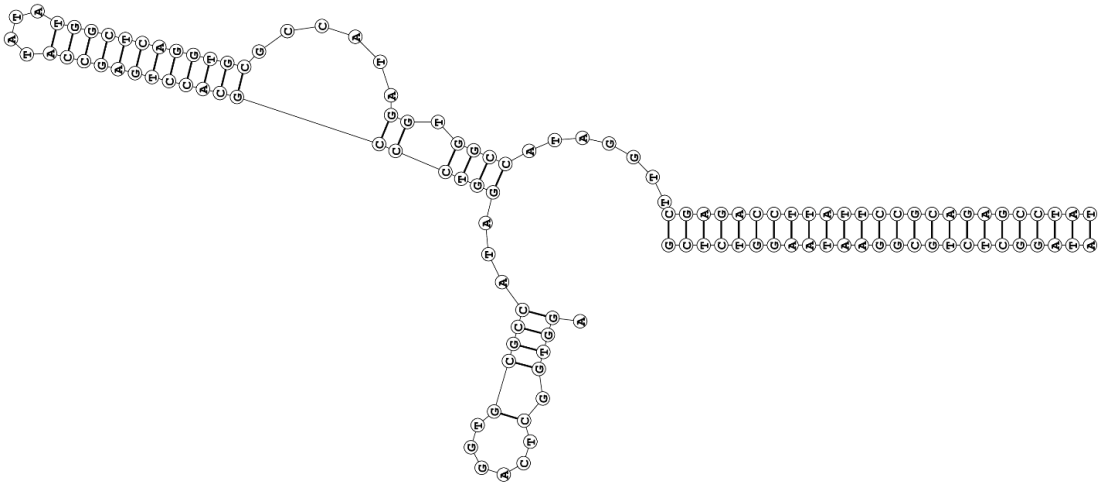

Structure 19

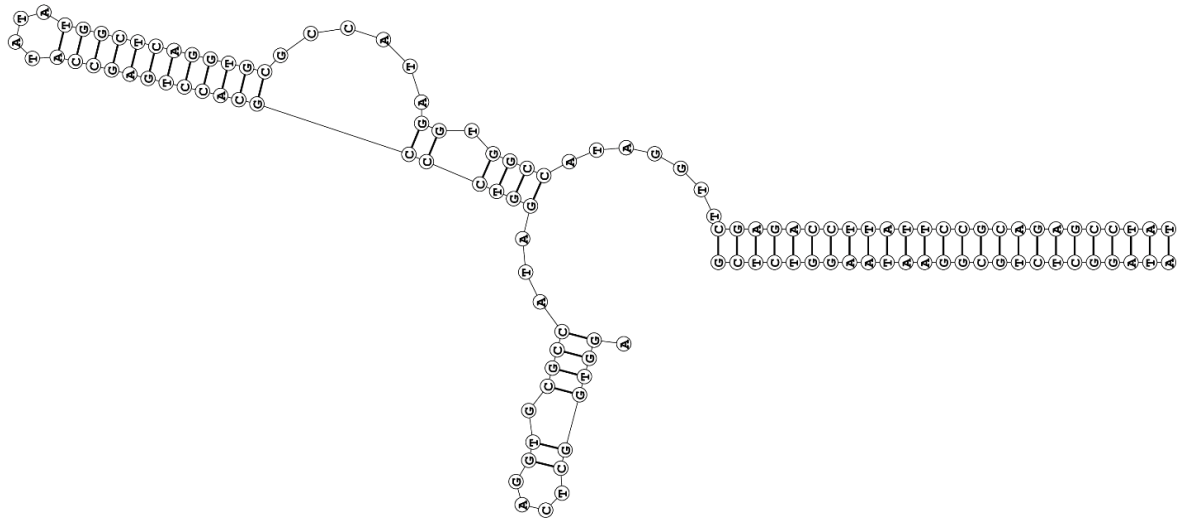

Structure 20

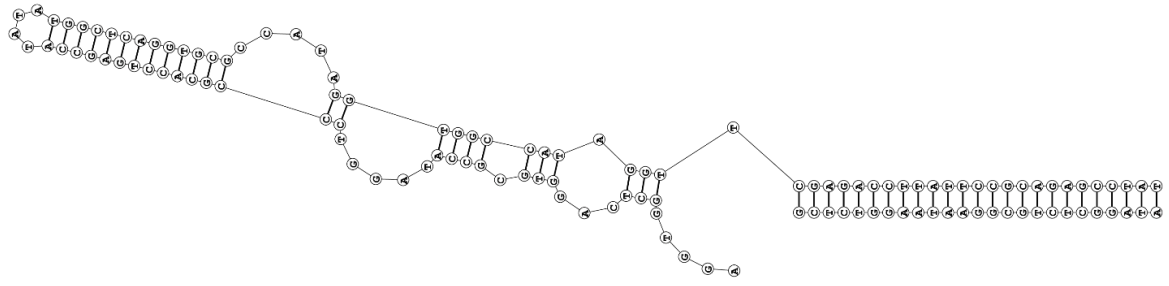

ENERGY = -83.5 probe_ 100bp target